



Spectroscopie atomique et mesures de grande précision : détermination de constantes fondamentales.

Catherine Schwob

► To cite this version:

Catherine Schwob. Spectroscopie atomique et mesures de grande précision : détermination de constantes fondamentales.. Physique Atomique [physics.atom-ph]. Université Pierre et Marie Curie - Paris VI, 2006. tel-00128345

HAL Id: tel-00128345

<https://theses.hal.science/tel-00128345>

Submitted on 31 Jan 2007

HAL is a multi-disciplinary open access archive for the deposit and dissemination of scientific research documents, whether they are published or not. The documents may come from teaching and research institutions in France or abroad, or from public or private research centers.

L'archive ouverte pluridisciplinaire **HAL**, est destinée au dépôt et à la diffusion de documents scientifiques de niveau recherche, publiés ou non, émanant des établissements d'enseignement et de recherche français ou étrangers, des laboratoires publics ou privés.

LABORATOIRE KASTLER BROSSEL

Habilitation à diriger des recherches

Catherine Schwob

**Spectroscopie atomique et mesures de grande précision :
détermination de constantes fondamentales**

soutenue le 6 décembre 2006

Jury : François BIRABEN, examinateur,
André CLAIRON, examinateur,
Jean-Marc FRIGERIO, examinateur,
Jean-Claude GARREAU, rapporteur,
Marc HIMBERT, rapporteur,
Jacques VIGUÉ, rapporteur.

Table des matières

1 Présentation générale	5
2 Spectroscopie de grande sensibilité et optique quantique	9
2.1 Introduction	9
2.2 Les limites à la sensibilité d'une mesure	10
2.3 Le principe de l'expérience	13
2.4 Les éléments du dispositif expérimental	14
2.4.1 L'OPO	14
2.4.2 Le faisceau laser auxiliaire	15
2.4.3 La détection du signal	17
2.5 Les résultats	17
2.6 Conclusion	17
3 Spectroscopie de l'atome d'hydrogène	25
3.1 Introduction	25
3.2 Le contexte	26
3.2.1 La constante de Rydberg	26
3.2.2 Les niveaux d'énergie de l'atome d'hydrogène	27
3.2.3 Les déterminations de R_∞ et du déplacement de Lamb	31
3.2.4 Les mesures tout en fréquence des transitions 2S-nS/D	33
3.3 La mesure de la transition 2S-12D dans l'hydrogène et le deutérium	35
3.3.1 Le schéma de fréquence	36
3.3.2 Le dispositif expérimental	36
3.3.3 Le traitement de données et les résultats	38
3.4 Conclusion et perspectives	42

4 Oscillations de Bloch et détermination de la constante de structure fine	83
4.1 Introduction	83
4.1.1 Le contexte	84
4.1.2 Les différentes déterminations de α	85
4.1.3 Le principe de notre mesure	88
4.2 Le dispositif expérimental	91
4.2.1 Le senseur inertiel	91
4.2.2 L'accélération cohérente des atomes	94
4.3 Les résultats	96
4.3.1 La configuration horizontale	96
4.3.2 La configuration verticale stationnaire : mesure de la période de Bloch	98
4.3.3 La configuration verticale accélérée : mesure de h/m_{Rb}	100
4.4 Comparaison avec l'expérience de Stanford	103
4.4.1 L'interférométrie atomique	104
4.4.2 La comparaison des expériences de Stanford et Paris	106
5 Perspectives	139
5.1 Améliorations sur l'expérience actuelle	139
5.1.1 Augmenter la sensibilité du senseur inertiel	139
5.1.2 Réduire les effets systématiques	140
5.2 Interférométrie avec des oscillations de Bloch	140
5.3 Vers une redéfinition du kilogramme	142
5.3.1 Propositions de redéfinition du kilogramme	143
5.3.2 Notre expérience de mesure de h/m associée à la balance du watt	145

Chapitre 1

Présentation générale

Depuis l'obtention de mon DEA en 1993, mon activité de recherche s'est toujours déroulée au Laboratoire Kastler Brossel.

De 93 à 97, j'ai effectué mon travail de thèse dans l'équipe d'Optique Quantique dirigée par Claude Fabre et Elisabeth Giacobino. L'objectif était d'utiliser les propriétés non classiques de la lumière pour améliorer la sensibilité sur une mesure de faible absorption par une transition atomique. La source de lumière non classique était un oscillateur paramétrique optique (OPO) en régime continu. Les faisceaux générés par conversion paramétrique dans un tel système (appelés faisceaux jumeaux, signal et complémentaire) présentent des corrélations quantiques et, en particulier, les fluctuations de la différence de leurs intensités sont inférieures à la limite quantique standard associée (ou "shot noise").

J'ai développé une expérience de détection d'une faible absorption basée sur un tel système. Plus précisément, j'ai détecté avec une sensibilité sub-shot noise le signal d'absorption de la transition à deux photons de l'atome de potassium $4S-5S$, l'un des photons étant fourni par l'un des faisceaux jumeaux, l'autre par une diode laser auxiliaire. Le signal était mesuré sur la différence des intensités des faisceaux de l'OPO.

Les résultats de cette expérience se sont révélés concluants, puisque le signal, correspondant à une absorption relative de $2,5 \times 10^{-7}$, a été détecté sur un signal de fond réduit de 35% par rapport à la limite quantique standard, avec un temps de mesure de 3 s. Ces résultats auraient néanmoins pu être meilleurs si nous avions disposé à l'époque d'un cristal présentant moins de pertes, et donc conservant une corrélation plus forte entre les faisceaux jumeaux.

A l'issue de ma thèse, j'ai rejoint l'équipe de Métrologie des Systèmes Simples, dirigée par François Biraben et Lucile Julien. Ce changement d'équipe de recherche a

constitué une reconversion thématique puisque je suis passée de l'optique quantique à la physique atomique orientée vers la métrologie. En dehors des aspects expérimentaux dans les deux cas basés sur l'optique et les lasers, le dénominateur commun de ces deux activités de recherche est la spectroscopie (de haute sensibilité pendant ma thèse, de haute résolution par la suite).

A l'époque de mon arrivée, en 1997, tous les efforts étaient concentrés sur la métrologie de l'atome d'hydrogène et la mesure de la constante de Rydberg, thèmes sur lesquels l'équipe possédait une longue expérience. Les transitions à partir du niveau métastable 2S-8D et 2S-10D avaient été mesurées par interférométrie dès 1986. La première mesure tout en fréquence de la transition 2S-8S/D avait été réalisée en 1993 pendant la thèse de François Nez. La précision sur la constante de Rydberg qui avait déjà atteint la valeur de $2,2 \times 10^{-11}$ s'était encore améliorée en 1996 grâce notamment au développement d'un standard de fréquence secondaire à 778 nm stabilisé sur une transition à deux photons du rubidium (incertitude de 8×10^{-12}).

J'ai tout d'abord travaillé sur la réalisation expérimentale de la chaîne de fréquence destinée à la mesure de la transition 2S-12D et participé aux séries d'enregistrements correspondantes. Le but de l'étude de cette transition était moins d'améliorer la précision sur la constante de Rydberg que de tester les corrections Stark qui avaient été rajoutées dans les profils de raie théoriques par Béatrice de Beauvoir et appliquées à la mesure de la fréquence des transitions 2S-8S/D¹.

La transition 2S-12D a marqué la fin de l'étude des transitions à partir du niveau métastable dans l'équipe. Afin d'améliorer les données spectroscopiques sur l'hydrogène, nous nous sommes concentrés sur la transition à partir du niveau fondamental 1S-3S. La connaissance de la fréquence de cette transition, associée à celle de la transition 1S-2S mesurée par l'équipe de T. Hänsch permet en particulier de déterminer le déplacement de Lamb du niveau 1S. L'expérience sur 1S-3S a débuté en 1991 avec la thèse de Sophie Bourzeix. Elle s'est poursuivie avec le travail de Gaëtan Hagel axé sur le développement d'une méthode de compensation de l'effet Doppler du second ordre, puis avec la thèse d'Olivier Arnoult qui a, en particulier, mis en oeuvre un peigne de fréquences référencé sur l'horloge à césium. L'objectif visé est la mesure absolue au kHz de la transition. Un tel résultat, associé aux travaux réalisés sur la transition 1S-2S permettrait de déduire une valeur de la constante de Rydberg à 5×10^{-12} , ainsi qu'une valeur du déplacement de Lamb de l'état 1S à 10 kHz.

A l'heure actuelle, la précision des mesures de la constante de Rydberg a rejoint celle des calculs. Mais la comparaison théorie-expérience comme test de l'électrodynamique

¹Les effets Stark linéaire et quadratique varient respectivement en n^2 et n^7 , n étant le nombre quantique principal.

quantique est limitée par la mauvaise connaissance de la taille de la distribution de charge du proton. Ceci motive l'expérience de spectroscopie de l'hydrogène muonique qui s'est développée à l'Institut Paul Scherrer dans le cadre d'une collaboration internationale. L'hydrogène muonique est composé d'un proton et d'un muon. Celui-ci étant plus lourd que l'électron, est plus sensible à la distribution de charge du proton. L'objectif de l'expérience est de mesurer la fréquence de la transition 2S-2P avec une incertitude relative de 3×10^{-5} , ce qui conduirait à une détermination du rayon de la distribution de charge du proton à 10^{-3} .

Le rôle de notre équipe a initialement consisté à développer un système laser titane saphir à 708 nm. Il s'est étendu à la mesure de fréquence du système laser complet et à la production de la radiation excitatrice à $6 \mu m$.

Cette expérience est rendue très délicate par la faible probabilité de transition (10^7 fois plus faible que dans le cas de l'atome d'hydrogène). Deux périodes de prises de données se sont déroulées à l'Institut Paul Scherrer entre juillet et octobre 2002 et entre juin et novembre 2003. La transition recherchée n'a pas été observée jusqu'à présent, probablement à cause d'une statistique de signal trop faible.

Depuis 1999, mis à part une petite contribution à l'expérience de mesure du "rayon du proton" et aux débuts du travail de thèse d'Olivier Arnoult sur le laser femtoseconde, mon activité de recherche est axée sur une nouvelle expérience visant à mesurer la vitesse de recul d'un atome de rubidium. La connaissance de la vitesse de recul constitue un moyen de déterminer le rapport h/m_{Rb} (h étant la constante de Planck et m_{Rb} la masse de l'atome) ainsi que la constante de structure fine α .

Le principe de notre méthode consiste à accélérer les atomes en leur transférant un grand nombre de fois la vitesse de recul au moyen d'oscillations de Bloch. Leur variation de vitesse entre le début et la fin du processus d'accélération est mesurée à l'aide d'un senseur inertiel composé de deux transitions Raman sélectives en vitesse. Nous avons tout d'abord accéléré les atomes suivant la direction horizontale, montrant ainsi l'excellente efficacité du processus utilisé. Nous sommes par la suite passés à une accélération suivant la verticale et avons pu transférer aux atomes près de 1800 vitesses de recul. Ce travail a abouti en 2005 à une détermination de α avec une incertitude relative de $6,7 \times 10^{-9}$ ce qui la rend compétitive avec les valeurs les plus précises obtenues en interférométrie atomique. Cette expérience a débuté avec la thèse de Rémy Battesti et s'est poursuivie avec celles de Pierre Cladé, Estéfania de Mirandes et Malo Cadoret.

Ce manuscrit suit l'ordre chronologique de mon activité de recherche. A la suite de ce chapitre introductif,

- le chapitre deux est un rappel de mes travaux de thèse sur l'optique quantique appli-

quée à la spectroscopie de grande sensibilité,

- le chapitre trois traite de la spectroscopie de l'atome d'hydrogène. Après avoir retracé le contexte et l'historique de la mesure de la constante de Rydberg, j'y décris les grandes lignes de l'étude de la transition 2S-12D.

- le chapitre quatre est dédié à l'expérience basée sur les oscillations de Bloch et visant à déterminer la constante de structure fine.

- le chapitre cinq conclut sur les perspectives de cette dernière expérience.

A la fin de chaque chapitre sont joints les articles les plus significatifs correspondant au thème développé.

Chapitre 2

Spectroscopie de grande sensibilité et optique quantique

2.1 Introduction

L'équipe de recherche dirigée par Claude Fabre et Elisabeth Giacobino est une équipe pionnière dans le domaine de l'optique quantique. Elle travaille depuis de nombreuses années sur la réduction des fluctuations quantiques de la lumière sur des systèmes très variés. Ce thème de recherche a débuté avec l'oscillateur paramétrique optique (OPO) (cristal non linéaire en cavité), puis il s'est étendu aux atomes froids ([1], [2], [3]), aux diodes lasers et aux VCSELs en mettant à profit le principe de la pompe régulière ([4], [5], [6], [7], [8], [9], [10], [11]), et, plus récemment aux micro-cavités ([12] [13], [14], [15]).

L'OPO s'est révélé être un système très riche pour produire des états comprimés, c'est-à-dire des états de la lumière présentant des fluctuations inférieures à la limite quantique standard (ou shot noise). En particulier, il permet de générer des faisceaux, que l'on qualifie par le terme "faisceaux jumeaux", dont les fluctuations de la différence des intensités sont corrélées au niveau quantique. D'autre part, utilisé en dessous du seuil d'oscillation, l'OPO produit du vide comprimé, c'est-à-dire un champ de valeur moyenne nulle dont les fluctuations sont en dessous de la limite quantique standard. Dès 1992, un tel état a été mis à profit dans une expérience de spectroscopie sub-shot noise [16]. Le faisceau pompe réfléchi par la cavité, ainsi que chacun des faisceaux produits par l'OPO présentent également un bruit d'intensité réduit.

La majeure partie de mon travail de thèse a consisté à mettre à profit les propriétés de réduction de bruit des faisceaux jumeaux produits par un OPO en régime continu

pour augmenter la sensibilité de mesures spectroscopiques au delà de la limite quantique standard. L'un des intérêts de cette approche est d'augmenter la sensibilité d'une mesure sans avoir recours aux techniques habituelles consistant à augmenter l'intensité lumineuse ou le temps de mesure. En effet, dans certains cas, une intensité lumineuse trop importante (générée par exemple par un OPO en impulsions) peut engendrer des phénomènes de saturation. Un temps de mesure très long exclut l'observation de phénomènes transitoires.

Ce chapitre, dédié à mon travail de thèse, et plus précisément à l'expérience de spectroscopie de grande sensibilité que j'ai développée, se décompose en quatre parties. J'y décris successivement l'intérêt d'utiliser les propriétés non classiques de la lumière en spectroscopie, le principe de la mesure, les points clés du montage expérimental et les résultats obtenus. L'article [17] dans lequel a été publiée cette expérience est joint à la fin du chapitre.

2.2 Les limites à la sensibilité d'une mesure

La sensibilité d'une expérience de spectroscopie est limitée par le bruit, ou plus précisement par les fluctuations d'intensité, du faisceau lumineux utilisé. Pour s'affranchir du bruit propre du faisceau, il est possible de réaliser une mesure différentielle au moyen d'une lame semi-réfléchissante (voir figure 2.1). La sensibilité est alors donnée par le bruit de photons (ou shot noise ou limite quantique standard), c'est-à-dire par la statistique poissonnienne des instants d'arrivée des photons sur les détecteurs. Ceci constitue la limite ultime d'une mesure en lumière classique. Pour aller au delà de la

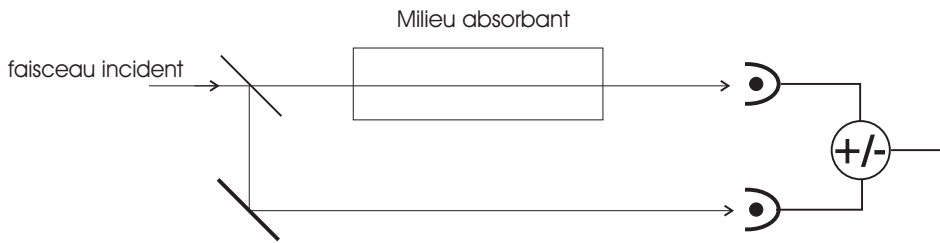


FIG. 2.1 – Principe de la mesure différentielle

limite quantique standard, il faut travailler sur le caractère quantique des fluctuations de la lumière. Avant de parler des faisceaux jumeaux produits par un OPO, je vais brièvement faire quelques rappels sur le bruit quantique en général.

Considérons l'opérateur champ électrique, caractérisé par une amplitude E_0 et une

pulsation ω . Il peut s'écrire sous la forme

$$\hat{E} = E_0(\hat{a} \exp(-i\omega t) + \hat{a}^+ \exp(i\omega t)) \quad (2.1)$$

\hat{a} et \hat{a}^+ étant respectivement les opérateurs d'annihilation et de création d'un photon, ou bien en termes de quadratures de champ,

$$\hat{E} = \hat{E}_1 \cos \omega t + \hat{E}_2 \sin \omega t \quad (2.2)$$

où \hat{E}_1 et \hat{E}_2 sont deux quadratures orthogonales avec $[\hat{E}_1, \hat{E}_2] \neq 0$.

L'inégalité de Heisenberg s'écrit :

$$\Delta E_1 \cdot \Delta E_2 \geq E_0^2 \quad (2.3)$$

en notant ΔE_1 et ΔE_2 les amplitudes des fluctuations associées respectivement aux quadratures \hat{E}_1 et \hat{E}_2 .

Dans le cas d'un faisceau présentant du bruit classique, les amplitudes ΔE_1 et ΔE_2 sont toutes deux supérieures à E_0 .

Un état cohérent est un état dont les fluctuations sont minimales suivant toutes les quadratures :

$$\Delta E_1 = \Delta E_2 = E_0 \quad (2.4)$$

Les fluctuations du champ sont alors représentées par un disque dans l'espace des phases et donnent la limite quantique standard associée à cet état (voir figure (2.2(A)).

Cependant, l'inégalité de Heisenberg n'interdit pas de comprimer les fluctuations sur l'une des quadratures du champ en dessous de la limite quantique standard, à condition que les fluctuations sur la quadrature orthogonale soient amplifiées en conséquence. On parle alors d'état comprimé. Dans l'espace des phases, les fluctuations d'un tel état sont représentées par la surface d'une ellipse, dont le petit axe correspond à la quadrature comprimée (\hat{E}_1 sur la figure (2.2(B))).

L'OPO est composé d'un milieu non linéaire d'ordre deux, placé dans une cavité optique. On réalise ainsi de la génération paramétrique, c'est-à-dire, la production à partir d'un faisceau pompe de pulsation ω_0 de deux faisceaux de pulsations ω_1 et ω_2 , appelés faisceaux signal et complémentaire tels que :

$$\omega_0 = \omega_1 + \omega_2 \quad (2.5)$$

La cavité optique permet de recycler la lumière ainsi produite et donc d'amplifier cet effet non linéaire. Les faisceaux de pulsation ω_1 et ω_2 étant créés au cours du même processus quantique, ils sont parfaitement corrélés à la sortie du cristal. Cet effet

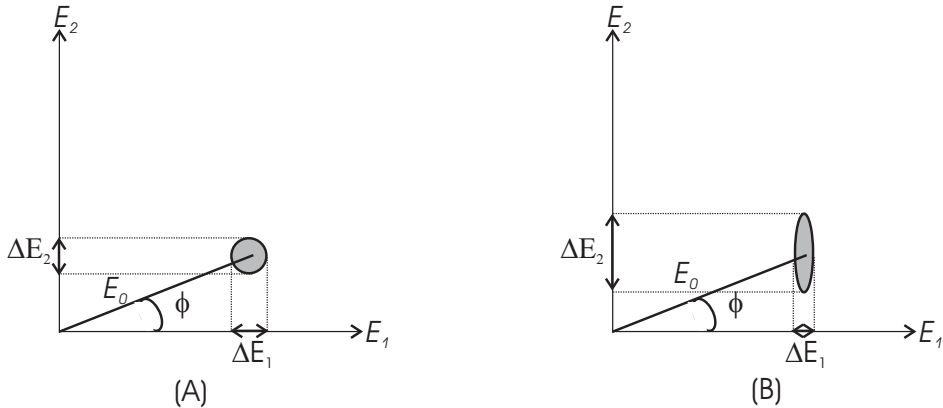


FIG. 2.2 – Représentation du champ électrique dans l'espace des phases. La valeur moyenne du champ est représentée par le trait de longueur E_0 et les fluctuations par une surface située à l'extrémité de ce trait. (A) état cohérent, (B) état comprimé suivant la quadrature \hat{E}_1 .

apparaît sur différentes observables des champs en fonction de la façon dont l'OPO est utilisé. En particulier, il se manifeste sur la différence des intensités des faisceaux signal et complémentaire produits au dessus du seuil d'oscillation, dont les fluctuations sont, dans le cas idéal, parfaitement identiques. Si l'on détecte la différence des intensités des deux faisceaux moyennée sur des temps très longs (c'est-à-dire longs devant la durée de vie de la cavité), on mesurera une quantité strictement nulle, sans fluctuations. Des taux de corrélation de 86 % ont été observés dans notre laboratoire [18]. Afin de pouvoir séparer les faisceaux jumeaux en polarisation, on utilise des cristaux non linéaires de type II (voir figure (2.3)).

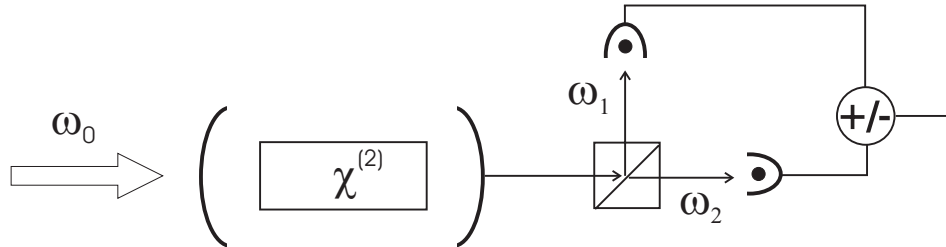


FIG. 2.3 – Détection des faisceaux jumeaux pour un cristal de type II. Les deux photodiodes doivent être parfaitement équilibrées.

Comparons maintenant les expressions des rapports signal à bruit correspondants à une mesure directe, à une mesure différentielle et finalement, à une mesure sur la différence des intensités des faisceaux jumeaux produits par l'OPO. On considère (comme

ce sera le cas expérimentalement) un milieu faiblement absorbant dont le coefficient de transmission α est proche de l'unité ($\alpha = 1 - \frac{a}{2}$ avec $a \ll 1$). Le rapport signal à bruit en puissance est égal au signal à résonance, divisé par le bruit hors résonance, soit

$$\frac{S}{B} = \frac{\bar{I}_{out}^{res2}}{\Delta^2 I_{out}} \quad (2.6)$$

où le signal est caractérisé par le carré du photocourant détecté par la photodiode à résonance (\bar{I}_{out}^{res2}) et le bruit par la variance de l'intensité lumineuse sortante ($\Delta^2 I_{out} = 2S_{I_{out}} \times \Delta\nu$ avec $S_{I_{out}}$ la densité spectrale de bruit en A^2/Hz et $\Delta\nu$, la bande passante d'analyse). On peut montrer que dans le cas de très faibles absorptions, le bruit rajouté par l'absorption est négligeable et que par conséquent l'équation (2.6) s'écrit (voir [19]) :

$$\frac{S}{B} = \frac{(\Re e(a))^2 \bar{I}_{in}}{2(1 + Ex)\Delta\nu} \quad (2.7)$$

où \bar{I}_{in} est la valeur moyenne du photocourant incident sur le milieu faiblement absorbant et Ex , l'excès de bruit de ce même faisceau par rapport à la limite quantique standard.

Considérons à présent le cas d'une mesure différentielle comme représentée sur la figure (2.1). On peut montrer que le rapport signal à bruit s'écrit :

$$\frac{S}{B} = \frac{(\Re e(a))^2}{4} \frac{\bar{I}_{in}}{2\Delta\nu} \quad (2.8)$$

A un facteur 4 près, cette expression est égale à la relation (2.7) en posant $Ex = 0$. Le rapport signal à bruit ainsi obtenu ne dépend donc pas de l'excès de bruit du faisceau incident. La sensibilité de la mesure est limitée par le bruit de photons. Le facteur 4 provient du fait que l'on perd la moitié de l'intensité lumineuse au passage de la lame semi-réfléchissante.

Dans le cas des faisceaux jumeaux produits par un OPO, on introduit $\Sigma(\Omega = 0)$, le taux de corrélation des faisceaux jumeaux à fréquence nulle et le rapport signal à bruit devient :

$$\frac{S}{B} = \frac{(\Re e(a))^2}{4} \frac{\bar{I}_{in}}{2\Delta\nu\Sigma(\Omega = 0)} \quad (2.9)$$

La sensibilité de la mesure n'est plus limitée par le bruit de photons du faisceau. Elle dépend à présent du taux de corrélation.

2.3 Le principe de l'expérience

Le principe général de l'expérience consiste à envoyer l'un des faisceaux jumeaux produits par l'OPO sur un milieu atomique faiblement absorbant et de détecter cette

absorption sur la différence des intensités. Afin de profiter d'un taux de corrélation maximum, nous travaillons à des fréquences de l'ordre du MHz, ce qui implique de détecter un signal modulé. Pour ne pas rajouter de bruit sur l'un des faisceaux de l'OPO, et donc ne pas dégrader le taux de corrélation, il est préférable d'utiliser un faisceau laser auxiliaire porteur de la modulation. Cette méthode, schématisée par la figure (2.4), implique de détecter une transition à deux photons (l'un étant produit par l'un des faisceaux jumeaux, l'autre par le laser auxiliaire). De plus, le fait d'appliquer la modulation sur un faisceau autre que le faisceau détecté permet de mesurer un signal sur fond noir (au lieu de détecter une variation de l'amplitude de modulation).

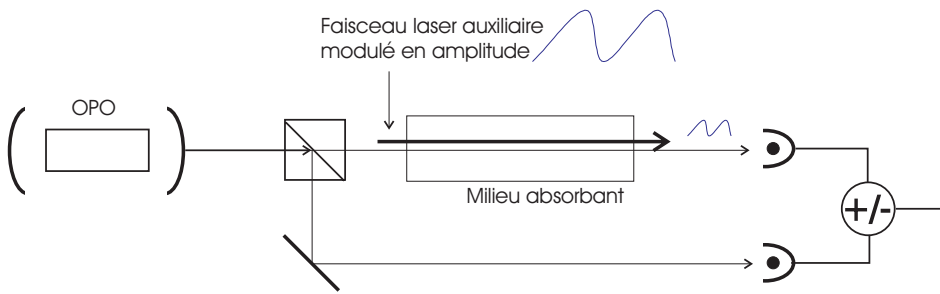


FIG. 2.4 – Schéma de principe de l'expérience de spectroscopie utilisant des faisceaux jumeaux. Les faisceaux traversant le milieu absorbant se propagent dans le même sens. Le signal détecté correspond donc à la raie élargie par effet Doppler, plus facile à pointer.

En résumé, l'expérience consiste à détecter un transfert de modulation du laser auxiliaire au faisceau jumeau par l'intermédiaire du milieu atomique, à résonance, ce qui revient à moduler la transmission du milieu atomique.

2.4 Les éléments du dispositif expérimental

Ce paragraphe récapitule brièvement les éléments clé de l'expérience et les contraintes associées (pour plus de détails, voir la référence [17] ci-jointe). Le signal atomique à détecter est la transition à deux photons 4S-5S de l'atome de potassium. Comme la longueur d'onde de l'un des photons est fixée à 1064 nm par l'OPO, l'autre doit être de l'ordre de 859 nm.

2.4.1 L'OPO

La chaîne laser dédiée à la production des faisceaux jumeaux est représentée par la figure (2.5). On utilise un OPO continu fonctionnant vers 1064 nm. Le cristal non

linéaire est un cristal de KTP dont l'accord de phase est réalisé à température ambiante. La cavité optique est triplement résonnante, c'est-à-dire résonnante pour les champs pompe, signal et complémentaire. La configuration semi-monolitique (le miroir d'entrée est constitué par la face d'entrée traitée du cristal) a été choisie car elle permet de balayer aisément la longueur de la cavité (grâce à une cale piézoélectrique solidaire du miroir de sortie) tout en gardant un caractère compact permettant de réduire les instabilités dues aux mouvements d'air et aux vibrations.

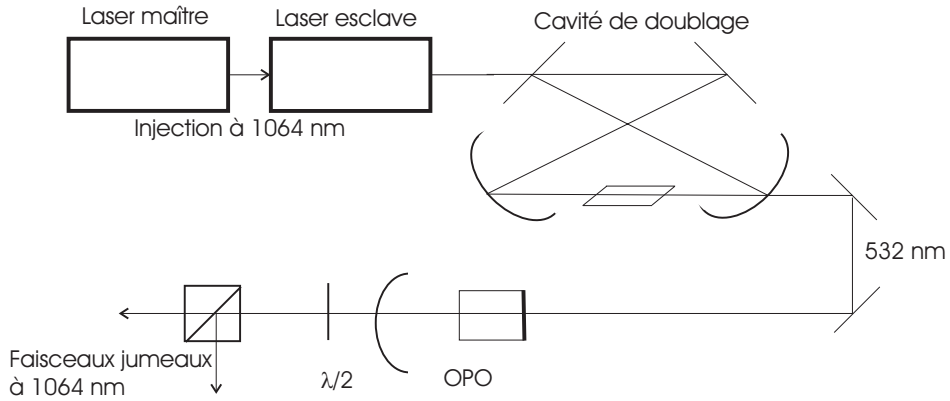


FIG. 2.5 – Les différents éléments constituant la source de faisceaux jumeaux.

Le faisceau de pompe est fourni par un laser Nd :YAG pompé par flash et doublé en cavité externe. Il est stabilisé en fréquence par injection d'un laser Nd :YAG commercial, pompé par diode et délivrant un faisceau de 350 mW. Le doublage est réalisé par un cristal de LBO placé dans une cavité en anneau de finesse de l'ordre de 50.

Finalement, pour un faisceau pompe de l'ordre de 5 W, on obtient environ 400 mW à 532 nm et typiquement 6 mW à 1064 nm par faisceau jumeau.

Le taux de corrélation entre les faisceaux jumeaux est de 1,88 dB à 3 MHz, ce qui correspond à une compression des fluctuations sur la différence des intensités de faisceaux jumeaux de 35 % par rapport à la limite quantique standard (figure (2.6))¹. Ce résultat, assez décevant par rapport à ce que l'on peut attendre d'un OPO, s'explique par un coefficient d'absorption du cristal de KTP important.

2.4.2 Le faisceau laser auxiliaire

Il est fourni par une diode laser à 859 nm. Sa fréquence peut être balayée sans saut de modes sur 7 GHz, ce qui est amplement suffisant puisque la largeur Doppler du

¹Il s'agit du taux de corrélation "utile" au niveau de la cellule de potassium, après les pertes subies au passage des différents éléments optiques. A la sortie de l'OPO, le taux de corrélation est de 3 dB.

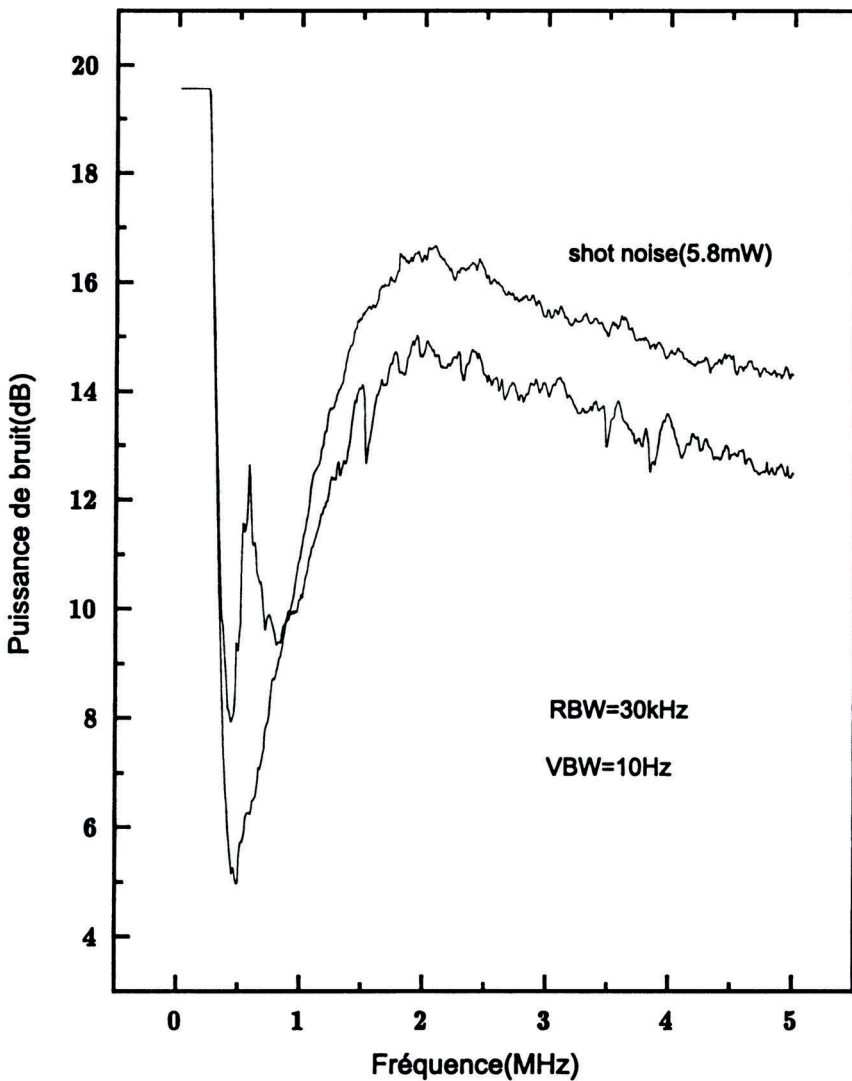


FIG. 2.6 – Taux de corrélation des faisceaux jumeaux comparé à la limite quantique standard. Courbe du haut : le shot noise de la somme des intensités des faisceaux jumeaux est obtenu en orientant la lame $\lambda/2$ représentée sur la figure 2.5 de façon à ce que les directions de polarisation des faisceaux soient à 45° des axes du cube. Courbe du bas : le taux de corrélation entre les faisceaux est obtenu en orientant la lame de façon à ce que les directions de polarisation des faisceaux soient parallèles aux axes du cube.

signal attendu est de l'ordre de 1 GHz.

2.4.3 La détection du signal

Le signal à détecter est une modulation d'amplitude. Cette modulation doit être appliquée sur le faisceau du laser auxiliaire. En effet, si on modulait l'un des faisceaux jumeaux, on détériorerait le taux de corrélation en sortie de l'OPO. L'avantage du choix de la modulation d'amplitude est qu'il permet de détecter le signal directement sur la quadrature sensible à la réduction de bruit, c'est-à-dire sur l'intensité des faisceaux.

Pour s'affranchir d'éventuels signaux parasites, on procède à une double modulation : l'une à 3 MHz réalisée au moyen d'un modulateur électro-optique, l'autre vers 660 Hz au moyen d'une roue dentée.

Le système de détection des faisceaux jumeaux est composé de deux photodiodes en InGaAS, équilibrées, de rendement quantique supérieur à 92 %. La double démodulation du signal est réalisée par deux détections synchrones.

2.5 Les résultats

Le signal expérimental est représenté par la figure (2.7). Il correspond à une absorption relative de $2,5 \times 10^{-7}$. La largeur Doppler de la transition à deux photons mesurée est de 1,6 GHz. Ce signal a été enregistré avec une bande passante de 3 Hz. Le bruit de fond est réduit de 1,88 dB, soit 35 % par rapport à la limite quantique standard. Cette expérience constitue, à ma connaissance, la première expérience de spectroscopie en lumière non classique, utilisant un OPO continu [17].

2.6 Conclusion

Au cours de mon travail de thèse, nous avons démontré expérimentalement la possibilité de réaliser des mesures spectroscopiques de grande sensibilité avec les faisceaux jumeaux produits par un OPO continu, fonctionnant au dessus du seuil d'oscillation. Le signal spectroscopique a été observé sur un bruit de fond réduit en mettant à profit les propriétés de corrélations quantiques des faisceaux. L'objectif de ce travail était de montrer qu'il était possible d'augmenter la sensibilité d'une mesure en utilisant un OPO. Par la suite, l'équipe d'optique quantique n'a pas poursuivi cet axe de recherche, mais d'autres groupes ont obtenu des résultats tout à fait remarquables sur des expériences analogues. En particulier, des signaux très peu intenses ont été mesurés dans des solvants contenant une très faible concentration d'absorbant, avec des faisceaux jumeaux corrélés à 9 dB sous la limite quantique standard. L'équipe de Shanxi a pu ainsi augmenter la sensibilité de la mesure de 7 dB par rapport au shot noise [20].

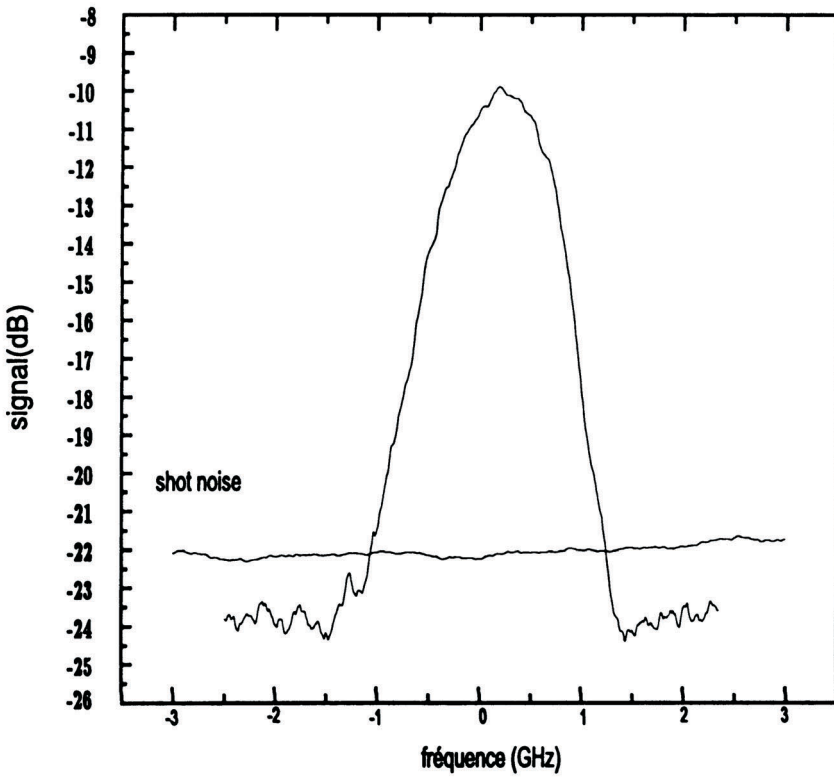


FIG. 2.7 – Spectroscopie en lumière non classique de la transition 4S-5S du potassium.

Par la suite, le groupe "OPO" de l'équipe d'optique quantique du LKB a orienté ses activités de recherche suivant deux axes. D'une part, il étudie en détail les propriétés aussi bien classiques que quantiques des milieux paramétriques dans le but de produire des états non-classiques de la lumière et de réaliser des protocoles d'information quantique ([21]).

D'autre part, le second thème, qui se positionne dans la continuité de mon travail de thèse, consiste à décrire les corrélations spatiales des faisceaux émis par un OPO. Ces études sont motivées par l'amélioration de la sensibilité dans les mesures de grande précision, en particulier en ce qui concerne l'imagerie quantique ([22], [23], [24]).

Article joint

P.H. Souto Ribeiro, C. Schwob, A. Maître and C. Fabre, Optics Lett., **22** (1997) 1893 :
"Sub-shot noise high-sensitivity spectroscopy with optical parametric oscillator twin
beams."

Sub-shot-noise high-sensitivity spectroscopy with optical parametric oscillator twin beams

P. H. Souto Ribeiro, C. Schwob, A. Maître, and C. Fabre

Laboratoire Kastler Brossel, Université Pierre et Marie Curie, Case 74, 75252 Paris Cedex 05, France

Received August 11, 1997

Nondegenerate optical parametric oscillators generate above-threshold signal and idler beams that have intensity fluctuations correlated at the quantum level (twin beams). We describe what is to our knowledge the first high-sensitivity spectroscopy experiment using twin beams emitted by a cw optical parametric oscillator: a very weak two-photon absorption signal, in the 10^{-7} range, is recorded on the $4S_{1/2} - 5S_{1/2}$ transition of atomic potassium with a noise background that is reduced by 1.9 dB with respect to the shot-noise limit of the light used in the experiment. © 1997 Optical Society of America

During recent years the interest in optical parametric oscillators (OPO's) has been steadily growing. On the one hand, these devices are able to produce laser-like beams in a vast range of wavelengths, which opens the way to numerous applications.¹ In particular, OPO's turn out to be promising sources for spectroscopic measurements because of their intrinsic narrow linewidth and their broad range of generated wavelengths, mainly in the pulsed regime. On the other hand, these devices are known to produce nonclassical states of light that have fluctuations below the standard quantum limit in various observables.^{2,3} In particular, when they are operated above threshold they produce twin beams that have highly correlated intensity fluctuations in the signal and idler modes,^{4,5} so the quantum noise in the difference between the two beam intensities is significantly reduced below the standard quantum limit. We show in this Letter that it is possible to take advantage of these two interesting features in a single experiment, and we demonstrate that one can use OPO's to perform a high-sensitivity spectroscopy experiment beyond the shot-noise limit.

Several experiments have shown that one can improve the sensitivity of a spectroscopic measurement by using either a squeezed vacuum⁶ or sub-Poissonian diode lasers.^{7,8} The experiments consisted of saturation absorption spectroscopy of the resonance lines of Cs and Rb and required either strongly absorbing species or intense light beams. Our purpose, on the contrary, is to show the potentialities of nonclassical light for the measurement of weakly absorbing species by use of moderate light powers. Let us also mention other experiments in which nonclassical light was used to detect weak signals beyond the shot-noise limit.^{9–11}

Let us consider here a simple absorption spectroscopy experiment in which the intensity of a light beam transmitted through an absorbing medium is directly recorded while the light frequency is scanned through resonance. The sensitivity of this experiment is limited by the intensity noise of the light source, which is usually above the shot-noise level. To improve the signal-to-noise ratio, spectroscopists use a differential measurement: A beam splitter placed before the absorbing region creates a reference beam, which is directly measured, and a transmitted beam,

which interacts with the absorbing medium. The absorption signal is then measured on the difference between the intensities of the transmitted beam and the reference beam. In this case the sensitivity of the measurement is limited by the shot noise of the incoming beam (before the beam splitter) because the differential technique suppresses the excess noise of the input beam but not the quantum-noise part. It is possible to go below this shot-noise limit if one uses the twin beams generated by an OPO: The absorption signal is measured on the difference between the intensities of the signal beam that is transmitted through the absorbing medium and the idler beam, which is used as a reference beam. The noise in this intensity difference can be zero in principle and is well below the shot-noise limit of the classical differential measurement in actual experiments.

Doubly or triply resonant OPO's are difficult to frequency tune continuously without mode hopping because of the need to fulfill simultaneous cavity resonance conditions.¹² Furthermore, as the noise reduction on the intensity difference is effective only at nonzero noise frequencies, transferring the signal in this frequency range requires a modulation technique. The modulation of one of the correlated beams usually degrades the quantum-noise reduction.¹³ We demonstrate here that the use of a two-photon transition, with the help of an auxiliary laser source, can circumvent these limitations: The two-photon resonance is induced by the signal beam from the OPO and by an auxiliary laser beam, which is frequency scanned and modulated; at resonance, the upper-state population, and therefore the absorption of the signal beam, is also modulated. It is then possible to record the modulated absorption of the signal beam transmitted through the medium on the difference between the signal and idler beam intensities without perturbing the quantum correlation between these two beams.

The experiment is performed on the $4S_{1/2} \rightarrow 5S_{1/2}$ two-photon transition in atomic potassium¹⁴ that is induced by the OPO signal beam at $\lambda_{\text{OPO}} \approx 1.064 \mu\text{m}$ (9394 cm^{-1}) and by an auxiliary diode laser at $\lambda_{\text{aux}} \approx 0.859 \mu\text{m}$ (11632 cm^{-1}). The energy mismatch between the $4P$ intermediate levels and the intermediate energy that is brought by one laser photon is roughly equal to 1400 cm^{-1} . Figure 1 shows

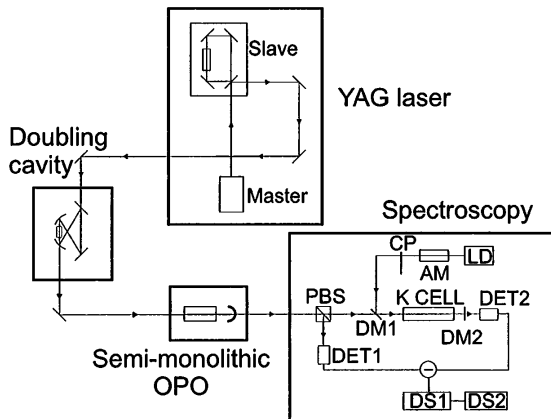


Fig. 1. Experimental setup.

the experimental setup. A flash-lamp-pumped, cw single-mode slave YAG laser with a power of 4 W, injected by a frequency-stable, low-power diode-pumped master YAG laser, is frequency doubled in a ring external doubling cavity containing a lithium triborate crystal. The power generated at 532 nm by this device is 900 mW at best and is typically of the order of 400 mW. It is used to pump a triply resonant semimonolithic OPO. The input mirror of the OPO cavity is highly reflective for the infrared and has a transmission of 10% for the green, and the output mirror has a transmission of 5% for the green and 4% for the infrared. The potassium titanyl phosphate (KTP) crystal used in the OPO is stabilized at room temperature, and the OPO cavity length is stabilized close to resonance by an electronic servo loop. We obtain the error signal by detecting the intensity of the idler beam and comparing its time-averaged value with a reference voltage. The signal and idler beams are separated at the output by a polarizing beam splitter (PBS). The idler beam is directly detected by a photodetector (DET1), whereas the signal beam is sent through the cell containing atomic potassium, heated to 230 °C, and then detected by a photodetector (DET2) identical to DET1. The total transmission of the different elements inserted into the signal beam is 85%. We use InGaAs Epitaxx ETX-300 p-i-n photodiodes with measured quantum efficiencies of 90%.

The auxiliary beam used to induce the two-photon transition, provided by a single-mode diode laser (LD) with an available power of 80 mW after the optical isolator, is amplitude modulated at $\nu_{HF} = 3$ MHz by an electro-optic modulator (AM) and chopped by a mechanical chopper (CP) at a frequency ν_{LF} of 650 Hz. It is then superimposed upon the signal beam by a dichroic mirror (DM1). The two beams are focused at the center of the potassium cell, with a common beam waist of 100 μm , corresponding to a Rayleigh length of 3 cm. This geometry allows us to maximize the two-photon transition probability in the 14-cm-long cell. After the cell, the auxiliary beam is rejected before DET2 by two dichroic mirrors (DM2), which ensures that no residual background modulation is detected by DET2 (at the 10^{-8} level). In these conditions the optical noise of the auxiliary laser beam plays no role

in the background noise of our signal detected on the twin-beam intensity difference. The signal and diode laser beams can also be sent to a homemade lambdameter to measure their wavelengths with an absolute accuracy of $10^{-6} \mu\text{m}$.

After photodetection, the spectroscopic signal is obtained by a two-step demodulation procedure: The first one (DS1) uses a local oscillator at frequency ν_{HF} of the electro-optic modulator, and the second (DS2) uses a reference signal synchronous with the low-frequency ν_{LF} modulation produced by the mechanical chopper. The amplitude and the phase of the demodulated signal are registered in a digital oscilloscope while the semiconductor laser wavelength is slowly scanned by a digital current ramp. The time constant for the filter of the lock-in amplifier is 300 ms, giving a final resolution bandwidth for the total detection system of ~ 3 Hz. This double modulation scheme has been adopted to record a signal at Fourier frequencies that are not generated in any electronic device in our experimental setup, which ensures that there is no interfering background signal at these frequencies. To compare the signal-to-noise ratio of our experimental setup with that of a shot-noise-limited experiment, we can replace the twin beams produced by the OPO by a laser beam generated by a single-mode YAG laser that has the same total intensity and is divided into two equal parts by the PBS, so that the noise recorded in the intensity difference is equal to the standard quantum-noise level. The quantum-noise reduction directly at the output of the OPO is estimated to be roughly 3 dB near 3 MHz. This value, smaller than in previous experiments,⁵ is limited by the nonnegligible losses in the KTP crystal that we used and by the stability of the setup. When it is measured in the spectroscopy setup with all its components, the quantum-noise reduction is further reduced by the losses in the different optical elements to a value of 1.9 dB at a noise frequency of 3 MHz.

Figure 2(a) displays the amplitude signal output of the lock-in amplifier, recorded with a 20-mW diode laser beam of 0.859287- μm wavelength and a 5.8-mW signal OPO beam of 1.064438- μm wavelength. The resonant two-photon modulation transfer signal

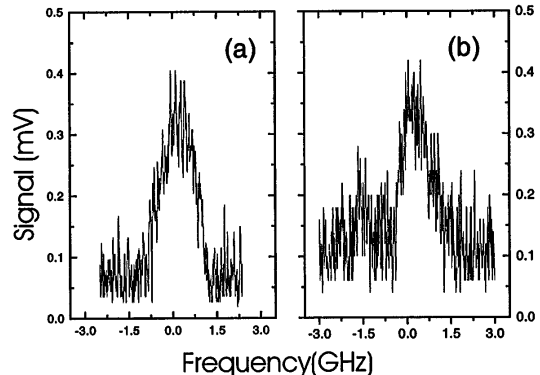


Fig. 2. Two-photon absorption signal as a function of the diode laser frequency, recorded on a 1.06- μm beam (a) produced by the OPO and (b) produced by a YAG laser of identical power.

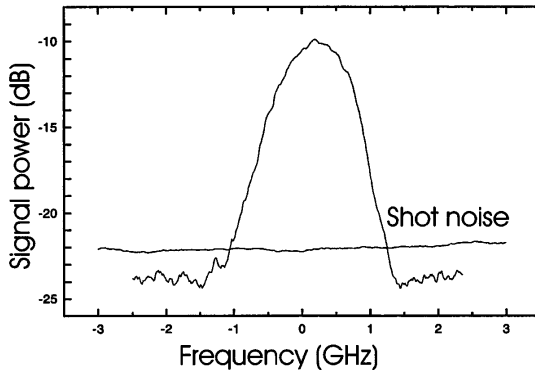


Fig. 3. Two-photon absorption signal as a function of the diode laser frequency, with the OPO signal beam in logarithmic power units. The flat trace shows the shot-noise level recorded with a YAG laser of identical power.

corresponds to a relative absorption of 2.5×10^{-7} of the signal beam. It is observed on a noise background that permits a minimum measured signal of 5×10^{-8} (signal-to-noise ratio of 1). Figure 2(b) shows the corresponding shot-noise-limited curve obtained with a YAG laser beam of $1.064198\text{-}\mu\text{m}$ wavelength and same power and a semiconductor laser operating at a $0.859448\text{-}\mu\text{m}$ wavelength. The noise background coincides in this case with the shot-noise level. By comparing the two figures one observes that the signal is the same in the two cases and that the noise is less when one uses the OPO twin beams instead of classic laser light. Note that the mean value, not only the variance, of the noise increases when the YAG laser is used. This result is due to our detection scheme on the amplitude signal given by the lock-in amplifier (i.e., the square root of the sum of the two quadrature signals of the lock-in). We chose this scheme because it permits a more convenient evaluation of the noise level in both cases.

Figure 3 shows the spectroscopic signal and the shot-noise level (which has been also averaged on longer time scales) in logarithmic power units, which allows us to evaluate directly the signal-to-noise ratio improvement obtained by use of the squeezed background instead of the classic differential detection scheme. The signal-to-noise ratio is 13.9 dB when one uses the twin beams, and this represents a 1.9-dB (35%) improvement on that in the shot-noise-limited experiment.

The resonance curves presented in Figs. 2 and 3, recorded with different beams propagating in the same direction, are Doppler broadened. The intrinsic linewidth of the signal beam generated by the OPO is much smaller. Using a Fabry-Perot mode analyzer, we measured it to ~ 30 MHz. This value is essentially limited by the thermal stability of the KTP crystal.

In summary, we have demonstrated, for the first time to our knowledge, that a two-photon absorption spectroscopy experiment using twin beams generated by an OPO has a sensitivity that is not limited by the shot-noise level of the beams used in the experiment. The ultimate sensitivity of our experiment, limited by the degree of quantum correlation between the signal and idler beams, is 5×10^{-8} when powers as

weak as 20 mW in the auxiliary beam and 6 mW in the OPO beam are used. These results illustrate the utility of cw OPO's as light sources for spectroscopy in the visible and near-infrared regions. The recent availability of quasi-phase-matched crystals as nonlinear media will significantly broaden the frequency range of these sources. This experiment shows, here in a real spectroscopy experiment, that the quantum correlations between twin beams can be used to improve the sensitivity beyond the shot-noise limit. The present performances represent only a moderate improvement of the signal-to-noise ratio. They are limited by the losses in production of the twin beams and in their propagation in the spectroscopy experimental setup and also by the poor stability of the total setup. Much better results are anticipated if better optical components (linear and nonlinear) and stabler pump sources for the OPO are used.

We thank J. P. Taran and H. Berger for helpful advice during this experiment. P. H. Souto Ribeiro is supported by a postdoctoral fellowship from the Conselho National de Desenvolvimento Científico e Tecnológico. The experiment has been partially funded by a European Community contract (ESPRIT IV ACQUIRE 20029). Laboratoire Kastler Brossel, from l'Ecole Normale Supérieure and l'Université P. M. Curie, is associated with the Centre National de la Recherche Scientifique.

References

- C. Fabre and J. P. Pocholle, eds., special issue on $\chi^{(2)}$ second-order nonlinear optics, *J. Eur. Opt. Soc. B* **9**, 131–293 (1997).
- L. A. Wu, J. Kimble, J. Hall, and H. Wu, *Phys. Rev. Lett.* **57**, 2520 (1986).
- E. Giacobino and C. Fabre, eds., special issue on quantum noise reduction in optical systems: experiments, *Appl. Phys. B* **55**, 189–303 (1992).
- A. Heidmann, R. J. Horowicz, S. Reynaud, E. Giacobino, C. Fabre, and G. Camy, *Phys. Rev. Lett.* **59**, 2555 (1987).
- J. Mertz, T. Debuisschert, A. Heidmann, C. Fabre, and E. Giacobino, *Opt. Lett.* **16**, 1234 (1991).
- E. Polzik, J. Carri, and H. J. Kimble, *Phys. Rev. Lett.* **68**, 3020 (1992).
- S. Kasapi, S. Lathi, and Y. Yamamoto, *Opt. Lett.* **22**, 478 (1997).
- F. Marin, A. Bramati, V. Jost, and E. Giacobino, *Opt. Commun.* **140**, 146 (1997).
- Y.-Q. Li, P. Lynam, M. Xiao, and P. Edwards, *Phys. Rev. Lett.* **78**, 3105 (1997).
- C. Nabors and R. Shelby, *Phys. Rev. A* **44**, 3266 (1991).
- W. Hai, X. Chang, D. P. Qing, X. C. Yang, Z. Yun, and P. Kunchi, presented at the Workshop on Quantum Communications and Measurement, Hakone, Japan, September 25–30, 1996.
- T. Debuisschert, A. Sizmann, E. Giacobino, and C. Fabre, *J. Opt. Soc. Am. B* **10**, 1668 (1993).
- E. Giacobino, C. Fabre, S. Reynaud, A. Heidmann, and R. Horowicz, in *Photons and Quantum Fluctuations*, E. Pike and H. Walther, eds. (Hilger, New York, 1988), p. 81.
- C. Harper and M. Levenson, *Opt. Commun.* **20**, 107 (1977).

Chapitre 3

Spectroscopie de l'atome d'hydrogène

3.1 Introduction

C'est pendant mon année d'ATER à l'Université Pierre et Marie Curie en 1997-98, dans l'équipe de François Biraben, Lucile Julien et François Nez, que j'ai abordé les domaines de recherche que sont la spectroscopie de grande résolution et la mesure de fréquences optiques. Jusqu'alors, mes efforts avaient pour but de faire sortir un signal d'absorption du bruit, en abaissant le niveau de bruit à l'aide des propriétés non classiques de la lumière. Dans l'équipe de Métrologie des Systèmes Simples, la spectroscopie est abordée sous un autre angle et l'objectif consiste à pointer le plus précisément possible le centre de la raie atomique pour réaliser une mesure d'intérêt métrologique.

Les atomes étudiés sont l'hydrogène et le deutérium et le but, la détermination de la constante de Rydberg. J'ai plus particulièrement travaillé sur la transition à partir du niveau métastable 2S-12D en mettant à profit l'étalon de fréquence développé par Béatrice de Beauvoir au cours de sa thèse [25].

Ce chapitre est divisé comme suit. Dans une première partie générale, je rappelle le contexte de la détermination de la constante de Rydberg et des déplacements de Lamb. Dans une deuxième partie, j'introduis la mesure de la transition 2S-12D. J'y décris brièvement le dispositif expérimental, le traitement des données et les résultats obtenus. Je conclus ce chapitre sur un bilan des expériences réalisées jusqu'ici et sur l'avenir de la spectroscopie de l'atome d'hydrogène.

3.2 Le contexte

3.2.1 La constante de Rydberg

La constante de Rydberg dans l'atome d'hydrogène est introduite de façon empirique par J.R. Rydberg en 1889 pour décrire la régularité observée dans le spectre de l'atome d'hydrogène :

$$\frac{1}{\lambda_{np}} = R_H \left(\frac{1}{n^2} - \frac{1}{p^2} \right) \quad (3.1)$$

où λ_{np} est la longueur d'onde mesurée et n et p deux entiers.

En 1913, N. Bohr décrit le mouvement d'un électron unique autour d'un centre attractif fixe, c'est-à-dire de masse infinie et donne l'expression de la fréquence de la transition $n \leftrightarrow p$.

$$\frac{1}{\lambda_{np}} = \frac{E_p - E_n}{hc} = \frac{me^4}{8\epsilon_0 h^3 c} \left(\frac{1}{n^2} - \frac{1}{p^2} \right) \quad (3.2)$$

où E_n et E_p sont respectivement les énergies des niveaux n et p , m la masse de l'électron, e sa charge, ϵ_0 la permittivité du vide, h la constante de Planck et c la vitesse de la lumière dans le vide.

D'où, l'expression de la constante de Rydberg :

$$R_\infty = \frac{me^4}{8\epsilon_0 h^3 c} \quad (3.3)$$

A partir de R_H , on remonte à R_∞ par l'intermédiaire du rapport $\frac{m}{M}$ où M est la masse du proton.

$$R_H = \frac{R_\infty}{1 + \frac{m}{M}} \quad (3.4)$$

Dans le but d'unifier les lois de la physique, on s'est depuis toujours attaché à les écrire en séparant les variables d'une part, les grandeurs dépendant du système considéré et celles n'en dépendant pas, d'autre part. Ces dernières sont les constantes fondamentales, parmi lesquelles on peut citer la masse de l'électron, sa charge, la constante gravitationnelle, la constante de Planck.... D'autres constantes, appelées constantes secondaires, s'écrivent comme des combinaisons de constantes fondamentales et apparaissent suffisamment souvent dans les lois de la physique pour qu'on leur donne un nom. C'est le cas de la constante de Rydberg et de la constante de structure fine sur laquelle je reviendrai dans le chapitre suivant. L'expression (3.3) montre que la constante de Rydberg relie entre elles cinq constantes fondamentales : la masse de l'électron, sa charge, la permittivité du vide, la constante de Planck et la vitesse de la lumière dans le vide.

En 1983, la définition du mètre a changé. Il est désormais défini à partir de la transition d'horloge de l'atome de césum et est égal à la longueur parcourue par la lumière dans le vide en $1/299792458^{me}$ de seconde. La vitesse de la lumière prend alors une valeur exacte, de même que la permittivité du vide ($\mu_0\epsilon_0c^2 = 1$) et la constante de Rydberg ne relie plus que trois constantes : m , e et h .

Périodiquement, le CODATA actuellement piloté par P. Mohr et B. Taylor collecte les mesures de constantes fondamentales et secondaires réalisées à travers le monde et procède à un ajustement du type moindres carrés afin d'établir une valeur "recommandée" pour chaque constante. La constante de Rydberg fait partie des constantes fondamentales les mieux connues.

3.2.2 Les niveaux d'énergie de l'atome d'hydrogène

Jusqu'ici, je n'ai évoqué, pour décrire la théorie de l'atome d'hydrogène, que le modèle de Bohr qui introduit la quantification de manière empirique. La première description quantique est donnée par l'équation de Schrödinger qui traite le problème à deux corps dans un cadre non relativiste. A ce niveau de la théorie, les niveaux d'énergie ne dépendent que du nombre quantique principal n et l'incertitude relative obtenue sur l'énergie des niveaux est de l'ordre de 10^{-5} . Pour augmenter le degré de précision, il est nécessaire de prendre en compte d'autres effets : les effets relativistes, les corrections radiatives, les effets de taille du noyau et la structure hyperfine.

Les effets relativistes

A la fin des années 20, Dirac prend en compte la vitesse de l'électron en donnant une description à la fois quantique et relativiste de la dynamique de l'électron dans le champ du proton. Il calcule les niveaux d'énergie de l'atome d'hydrogène en considérant un proton de masse infinie et fait apparaître une correction du premier ordre en α^2 (où α est la constante de structure fine) de l'ordre de 10^{-5} en valeur relative. Il introduit la dépendance de l'énergie des niveaux vis à vis du moment angulaire total J . L'équation de Dirac n'étant pas soluble pour un système à deux corps, on réalise un traitement perturbatif en $\frac{m}{M}$ (pour tenir compte de la masse finie du proton) et en α . L'ordre zéro de ce développement, noté $E_{nJ}^\mu(\text{Dirac})$ (où μ est la masse réduite $\mu = \frac{m}{1+\frac{m}{M}}$) est le résultat de l'équation de Dirac pour une particule de masse réduite μ . La première correction relativiste est due à l'effet de recul du noyau et est de l'ordre de $\frac{m}{M}\alpha^2$ par rapport à l'énergie du niveau fondamental. Elle ne dépend que du nombre quantique

principal n et a pour expression :

$$E_n(\text{recul}) = -\frac{\mu^2 c^2}{M + m} \frac{(Z\alpha)^4}{8n^4} \quad (3.5)$$

Finalement, on écrit l'énergie d'un niveau décrit par les trois nombres quantiques n , L et J sous la forme :

$$E_{n,L,J} = E_{nJ}^\mu(\text{Dirac}) + E_n(\text{recul}) + E(\text{Lamb}) \quad (3.6)$$

où $E(\text{Lamb})$ regroupe les corrections relativistes d'ordre supérieur, les corrections radiatives, les effets de taille de proton.

L'électrodynamique quantique (QED)

L'interaction entre l'électron et le champ électromagnétique est quantifiée et décrite par l'électrodynamique quantique. Les termes les plus importants sont :

- la "self energy" à une boucle, qui correspond à l'émission et à l'absorption virtuelle d'un photon par l'électron et est en α^3 ¹. Son incertitude est de $1,3 \times 10^{-9}$ pour les états 1S et 2S.
- la polarisation du vide, qui correspond à la création virtuelle d'une paire électron-positron et est en α^3 également. Elle est connue à 2×10^{-8} .
- le recul relativiste "pur" du proton dû aux photons échangés entre l'électron et le proton, en $\frac{m}{M}\alpha^3$. Il est connu à 3×10^{-4} .
- la "self energy" à deux boucles, qui correspond à l'émission et à l'absorption virtuelle de deux photons par l'électron, et est en α^4 . Son incertitude est de $5,3 \times 10^{-3}$.

Les corrections les plus importantes sont donc en α^3 . Elles sont dix fois plus faibles que les corrections de structure hyperfine ou d'effet de recul du proton. Elles sont importantes pour les niveaux S et varient en première approximation en $\frac{1}{n^3}$. Le terme de "self energy" à deux boucles constitue la contribution dominante à l'incertitude due à la QED dans la connaissance du déplacement de Lamb. Ce terme a d'ailleurs été récemment ré-évalué [26]. Il faut être conscient du fait que ces calculs sont extrêmement longs et complexes. Chaque correction s'écrit comme un développement en série logarithmique dont la convergence peut être très lente. Ainsi, un coefficient important placé devant un terme d'ordre supérieur, peut le rendre comparable au terme de l'ordre précédent.

A l'heure actuelle, la précision sur le déplacement de Lamb est limitée par la connaissance du "rayon" du proton, et non par la QED.

¹Pour l'ordre de grandeur des corrections, je n'ai considéré que le cas de l'hydrogène, c'est-à-dire $Z = 1$.

La distribution de charge de proton

Cet effet n'est important que pour les états S, pour lesquels l'équation de Schrödinger prévoit une probabilité de présence non nulle de l'électron à la position du proton. Ceci se traduit par une pénétration de l'électron à l'intérieur du volume fini du proton que l'on ne doit donc plus considérer comme une charge ponctuelle, mais comme une distribution de charge de rayon fini. La correction sur l'énergie des niveaux de l'atome d'hydrogène varie comme la valeur quadratique du "rayon" du proton $\langle r^2 \rangle^2$. L'incertitude sur cette correction est donc liée à l'incertitude sur $\langle r^2 \rangle$. La valeur la plus juste, obtenue à partir des expériences de diffusion d'électrons, est 0,895(18) fm [27]. La fréquence de la transition 1S-2S peut être calculée à partir de l'équation (3.6) et des corrections QED énumérées précédemment, en prenant comme valeur du rayon du proton 0,875 fm³. On obtient : $\nu_{1S-2S} = 2\ 466\ 061\ 413\ 191,75$ kHz [28]. Cette transition a également été déterminée expérimentalement par l'équipe de T. Hänsch à Garching ($\nu_{1S-2S} = 2\ 466\ 061\ 413\ 187,103$ (46) kHz) [29]. Initialement, ces deux fréquences coïncidaient parfaitement. L'écart actuel, au niveau du kHz, s'explique par la modification récente du déplacement de Lamb L_{1S} [26]. Pour faire coïncider ces deux valeurs à nouveau, le rayon du proton a été ré-évalué et vaut à présent 0,8769 (68) fm. Il est donc conditionné par l'exactitude des calculs QED. Ceci montre bien l'importance d'une mesure indépendante du rayon du proton.

C'est dans ce contexte qu'une collaboration internationale s'est formée autour de la spectroscopie de l'hydrogène muonique, dans le but de déterminer le rayon de la distribution de charge de proton à 10^{-3} à partir de la mesure du déplacement de Lamb L_{2S} à 18 ppm, la QED dans l'hydrogène muonique ayant récemment atteint une précision de 20 ppm.

L'électron de l'atome d'hydrogène est remplacé par un muon, qui étant 207 fois plus lourd, orbite plus près du proton et est donc plus sensible à sa distribution de charge. Comme le montre le tableau (3.1), les effets QED sont donc amplifiés et L_{2S} passe du domaine RF au domaine optique (49 THz ~ 6 μm). La contribution du rayon du proton à L_{2S} passe de $1,4 \times 10^{-4}$ pour l'hydrogène à presque 2% pour l'hydrogène muonique.

La longueur d'onde d'excitation de la transition 2S-2P est donc égale à 6 μm. Sa largeur naturelle, proportionnelle à la masse du muon, est de l'ordre de 20 GHz. Cependant, la force d'oscillateur variant en $\frac{1}{m^3}$ où m est la masse de la particule (électron ou muon), la probabilité de transition est environ 10^7 fois plus faible que dans le cas

²Plus précisément, cet effet est en $(\frac{\langle r \rangle}{\lambda_c})^2 \alpha^2$ où λ_c est la longueur d'onde de Compton.

³Cette valeur est déduite de la mesure publiée dans la référence [27] et de toutes les données disponibles tirées des mesures de fréquence dans l'hydrogène et le deutérium.

2S-2P	fluctuations du vide	polarisation du vide	"rayon" du proton	total
ep	1085,8 MHz	-26,9 MHz	0,146 MHz	1057,8 MHz
μp	0,1 THz	-49,94 THz	0,93 THz	-49,05 THz

TAB. 3.1 – Différentes contributions au déplacement de Lamb 2S dans le cas de l'hydrogène et de l'hydrogène muonique.

de l'atome d'hydrogène, ce qui rend l'expérience très délicate. Pour atteindre la précision escomptée sur la distribution de charge du proton, il est nécessaire de mesurer la fréquence de la transition 2S-2P avec une incertitude relative de 3×10^{-5} , soit environ 2 GHz, ce qui correspond à un dizième de la largeur naturelle.

L'expérience a lieu à l'Institut Paul Scherrer à Villigen en Suisse, dont l'accélérateur

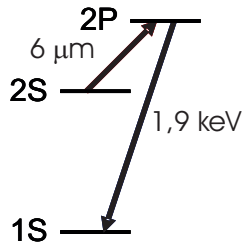


FIG. 3.1 – Niveaux d'énergie de l'hydrogène muonique.

permet de produire des muons à partir d'un faisceau de protons énergétiques. Depuis 1999, notre équipe, et en particulier François Nez et Lucile Julien, a rejoint cette collaboration avec comme objectif de mettre en oeuvre la chaîne laser permettant d'exciter la transition 2S-2P dans l'hydrogène muonique.

Le principe de l'expérience est le suivant : des muons de basse énergie sont produits dans un piège cyclotron, transportés dans un solénoïde courbe, détectés par deux détecteurs rapides et enfin, arrêtés dans une cible de dihydrogène. Le signal des deux détecteurs rapides, correspondant au passage d'un muon, permet de déclencher le tir laser. Les muons sont capturés dans un niveau d'énergie élevé de l'hydrogène muonique ($n \approx 14$) et se déexcitent à 99% vers le niveau fondamental en émettant un rayon X à 2 keV et à 1% vers le niveau métastable 2S. Les atomes métastables subissent alors un tir laser à $6 \mu\text{m}$ qui les fait passer sur le niveau 2P d'où ils se déexcitent en émettant un rayon X (K_α) à 1,9 keV. La source à $6 \mu\text{m}$ doit allier puissance et rapidité afin que le tir laser soit déclenché sur le passage d'un muon dont la durée de vie est de $2,2 \mu\text{s}$. Cette expérience est décrite en détail dans le mémoire d'habilitation de François Nez

ainsi que dans la référence [30], le système laser dans la référence [31]. Il faut noter qu'il ne s'agit pas là d'une mesure indépendante de la QED, mais cette théorie a été testée avec succès au niveau de 10 ppm, de sorte qu'elle ne constitue pas une limitation au résultat de cette expérience.

3.2.3 Les déterminations de R_∞ et du déplacement de Lamb

Les mesures de fréquence dans l'hydrogène (et le deutérium) ont pour objectif de déterminer la constante de Rydberg et les déplacements de Lamb. Différentes approches ont été adoptées au fil des ans.

Pour simplifier les expressions, j'écrirai dans la suite de ce paragraphe les fréquences des transitions comme la somme de deux termes : un premier terme proportionnel à R_∞ ⁴, le second terme étant le déplacement de Lamb, soit

$$\nu_{nS-mS} = R_\infty c[\eta(mS) - \eta(nS)] + (L_{mS} - L_{nS}) \quad (3.7)$$

où η est un facteur numérique de proportionnalité.

Les transitions 2S-nS et 2S-nD à partir du niveau métastable

Les fréquences de ces transitions s'écrivent donc :

$$\nu_{2S-nS/D} = R_\infty c(\eta(nS/D) - \eta(2S)) + (L_{nS} - L_{2S}) \quad (3.8)$$

Le déplacement de Lamb du niveau 2S a été mesuré à 9 kHz (9×10^{-6}) par spectroscopie micro-onde. Ceux des niveaux n ($n = 6, 8, 10, 12, \dots$) sont connus théoriquement à mieux que le kHz et ne constituent donc pas une limitation. Jusqu'au début des années 90, les mesures de fréquences dans l'hydrogène et le deutérium étaient moins précises que celle de L_{2S} et une seule équation était suffisante pour déterminer R_∞ ⁵.

Les transitions à partir du niveau fondamental

Ces transitions présentent des avantages notables. Partant du niveau fondamental, elles impliquent un nombre d'atomes beaucoup plus important que le niveau métastable et permettent donc d'obtenir un bon rapport signal à bruit avec des puissances lumineuses et donc des déplacements lumineux plus faibles. Leur principal inconvénient

⁴Le terme $E_n(recul)$ de l'équation (3.6) en α^4 est proportionnel à $R_\infty \alpha^2$ en écrivant $\alpha^2 = 2hR_\infty/(mc)$.

⁵A titre d'exemple, l'incertitude sur les mesures des fréquences des transitions 2S-8D_{5/2} dans l'hydrogène et le deutérium, réalisées pendant la thèse de Béatrice de Beauvoir, était inférieure à 5 kHz.

résidé dans le fait que les longueurs d'onde d'excitation se trouvent dans l'ultraviolet et sont donc difficiles à produire.

La transition 1S-2S

L'équipe de T. Hänsch travaille depuis de nombreuses années sur la transition 1S-2S qui présente l'avantage d'avoir une très faible largeur naturelle (1.3 Hz à comparer aux largeurs de 100 à 500 kHz des transitions 2S-nS/D). La longueur d'onde du laser exciteur est de 243 nm. Afin de déterminer L_{1S} , cette fréquence a été initialement comparée à celle de la transition 2S-4S/D, ces deux fréquences étant dans un rapport de 4 au premier ordre de l'équation de Dirac [32]. Depuis 1997, cette transition est mesurée tout en fréquence. Les dernières mesures publiées, obtenues au moyen d'un peigne de fréquences optiques référencé sur l'horloge transportable à atomes froids du BNM-SYRTE, font état d'une incertitude sur le pointé du centre de la raie égale à 23 Hz, ce qui correspond à une incertitude relative sur la fréquence mesurée de $1,8 \times 10^{-14}$ [33]. La fréquence de la transition 1S-2S peut s'écrire :

$$\nu_{1S-2S} = R_\infty c(\eta(2S) - \eta(1S)) + (L_{2S} - L_{1S}) \quad (3.9)$$

Les inconnues de cette équation sont R_∞ , L_{1S} et L_{2S} . Or les différentes contributions des déplacements de Lamb étant en $1/n^3$, on peut calculer la grandeur $L^{(2)} = L_{1S} - 8L_{2S}$ plus précisément que L_{1S} ou L_{2S} (de même pour $L^{(3)} = L_{1S} - 27L_{3S}$) [34]. En remplaçant L_{2S} par son expression en fonction de $L^{(2)}$ et L_{1S} dans la relation (3.9), il reste deux inconnues R_∞ et L_{1S} . La seconde équation est fournie par la fréquence d'une transition 2S-nS/D. On a pu ainsi déterminer R_∞ à $6,6 \times 10^{-12}$ et L_{1S} à $2,7 \times 10^{-6}$ ⁶. La limitation de cette méthode provient de la connaissance des fréquences des transitions 2S-nS/D.

La transition 1S-3S

Toujours dans le but de déterminer R_∞ et L_{1S} , on peut utiliser une seconde transition à partir du fondamental : 1S-3S. On a alors un système de deux équations :

$$\nu_{1S-2S} = R_\infty c(\eta(2S) - \eta(1S)) + (L_{2S} - L_{1S}) \quad (3.10)$$

$$\nu_{1S-3S} = R_\infty c(\eta(3S) - \eta(1S)) + (L_{3S} - L_{1S}) \quad (3.11)$$

De même que précédemment, en introduisant $L^{(2)}$ et $L^{(3)}$, on peut éliminer L_{2S} (et L_{3S}) et on se retrouve donc avec un système de deux équations à deux inconnues R_∞ et L_{1S} . Une mesure de la fréquence de la transition 1S-3S au niveau du kHz, associée à celle de la transition 1S-2S permettrait de déduire une valeur de la constante de Rydberg à 5×10^{-12} et de L_{1S} à environ 10 kHz.

⁶En réalité, l'ensemble des données disponibles sur l'hydrogène et le deutérium est pris en compte et un ajustement par la méthode des moindres carrés est réalisé.

Notre équipe s'est lancée en 1991 dans la mesure de la transition 1S-3S, pour laquelle la fréquence d'excitation correspond à une longueur d'onde de 205 nm. L'idée de départ était de déduire L_{1S} par comparaison de 1S-3S et 2S-6S/D, ces deux transitions étant dans un rapport 4. La difficulté majeure consiste à produire la radiation à 205 nm, à partir d'un laser titane-saphir quadruplé en fréquence. La mise en oeuvre du dispositif expérimental et une première détermination de L_{1S} à 47 kHz (à 6×10^{-6} en valeur relative) ont fait l'objet du travail de thèse de Sophie Bourzeix [35] [36]. L'expérience s'est poursuivie vers une mesure absolue de la transition 1S-3S, pendant les thèses de Gaëtan Hagel et Olivier Arnoult.

L'une des contributions majeures du travail de thèse de Gaëtan Hagel a consisté à mettre en oeuvre un schéma expérimental original pour compenser l'effet Doppler du second ordre (l'effet Doppler du premier ordre étant supprimé grâce à l'utilisation de l'excitation à deux photons) [37]. Cette méthode a été initialement proposée en 1991 par François Biraben [38]. Elle consiste à opposer au déplacement de fréquence $\delta_{Doppler}$ induit par cet effet ($\delta_{Doppler} = -\nu_0 \frac{v^2}{2c^2}$, où ν_0 est la fréquence atomique, v la vitesse des atomes et c la vitesse de la lumière) le déplacement Stark, δ_{Stark} , induit par le champ électrique motionnel, dû à l'application d'un champ magnétique transverse par rapport au jet atomique ($\delta_{Stark} \propto \frac{E^2}{\Delta\nu_{SP}} = \frac{v^2 B^2}{\Delta\nu_{SP}}$ où E et B sont respectivement l'amplitude des champs électrique et magnétique et $\Delta\nu_{SP}$ l'écart d'énergie entre les niveaux S et P). $\delta_{Doppler}$ et δ_{Stark} étant tous deux proportionnels à v^2 et de signes opposés, ils peuvent théoriquement se compenser. Concrètement, les calculs réalisés par Gaëtan Hagel montrent que le décalage Doppler ne peut être totalement compensé. Néanmoins, il a précisément calculé la courbe de dispersion de la transition 1S-3S($F=1, m_F = \pm 1$) en fonction du champ B appliqué et l'a utilisée pour mesurer le décalage Doppler du second ordre [39].

Cette expérience de longue haleine se poursuit avec le travail de thèse d'Olivier Arnoult. La principale amélioration du montage expérimental réside dans la mise en oeuvre d'un laser titane-saphir à modes bloqués permettant de générer un peigne de fréquences optiques, directement référencé par rapport à l'horloge à césium du BNM-SYRTE. La mesure absolue de la transition 1S-3S est imminente...

3.2.4 Les mesures tout en fréquence des transitions 2S-nS/D

Les transitions 2S-nS/D sont excitées par un laser accordable dans un jet d'atomes d'hydrogène dans le niveau métastable 2S. Ce jet est placé dans une cavité Fabry Perot afin de permettre l'excitation à deux photons et d'assurer la puissance lumineuse

nécessaire. A l'extrémité du jet, les atomes du niveau 2S sont couplés par un champ électrique vers le niveau 2P et peuvent ainsi se déexciter par fluorescence Lyman α à 121 nm, détectée par deux photomultiplicateurs sensibles à l'ultraviolet. Lorsque le laser est à résonance avec la transition à deux photons, le niveau métastable se dépeuple entraînant ainsi une diminution du signal de fluorescence. La détermination de la fréquence de la transition est déduite de la mesure de la fréquence du laser à résonance.

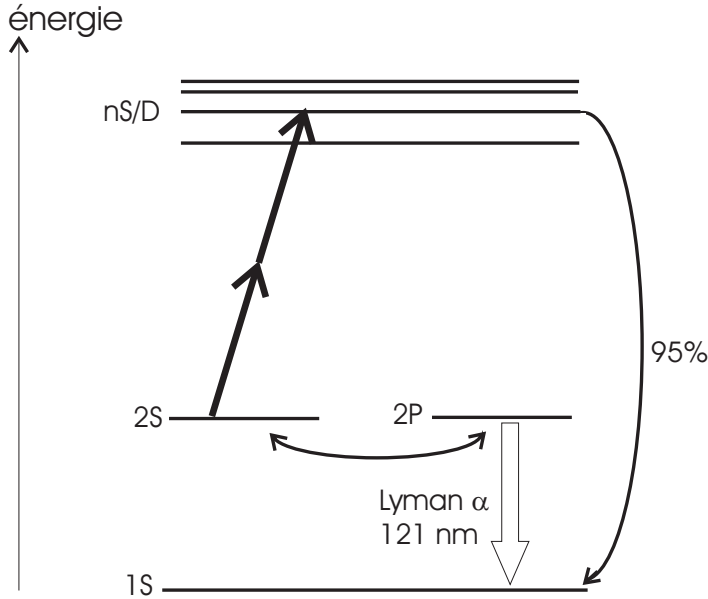


FIG. 3.2 – Niveaux d'énergie de l'atome d'hydrogène

La première mesure tout en fréquence est réalisée en 1993 sur la transition 2S-8S/D pendant la thèse de François Nez [40]. La précision atteinte est de $2,2 \times 10^{-11}$ [41]. Elle est limitée par la stabilité en fréquence des deux lasers étalons He-Ne/I₂ et He-Ne/CH₄.

Au cours de sa thèse, Béatrice de Beauvoir a développé un nouvel étalon de fréquence dans le but de mesurer la transition 2S-8S/D. Il s'agit d'une diode laser à 778 nm, stabilisée sur la transition à deux photons 5S-5D de l'atome de rubidium. Ce laser étalon présente des qualités métrologiques dix fois supérieures à celles du laser He-Ne stabilisé sur l'iode : sa stabilité relative est de 4×10^{-13} sur 1 s et sa reproductibilité de 3×10^{-12} . De plus, il permet une mesure relativement aisée de la transition 2S-8S/D de l'hydrogène grâce à la quasi-coïncidence des fréquences des deux transitions :

$$\nu(2S - 8S/D) = \nu_{Rb}(5S - 5D) + 40 \text{ GHz} \quad (3.12)$$

les 40 GHz étant mesurés par battement avec une source hyperfréquence sur une diode Schottky. Ce nouvel étalon de fréquence sera par la suite, utilisé pour d'autres transitions, en particulier 2S-12D.

Un chaîne de multiplication de fréquence, développée au BNM-SYRTE par l'équipe d'André Clairon relie la fréquence d'une diode laser étalon du même type à celle du laser à CO_2 stabilisé sur une raie hyperfine de la molécule OsO_4 . La fréquence de ce dernier est mesurée par rapport à l'horloge à césium.

Une autre avancée déterminante de cette période est le lien par fibre optique entre le LKB et le BNM-SYRTE qui permet de mesurer le laser exciteur de la transition directement par rapport à l'horloge à césium (en comparant les fréquences des diodes étalons du LKB et du BNM-SYRTE) [42]. La précision obtenue sur la constante de Rydberg est alors de 8×10^{-12} .

Cette transition a également été mesurée dans l'atome de deutérium pour lequel on a :

$$\nu(2S - 8S/D) = \nu_{Rb}(5S - SD) + 144 \text{ GHz} \quad (3.13)$$

3.3 La mesure de la transition 2S-12D dans l'hydrogène et le deutérium

En 1996, mettant à profit ce nouvel étalon de fréquence, l'équipe se lance dans la mesure de la transition 2S-12D. Elle est a priori intrinsèquement plus précise que celle de la transition 2S-8D car la largeur de raie est plus faible (572 kHz pour 2S-8D, 172 kHz pour 2S-12D). Un autre avantage d'une telle transition est qu'elle est plus sensible aux champs électriques parasites, les effets Stark quadratique et linéaire variant en n^7 et en n^2 respectivement. Son étude permet donc de tester les corrections Stark qui avaient été rajoutées dans les profils de raie théoriques dans le cadre des mesures des fréquences des transitions 2S-8S/D. De plus, du point de vue de la difficulté expérimentale, la mesure de ces transitions n'implique que peu de modifications sur la chaîne de fréquence utilisée pour les transitions 2S-8S/D. Un autre intérêt de la mise en oeuvre de la chaîne de fréquence nécessaire à la mesure des transitions 2S-12D est le transfert en phase de la fréquence du laser de référence à CO_2 du BNM-SYRTE (voir équation 3.15).

Le résultat de cette mesure, détaillée dans la suite de ce chapitre ainsi que dans la référence [43] jointe, s'est finalement révélé moins précis ($1,2 \times 10^{-11}$) que celui obtenu sur la transition 2S-8S/D à cause d'un rapport signal à bruit plus faible et d'un effet Stark quadratique plus grand. Néanmoins, en prenant en compte cette mesure, effectuée sur l'hydrogène et le deutérium, et toutes les mesures de grande précision réalisées dans

l'équipe et dans d'autres groupes, la constante de Rydberg a pu être déterminée avec une incertitude relative de $7,7 \times 10^{-12}$ [43].

3.3.1 Le schéma de fréquence

Le schéma de fréquence qui nous a permis de mesurer la transition 2S-12D dans les atomes d'hydrogène et de deutérium comporte deux équations :

$$\nu(2S - 12D)_{750nm} + \nu(DL_{int})_{809nm} = 2\nu(DL/Rb)_{778nm} \quad (3.14)$$

$$\nu(2S - 12D)_{750nm} - \nu(DL_{int})_{809nm} = \nu(CO_2P(8))_{10\mu m} \quad (3.15)$$

où $\nu(DL_{int})_{809nm}$ représente la fréquence d'une diode laser intermédiaire à 809 nm, $\nu(DL/Rb)_{778nm}$ est la fréquence de notre diode laser étalon, stabilisée sur la transition à deux photons du rubidium et $\nu(CO_2P(8))_{10\mu m}$ la fréquence du laser à CO₂ du SYRTE, stabilisé sur la raie *P*(8) de la molécule de *OsO*₄ et référencé par rapport à l'horloge à césum. Dans le cas du deutérium, la fréquence du laser à CO₂ doit être stabilisée sur la raie *R*(4).

L'équation (3.14) est réalisée au LKB, l'équation (3.15) au SYRTE, les deux laboratoires étant reliés par deux fibres optiques de 3 km de long installées durant la thèse de Béatrice de Beauvoir [42].

On constate que la réalisation de ce schéma de fréquence nécessite l'introduction d'un laser auxiliaire à 809 nm. Plus précisément, la chaîne de fréquence développée pour cette mesure est représentée par la figure (3.3). Elle nécessite la mise en oeuvre d'un doublage et d'une somme de fréquence pour la partie développée au LKB.

3.3.2 Le dispositif expérimental

Le dispositif expérimental est détaillé dans l'article [43] joint au manuscrit.

L'objectif de la chaîne de fréquence est donc de mesurer très précisément la fréquence du laser TiSa_{hyd} qui excite la transition à deux photons dans l'hydrogène ou le deutérium. Ce laser est asservi sur le pic d'une cavité Fabry Perot ultra-stable, elle-même référencée sur le laser hélium-néon stabilisé sur l'iode.

Il faut, d'une part, réaliser le premier terme de l'égalité (3.14). Pour cela, la source à 809 nm est fournie par une diode laser en cavité étendue (DL_{int}) de puissance de sortie de l'ordre de 30 mW. La fréquence d'un second laser TiSa (TiSa_{aux}) délivrant environ 300 mW à 750 nm est sommée avec celle de la diode à 809 nm dans un cristal de LBO, fournissant ainsi un faisceau à 389 nm. Les faisceaux TiSa_{aux} et DL_{int} sont modulés en

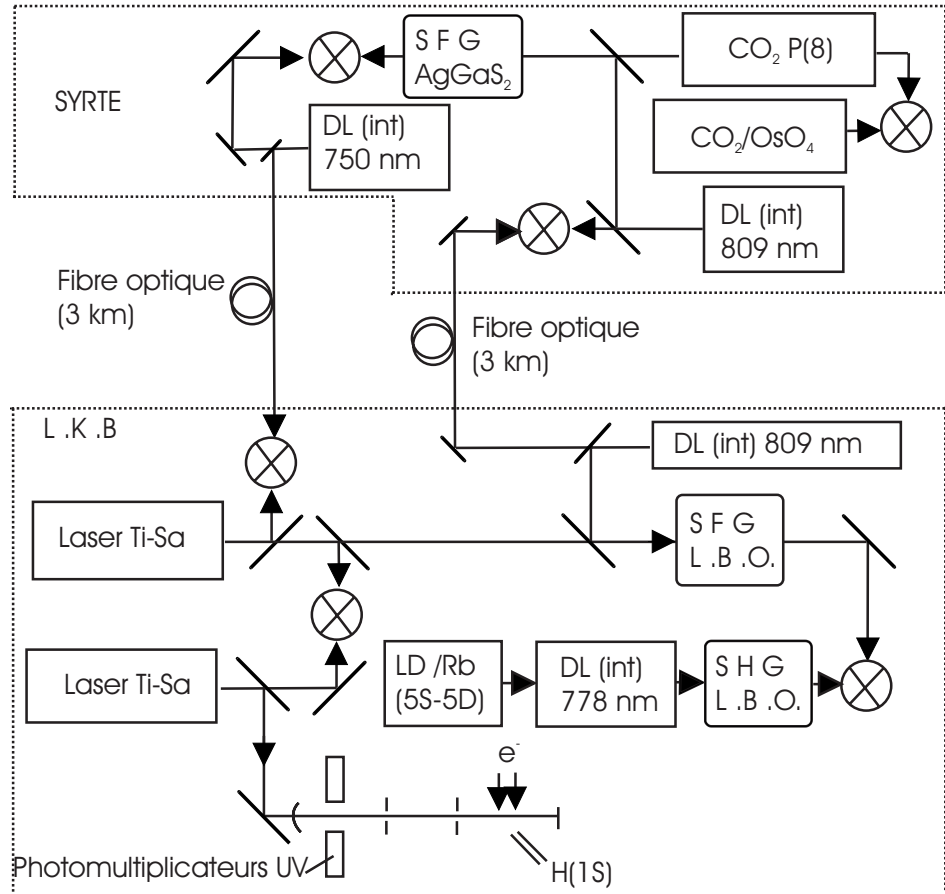


FIG. 3.3 – Chaîne de multiplication de fréquence pour la mesure de la transition 2S-12D

fréquence et asservis sur deux pics d'une seconde cavité Fabry Perot ultra-stable. Pour réaliser le second membre de l'égalité (3.14), une diode laser d'une puissance de sortie de 50 mW est injectée par la diode étalon stabilisée sur la transition à deux photons du rubidium et doublée en fréquence au moyen d'un cristal de LBO, placé dans une cavité en anneau. On obtient ainsi environ $10 \mu\text{W}$ dans l'ultraviolet. Un filtre suiveur est asservi en phase sur le battement à la fréquence δ_1 entre les deux faisceaux ultraviolets.

L'équation (3.15) est réalisée au SYRTE. Une partie du faisceau de la diode laser à 809 nm est envoyée au SYRTE par fibre optique et asservie en phase sur une source à 809 nm locale. La fréquence de cette dernière est sommée à la fréquence d'un laser à CO_2 intermédiaire dans un cristal de AgGaS_2 pour produire un faisceau à 750 nm. Ce faisceau rouge permet d'asservir en phase, avec un décalage de fréquence δ , une diode laser à 750 nm qui est renvoyée au LKB via la seconde fibre optique. Cette diode laser à

750 nm est décalée de $\nu(CO_2) + \delta$ par rapport à celle à 809 nm. Nous utilisons alors un second filtre suiveur pour compter le battement de fréquence δ_2 entre la diode à 750 nm et la fréquence du laser $TiSa_{aux}$. Finalement, on mesure la fréquence δ_3 du battement entre les lasers $TiSa_{aux}$ et $TiSa_{hyd}$. Dans le cas de l'hydrogène, δ_3 vaut 2,4 GHz et est mesuré sur une photodiode rapide. Dans le cas du deutérium, cette fréquence étant plus élevée ($\delta_3=41,3$ GHz), la détection du battement nécessite l'utilisation d'une diode Schottky.

Finalement la fréquence du laser $TiSa_{hyd}$ est déduite de la mesure des fréquences δ_1 , δ_2 et δ_3 .

$$\nu(TiSa_{hyd}) = \nu(DL/Rb)_{778nm} + \frac{1}{2}(\nu(CO_2) + \delta + \delta_1 + \delta_2) + \delta_3 \quad (3.16)$$

L'avantage de ce schéma expérimental est qu'il permet de compter toutes les fréquences localement, en l'occurrence au LKB. Il fournit, à mon avis, une bonne illustration de la complexité des chaînes de fréquence antérieures à l'apparition des peignes de fréquences optiques.

3.3.3 Le traitement de données et les résultats

Le traitement des données consiste à ajuster les signaux expérimentaux sur des formes de raie calculées, prenant en compte le plus d'effets possibles, susceptibles d'élargir les spectres ou de déplacer leur fréquence centrale. Le calcul des formes de raie s'est affiné au cours de temps et est très bien détaillé dans la thèse de Béatrice de Beauvoir [25]. J'en décris ici uniquement le principe en insistant sur la prise en compte de l'effet Stark, partie à laquelle j'ai largement contribué, notamment par le calcul des coefficients de couplage (voir l'article joint [44]). Ce travail nous a permis de disposer pour l'ajustement des signaux expérimentaux, de nouveaux profils de raie, plus précis que les précédents.

La procédure d'ajustement

Le principe de calcul de la forme de raie est de déterminer la probabilité de destruction des métastables pour une trajectoire atomique donnée dans la zone d'interaction avec l'onde laser, puis de moyenner sur toutes les trajectoires possibles ainsi que sur toutes les vitesses atomiques.

La procédure d'ajustement des courbes expérimentales sur les formes de raie théoriques est la suivante :

- à partir de la forme de raie théorique, on calcule les formes de raies pour différentes

puissances intracavité.

- on réalise alors une première convolution avec une gaussienne dont la largeur Δ_ω prend en compte différentes causes d'élargissement (largeur en fréquence du laser, élargissement dû au temps de transit transversal les trajectoires atomiques n'étant pas strictement parallèles au faisceau laser, élargissement Zeeman, élargissement par collisions).
- une seconde convolution avec une gaussienne de largeur Δ_P traduit les fluctuations de la puissance lumineuse vue par les atomes.

On a quatre paramètres ajustables : le nombre de métastables hors résonance, la puissance lumineuse, la fréquence centrale de la transition atomique non corrigée des déplacements lumineux, de l'effet Doppler du second ordre, de la structure hyperfine du niveau D, et finalement la largeur de la gaussienne Δ_ω . Au cours de l'ajustement, on effectue une interpolation quadratique pour la puissance et linéaire pour la fréquence.

L'effet Stark

Dans notre dispositif expérimental, les champs électriques parasites sont réduits à quelques mV/cm grâce à une couche d'Aquadag recouvrant l'intérieur de l'enceinte à vide (l'Aquadag est constitué de graphite colloïdal conducteur en suspension dans une solution d'ammoniaque). Néanmoins, comme l'élément de matrice de l'hamiltonien Stark $V_S = -\mathbf{d} \cdot \mathbf{E}$ (où \mathbf{E} est le champ électrique et \mathbf{d} le moment dipolaire) varie en n^2 , un tel champ électrique peut déplacer et élargir les raies surtout pour les transitions 2S-12D. Le couplage entre états $|nLJFm_F\rangle$ et $|nL'J'F'm_{F'}\rangle$ induit un effet Stark quadratique variant en n^7 pour $J \neq J'$ et un effet Stark linéaire variant en n^2 pour $J = J'$. Un calcul au second ordre donne la contribution quadratique. Comme la partie anisotrope de cette contribution est très petite (1,8% pour les niveaux 12D_{5/2}), seule la partie scalaire, c'est-à-dire la valeur moyenne sur les sous-niveaux m_F , indépendante du nombre quantique F , doit être prise en compte.

L'effet Stark linéaire couple, par exemple dans le cas des transitions 2S-12D, les 12 sous-niveaux 12D_{5/2}(F, m_F) avec les 12 sous-niveaux 12F_{5/2}(F, m_F). Sa contribution est plus complexe à déterminer et est susceptible de décaler le barycentre de la raie. Le champ électrique parasite est évalué à partir de la largeur des transitions 2S-15D et 2S-20D, enregistrées à la fin des périodes de prises de données des transitions 2S-8S/D par exemple. Jusqu'en 1993, les fréquences mesurées étaient directement corrigées du champ électrique. Puis, la précision des mesures augmentant, il s'est avéré nécessaire de prendre en compte les corrections dues à l'effet Stark dans les calculs de forme de raie.

Le principe du calcul, détaillé dans l'article joint [44], consiste à prendre en compte simultanément la largeur naturelle et le couplage par effet Stark. On considère un état initial $|g\rangle$ couplé à p états $|e\rangle$ par la lumière, ces états $|e\rangle$ étant mélangés à p états $|f\rangle$ par l'hamiltonien Stark V_S . L'évolution de l'opérateur matrice densité ρ s'écrit :

$$\frac{d\rho}{dt} = \frac{1}{i\hbar}[(H_0 + V_L + V_S), \rho] \quad (3.17)$$

où H_0 représente l'hamiltonien non perturbé, V_L l'excitation à deux photons.

On fait l'approximation des champs tournants et si la fréquence de Rabi de la transition à deux photons est très petite par rapport à la largeur naturelle des états $|e\rangle$, on peut négliger les populations et les cohérences des états excités. Dans le référentiel tournant, on remplace l'opérateur matrice densité par l'opérateur σ :

$$\begin{aligned}\sigma_{gg} &= \rho_{gg} \\ \sigma_{eg} &= \rho_{eg} \exp(2i\omega t) \\ \sigma_{ge} &= \rho_{ge} \exp(-2i\omega t)\end{aligned}$$

et on introduit les différences de fréquence :

$$\begin{aligned}\Delta_e &= 2\omega - \omega_e \\ \Delta_f &= 2\omega - \omega_f\end{aligned}$$

où ω est la fréquence d'excitation.

On peut ainsi écrire l'équation d'évolution de σ_{gg} , les p équations d'évolution de σ_{eg} ainsi que celles de σ_{fg} . On suppose ensuite que les cohérences σ_{eg} et σ_{fg} suivent adiabatiquement la population σ_{gg} , c'est-à-dire que

$$\frac{d\sigma_{eg}}{dt} = \frac{d\sigma_{fg}}{dt} = 0 \quad (3.18)$$

Finalement, on obtient p équations pour σ_{gg} en fonction des p inconnues σ_{eg} , ce qui peut s'écrire sous la forme :

$$A[\sigma_{eg}] = i\left[\frac{\Omega_e}{2}\right]\sigma_{gg} \quad (3.19)$$

où les éléments de matrice de l'opérateur A se calculent en fonction des coefficients de couplage entre les différents états e et f . Ω_e est la fréquence de Rabi à deux photons. L'équation d'évolution de la population de l'état fondamental s'écrit finalement :

$$\frac{d\sigma_{gg}}{dt} = -\Gamma_{gg}\sigma_{gg} = 2\Re e\left[\frac{\Omega_e}{2}\right]^T A^{-1}\left[\frac{\Omega_e}{2}\right]\sigma_{gg} \quad (3.20)$$

où Γ_{gg} est la probabilité de transition à deux photons. Soit,

$$\Gamma_{gg} = -2\Re e\left[\frac{\Omega_e}{2}\right]^T A^{-1}\left[\frac{\Omega_e}{2}\right] \quad (3.21)$$

Comme on ne connaît pas la direction du champ électrique, il est nécessaire de calculer les formes de raies pour les deux composantes, c'est-à-dire parallèle et perpendiculaire à la direction de polarisation du laser.

On ajuste ensuite le profil calculé pour différentes valeurs du champ électrique sur les courbes expérimentales sans convolution par la gaussienne de largeur $\Delta\omega$. Ceci nous a permis d'évaluer le champ parasite à $2,0(1,0)$ mV/cm pour la série d'enregistrements de la transition 2S-12D. En faisant la différence entre les centres des profils correspondants à $E=0$ mV/cm et $E=2$ mV/cm, nous en avons déduit un déplacement Stark de $-2,1(1,2)$ kHz pour le niveau $12D_{5/2}$ et de $-6,0(4,9)$ kHz pour le niveau $12D_{3/2}$ dans l'hydrogène et le deutérium.

Les résultats sur la mesure de la transition 2S-12D et sur la constante de Rydberg

En 1998, nous avons procédé à la mesure des transitions $2S_{1/2}(F)-12D_{5/2}$ et $2S_{1/2}(F)-12D_{3/2}$ dans l'hydrogène ($F=1$) et dans le deutérium ($F=3/2$). Pour chaque transition, le signal atomique est enregistré pour au moins 50 valeurs de la puissance lumineuse. 237 enregistrements, d'une durée de 20 minutes chacun, ont été réalisés. Un spectre typique est représenté sur la figure (3.4). L'incertitude statistique sur la fréquence mesurée pour chaque transition est de l'ordre de 6×10^{-12} . A cette incertitude statistique, il faut rajouter les effets systématiques estimés, dans le cas de la transition $2S_{1/2}(F=1$ ou $3/2)-12D_{5/2}$, à 2,1 kHz pour l'effet Stark, 1 kHz pour l'effet Doppler du second ordre, 2 kHz pour la mesure de la diode laser étalon stabilisée sur le rubidium, et finalement 4,5 kHz pour les imperfections du modèle théorique.

En utilisant la valeur du déplacement de Lamb L_{2S-2P} obtenue par spectroscopie micro-onde, on peut déduire de notre mesure de la transition $2S_{1/2}-12D_{5/2}$ une détermination de la constante de Rydberg avec une incertitude relative de $1,2 \times 10^{-11}$. Ce résultat, en bon accord avec les précédents, est cependant légèrement moins précis que celui obtenu à partir des transitions 2S-8D. Ceci est principalement dû à un rapport signal à bruit plus faible ainsi qu'à un effet Stark plus important. Ce dernier est néanmoins plus précisément évalué grâce au travail réalisé sur le calcul des formes de raie.

L'article joint [43] reprend cette mesure ainsi que toutes les mesures de précision réalisées sur l'hydrogène et le deutérium afin de déterminer la constante de Rydberg et les déplacements de Lamb des niveaux 1S et 2S. L'incertitude relative de la constante de Rydberg ainsi obtenue est égale à $7,7 \times 10^{-12}$.

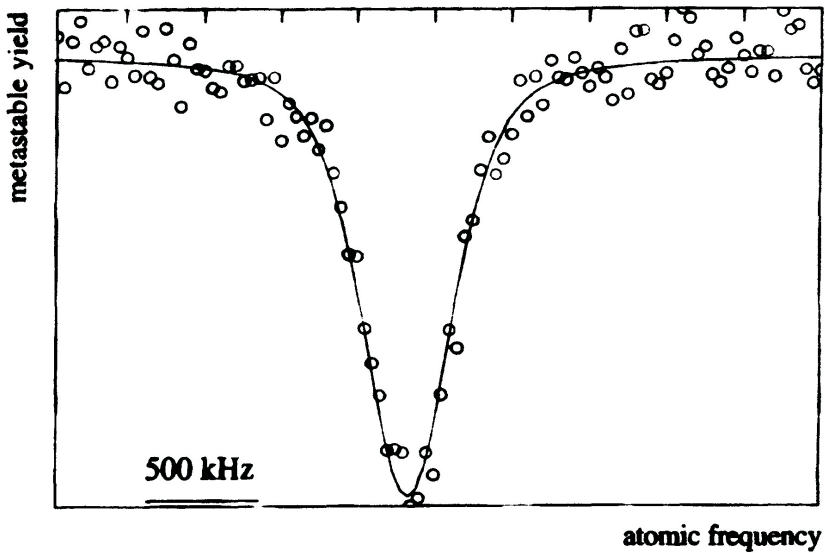


FIG. 3.4 – Spectre de la transition $2S_{1/2}(F = 1) - 12D_{5/2}$

3.4 Conclusion et perspectives

Les expériences de spectroscopie à deux photons dans les atomes d'hydrogène et de deutérium, qui ont débuté dans notre équipe en 1986, ont permis d'améliorer la connaissance de la constante de Ryberg d'un facteur 25.

Expérimentalement, la précision des mesures à partir du niveau 2S est actuellement limitée par le nombre de métastables participant à la transition. En effet, l'utilisation d'une importante puissance lumineuse, nécessaire à assurer un rapport signal à bruit correct pour pallier la faiblesse du nombre d'atomes, engendre des effets systématiques et élargit la raie à cause de l'inhomogénéité des déplacements lumineux. Une autre limitation est donnée par la connaissance expérimentale du déplacement de Lamb du niveau 2S.

En ce qui concerne les transitions à partir du niveau fondamental, la mesure de la transition 1S-3S est en cours dans notre équipe. Une mesure au kHz permettrait de déterminer la constante de Rydberg à 5×10^{-12} , mais surtout le déplacement de Lamb du niveau 1S au niveau de la dizaine de kHz.

La compétition qui existe entre notre groupe et celui de T.W. Hänsch a initié le développement de nouveaux outils expérimentaux, dédiés à la mesure de fréquences optiques :

l'étalon de fréquence qu'est la diode laser stabilisée sur la transition à deux photons 5S-5D du rubidium, les peignes de fréquences générés par laser titane-saphir femto-seconde. Les résultats obtenus dans les deux équipes se sont révélés complémentaires pour l'amélioration de la connaissance de la constante de Rydberg. Ils le seront également pour la détermination du déplacement de Lamb du niveau 1S en combinant les mesures des transitions 1S-2S et 1S-3S.

En ce qui concerne la théorie, les techniques actuelles de calcul des corrections QED semblent avoir atteint leurs limites. De nouveaux développements passent par une meilleure connaissance de la distribution de charge du proton. Cet état de fait stimule le projet de grande envergure qu'est la spectroscopie de la transition 2S-2P de l'hydrogène muonique développée autour de l'accélérateur du PSI. En effet, une mesure précise du "rayon du proton" permettrait de tester les prédictions de l'électrodynamique quantique et d'améliorer la précision sur la constante de Rydberg.

Articles joints

C. Schwob, L. Jozefowski, B. de Beauvoir, L. Hilico, F. Nez, L. Julien, F. Biraben, O. Acef, J.-J. Zondy et A. Clairon, Phys. Rev. Lett. **82** (1999) p.4960-4963 : "Optical frequency measurement of the 2S-12D transitions in hydrogen and deuterium : Rydberg constant and Lamb shift determinations"

B. de Beauvoir, C. Schwob, O. Acef, J.-J. Zondy, L. Jozefowski, L. Hilico, F. Nez, L. Julien, A. Clairon et F. Biraben, Eur. Phys. J. D **12** (2000) p.61-93 : "Metrology of the hydrogen and deuterium atoms : determination of the Rydberg constant and Lamb shifts".

Optical Frequency Measurement of the 2S-12D Transitions in Hydrogen and Deuterium: Rydberg Constant and Lamb Shift Determinations

C. Schwob, L. Jozefowski, B. de Beauvoir, L. Hilico,* F. Nez, L. Julien, and F. Biraben

*Laboratoire Kastler Brossel, Ecole Normale Supérieure et Université Pierre et Marie Curie,
Laboratoire associé au CNRS UMR 8552, 4 place Jussieu, Tour 12 E01, 75252 Paris Cedex 05, France*

O. Acef and A. Clairon

*Laboratoire Primaire du Temps et des Fréquences, Bureau National de Métrologie-Observatoire de Paris,
61 avenue de l'Observatoire, 75014 Paris, France*
(Received 22 December 1998)

We have performed a pure optical frequency measurement of the 2S-12D two-photon transitions in atomic hydrogen and deuterium. From a complete analysis taking into account this result and all other precise measurements (by ourselves and other authors), we deduce optimized values for the Rydberg constant, $R_\infty = 109\,737\,315\,685\,16(84) \text{ cm}^{-1}$ (relative uncertainty of 7.7×10^{-12}) and for the 1S and 2S Lamb shifts $L_{1S} = 8172.837(22) \text{ MHz}$ and $L_{2S-2P} = 1057.8446(29) \text{ MHz}$ [respectively, $L_{1S} = 8183.966(22) \text{ MHz}$, and $L_{2S-2P} = 1059.2337(29) \text{ MHz}$ for deuterium]. These are now the most accurate values available. [S0031-9007(99)09458-2]

PACS numbers: 06.20.Jr, 21.10.Ft, 31.30.Jv

For many years, Doppler free two-photon spectroscopy has been applied to the hydrogen atom in order to test quantum electrodynamics calculations and to improve the precision of the Rydberg constant R_∞ [1]. Recently, the uncertainty of the measurements has been reduced to a level below 10^{-11} thanks to optical frequency-multiplication chains, which link the measured frequency via intermediate standard lasers to the caesium clock. With such a chain, Hänsch and co-workers have taken advantage of the small natural width of the 1S-2S two-photon transition (1.3 Hz) to measure this frequency with an uncertainty of 3.4×10^{-13} [2]. In our group, we have made absolute frequency measurements of the 2S-8S/D transitions with an accuracy better than 8×10^{-12} [3]. In this last case, the precision was limited by the line shape analysis which becomes complicated by a large broadening (up to 1 MHz) due to the inhomogeneous light shift. The comparison of the 1S-2S and 2S-8S/D measurements has provided very precise determinations of R_∞ and of the Lamb shift [2,3]. Nevertheless, in order to confirm our 2S-8S/D frequency measurements, we have built a new chain to measure the frequencies of another transition, that is the 2S-12D transition. This transition yields complementary information to our study of the 2S-nS/nD transitions, because it is very sensitive to stray electric fields (the shift due to the quadratic Stark effect varies as n^7), and so such a measurement is a stringent test of Stark corrections to the Rydberg levels. In this Letter, we present these new results and make a complete analysis of the optical frequency measurements to determine the best values for R_∞ and the Lamb shifts.

Our new frequency chain uses two standard lasers, a laser diode stabilized on the 5S-5D two-photon transition of rubidium (LD/Rb laser, $\lambda = 778 \text{ nm}$, $\nu = 385 \text{ THz}$)

and a CO₂ laser stabilized to an osmium tetraoxide line (labeled CO₂/OsO₄, $\lambda \approx 10 \mu\text{m}$, $\nu \approx 29 \text{ THz}$). In 1996, the frequencies of three LD/Rb lasers, one in the Laboratoire Kastler Brossel (LKB) and two in the Laboratoire Primaire du Temps et des Fréquences (LPTF), were measured with a frequency chain which connected the LD/Rb laser to the CO₂/OsO₄ standard [4]. More recently, the frequency measurement of this CO₂/OsO₄ standard has been remade with respect to the Cs clock with an uncertainty of 20 Hz (i.e., a relative uncertainty of 7×10^{-13}) [5]. This last measurement corrects the previous one of the CO₂/OsO₄ standard by -87 Hz . With this correction, the frequency of the LD/Rb standard laser working at the LKB is 385 285 142 369.4(1.0) kHz. We have kept a conservative uncertainty of 1 kHz which takes into account the day-to-day repeatability and the long term stability of the LD/Rb standard and the accuracy of the CO₂/OsO₄ standard ($13 \times 20 \text{ Hz}$).

The frequency gap between the 2S-12D lines ($\lambda \approx 750 \text{ nm}$, $\nu \approx 399.5 \text{ THz}$) and the LD/Rb standard is almost equal to half of the CO₂/OsO₄ standard frequency. We have built an optical frequency divider to reduce this frequency by a factor of 2 [2,6]. The different parts of the experiment are carried out simultaneously at the LKB and LPTF (see Fig. 1). The two laboratories are linked by two, 3 km long, optical fibers which are used, via a phase coherent chain, to transfer the CO₂/OsO₄ frequency reference from LPTF to LKB. The frequency shift introduced by these optical fibers is at most 3 Hz [7]. We use an auxiliary laser at 809 nm ($\nu \approx 370.5 \text{ THz}$) and the laser frequencies satisfy the equations,

$$\begin{aligned}\nu(2S-12D) + \nu(809) &= 2\nu_{\text{Rb}}, \\ \nu(2S-12D) - \nu(809) &= \nu(\text{CO}_2).\end{aligned}$$

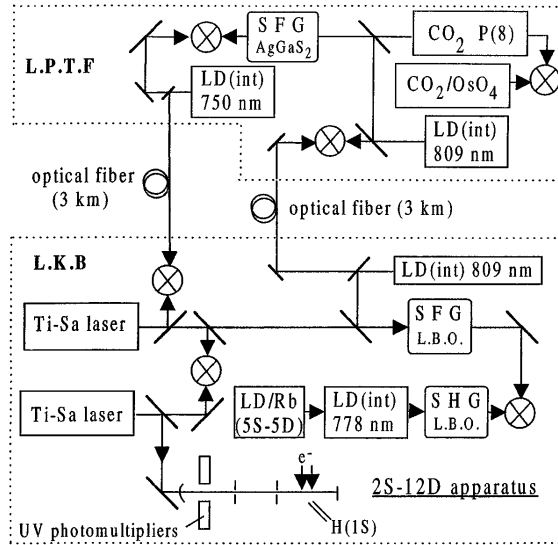


FIG. 1. Outline of the frequency chain between the $2S$ - $12D$ hydrogen frequencies and the LD/Rb and CO_2/OsO_4 standards. The details are explained in the text.

A laser diode (power of 50 mW) is injected by the LD/Rb standard at 778 nm and frequency doubled in a LiB_3O_5 (LBO) crystal placed in a ring cavity. The generated UV beam is frequency compared to the frequency sum (made also in an LBO crystal) of the 750 and 809 nm radiations produced by a first titanium-sapphire laser (about 300 mW) and a laser diode (about 30 mW). One part of the 809 nm radiation is sent via one fiber to the LPTF. There, a 809 nm local laser diode is phase locked on the LKB one. A frequency sum of this 809 nm laser diode and of an intermediate CO_2 laser in an $AgGaS_2$ crystal generates a wave at 750 nm. This wave is used to phase lock a laser diode at 750 nm which is sent back to the LKB by the second fiber. In such a way, the two equations are simultaneously satisfied and all the frequency counting is performed in the LKB. A second titanium-sapphire laser induces the two-photon transitions. For the hydrogen measurements, the CO_2 intermediate laser uses the $P(8)$ line [respectively, $CO_2 R(4)$ line for deuterium], and the residual frequency difference between the two titanium-sapphire lasers is about 2.5 GHz (respectively, 41.3 GHz for deuterium). These frequency beat notes are detected with a photodiode or a Schottky diode.

The hydrogen experiment has been described elsewhere [3,8]. To reduce the collisional and transit time broadening, the two-photon transitions are induced in a metastable atomic beam collinear with the laser beams. We use a highly stable titanium-sapphire laser with a frequency jitter and a long term stability of a few kHz [9]. Thanks to an enhancement cavity surrounding the atomic beam, the optical power can be as much as 50 W in each direc-

tion with a beam waist of $646 \mu m$. At the end of the atomic beam, an electric field quenches the metastable atoms and we detect the Lyman- α fluorescence to measure the metastable yield. As the excited $12D$ states decay preferentially to the $1S$ ground state in a proportion of 95%, the optical excitation can be detected via the corresponding decrease of the $2S$ beam intensity. The acquisition and analysis of the experimental data follow the same procedure as in Ref. [8]. To evaluate the light shift, which is the major source of shift and broadening, we record the atomic signal for different laser intensities, and we extrapolate the line position to zero light power. For each recording, a theoretical profile is fitted to the experimental curve. This theoretical line shape takes into account the light shift, the saturation of the transition, the small hyperfine structure of the $12D$ levels, the photoionization, the small deviation of the atomic trajectories due to the light forces, as well as the second-order Doppler shift. The velocity distribution is measured by monitoring the Doppler shifted $2S$ - $6P$ transition. Each fit gives both the experimental line center and the line position corrected for light shift and hyperfine structure of the $12D$ level. As we measure continuously the various beat frequencies of our frequency chain, we can deduce the absolute frequency of the line. Finally, the result is corrected for the shift due to black-body radiation (2.1 kHz for the $12D$ levels at 330 K [10]) and for the Stark shift due to stray electric fields. To evaluate these fields, we have studied the $2S$ - $20D$ transitions. In this case, the broadening due to the linear Stark effect is large (it varies as n^2) and, from the line shape of the $2S$ - $20D$ transitions, we deduce a mean value of the stray electric fields of 2.0 (1.0) mV/cm. A careful analysis of the Stark effect, including the mixing of the quasidegenerate levels ($D_{5/2}$ - $F_{5/2}$ and $D_{3/2}$ - $P_{3/2}$), gives a Stark shift of -2.1 (1.2) kHz and -6.0 (4.9) kHz for the $12D_{5/2}$ and $12D_{3/2}$ levels.

We have studied the $2S_{1/2}(F = 1 \text{ or } 3/2)$ - $12D_{5/2}$ and $2S_{1/2}(F = 1 \text{ or } 3/2)$ - $12D_{3/2}$ transitions in hydrogen and deuterium. For each transition, the atomic signal is recorded for at least 50 light powers, and, in total, we have used 237 runs (20 min long) for data collection. The measured frequencies (after correction of the hyperfine structures) are reported in Table I. The quoted uncertainties are due only to the statistics. The two experimental results for the $12D_{5/2}$ and $12D_{3/2}$ levels can be compared by taking into account the theoretical value of the fine structure and the Lamb shift of the $12D$ levels. Following recent calculations of the Bethe logarithm [11], these Lamb shifts are $L_{12D_{3/2}} = -17.6(2)$ kHz and $L_{12D_{5/2}} = 21.5(2)$ kHz in hydrogen and deuterium. Finally, we obtain two independent values of the $2S_{1/2}$ - $12D_{5/2}$ interval (see Table I) which are in fair agreement for hydrogen and deuterium. The average values are, respectively, 799 191 727 402.8(6.7) kHz and 799 409 184 967.6(6.5) kHz. These uncertainties (1 standard deviation) are due to the statistical error, the

TABLE I. Frequencies of the $2S$ - $12D$ two-photon transitions.

Transition	Measured frequency (MHz)	$2S_{1/2}$ - $12D_{5/2}$ Deduced frequency (MHz)
Hydrogen		
$2S_{1/2}$ - $12D_{5/2}$	799 191 727.4037 (47)	799 191 727.4037
$2S_{1/2}$ - $12D_{3/2}$	799 191 710.4727 (62)	799 191 727.3999
Mean value of the $2S_{1/2}$ - $12D_{5/2}$ measurements:		799 191 727.4028 (67)
Deuterium		
$2S_{1/2}$ - $12D_{5/2}$	799 409 184.9668 (45)	799 409 184.9668
$2S_{1/2}$ - $12D_{3/2}$	799 409 168.0380 (44)	799 409 184.9698
Mean value of the $2S_{1/2}$ - $12D_{5/2}$ measurements:		799 409 184.9676 (65)

Stark effect (2.1 kHz), the second-order Doppler effect (1 kHz), the stability and the measurement of the LD/Rb standard laser (2 kHz), and the imperfections of the theoretical model (4.5 kHz). These measurements are slightly less precise than our previous ones of the $2S$ - $8S/D$ transitions [3,12], because of the smaller signal-to-noise ratio and the larger quadratic Stark effect.

Table II gives the values of the Rydberg constant deduced from different transitions by several methods. It is convenient to express an energy level in hydrogen as the sum of two terms: the first, given by the Dirac equation and by the first relativistic correction due to the recoil of the proton, is known exactly, apart from the uncertainties in the physical constants involved (mainly R_∞). The second term is the Lamb shift, which contains all the other corrections, i.e., the QED corrections, the other relativistic corrections, and the effect of the proton charge distribution. Consequently, to extract R_∞ from the accurate measurements one needs to know the Lamb shifts. For this analysis, the theoretical values of the Lamb shifts are sufficiently precise, except for those of the $1S$ and $2S$ levels. In hydrogen, there have been several precise determinations of the $2S_{1/2}$ - $2P_{1/2}$ splitting

by microwave spectroscopy [13] and by the anisotropy method [14]. Using the mean value of these results [$L_{2S-2P} = 1057.8454(65)$ MHz], we can deduce from our $2S_{1/2}$ - $12D_{5/2}$ determination a value of the Rydberg constant $R_\infty = 109 737.315 684 5(13)$ cm $^{-1}$. The uncertainty (1.2×10^{-11}) comes from the frequency measurement (8.4×10^{-12}), the $2S$ Lamb shift (8.1×10^{-12}), and the proton-to-electron mass ratio (1.3×10^{-12}) [15]. To compare our present result with our earlier one [3], Table II gives the Rydberg constant value deduced from the $2S$ - $8D$ measurement with the same procedure. These two values are in acceptable agreement (they differ by about 1 standard deviation). Although slightly less precise, our new result confirms our previous one and shows that the correction due to the quadratic Stark effect is well analyzed (this correction is 17 times larger for the $12D$ than for the $8D$ levels). Table II gives the average of these two results with an uncertainty of 10^{-11} . This result is the most precise if we do not make theoretical assumptions concerning the $1S$ and $2S$ Lamb shifts.

The other methods to determine R_∞ use the $1/n^3$ scaling law of the Lamb shift which gives the theoretical value of the linear combination of the Lamb shifts

TABLE II. Determination of the Rydberg constant R_∞ .

Method and transitions involved	$(R_\infty - 109737) \text{ cm}^{-1}$
Determination of R_∞ from the $2S$ - nD and $2S$ - $2P$ measurements	
$2S$ - $12D$ and $2S$ - $2P$ in hydrogen	0.315 6845 (13)
$2S$ - $8D$ and $2S$ - $2P$ in hydrogen	0.315 6858 (13)
$2S$ - $12D$, $2S$ - $8D$, and $2S$ - $2P$ in hydrogen	0.315 6852 (11)
Determination of R_∞ without the $2S$ - nS/D measurements	
$1S$ - $2S$, $2S$ - $2P$, and $1/n^3$ law in hydrogen	0.315 6854 (20)
Determination of R_∞ from linear combination of optical frequencies measurements	
$2S$ - $12D$, $1S$ - $2S$, and $1/n^3$ law in hydrogen	0.315 6838 (17)
$2S$ - $12D$, $1S$ - $2S$, and $1/n^3$ law in deuterium	0.315 6838 (16)
$2S$ - $12D$, $1S$ - $2S$, and $1/n^3$ law in hydrogen and deuterium	0.315 6838 (13)
$2S$ - $8D$, $1S$ - $2S$, and $1/n^3$ law in hydrogen and deuterium	0.315 6861 (12)
$2S$ - $8D$, $2S$ - $12D$, $1S$ - $2S$, and $1/n^3$ law in hydrogen and deuterium	0.315 6850 (10)
General least squares adjustment in hydrogen and deuterium	0.315 685 16 (84)

$L_{1S}-8L_{2S}$ [16]. Using this relation and the measurements of the $2S$ Lamb shift, it is possible to extract a value of R_∞ from the very precise measurement of the $1S-2S$ transition [2]. The result, independent of our $2S-nD$ measurements, is given in the second part of Table II and agrees perfectly with the value deduced from the $2S-nD$ frequencies.

Finally, in the third part of Table II, we give the values of R_∞ obtained from the linear combination of several optical frequencies. For example, if we consider the frequencies ν_{1S-2S} and ν_{2S-12D} of the $1S-2S$ and $2S-12D$ intervals, we can form the linear combination $7\nu_{2S-12D}-\nu_{1S-2S}$, where the theoretically well-known quantity $L_{1S}-8L_{2S}$ appears. This method is independent of the microwave measurements of the $2S$ Lamb shift and is relevant for both hydrogen and deuterium. If we consider the $1S-2S$ and $2S-12D$ transitions, the values obtained for hydrogen and deuterium are in excellent agreement (see Table II). With a least squares procedure, it is possible to apply this method to several transitions. If we use all the precise optical frequency measurements in hydrogen and deuterium (transitions $1S-2S$, $2S-8D$, and $2S-12D$), we obtain a value of R_∞ more precise than the previous ones. This method also provides very accurate determination of the $1S$ and $2S$ Lamb shifts, $L_{1S} = 8172.834(26)$ MHz and $L_{2S-2P} = 1057.8442(34)$ MHz [respectively, $8183.963(26)$ MHz and $1059.2333(34)$ MHz for deuterium]. This result for the $2S$ Lamb shift is independent and more precise than the direct determinations made by microwave spectroscopy.

To make an average of these various determinations of R_∞ , we have performed a least squares adjustment which takes into account the measurements of the $2S$ Lamb shift [13,14], the optical frequency measurements of the $1S-2S$ [2], $2S-8D$ [3], and $2S-12D$ transitions in hydrogen and deuterium, and also the measurements of the $1S$ Lamb shift made by frequency comparison of the $1S-2S$ and $2S-4S/P/D$ transitions [17,18] or of the $1S-3S$ and $2S-6S/D$ ones [19]. We obtain the values $R_\infty = 109\,737.315\,685\,16(84)$ cm $^{-1}$, $L_{1S} = 8172.837(22)$ MHz, and $L_{2S-2P} = 1057.8446(29)$ MHz [respectively, $8183.966(22)$ MHz and $1059.2337(29)$ MHz for deuterium]. These values, which take into account all the most recent results, are the most precise to date. The $1S$ Lamb shift value is in poor agreement with the more recent calculation in hydrogen [$L_{1S} = 8172.731(40)$ MHz with the proton radius $r_p = 0.862(12)$ fm [20]]. Assuming the validity of these QED calculations, we deduce $r_p = 0.900(16)$ fm.

To conclude, we have made an optical frequency measurement of the $2S-12D$ transition in hydrogen and deuterium. This result confirms our previous work on the $2S-8S/D$ transitions and, furthermore, we have reduced the uncertainty in the Rydberg constant to less than $7.7 \times$

10^{-12} . We present also an exhaustive analysis of the most accurate measurements in hydrogen and deuterium which shows that the optical frequency measurements have superseded the microwave determination of the $2S$ Lamb shift. The precision is now limited by the uncertainties of the $2S-nD$ frequencies.

The authors are indebted to B. Cagnac for many stimulating discussions, and they thank M. D. Plimmer for critical reading of the manuscript. This work is partially supported by the Bureau National de Métrologie.

*Affiliated with Université d'Evry Val d'Essonne, France.

- [1] See, for example, B. Cagnac, M. D. Plimmer, L. Julien, and F. Biraben, Rep. Prog. Phys. **57**, 853 (1994).
- [2] Th. Udem *et al.*, Phys. Rev. Lett. **79**, 2646 (1997); A. Huber *et al.*, Phys. Rev. Lett. **80**, 468 (1998).
- [3] B. de Beauvoir *et al.*, Phys. Rev. Lett. **78**, 440 (1997).
- [4] D. Touahri *et al.*, Opt. Commun. **133**, 471 (1997).
- [5] G. D. Rovera and O. Acef, IEEE Trans. Instrum. Meas. (to be published).
- [6] H. R. Telle, D. Meschede, and T. W. Hänsch, Opt. Lett. **15**, 532 (1990).
- [7] B. de Beauvoir *et al.*, Eur. Phys. J. D **1**, 227 (1998).
- [8] J. C. Garreau, M. Allegrini, L. Julien, and F. Biraben, J. Phys. (Paris) **51**, 2263 (1990); **51**, 2275 (1990); **51**, 2293 (1990).
- [9] S. Bourzeix, M. D. Plimmer, F. Nez, L. Julien, and F. Biraben, Opt. Commun. **99**, 89 (1993).
- [10] J. W. Farley and W. H. Wing, Phys. Rev. A **23**, 2397 (1981).
- [11] G. W. F. Drake and R. A. Swainson, Phys. Rev. A **41**, 1243 (1990).
- [12] We have remade the analysis of our $2S-8S/D$ measurements to take into account the improvements of the theoretical line shapes and the corrections due to the standard laser, the black-body radiation, and the Stark effect. With the same more conservative uncertainties, the results are $\nu(2S_{1/2}-8D_{5/2}) = 770\,649\,561\,581.1(5.9)$ kHz and $\nu(2S_{1/2}-8D_{5/2}) = 770\,859\,252\,848.3(5.5)$ kHz for hydrogen and deuterium.
- [13] S. R. Lundeen and F. M. Pipkin, Phys. Rev. Lett. **46**, 232 (1981); E. W. Hagley and F. M. Pipkin, Phys. Rev. Lett. **72**, 1172 (1994); U. Jentschura and K. Pachucki, Phys. Rev. A **54**, 1853 (1996).
- [14] A. van Wijngaarden, F. Holuj, and G. W. F. Drake, Can. J. Phys. **76**, 95 (1998).
- [15] D. L. Farnham, R. S. Van Dyck, and P. B. Schwinberg, Phys. Rev. Lett. **75**, 3598 (1995).
- [16] S. G. Karshenboim, Z. Phys. D **39**, 109 (1997).
- [17] M. Weitz *et al.*, Phys. Rev. Lett. **72**, 328 (1994).
- [18] D. J. Berkeland, E. A. Hinds, and M. G. Boshier, Phys. Rev. Lett. **75**, 2470 (1995).
- [19] S. Bourzeix *et al.*, Phys. Rev. Lett. **76**, 384 (1996).
- [20] S. Mallampalli and J. Sapirstein, Phys. Rev. Lett. **80**, 5297 (1998).

Metrology of the hydrogen and deuterium atoms: Determination of the Rydberg constant and Lamb shifts

B. de Beauvoir¹, C. Schwob¹, O. Acef², L. Jozefowski¹, L. Hilico^{1,a}, F. Nez¹, L. Julien¹, A. Clairon², and F. Biraben^{1,b}

¹ Laboratoire Kastler Brossel, École Normale Supérieure et Université Pierre et Marie Curie^c, 4 place Jussieu, 75252 Paris Cedex 05, France

² Laboratoire Primaire du Temps et des Fréquences, Bureau National de Métrologie-Observatoire de Paris, 61 avenue de l'Observatoire, 75014 Paris, France

Received 9 March 2000

Abstract. We present a detailed description of several experiments which have been previously reported in several letters: the determination of the 1S Lamb shift in hydrogen by a comparison of the frequencies of the 1S–3S and 2S–6S or 2S–6D two-photon transitions, and the measurement of the 2S–8S/D and 2S–12D optical frequencies. Following a complete study of the lineshape of the two-photon transitions, we provide the updated values of these frequencies which have been used in the 1998 adjustment of the fundamental constants. From an analysis taking into account these results and several other precise measurements by other authors, we show that the optical frequency measurements have superseded the microwave determination of the 2S Lamb shift and we deduce optimized values for the Rydberg constant, $R_\infty = 109\,737\,315\,685\,50(84) \text{ cm}^{-1}$ (relative uncertainty of 7.7×10^{-12}) and for the 1S and 2S Lamb shifts $L(1S) = 8\,172\,840(22) \text{ MHz}$ and $L(2S-2P) = 1\,057\,8450(29) \text{ MHz}$ (respectively, $8\,183\,970(22) \text{ MHz}$ and $1\,059\,2341(29) \text{ MHz}$ for deuterium). These are now the most accurate values available.

PACS. 06.20.Jr Determination of fundamental constants – 21.10.Ft Charge distribution – 31.30.Jv Relativistic and quantum electrodynamic effects in atoms and molecules

1 Introduction

Over the past two decades the absolute measurement of wavelengths or frequencies of hydrogen has been continuously improved with the aim of determining the Rydberg constant and testing quantum electrodynamics calculations. With the interferometric measurements, the relative accuracy was in the range of one part in 10^{10} . A review of these results is provided in reference [1]. Recently, the interferometric measurements have been superseded by accurate optical frequency ones. The latter make use of frequency-multiplication chains which link the measured frequency, *via* intermediate standard lasers, to the caesium clock. With this method, Hänsch and collaborators have measured the optical frequency of the 1S–2S two-photon transition with an accuracy better than 3.4×10^{-13} [2,3]. In our group, we have studied the 2S–nS and 2S–nD two-photon transitions. In 1993, we measured the optical frequencies of the $2S_{1/2}-8S_{1/2}$, $2S_{1/2}-8D_{3/2}$ and $2S_{1/2}-8D_{5/2}$ transitions in hydrogen with a frequency chain using two standard lasers (the iodine stabilized and the methane sta-

bilized helium-neon lasers) and obtained a precision in the range of 10^{-11} [4,5]. In 1996, we remade these measurements in hydrogen and deuterium with an accuracy better than one part in 10^{11} [6]. We used a new frequency chain with a new standard laser, namely a diode laser at 778 nm stabilized on the 5S–5D two-photon transition of rubidium (LD/Rb laser). The frequency of this standard was measured with a frequency chain at the *Laboratoire Primaire du Temps et des Fréquences* (LPTF) [7]. More recently, in order to check these 2S–8S/D frequency measurements, we have built a new chain to measure the frequencies of the 2S–12D transitions in hydrogen and deuterium [8]. In parallel, we have taken advantage of our experimental set-up on the 2S–nS/D transitions to deduce the Lamb shift of the 1S level *via* a comparison of the frequencies of the 1S–3S and 2S–6S/D transitions [9].

The aim of this paper is to relate in detail these experiments. Section 2 describes our apparatus for the observation of the 2S–nS and 2S–nD transitions, which is the corner stone of our hydrogen experiments. The Doppler free two-photon transitions, in the range 750–820 nm, are induced by a highly stable titanium-sapphire laser. To reduce the transit time broadening, we use an atomic beam colinear with the laser beam. Section 3 is devoted to the line shape analysis of the 2S–nS/D transitions. We follow

^a Affiliated with Université d'Évry Val d'Essonne, France.

^b e-mail: biraben@spectro.jussieu.fr

^c Laboratoire associé au CNRS, UMR 8552.

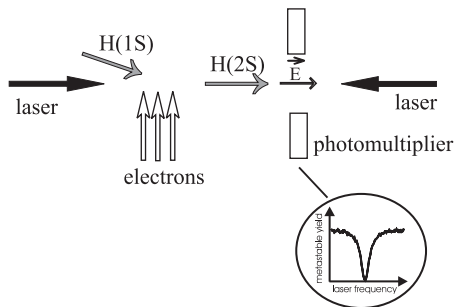


Fig. 1. Experimental geometry of laser and atom beams to observe the $2S-nS$ and $2S-nD$ two-photon transitions. When the laser frequency is scanned over the resonance, we observe a decrease of the metastable yield (see the inset).

the same procedure as in our previous work [10–12]. We calculate the two-photon transition probability for a single atom and average over all the possible trajectories. In our recent calculations, we have taken into account the small hyperfine structure of the D levels, photoionisation effects, the small deviation of the atomic trajectories due to the light forces, as well as the second-order Doppler effect. We present the data analysis procedure and calculate the corrections due to stray electric fields. The optical frequency measurements are presented in Section 4. We describe the rubidium optical frequency standard and the various frequency chains used to measure the $2S-8S/D$ and $2S-12D$ transitions. Finally, we give the up-to-date results, which take into account the best line shape analysis and the most recent measurements of the optical frequency standards. The comparison of the $1S-3S$ and $2S-6S/D$ frequencies is described in Section 5. Finally, in Section 6, we analyse all these results to deduce the Rydberg constant and the Lamb shifts of the $1S$ and $2S$ levels. We show that the optical frequency measurements have superseded the radiofrequency measurements of the $2S$ Lamb shift and, using a least squares procedure which takes into account all the precise measurements in hydrogen and deuterium, we deduce a value of the Rydberg constant with a relative uncertainty of 7.7×10^{-12} .

2 Spectroscopy of the $2S-nS$ and $2S-nD$ transitions

2.1 Method

The principle of the experiment has been described previously [10]. The experimental geometry is illustrated in Figure 1. A metastable atomic beam is formed by electronic excitation of a $1S$ hydrogen atomic beam. Due to the inelastic collision with the electron, the atomic trajectory is deviated by an angle of about 20° . We use this deviation to make colinear, after the collision, the $2S$ atomic beam with the laser beams. At the end of the atomic beam we monitor the metastable yield: an electric field quenches the metastable state and we detect the Lyman- α fluorescence. When the laser frequency is in resonance with the

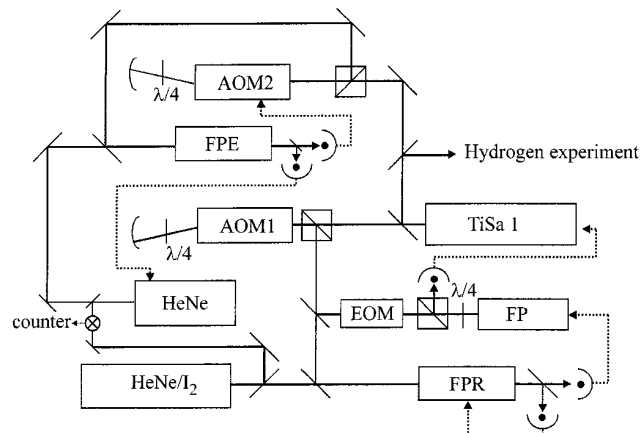


Fig. 2. Experimental setup for the frequency stabilisation of the titanium-sapphire laser. The explanations are given in the text (TiSa1: titanium-sapphire laser, HeNe/I₂: iodine stabilized helium-neon laser, He-Ne: auxiliary helium-neon laser, AOM1 and AOM2: acousto-optic modulators, EOM: electro-optic modulator, FP, FPR and FPE: Fabry-Perot cavities).

$2S-nS/D$ transition, the atoms in the nS or nD states undergo a radiative cascade towards the $1S$ state in a proportion of about 95%. It occurs an optical quenching of the metastable level before the detection region and the optical excitation can be detected *via* the corresponding decrease of the $2S$ beam intensity (see Fig. 1).

2.2 Laser source

To induce the optical excitation, we use a home-made titanium-sapphire laser which has been described previously [13]. With a pump power of 13 W (from a Spectra-Physics 2030 argon ion laser), the single frequency output power is about 2 W at 800 nm. For some experiments [4, 5, 8], we use a second titanium-sapphire laser with the same pump laser and the available power is reduced to about 1 W. For the high-resolution hydrogen spectroscopy, we require a narrow laser bandwidth and a good long term frequency stability. The frequency stabilisation set-up is shown in Figure 2. The short term and long term stability are assured with two Fabry-Perot cavities, labelled FP and FPR respectively. The principle of this stabilisation arrangement is to lock the titanium-sapphire laser on the FP cavity, the FP cavity to the FPR cavity and, finally, the FPR cavity to an iodine stabilized helium-neon laser. A secondary laser beam from the titanium-sapphire laser is splitted after a double pass through an acousto-optic modulator (model 3200 from Crystal Technology at 200 MHz, labelled AOM1 in Fig. 2) and sent on the FP and FPR cavities. The FP cavity (free spectral range 600 MHz and finesse of about 400) is placed in a robust vacuum box (wall thickness of 2 cm) and carefully isolated from the external vibrations[13]. To reduce the frequency jitter, the laser is locked, in a first step, on the FP cavity. We use an FM sideband method [14]: the laser beam sent in the FP cavity is phase modulated at about

15 MHz with an electro-optic modulator (Gsänger PM25, labelled EOM in Fig. 2). From the modulation detected on the beam reflected by the FP cavity, we extract an error signal which controls the piezoelectric and electro-optic transducers monitoring the length of the laser cavity. Thanks to this servo-loop, the frequency jitter is reduced from 500 kHz (free running laser) to about 2 kHz [13].

The long term stability is guaranteed by the reference Fabry-Perot cavity FPR. This cavity is very stable. It consists of a 50 cm long zerodur spacer and two silver coated mirrors, one flat and one spherical (60 cm curvature radius). Its finesse is about 75 at 633 nm and 120 at 800 nm. A piezoelectric transducer (PZT) moves the flat mirror thanks to a mechanical construction (made in fused silica) which avoid the rotation of the mirror (the principle is to deform a parallelogram) [15]. This cavity is also placed in a vacuum box with the same design that for the FP cavity. To obtain the long term stability, the FPR cavity is irradiated simultaneously by an iodine stabilized helium-neon laser and a part of the titanium-sapphire laser (after the double pass in the acousto-optic modulator). A first servo-loop locks the FPR length to the helium-neon wavelength (we use the 10 kHz frequency modulation of the helium-neon laser). As the zerodur spacer is very stable, we have always used, since ten years, the same fringes of the FPR cavity (1 580 868 or 1 580 869 following the PZT voltage). The length of the FPR cavity is also modulated (frequency of about 4.2 kHz). This modulation is detected on the transmission of the titanium-sapphire laser and a second servo-loop locks the length of the FP cavity to the FPR cavity. To scan the laser frequency, we sweep the frequency of the radiofrequency wave which drives the acousto-optic modulator. With this arrangement, the lengths of the two FP and FPR cavities are fixed and the commutation time of the laser frequency is only limited by the bandwidth of the first servo-loop on the FP cavity (about 50 kHz). An other advantage of this system with two cavities is that the accuracy is given by the servo-loop on the FPR cavity. This accuracy is better than the accuracy of the first servo-loop on the FP cavity for two reasons: (i) the modulation of the FPR cavity is small (about 10% of the cavity bandwidth) and the error signal is less perturbed by the transverse modes of the FPR cavity which appear when the laser beam is not perfectly mode matched on the cavity, (ii) the transmission signal of the cavity is an Airy function which has approximatively a symmetric Lorentzian profile. It is not the case for the servo-loop on the FP cavity which is made with the reflected beam by the cavity. In this case, the profile of the resonance of the cavity can be dissymmetric because of the losses of the mirrors (it is the sum of an absorption and a dispersion shapes due to the phase shift between the first reflection on the input mirror and the beam which comes out of the cavity) [15].

Thanks to our optical frequency measurements (see Sect. 4), we have tested the metrological features of this laser system. For instance, we have very often measured the optical frequency of the fringe 1 286 174 of the FPR cavity which is close to the 2S–8S/D two-photon transition

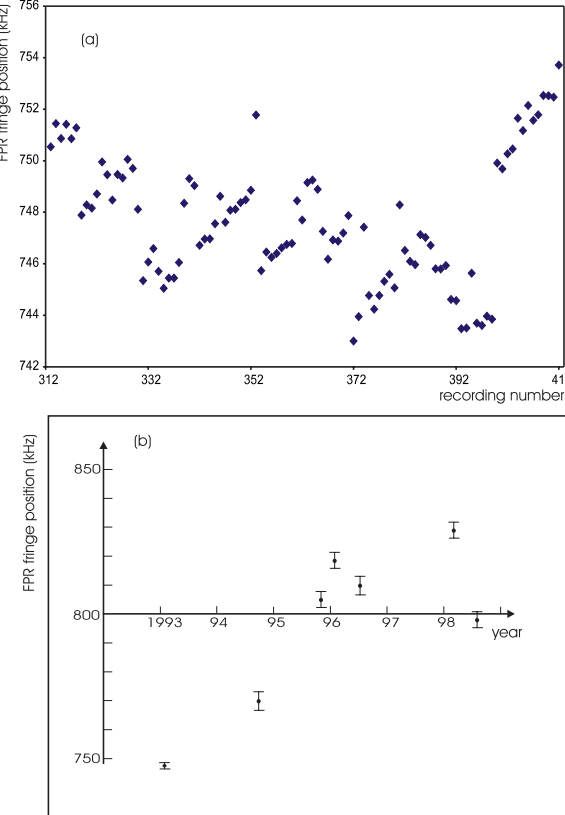


Fig. 3. Absolute frequency of the fringe 1 286 174 of the FPR cavity when the fringe 1 580 868 is locked to the *d* line of the iodine stabilized He-Ne laser. The values are in kHz and we have subtracted 385 325 GHz. (a) Measurements made in 1993: each point is the value obtained during a 20 minutes recording of the 2S–8S/D transitions in hydrogen. The measurements were made during about two weeks. The mean value is 385 325 000 747.7(2.5) kHz. (b) Drift of the fringe frequency on the period 1993–1998.

in hydrogen. The results are reported in Figures 3a and 3b. Figure 3a shows a series of measurements made in 1993 [5]. Each point is the mean of a 20 minutes recording (see Sect. 2.3). The standard deviation of these data is about 2.5 kHz, *i.e.* a day-to-day stability of 7×10^{-12} . Figure 3b shows the results since several years. During five years, we have observed a frequency drift of about 100 kHz which is perhaps due to an aging of the silver coating.

We use also several other interferometers to control the wavelength of the laser: a lambdameter (typical accuracy 10^{-3} nm), a 3 cm Fabry-Perot cavity (placed in a vacuum box and scanned by pressure variation) and an other, 50 cm long, Fabry-Perot cavity (labelled FPE in Fig. 2). This cavity has the same design that the FPR cavity, except that there is no PZT. To know the length of the FPE cavity, an auxiliary He-Ne laser is locked on a fringe of this cavity and we measure the beat frequency between the two He-Ne lasers. Simultaneously, a secondary beam of the titanium-sapphire laser is sent on the FPE cavity after a double pass in an acousto-optic modulator (labelled AOM2 in Fig. 2). The frequency of this AOM

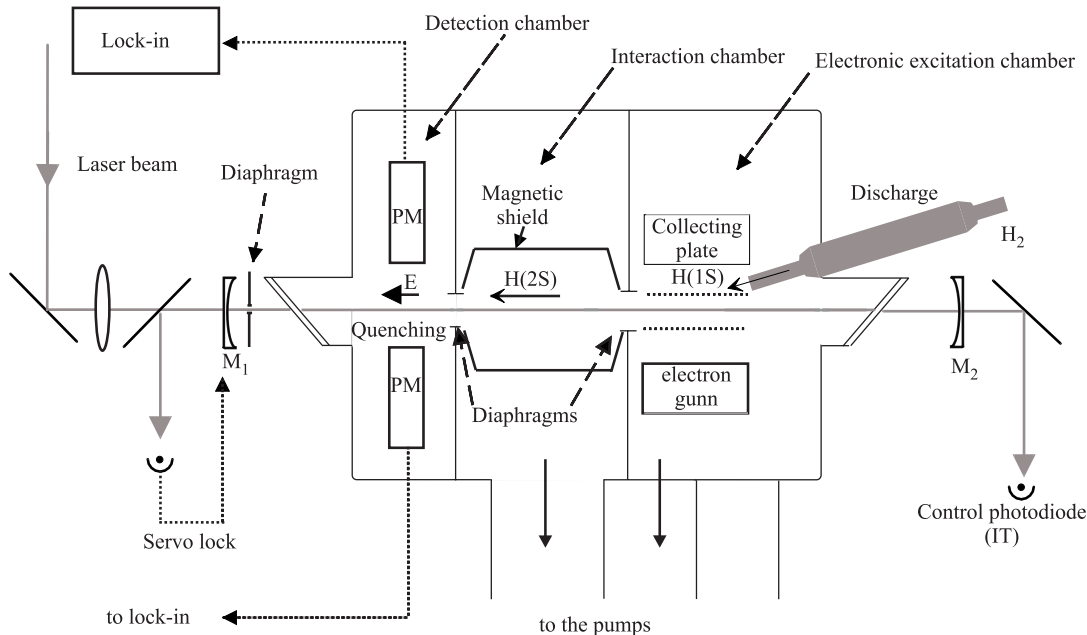


Fig. 4. The metastable hydrogen atomic beam. The three vacuum chambers are not sketched with the same scale: following the laser beams axis, the sizes of the electronic excitation chamber, interaction chamber and detection chamber are respectively 10 cm, 56 cm and 7 cm. M1 and M2: mirrors of the enhancement cavity, PM: photomultiplier.

is locked in order that the transmitted beam is in resonance with the FPE cavity. By this way, we can know the frequencies of the fringes of the FPE cavity with respect to the ones of the FPR cavity. As the free spectral range of the two cavities are slightly different (299.590 MHz and 299.700 MHz for the FPR and FPE cavity respectively), there is a Vernier effect between the two cavities: the relative positions of the fringes of the two cavities are similar every about 2700 fringes (*i.e.* 1.6 nm in terms of wavelength) and, from these measurements, we can deduce the numbers of the fringes of the FPR and FPE cavities with a typical uncertainty of one fringe.

2.3 The metastable hydrogen atomic beam

2.3.1 The atomic beam apparatus

Our metastable atomic beam is sketched in Figure 4. It is very similar to a first apparatus described in reference [16]. The metastable atomic beam is produced in two steps: molecular hydrogen is dissociated in a water cooled Pyrex tube by a radiofrequency discharge (about 26 MHz). An atomic beam flows through a Teflon nozzle and effuses into a first vacuum chamber, which is evacuated by an oil diffusion pump (Alcatel 6250, pumping speed of 2 500 l/s) to a pressure of about 10^{-4} mbar. Thereafter ground state atoms are excited to the 2S metastable state by electronic bombardment (in an equipotential region to prevent the quenching of the metastable atoms, see details in Ref. [16]). The optical excitation takes place in the second vacuum chamber, where the metastable atomic beam

is delimited by two holes, 7 mm in diameter, 56 cm apart (this metastable atomic beam makes an angle of 20° with the 1S atomic beam). To evacuate this chamber, we use a cryogenic pump (CTI-Cryogenics CT8, pumping speed of 2 000 l/s for hydrogen) and the running pressure is typically 10^{-6} mbar. In our first experiments [4, 5, 9], the ambient magnetic field was reduced to less than 20 mG by three pairs of coils. More recently [6, 8], we have placed a magnetic shield in the second vacuum chamber (see Fig. 4). To reduce the stray electric fields, the walls of the chamber and the magnetic shield are painted with Aquadag, a conductive colloidal graphite suspension in an ammonia solution. This chamber is also permanently heated to 330 K to prevent the formation of any insulating deposits on the walls and the magnetic shield. From the line shape analysis of the 2S- n D transitions (n in the range 15–20), which are very sensitive to the stray electric fields, we have deduced that this painting reduces the stray electric fields from several tens of millivolts per centimetre to about 3 mV/cm (see Sect. 3). To preserve this property, the Aquadag paint is renewed approximatively about once a year. The metastable atoms are detected in the third vacuum chamber, which is simply evacuated through the 7 mm hole between the two vacuum chambers. An applied electric field quenches the 2S state and two photomultipliers (Hamamatsu R1459) detect the Lyman- α fluorescence. The two photomultiplier windows are 1 cm apart around the quenching region, and the detection solid angle is: $\Omega/4\pi \simeq 60\%$. To detect the photomultiplier signal, the quenching voltage is square-wave modulated at about 1.45 kHz and we use a lock-in amplifier (ATNE ADS2). From the photomultiplier current, we estimate the

metastable beam intensity to be at best 2×10^7 atoms/s (4×10^7 for deuterium). Nevertheless, we work usually with a metastable yield of about 8×10^6 atoms/s, regime where the signal-to-noise ratio is better.

To maximise the excitation rate for the $2S-nS/D$ two-photon transitions, the whole metastable atomic beam is placed inside an enhancement cavity whose optical axis is in coincidence with the atomic beam. This cavity is formed by two mirrors, 101 cm apart, one flat (high reflector) and the other concave (4 m curvature radius, transmission of about 1.1%). With this geometry, the beam waist is about 660 μm . To reduce the perturbations due to the vibrations of the cryogenic pump, this cavity is mounted on a small granite bench ($220 \times 20 \times 13 \text{ cm}^3$) which is carefully isolated from the vacuum apparatus. The two mirrors are mounted on piezoelectric transducers and the length of the cavity is locked to the laser wavelength by monitoring the reflected beam polarisation [17]. In this servo-loop, the rapid length fluctuations are corrected by a small PZT acting on the flat mirror, which is of a small size (8 mm in diameter, 4 mm thick). Inside the cavity, the optical power can be as much as 100 W in each direction. This light intensity is controlled with a photodiode which measures the small intensity transmitted by the high reflector.

2.3.2 Velocity distribution of the metastable atoms

A precise knowledge of the velocity distribution of the atoms is necessary to calculate the line shapes of the two-photon lines and to deduce the corrections due to the second order Doppler effect. We have measured this velocity distribution by observing the Doppler broadened $2S-6P$ transition at 410 nm with a collinear laser beam. This laser source is obtained from the titanium-sapphire laser by a frequency doubling in an LBO crystal (see Ref. [13] and Sect. 5). For this measurement, we remove the concave mirror of the enhancement cavity. The beam at 410 nm (typical power of 100 mW) is sent along the metastable beam and a fraction of the laser beam (about 30%) is reflected by the flat mirror of the enhancement cavity, so that the atoms see two counterpropagating waves. Usually, the measurements are made with two different beam waists, one matched to the diameter of the metastable beam (7 mm), the other more focused (about 2 mm) and we have observed that the results are not sensitive to the beam waist. For the detection, the quenching voltage in the third vacuum chamber is applied continuously and the laser beam is chopped at about 120 Hz. At this frequency, the duration of the square-modulation of the light (4 ms) is long with respect to the atomic transit time through the second vacuum chamber (190 μs for an atom at 3 km/s), so that only the very slow atoms (velocity of about 70 m/s) are not detected with this method. The laser frequency is scanned by locking the titanium-sapphire on the successive fringes of the FPR cavity. A typical recording is shown in Figure 5. The signal is split into two peaks, separated by 19 GHz, which are due to the two counterpropagating waves at 410 nm. In a first rough analysis, this separation $\Delta\nu$ corresponds to a beam velocity $c\Delta\nu/2\nu_0$ of

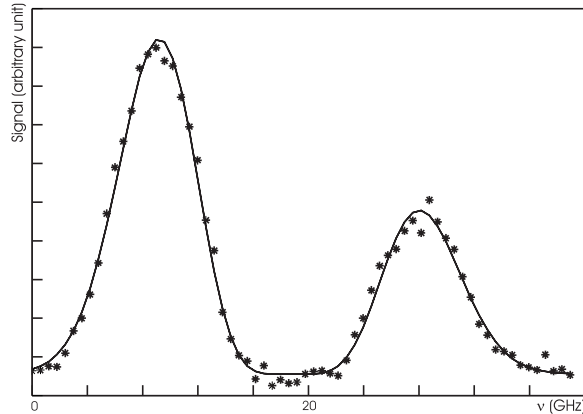


Fig. 5. Doppler broadened profile of the $2S-6P$ transition at 410 nm (the frequency is two times the frequency of the titanium-sapphire laser at 820 nm).

3.9 km/s (c is the velocity of light and ν_0 the frequency of the $2S-6P$ transition). The maximum signal is about 10% of the total metastable yield. Because of the long interaction time between the atom and the laser beam, there is a large saturation and the velocity classes are broadened to about 360 MHz, when the natural width of the $6P$ level is 3.9 MHz.

Due to the electronic excitation of the metastable atoms, the velocity distribution $f(v)$ in the beam should vary as $v^4 \exp(-v^2/2\sigma^2)$, where σ is related to the mass M of the atom and the temperature as $\sigma = \sqrt{kT/M}$ [16]. In our case, we have observed that the velocity distribution can be more narrow and we have fitted the data with a velocity distribution of the form:

$$f(v) \sim v^n \exp(-v^2/2\sigma^2) \quad (1)$$

where n is an integer which can be different from 4. With this distribution, the second order Doppler shift δ_D of a transition of frequency ν_{trans} is, in a simple model (see Ref. [11]):

$$\delta_D = -\frac{n}{2} \left(\frac{\sigma}{c} \right)^2 \nu_{\text{trans}}. \quad (2)$$

In our first papers [4,5,9], we used simply the equation (2) to determine the second order Doppler shift. In our more recent work [6,8], the velocity distribution is directly included in the line shape calculation of the $2S-nS/D$ transitions (see Sect. 3).

If we suppose that the light intensity is uniform along an atomic trajectory, the shape $F(\nu)$ of the Doppler broadened $2S-6P$ line is:

$$F(\nu) \sim \int_0^\infty f(v) H(v, \nu) dv \quad (3)$$

$$H(v, \nu) = 1 - \exp \left\{ -\frac{1}{v} [I_+ L(\nu - \nu_0(1 + v/c)) + I_- L(\nu - \nu_0(1 - v/c))] \right\} \quad (4)$$

Table 1. Velocity distribution of the hydrogen and deuterium atomic beam.

date	n	σ (m/s)	v_{Max} (m/s)	$\delta_{\text{2S-8D}}$ (kHz)
hydrogen				
1988 [11, 16]	4	1525 (10)	3050 (20)	-39.9 (1.0)
1992 [4]	5	1385 (30)	3100 (70)	-41.0 (2.0)
1993 [5]	5	1406 (33)	3144 (75)	-42.4 (2.0)
1996 [6]	5	1814 (13)	4056 (29)	-70.6 (1.0)
1997 [8]	6	1614 (11)	3953 (27)	-67.0 (1.0)
deuterium				
1988 [11, 16]	4	983 (10)	1966 (20)	-16.6 (1.0)
1997 [6]	7	995 (10)	2633 (26)	-29.7 (1.0)
1998 [8]	6	1044 (10)	2557 (24)	-26.3 (1.0)

where I_+ and I_- are proportional to the intensity of the two travelling waves and $L(\nu)$ is the Lorentzian profile of the 2S–6P transition. In this equation, we have neglected the fine and the hyperfine structures of the 2S and 6P levels (the largest is the 6P fine structure $\Delta\nu_0 \sim 400$ MHz). A simple model shows that this approximation leads to, for the second order Doppler shift, a relative error of $(\Delta\nu_0/\Delta\nu)^2 \simeq 5 \times 10^{-4}$ (*i.e.* an error of about 40 Hz for the frequencies of the 2S–nS/D transitions). The function $H(v, \nu)$ describes the two velocity classes which are excited by the two travelling waves. Because of the saturation of 2S–6P transition, the width of these velocity classes varies as $1/\sqrt{\nu}$. Consequently the function $H(v, \nu)$ can be approximated by two square functions of v at the velocities $v_0 = \pm c(\nu - \nu_0)/\nu_0$, with a height of unity and a width proportional to $1/\sqrt{|v_0|}$. With these approximations, the shape $F(\nu)$ becomes:

$$F(\nu) = A(\nu - \nu_0)^{n-1/2} \exp \left[-(\nu - \nu_0)^2 / 2\sigma_\nu^2 \right] \quad \text{if } \nu > \nu_0 \quad (5)$$

$$F(\nu) = B(\nu_0 - \nu)^{n-1/2} \exp \left[-(\nu - \nu_0)^2 / 2\sigma_\nu^2 \right] \quad \text{if } \nu < \nu_0 \quad (6)$$

where A and B are two adjustable constants and $\sigma_\nu = \nu_0\sigma/c$. From the fit of the profile $F(\nu)$ to the experimental data, we deduce the integer n and the parameter σ which describe the velocity distribution.

The results for the measurements made since 1988 are given in Table 1 where we also show the most probable velocity $v_{\text{Max}} = \sqrt{n}\sigma$ and the second order Doppler shift $\delta_{\text{2S-8D}}$ of the 2S–8D transition (Eq. (2)). We can make two comments: (i) during the period 1988–1993, the typical velocity of the hydrogen beam was very stable, v_{Max} being around 3.1 km/s. By contrast, in the experiments made since 1996, the atoms have been distinctly more rapid, with a velocity of about 4 km/s. This velocity increase appeared after an accidental contamination of the vacuum apparatus by the oil of the diffusion pump. After this

pollution, the beam velocity was less reproducible and, in spite of our careful cleaning of the vacuum system, we have never been able to obtain the original characteristics of the atomic beam. This effect is probably due to the destruction of the slow atoms by the stray electric fields which are more important in the first vacuum chamber since this contamination. (ii) On the other hand, the ratio between the hydrogen and deuterium velocities is very stable with a value of 1.55. This value is slightly different from the $\sqrt{2}$ factor to be expected for a thermal beam. This fact can be explained by the deviation due to the electronic excitation of the 2S level. For deuterium, the mean deviation is only 14° and the 20° angle of our atomic beam apparatus selects the slow deuterium atoms.

2.4 Data acquisition

The experiment is driven by a microcomputer which commands the frequency of the titanium-sapphire laser (through the synthesizer which drives the AOM1), performs the acquisition of the atomic signal and records several other parameters of the experiment: the signal of the photodiode which monitors the light intensity inside the enhancement cavity, the frequency of the beat note between the two He–Ne lasers, the modulation frequency of the AOM2 and several other frequency measurements used to determine the optical frequency of the laser (see Sect. 4). The atomic spectrum is divided in 101 frequency points. For each point, the duration of the measurement is 1 s (the signal of the lock-in amplifier which detects the atomic signal is acquired 10 times every 100 ms with a time constant of 100 ms) and there is a dead time of about 300 ms for the acquisition procedure by the computer and the shift of the laser frequency. To reduce the effect of the low drift of the metastable yield, the sweep of the line is not regular: the 101 points are obtained by 10 scans of the line in the following order:

	0	10	20	30...80	90	100
99	89	79	69...19	9		
	8	18	28	38...88	98	
...						
91	81	71	61...11	1		

Finally, the laser frequency is scanned ten times across the atomic resonance during a 22 minutes run. After an average of these 10 scans, the relative noise of the metastable yield is about 0.3%.

Figure 6 shows a typical signal obtained in the case of the $2\text{S}_{1/2}(F=1)-8\text{D}_{5/2}$ transition of hydrogen. In this recording, the decrease of the metastable intensity is 13% and the linewidth 1.13 MHz (in terms of atomic frequency). By comparison with the natural width of the 8D level (572 kHz), there is a large broadening which is mainly due to the inhomogeneous light shift experienced by the atoms through the Gaussian profile of the laser beams. To evaluate this effect, we record the signal for several laser intensities and we made an extrapolation

Table 2. Some features of the observed transitions.

transition	number of runs	amplitude of a scan	width variation	maximum amplitude
hydrogen				
2S _{1/2} (F = 1)-6D _{5/2} [9]	49	10 MHz	1.8 MHz to 3.4 MHz	19.7%
2S _{1/2} (F = 1)-6S _{1/2} [9]	91	4 MHz	400 kHz to 1.2 MHz	5.7%
2S _{1/2} (F = 1)-8D _{5/2} [5]	20	8 MHz	900 kHz to 2.1 MHz	18.6%
2S _{1/2} (F = 1)-8D _{3/2} [5]	24	8 MHz	900 kHz to 1.9 MHz	16.0%
2S _{1/2} (F = 1)-8S _{1/2} [5]	47	4 MHz	330 kHz to 800 kHz	5.1%
2S _{1/2} (F = 1)-8D _{5/2} [6]	90	8 or 12 MHz	750 kHz to 2.0 MHz	21.7%
2S _{1/2} (F = 1)-8D _{3/2} [6]	53	8 or 12 MHz	800 kHz to 1.6 MHz	18.5%
2S _{1/2} (F = 1)-8S _{1/2} [6]	77	2.8 or 4 MHz	300 kHz to 950 kHz	6.7%
2S _{1/2} (F = 1)-12D _{5/2} [8]	78	3.6 MHz	300 kHz to 600 kHz	8.7%
2S _{1/2} (F = 1)-12D _{3/2} [8]	62	3.6 MHz	300 kHz to 600 kHz	6.7%
deuterium				
2S _{1/2} (F = 3/2)-8D _{5/2} [6]	41	8 or 12 MHz	750 kHz to 2.2 MHz	19.8%
2S _{1/2} (F = 3/2)-8D _{3/2} [6]	49	8 or 12 MHz	700 kHz to 2.0 MHz	19.5%
2S _{1/2} (F = 3/2)-8S _{1/2} [6]	47	2.8 or 4 MHz	250 kHz to 1.0 MHz	7.3%
2S _{1/2} (F = 3/2)-12D _{5/2} [8]	44	3.6 MHz	300 kHz to 650 kHz	9.1%
2S _{1/2} (F = 3/2)-12D _{3/2} [8]	54	3.2 MHz	350 kHz to 650 kHz	8.3%

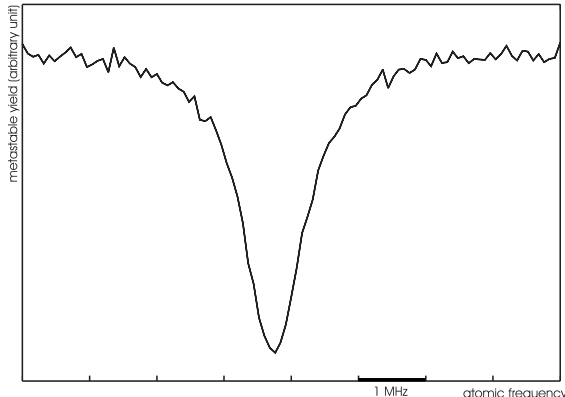


Fig. 6. Typical two-photon transition signal, recorded as a decrease of the metastable beam intensity. Example of the 2S_{1/2}(F = 1)-8D_{5/2} transition of hydrogen: the decrease of the metastable yield is 13%.

to zero light power. Consequently, the data acquisition takes 3 or 4 days for each atomic transition. Table 2 gives some details for the measurements which have been made during the period 1993–1998 [5, 6, 8, 9]. For each transition, we indicate the number of the runs used for the extrapolation, the amplitude of the frequency scan (in terms of atomic frequency), the range of variation of the line width with the light power and the maximum amplitude of the observed signal.

3 Line shape analysis

3.1 Expression for the line shape

Figure 7 shows an atomic trajectory in the laser-atom interaction region (the second vacuum chamber). In this

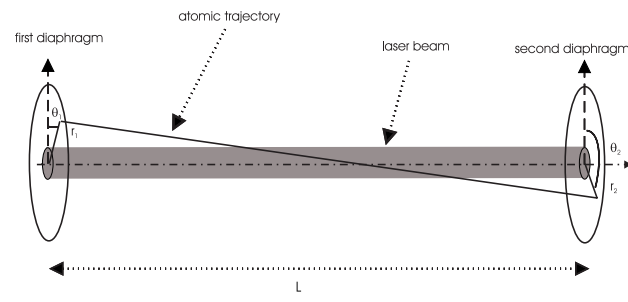


Fig. 7. Schematic view of an atom trajectory in the laser-atom interaction region.

region, the collisions are negligible and the atomic trajectories are straight lines passing through the two diaphragms (the small deviation of the atomic trajectory due to the forces induced by the light shifts will be studied below). The calculation procedure is the following. In a first step, we calculate for each trajectory the destruction probability of the metastable atom when it crosses the laser beam. Then we make an average over all the possible trajectories.

3.1.1 Two-photon excitation rate

The two-photon transition probability Γ_g between two states $|g\rangle$ and $|e\rangle$ (energies E_g and E_e) is given by [11, 18]:

$$\Gamma_g = \frac{n^2 \omega^2}{\varepsilon_0^2 \hbar^2} \left| \sum_r \frac{\langle e | \mathbf{d} \cdot \boldsymbol{\varepsilon} | r \rangle \langle r | \mathbf{d} \cdot \boldsymbol{\varepsilon} | g \rangle}{\omega - \omega_{rg}} \right|^2 \times \frac{\Gamma_e}{(2\omega - \omega_{eg})^2 + (\Gamma_e/2)^2} \quad (7)$$

$$\Gamma_g = \left(\frac{4\pi a_0^2}{mc^2\alpha} \right)^2 \sum_e \frac{|\langle e | Q_{\text{tp}} | g \rangle|^2 \Gamma_e (1 + c_{\text{io}} I) I^2}{[2\omega - (\omega_{eg} (1 - v^2/c^2) + c_{\text{ls}} I)]^2 + [\Gamma_e (1 + c_{\text{io}} I)/2]^2 (1 + c_{\text{sat}} I^2)} \quad (10)$$

Table 3. 2S–nS/D two-photon transition amplitude $\langle e | Q_{\text{tp}} | g \rangle$ and natural width of the excited level.

transitions	$\langle e Q_{\text{tp}} g \rangle$ (a.u.)	$\Gamma_e/2\pi$
2S–6S	-14.711	297 kHz
2S–8S	-14.921	144 kHz
2S–6D	-133.16	1.337 MHz
2S–8D	-92.937	572 kHz
2S–12D	-55.033	172 kHz
2S–15D	-40.677	88.7 kHz
2S–20D	-27.187	19.0 kHz

where n is the number of photons per unit volume for each counterpropagating wave, ω the laser frequency, ε the polarisation, $\omega_{ij} = (E_i - E_j)/\hbar$, \mathbf{d} the electric dipole moment operator and Γ_e the natural width of the excited state (we suppose that the natural width of the state $|g\rangle$ is negligible). The summation is made over all the possible states $|r\rangle$ (including the continuum). We introduce the two-photon operator Q_{tp} . In our experiment, the polarisation of the laser beam is linear (because of the Brewster windows of the vacuum apparatus placed in the enhancement cavity). For a polarisation along the z -axis, Q_{tp} is given in atomic units ($\hbar = \alpha c = m = 1$) by:

$$Q_{\text{tp}} = \sum_r \frac{z|r\rangle \langle r| z}{\omega - \omega_{rg}}. \quad (8)$$

With this notation, equation (7) becomes:

$$\Gamma_g = \left(\frac{4\pi a_0^2}{mc^2\alpha} \right)^2 \frac{|\langle e | Q_{\text{tp}} | g \rangle|^2 \Gamma_e I^2}{(2\omega - \omega_{eg})^2 + (\Gamma_e/2)^2} \quad (9)$$

where I is the power density of the light ($I = n\hbar\omega/c$), a_0 the Bohr radius, α the fine structure constant and m the electron mass. For the transitions studied in this paper, Table 3 gives the values of the matrix element $\langle e | Q_{\text{tp}} | g \rangle$ (calculated in Ref. [11]) for an atom without electronic and nuclear spin, and the natural width of the excited level.

In the calculation of the line shape of the 2S–nS/D transitions, we have taken into account the fine and hyperfine structures of the S and D levels, the light shift, the second order Doppler effect, the photoionisation of the upper level and the saturation of the two-photon transition. The states $|g\rangle$ and $|e\rangle$ are the magnetic hyperfine sublevels $|F_g m_F\rangle$ and $|F_e m_F\rangle$ (F_i is the total angular momentum of the state $|i\rangle$, $|i\rangle = |g\rangle$ or $|e\rangle$). We have the selection rule $\Delta m_F = 0$. Then the two-photon transition probability

becomes:

see equation (10) above.

The coefficients c_{ls} , c_{io} and c_{sat} describe the light shift, the photoionisation, and the saturation of the two-photon transition.

Following the notations of reference [11], the light shift coefficient is given by:

$$c_{\text{ls}} = \left(\frac{4\pi a_0^2}{mc^2\alpha} \right) (\beta_e - \beta_g)$$

where β_i are the matrix elements of the light shift operator Q_{ls} . We have:

$$Q_{\text{ls}} = \sum_r \left[\frac{z|r\rangle \langle r| z}{\omega_{ir} + \omega} + \frac{z|r\rangle \langle r| z}{\omega_{ir} - \omega} \right] \quad (\text{atomic units}). \quad (11)$$

The light shift operator is the sum of a scalar operator Q_{ls}^0 and of an operator of rank 2 Q_{ls}^2 . For the state $|i\rangle = |nLJFm_F\rangle$ (n principal quantum number, L and J orbital and electronic momenta), straightforward algebra gives:

$$\begin{aligned} \langle i | Q_{\text{ls}} | i \rangle &= \frac{\langle nL \| Q_{\text{ls}}^0 \| nL \rangle}{\sqrt{2L+1}} \\ &\quad + (-1)^{F-m_F} \begin{pmatrix} F & 2F \\ -m_F & 0 m_F \end{pmatrix} \langle JF \| Q_{\text{ls}}^2 \| JF \rangle \end{aligned} \quad (12)$$

where:

$$\begin{aligned} \langle JF \| Q_{\text{ls}}^2 \| JF \rangle &= \\ &\quad (-1)^{F+I+2J+L+S} (2F+1)(2J+1) \\ &\quad \times \left\{ \begin{matrix} J & 2 & J \\ F & I & F \end{matrix} \right\} \left\{ \begin{matrix} L & 2 & L \\ J & S & J \end{matrix} \right\} \langle nL \| Q_{\text{ls}}^2 \| nL \rangle. \end{aligned}$$

The calculation of the matrix elements $\langle nL \| Q_{\text{ls}}^0 \| nL \rangle$ and ionisation coefficient c_{io} has been made with a method using Sturmian functions [19] (the coefficient c_{io} can be also obtained with the Fermi's golden rule, see Refs. [11, 20, 21]). Table 4 gives the values of these parameters. The effect of the ionisation is not entirely negligible. For example, for a laser beam of 100 W with a waist of 660 μm , the ionisation rate of the 8S level is, at the center of the beam, $1.5 \times 10^5 \text{ s}^{-1}$, *i.e.*, because of this ionisation probability, the width of the 8S level increases by 24 kHz. The saturation coefficient c_{sat} can be obtained by using an effective Hamiltonian [22]. Its expression is:

$$c_{\text{sat}} = 8 \left(\frac{4\pi a_0^2}{mc^2\alpha} \right)^2 \frac{|\langle e | Q_{\text{tp}} | g \rangle|^2}{\Gamma_e^2}. \quad (13)$$

Table 4. Light shift and ionisation coefficients for the 2S–nS or 2S–nD transitions studied in this paper (expressed in atomic units).

transitions	$\langle nL_g \ Q_{ls}^0 \ nL_g \rangle$ (a.u.)	$\langle nL_e \ Q_{ls}^0 \ nL_e \rangle$ (a.u.)	$\langle nL_e \ Q_{ls}^2 \ nL_e \rangle$ (a.u.)	ionisation coefficient c_{io} (m^2W^{-1})
2S–6S	−290.96	324.42	0	1.536×10^{-9}
2S–8S	−355.31	291.35	0	1.144×10^{-9}
2S–6D	−290.96	727.20	34.99	2.315×10^{-10}
2S–8D	−355.31	648.51	19.19	1.805×10^{-10}
2S–12D	−428.53	603.94	6.78	1.517×10^{-10}

Table 5. Data for the calculation of the 2S($F = 1$)–8D $_{5/2}$ two-photon line shape.

transition	F_e	hyperfine shift	a_{hfs}	weight of the F_e level	β_{2S} (a.u.)	β_{F_e} (a.u.)
hydrogen						
$2S_{1/2}(F = 1)$ –8D $_{5/2}$	2	−82.3 kHz	2/9	−355.31	288.19	
	3	59.4 kHz		−355.31	286.88	
deuterium						
$2S_{1/2}(F = 3/2)$ –8D $_{5/2}$	3/2	−25.6 kHz	1/15	−355.31	290.02	
	5/2	−7.3 kHz		−355.31	289.16	
	7/2	18.3 kHz		−355.31	287.22	

This effect is also not negligible: with the same laser beam parameters as above, the value of $c_{\text{sat}}I^2$ is about 0.1 for the 2S $_{1/2}$ –8D $_{5/2}$ transition.

In the case of the 2S–nS transition, the two-photon operator is scalar and we have the selection rules $\Delta F = 0$, $\Delta m_F = 0$. In equation (10) the summation over the states $|e\rangle$ is reduced to a single term and, for the two-photon matrix element, we have $\langle nL_e J_e F m_F | Q_{\text{tp}} | 2L_g J_g F m_F \rangle = \langle nL_e m_L | Q_{\text{tp}} | 2L_g m_L \rangle$. For the 2S–nD transition, the two-photon operator is quadrupolar and, in equation (10), we have to make the sum, for each m_F value, on all the states $|F_e m_F\rangle$. Nevertheless, as the quadrupolar term of the light shift is very small (see Tab. 4), we have used the mean values (with respect to the magnetic quantum number m_F) of the light shift coefficient c_{ls} (given by Eq. (12)) and of the intensities of the hyperfine components. With these approximations, the two-photon transition probability Γ_g does not depend on m_F . The summation in equation (10) is made over the F_e quantum number and the two-photon fine and hyperfine intensities are given by:

$$|\langle nL_e J_e F m_F | Q_{\text{tp}} | 2L_g J_g F m_F \rangle|^2 = a_{\text{fs}} a_{\text{hfs}} |\langle nL_e m_L | Q_{\text{tp}} | 2L_g m_L \rangle|^2. \quad (14)$$

The matrix elements $\langle nL_e m_L | Q_{\text{tp}} | 2L_g m_L \rangle$ have been given in Table 3. The coefficient a_{fs} takes into account the fine structure of the D level. It is proportional to the degeneracy $2J_e + 1$ (0.4 and 0.6 for the D $_{3/2}$ and D $_{5/2}$ levels). The coefficient a_{hfs} describes the intensity of the

hyperfine components and is proportional to [12]:

$$(2F_e + 1) \left\{ \begin{array}{c} J_e \ J_g \ 2 \\ F_g \ F_e \ I \end{array} \right\}^2.$$

As an example, Table 5 gives the numerical values used in equation (10) for the 2S($F = 1$)–8D $_{5/2}$ transition. The hyperfine splittings are calculated with the Fermi's formula [20].

3.1.2 Destruction probability of the metastable atoms

We consider an atomic trajectory between two points (r_1, θ_1) and (r_2, θ_2) on the diaphragms which delimit the metastable beam (see Fig. 7). If the laser beam is aligned with the x -axis, the laser intensity varies along the atomic trajectory as:

$$I(x, \rho) = I_0 \left(\frac{w_0}{w(x)} \right)^2 \exp \left[-2 \left(\frac{\rho}{w(x)} \right)^2 \right] \quad (15)$$

where x is the coordinate along the laser beam, ρ the radial distance to the laser beam axis, $w(x)$ the radius of the laser beam. Along the atomic trajectory, ρ is a function $\rho(x)$ and, if we assume that the transit time of the atom through the laser beam is long with respect to the life time $1/\Gamma_e$ of the excited level, the two-photon transition probability Γ_g becomes a function of x . The probability that the atom undergoes a transition during this trajectory is:

$$P(r_1, \theta_1, r_2, \theta_2) = 1 - \exp - \int_0^L \frac{\Gamma_g(x) dx}{v_x} \quad (16)$$

Table 6. Two-photon cascade probability R_n from the nS or nD levels to the $2S$ metastable state.

level	6S	6D	8S	8D	12D	15D	20D
R_n	0.0740	0.0463	0.0815	0.0513	0.0548	0.0558	0.0567

Table 7. Partition of the probability R_n between the two hyperfine levels of the metastable state when the two-photon excitation is made from the $2S_{1/2}(F = 1)$ hyperfine sublevel ($F = 3/2$ for deuterium).

upper level	$nS_{1/2}$	$nD_{3/2}$	$nD_{5/2}$
hydrogen			
p_0	$(4/27)R_n$	$(32/135)R_n$	$(2/15)R_n$
p_1	$(23/27)R_n$	$(103/135)R_n$	$(13/15)R_n$
deuterium			
$p_{1/2}$	$(16/81)R_n$	$(128/405)R_n$	$(8/45)R_n$
$p_{3/2}$	$(65/81)R_n$	$(277/405)R_n$	$(37/45)R_n$

where v_x is the component of the atom velocity along the x axis and L the distance between the two diaphragms. We have to correct this expression to take into account the hyperfine structure and the repopulation of the $2S$ level.

(i) *Hyperfine structure of the metastable state.* In our experiment, we resolve the hyperfine structure of the metastable state and we have studied the most intense transitions starting from the $2S_{1/2}(F = 1)$ hyperfine level ($2S_{1/2}(F = 3/2)$ for deuterium). As we detect all the metastable atoms we have to multiply the equation (16) by a coefficient C_{hfs} which describes the population of the two hyperfine levels. By observing some transitions starting from the $2S_{1/2}(F = 0)$ hyperfine level ($2S_{1/2}(F = 1/2)$ for deuterium), we have measured these populations:

$$\begin{aligned} C_{\text{hfs}}(F = 1) &= 80\% && \text{in hydrogen,} \\ C_{\text{hfs}}(F = 3/2) &= 67.6\% && \text{in deuterium.} \end{aligned}$$

These values are slightly different from the statistical weights ($3/4$ and $2/3$ respectively). This effect is probably due to a larger quenching of the $2S_{1/2}(F = 0)$ ($2S_{1/2}(F = 1/2)$ in deuterium) which is closer to the $2P_{1/2}$ level and more sensitive to the stray electric fields.

(ii) *Repopulation of the metastable state.* When an atom is excited to the nS or nD level, it can undergo a radiative cascade towards the $2S_{1/2}$ level with the probability $R_n = p_0 + p_1$ ($p_{1/2} + p_{3/2}$ for deuterium), where the probabilities p_0 and p_1 ($p_{1/2}$ and $p_{3/2}$ for deuterium) are correlated to the two $2S_{1/2}(F = 0)$ and $2S_{1/2}(F = 1)$ levels (respectively $F = 1/2$ and $F = 3/2$ for deuterium). These probabilities have been calculated taking into account only the two photon cascades [11]. The values relevant to this paper are given in Tables 6 and 7.

Finally, after solving the rate equations which describe the evolution of the populations of the two hyperfine sublevels, we obtain the destruction probability of a

metastable atom at the end of its trajectory:

$$\begin{aligned} P'(r_1, \theta_1, r_2, \theta_2) &= C_{\text{hfs}} \left(1 - \frac{p_0}{1 - p_1} \right) \\ &\times \left[1 - \exp - \frac{1}{v_x} \int_0^L (1 - p_1) \Gamma_g(x) dx \right]. \quad (17) \end{aligned}$$

For deuterium, we have to replace in equation (17) the probabilities p_0 and p_1 by $p_{1/2}$ and $p_{3/2}$. The first factor describes the optical pumping from the $F = 1$ hyperfine sublevel to the $F = 0$ one. The factor $1 - p_1$ in the integral describes the inefficiency of the two-photon excitation when the atom comes back to the initial $F = 1$ hyperfine sublevel.

Up to now, we have supposed that the atomic trajectories were straight lines. Let us consider the effect of the force due to the light shift of the metastable state. As the $2S$ state is down shifted (see Tab. 4), the atom is attracted towards the axis of the laser beam by a force $F_\rho(x, \rho)$ (we neglect the component of this force along the x -axis):

$$F_\rho(x, \rho) = -\hbar \beta_g \left(\frac{4\pi a_0^2}{mc^2 \alpha} \right) \frac{\partial}{\partial \rho} I(x, \rho).$$

The acceleration due to this force is considerable. For example, for a laser beam of 100 W with a waist of $660 \mu\text{m}$, the maximum radial acceleration is about 350 m/s^2 . Nevertheless, because of the small transit time of the atom through the second vacuum chamber (typically $190 \mu\text{s}$), the deviation from a straight trajectory is small, about a few micrometres. Even so, in the case of the $2S$ - nD transitions, which give the most accurate results, we have included this effect for the line shape calculation. The atomic trajectory is calculated step by step to determine the function $\rho(x)$ which is used to obtain the intensity $I(x, \rho)$ (Eq. (15)) and the two-photon transition probability $\Gamma_g(x)$ (Eq. (10)).

3.1.3 Summation on the atomic trajectories and velocities

The last step of this calculation is to make a summation of equation (17) over all velocities and all possible trajectories. We have studied the velocity distribution $f(v)$ in Section 2 and these functions are given in Table 1. On the other hand, we do not know the exact distribution of the atomic trajectories. Because of the recoil of the atom involved by the electronic excitation of the $2S$ state, there is a large dispersion in the direction of the metastable atoms. For this reason, we can suppose a uniform distribution for the points (r_2, θ_2) at the end of the atomic beam. This is not the case however at the beginning of the beam. The distribution of the metastable atoms can depend on the

spatial distribution of the 1S hydrogen atoms, the electron density or the quenching stray electric fields. Our approach has been to simulate the spatial distribution of the points (r_1, θ_1) by a uniform one on a virtual diaphragm centered on the real diaphragm at the beginning of the beam but with a smaller radius R_1 . In this case the line shape $L(\omega)$ is given by:

$$L(\omega) = \frac{4}{\pi R_1^2 R_2^2} \int_0^\infty f(v) dv \int_0^{R_1} r_1 dr_1 \int_0^{R_2} r_2 dr_2 \times \int_0^\pi d\theta_2 P'(r_1, \theta_1, r_2, \theta_2). \quad (18)$$

We have supposed that we have a cylindrical symmetry and that the laser beam is well aligned with respect to the atomic beam. R_2 is the radius of the real diaphragm at the end of the atomic beam ($R_2 = 3.5$ mm). As explained below, the radius R_1 is determined during the analysis of the experimental curves to obtain a correct evaluation of the light shift. A typical value is $R_1 = 2$ mm.

3.1.4 Other broadening and shifting effects

In the above analysis, we have neglected several other effects which can broaden or shift the line. The Stark effect produced by the stray electric fields, which can induce a significant shift, will be studied subsequently. The other effects are the following.

- (i) *Laser line width.* The jitter of our laser is about 2 kHz (see Sect. 2) corresponding to a line broadening of 4 kHz in terms of atomic frequency.
- (ii) *Finite transit time.* Though the metastable atomic beam and the laser beam are colinear, the broadening due to the finite transit time of the atoms through the laser beam is not entirely negligible. For an atomic trajectory making an angle θ with the laser beam, the line broadening is $2v \sin \theta \sqrt{\ln 2}/\pi w$ [23]. In the case of the largest possible angle θ (about 0.6°), this broadening is 32 kHz for a velocity of 4 km/s and a waist of 660 μ m.
- (iii) *Residual magnetic field.* As the atomic beam is placed in a magnetic shield, the residual magnetic field is about 1 mG. For the 2S–nS transitions, the Zeeman splittings of the 2S and nS levels are similar. Because of the selection rules $\Delta F = 0$, $\Delta m_F = 0$, there is no broadening. In the case of the 2S–nD transition, the broadening due to the Zeeman effect can be about 10 kHz, but there is no shift if the laser polarisation is linear.
- (iv) *Black body radiation.* The black body radiation induces transitions between the different hydrogen energy levels. Consequently, there is a depopulation of each level of the two-photon transition, *i.e.* a broadening of the line, and a shift. These effects are studied in detail in reference [24] for a temperature of 300 K. In our experiment, the magnetic shield which surrounds the atomic beam is heated at about 330 K.

Table 8. Broadening and shift due to the black body radiation.

transition	broadening	shift
2S–6S	1.2(0.1) kHz	-360(90) Hz
2S–6D	1.7(0.2) kHz	-430(105) Hz
2S–8S	4.4(0.4) kHz	520(130) Hz
2S–8D	5.5(0.5) kHz	650(160) Hz
2S–12D	7.1(0.7) kHz	2.1(0.5) kHz

If we assume an uncertainty of 30 K to take into account the inhomogeneity of the heating, we obtain the broadenings and shifts given in Table 8. Using the data of reference [24], we have supposed that the broadening varies as the temperature T and the shift as $T^{2.7}$.

3.2 Analysis of the data

3.2.1 Fit procedure

The aim of this analysis is to determine very precisely, with respect to our very stable FPR cavity, the transition frequency, corrected for the light shift, the second order Doppler effect and the nD hyperfine structure. As the two-photon transitions are observed by measuring the decrease of the metastable yield, we can calibrate this decrease with respect to the intensity of the metastable beam when the laser is off resonance. The principle of the adjustment procedure is hence the following: from the amplitude of this decrease we deduce the optical power and, consequently, the light shift.

In practice the theoretical curves given by equation (18) are adjusted to fit the experimental data. As the numerical calculations of the theoretical line shape are long (there is a quintuple integration), we calculate a set of theoretical curves for several laser powers P ($P = \pi w_0^2 I_0/2$) from 5 W to 150 W with a step of 5 W, and as a function of 301 atomic frequency points. The frequency steps are adjusted to the line width (50 kHz for the 2S–6D and 2S–8D transitions, 25 kHz for the 2S–12D and 20 kHz for the 2S–6S and 2S–8S). We obtain the curves $L(\omega, P)$. Then we make two convolutions: a first convolution following ω by a Gaussian curve of width Δ_ω which takes into account the broadening effects which are not included in the line shape, and a second convolution following P by an other Gaussian curve of width Δ_P which describes the fluctuations of the light power seen by the atoms. The width Δ_P is deduced, for each recording, from the light intensity measurements obtained using the enhancement cavity by a photodiode. Finally, the four parameters of the adjustment are the metastable yield when the laser is off resonance, the light power P , the frequency of the atomic transition CLP (without the light shift, the second order Doppler effect and the hyperfine structure of the D level) and the Gaussian broadening Δ_ω . During the adjustment, we make an interpolation, quadratically for the power and linearly for the frequencies.

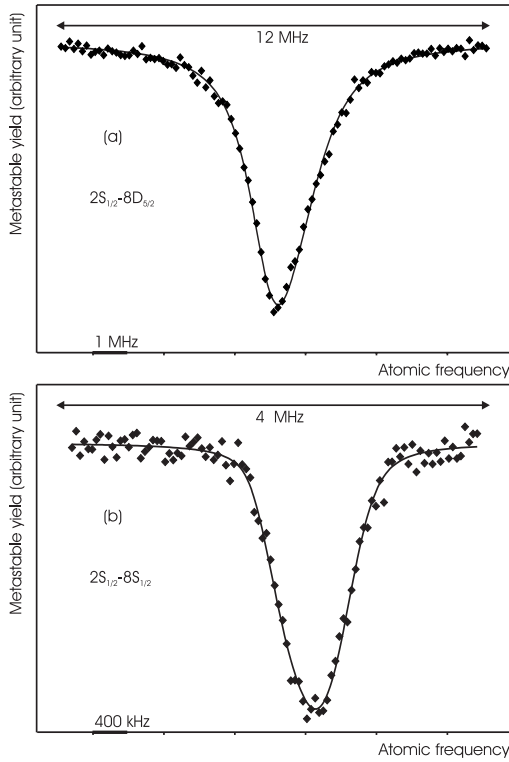


Fig. 8. Fit of the experimental line profile with the theoretical one. (a) $2S_{1/2}(F=3/2)$ - $8D_{5/2}$ transition in deuterium. (b) $2S_{1/2}(F=3/2)$ - $8S_{1/2}(F=3/2)$ transition in deuterium. The light powers deduced from the fits are respectively 90.6(2.2) W and 96.2(2.6) W and the decreases of the metastable yield 18% and 6%.

Figures 8a and 8b show two examples of adjustments in the case of the $2S_{1/2}$ - $8D_{5/2}$ and $2S_{1/2}$ - $8S_{1/2}$ transitions of deuterium. The asymmetry of the experimental recordings, which appears for both transitions, but with different signs, is well reproduced by the theoretical profiles. For the $2S_{1/2}$ - $8S_{1/2}$ transition, this asymmetry is related to the quadratic dependence with $I(x, \rho)$ of the atomic excitation rate at any point in the beam, since the light shift is linear with $I(x, \rho)$. Thus, the more shifted contributions to the signal are also the more intense. In the case of the $2S_{1/2}$ - $8D_{5/2}$ transition, there is a very large saturation of the two-photon excitation probability. This saturation reduces the weight of the more shifted contributions to the signal, so that the sign of the asymmetry is reversed. In both cases, experimental and theoretical profiles are in excellent agreement.

3.2.2 Extrapolation versus the light power

The most crucial point of our analysis is the determination of the optical power seen by the atoms. A first test is to compare the fitted power P with the signal IT given by the photodiode placed after the enhancement cavity (see Fig. 9). There is a good agreement between these

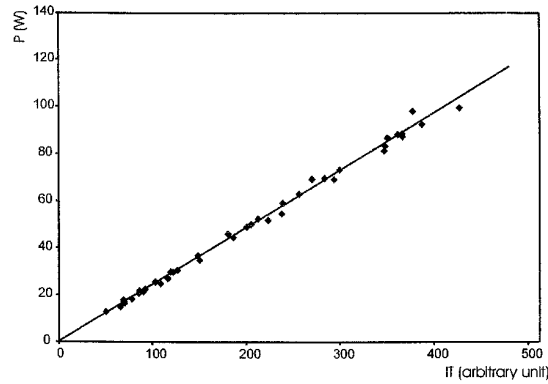


Fig. 9. Fitted power P versus the photodiode signal IT for the $2S_{1/2}(F=3/2)$ - $8D_{5/2}$ transition in deuterium (40 recordings).

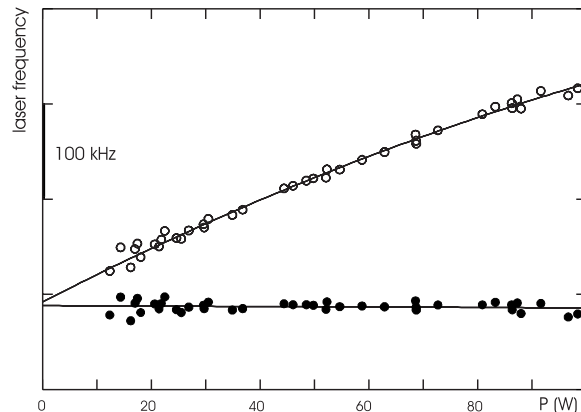


Fig. 10. Extrapolation of the half maximum center (○) and of the line position corrected for the light-shift, second-order Doppler effect and 8D hyperfine structure (●) versus the light power P in the case of the $2S_{1/2}(F=3/2)$ - $8D_{5/2}$ transition of deuterium.

data which lie in a linear ratio. We use the slope of this straight line P/IT as a parameter to control the optical alignment of the experiment: the slope P/IT is maximised to obtain the best matching between the laser beams and the atomic beam. The slope P/IT is also determined by the distribution of the atomic trajectories. For example, if we increase the radius R_1 of the first diaphragm, the theoretical curves exhibit a smaller decrease of the metastable yield, and, consequently, the fitting procedure gives a larger light power P . To determine the correct value for R_1 , we study the shift of the line position *versus* the laser power. For each record, the adjustment procedure gives us the corrected line position CLP and the half-maximum center of the line HMC . Figure 10 shows a typical extrapolation of the HMC and CLP data *versus* the light power. Because of the saturation of the two-photon transition probability, the variation of HMC is not exactly linear with P . The shift of the line is about 400 kHz for a power of 100 W. On the other hand, there is no variation of the corrected line position. This result has been obtained by varying the radius R_1 to eliminate

Table 9. Calculation of the position of the line in the case of the $2S_{1/2}$ – $8D_{3/2}$ transition in hydrogen. The extrapolated values are the absolute frequencies given in terms of laser frequency (*i.e.* $CLP/2$). Here we have indicated only the last digits and the real value is obtained by adding 385 324 GHz.

distribution of the trajectories	$R_1 = 1.8$ mm	$R_1 = 2$ mm
slope of the straight line P/IT (arb. units)	0.224	0.246
extrapolation of CLP versus P (MHz)	730.029 80	730.030 72
uncertainty (kHz)	3.27	3.23
extrapolation of CLP versus IT (MHz)	730.030 35	730.031 05
uncertainty (kHz)	3.21	3.20
mean of the extrapolation versus P and IT (MHz)	730.030 07	730.030 88
uncertainty (kHz)	3.24	3.20
slope of the straight line CLP versus P (MHz/W)	9×10^{-5}	-8×10^{-5}
final position of the line (MHz)	730.030 5(33)	
(interpolated position for a slope null)		
interpolated value for P/IT (arb. units)	0.236	
interpolated value for R_1	1.9 mm	

the variations of CLP with P . In practice, to obtain the position of the line, we use the following procedure: we make the mean of the linear extrapolations of CLP versus P and IT for two values of R_1 (for example 1.8 and 2 mm) and we interpolate these data to null the slope of the straight line $CLP(P)$. The details of this method are illustrated in Table 9 in the case of the $2S_{1/2}$ – $8D_{3/2}$ transition in hydrogen. For this extrapolation, we have used the absolute frequency measurement described in Section 4 and the corrected line position CLP is not related to the FPR cavity but is an absolute frequency.

The uncertainties given in this table are only statistical. For each recording, the adjustment procedure gives an uncertainty for CLP which is deduced from the disagreement between the experimental and the theoretical curves. The linear extrapolation is made with a weighted least squares method. We calculate an *a priori* uncertainty σ_1 given by the propagation of the uncertainties of each record through the least squares calculations. This uncertainty does not depend on the dispersion of the points (CLP, P) with respect to a straight line. Next we calculate an *a posteriori* uncertainty σ_2 which takes into account this dispersion and is given by:

$$\sigma_2 = \sigma_1 t_{1\sigma} \sqrt{\frac{\chi^2}{n - 2}}$$

where n is the number of recordings involved in the extrapolation and χ^2 the weighted least squares sum. The coefficient $t_{1\sigma}$ is estimated from the Student's t -distribution to obtain one standard deviation (*i.e.* $A(t_{1\sigma}|n-2) = 0.683$). Finally, we choose whichever value σ_1 and σ_2 which is largest.

We can test the consistency of our analysis by comparing, for several transitions, the interpolated values of P/IT and R_1 which correspond to the elimination of the variation of CLP with P . For example, the data obtained during the measurements of the 2S–8S/D transitions [6] are given in Table 10. The dispersion of the values of P/IT ,

Table 10. Values of the slope of the straight line P versus IT and of the radius R_1 of the first diaphragm which correspond to the best determination of the light shift.

transition	R_1 (mm)	P/IT (arb. units)
hydrogen		
$2S_{1/2}$ – $8D_{5/2}$	1.80	0.230
$2S_{1/2}$ – $8D_{3/2}$	1.91	0.236
$2S_{1/2}$ – $8S_{1/2}$	1.89	0.259
$2S_{1/2}$ – $8D_{5/2}$	2.00	0.262
deuterium		
$2S_{1/2}$ – $8D_{5/2}$	1.73	0.225
$2S_{1/2}$ – $8D_{3/2}$	1.75	0.225
$2S_{1/2}$ – $8S_{1/2}$	1.82	0.257

which is not negligible, is probably due to the variation of the optical alignment of the experiment. We have also estimated directly this ratio from the light power transmitted by the enhancement cavity and the transmission of the end mirror of this cavity. We obtain the value $P = 0.259 \times IT$ with a typical uncertainty of 5%. This result is in acceptable agreement with the values given in Table 10. The same table also shows that the spatial distribution of the trajectories is more concentrated for deuterium (R_1 is smaller than for hydrogen). This is probably due to the larger quenching probability of the metastable deuterium atoms which are slower: the equipotential region where the metastable atoms are produced is reduced.

Some examples of the line width variations with the light power are shown in Figures 11a–11c in the case of the $2S_{1/2}$ – $8S_{1/2}$, $2S_{1/2}$ – $8D_{5/2}$ and $2S_{1/2}$ – $12D_{5/2}$ transitions. The widths (full width at half maximum in terms of atomic frequency) deduced from the theoretical curves $L(\omega, P)$ correspond to the solid curves. We observe that the experimental widths are larger than the theoretical

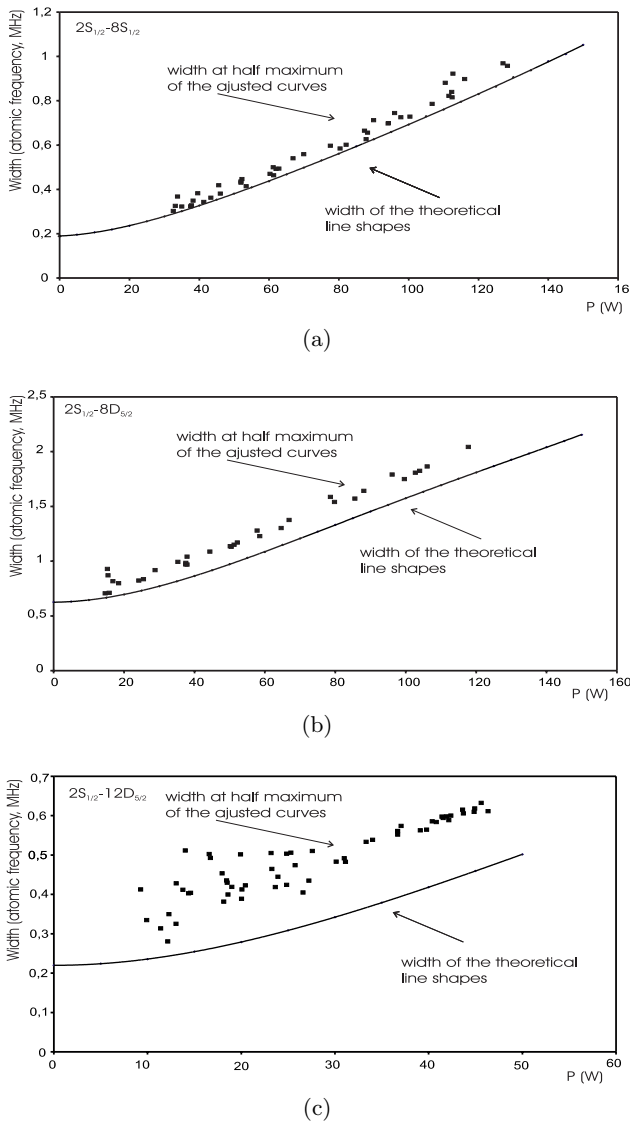


Fig. 11. Variation of the line width (full width at the half maximum in terms of atomic frequency) *versus* the light power P . (a) $2S_{1/2}(F=1)$ - $8S_{1/2}(F=1)$ transition of hydrogen. (b) $2S_{1/2}(F=1)$ - $8D_{5/2}$ transition of hydrogen. (c) $2S_{1/2}(F=1)$ - $12D_{5/2}$ transition of hydrogen.

ones, especially for the $2S$ - nD transitions. These differences can be explained by the various effects which are not taken into account in the theoretical line shapes: the frequency jitter of the laser, the finite transit time, the residual Zeeman effect (for the $2S$ - nD transitions), black body radiation, the fluctuations of the light intensity seen by the atoms or the Stark effect due to stray electric fields.

Finally, to take into account the imperfections of our theoretical analysis, we introduce another uncertainty divided in two parts. (i) An uncertainty related to the optical alignment of the experiment. We have made a simulation of a bad alignment between the atomic beam and

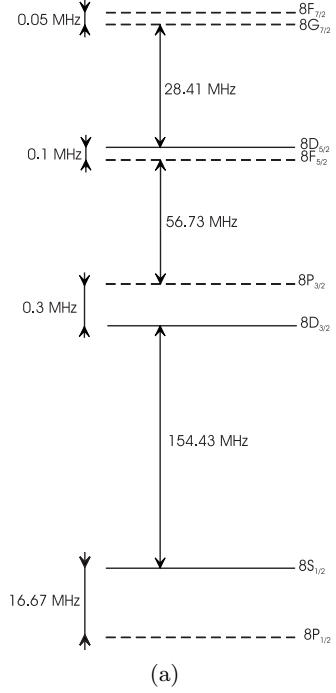
the laser beam [25] and we estimate this uncertainty to 4 kHz (in terms of atomic frequency). We consider that these uncertainties are correlated for a given series of extrapolations (for example the transitions $2S$ - $8S/D$ in hydrogen, which are made in a relatively short time), but uncorrelated for the hydrogen and deuterium measurements and for the transitions with different principal quantum numbers. (ii) A theoretical uncertainty, common to all the measurements, which takes into account the possible incompleteness of our theoretical calculation. We have estimated this uncertainty from our results with different theoretical line shapes. For example, when we modified the theoretical calculations to include the ionisation of the upper level, the deviation of the atomic trajectories, or to reduce the step of the set of theoretical curves $L(\omega, P)$ from 10 W to 5 W, the shifts of the $2S_{1/2}$ - $8D_{5/2}$ extrapolation in hydrogen were successively -640 Hz, 280 Hz and 1.4 kHz (in terms of atomic frequency). Finally, we have assumed that the effects neglected have the same order of magnitude and adopted a value of 2 kHz for this theoretical uncertainty.

3.3 Stark effect

3.3.1 Theoretical background

In our experiment, the stray electric fields are reduced to a few mV/cm thanks to the Aquadag coating. Nevertheless, as the matrix element of the Stark Hamiltonian $V_S = -\mathbf{d} \cdot \mathbf{E}$ (\mathbf{E} is the electric field) varies with the principal quantum number as n^2 , this small electric field can shift and broaden the lines, mainly for the $2S$ - $12D$ transitions. The Stark coupling between the states $|nLJFm_F\rangle$ and $|n'L'J'F'm'_F\rangle$ induces a quadratic Stark effect if $J \neq J'$ and a linear Stark effect if $J = J'$ which vary as n^7 and n^2 respectively. For instance, if we consider the energy levels for $n = 8$ (see Figs. 12a-12b), the quadratic Stark shift of the $8D_{5/2}$ level is due to the interaction with the $8P_{3/2}$ and $8F_{7/2}$ levels when the linear Stark effect is due to the mixing between the $8D_{5/2}$ and $8F_{5/2}$ levels. A straightforward second order calculation gives the quadratic Stark shift. As the anisotropic part of the quadratic Stark shift is small (7.6% and 1.8% for the $8D_{5/2}$ and $12D_{5/2}$ levels), we have considered only the scalar part of this shift (*i.e.* the mean shift for the m_F sub-levels) which does not depend on the quantum number F . Table 11 gives the results for $n = 8$ and $n = 12$.

The linear Stark shift is more difficult to analyse. For example, the $8D_{5/2}$ and $8F_{5/2}$ hyperfine levels are mixed (see Fig. 12b) and these structures are smaller than the natural widths of the $8D$ and $8F$ levels (572 kHz and 285 kHz respectively). Consequently, in the experiment, we are not able to resolve these structures and we observe together the $8D_{5/2}$ and $8F_{5/2}$ levels. Nevertheless, to a first approximation, the shift of the line is null. If we assume that the effect of the electric field on the initial state g of the transition is negligible, the position ω_{tr}



(a)

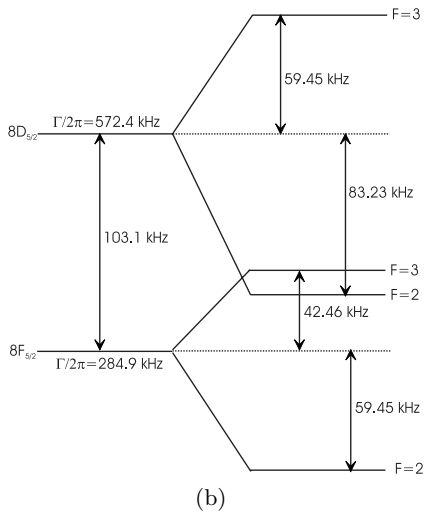


Fig. 12. (a) Fine structure and Lamb shifts of the 8S, 8P, 8D and 8F levels. The solid line corresponds to the levels which are excited with a two-photon transition from the metastable state. (b) Hyperfine structure of the 8D_{5/2} and 8F_{5/2} levels in hydrogen.

of the transition is:

$$\omega_{\text{tr}} = \frac{\sum_i |\langle g | Q_{\text{tp}} | \Psi_i \rangle|^2 \omega_i}{\sum_i |\langle g | Q_{\text{tp}} | \Psi_i \rangle|^2} \quad (19)$$

where Q_{tp} is the two-photon operator (Eq. (8)), Ψ_i the eigenvectors with the energies $\hbar\omega_i$ of the Hamiltonian $H_0 + V_S$ (H_0 being the Hamiltonian without electric field, $\hbar\omega_g$

Table 11. Coefficients of the quadratic Stark shift for some $n = 8$ and $n = 12$ levels.

level	quadratic Stark shift (MHz V ⁻² cm ²)
8S _{1/2}	77.69
8P _{3/2}	-39.11
8D _{3/2}	-36.29
8D _{5/2}	-53.59
8F _{5/2}	-45.28
12P _{3/2}	-698.10
12D _{3/2}	-684.87
12D _{5/2}	-1029.44
12F _{5/2}	-965.73

the zero energy). Then we can write:

$$\omega_{\text{tr}} = \frac{\langle g | Q_{\text{tp}} (H_0 + V_S) P_e Q_{\text{tp}}^+ | g \rangle}{\hbar \langle g | Q_{\text{tp}} P_e Q_{\text{tp}}^+ | g \rangle}. \quad (20)$$

We have introduced the projector on the subspace of the excited states $P_e = \sum_i |\Psi_i\rangle \langle \Psi_i|$. Then, because of parity conservation (Q_{tp} and V_S are respectively even and odd), we have $\langle g | Q_{\text{tp}} V_S P_e Q_{\text{tp}}^+ | g \rangle = 0$ and the barycentre of the line does not depend on the electric field.

In our case, which is far more complicated, there are several limitations to the validity of this argument.

- (i) Equation (19) does not take into account the strong saturation of the two-photon transition which modifies the weights of each component i .
- (ii) We ignore the different natural widths of the upper states.
- (iii) The adjustment procedure gives a line position which is not necessarily the barycentre of the line. For these reasons, we present now a line shape calculation taking into account the linear Stark effect.

3.3.2 Line shape in presence of an electric field

The aim of this calculation is to consider simultaneously the natural width and the Stark coupling. The initial state g is coupled to a set of p states e (for instance the 12 sublevels $8D_{5/2}(F, m_F)$) by the optical excitation. The states e are mixed with the p states f (for instance the 12 sublevels $8F_{5/2}(F, m_F)$) by the Stark Hamiltonian V_S . The evolution of the density operator ρ is:

$$\frac{d\rho}{dt} = \frac{1}{i\hbar} [(H_0 + V_L + V_S), \rho] + \Gamma\rho \quad (21)$$

where the operators V_L and Γ describe the two-photon excitation and the spontaneous emission. We make the rotating wave approximation and we introduce the two-photon Rabi frequencies Ω_e :

$$\langle e | V_L | g \rangle = \frac{\Omega_e}{2} \exp(-2i\omega t),$$

$$\Omega_e = \frac{8\pi a_0^2 |\langle e | Q_{\text{tp}} | g \rangle| I}{mc^2 \alpha}. \quad (22)$$

If we assume that $\Omega_e \ll \Gamma_e$, we can neglect the populations and coherences $\rho_{ee'}$, $\rho_{ff'}$ or ρ_{ef} of the upper levels. In the rotating frame, we replace the density operator by an operator σ with $\sigma_{gg} = \rho_{gg}$, $\sigma_{eg} = \rho_{eg} \exp(2i\omega t)$ and $\sigma_{ge} = \rho_{ge} \exp(-2i\omega t)$ and we introduce the frequency detunings $\Delta_e = 2\omega - \omega_e$ and $\Delta_f = 2\omega - \omega_f$. In this way, we obtain from equation (21) a set of equations:

$$\frac{d\sigma_{gg}}{dt} = -\frac{i}{2} \sum_e \Omega_e (\sigma_{eg} - \sigma_{ge}), \quad (23)$$

$$\begin{aligned} \frac{d\sigma_{eg}}{dt} &= \left(i\Delta_e - \frac{\Gamma_e}{2} \right) \sigma_{eg} - i \frac{\Omega_e}{2} \sigma_{gg} \\ &\quad - \frac{i}{\hbar} \sum_f V_{ef} \sigma_{fg} \quad (p \text{ equations}), \end{aligned} \quad (24)$$

$$\begin{aligned} \frac{d\sigma_{fg}}{dt} &= \left(i\Delta_f - \frac{\Gamma_f}{2} \right) \sigma_{fg} - \frac{i}{\hbar} \sum_e V_{fe} \sigma_{eg} \quad (p \text{ equations}). \end{aligned} \quad (25)$$

We have introduced the matrix elements $V_{fe} = \langle f | V_S | e \rangle$. Then we assume that the optical coherences σ_{eg} and σ_{fg} follow adiabatically the population σ_{gg} , *i.e.* that:

$$\frac{d\sigma_{eg}}{dt} = 0 \quad \text{and} \quad \frac{d\sigma_{fg}}{dt} = 0.$$

With these hypotheses, the equations (24, 25) become:

$$\begin{aligned} \left(i\Delta_e - \frac{\Gamma_e}{2} \right) \sigma_{eg} + \sum_{e',f} \frac{V_{ef} V_{fe'}}{\hbar^2 (i\Delta_f - \Gamma_f/2)} \sigma_{e'g} = \\ i \frac{\Omega_e}{2} \sigma_{gg} \quad (p \text{ equations}). \end{aligned} \quad (26)$$

We obtain a set of p equations with p unknowns σ_{eg} . If we introduce the column vectors $[\sigma_{eg}]$ and $[\Omega_e/2]$, the set of equations (26) becomes:

$$A [\sigma_{eg}] = i \left[\frac{\Omega_e}{2} \right] \sigma_{gg}$$

where the matrix elements of the $p \times p$ operator A are the coefficients of the set of equations (26). With these notations, the equation (23) becomes:

$$\frac{d\sigma_{gg}}{dt} = 2 \operatorname{Re} \left[\frac{\Omega_e}{2} \right]^T A^{-1} \left[\frac{\Omega_e}{2} \right] \sigma_{gg}. \quad (27)$$

This equation describes the evolution of the population σ_{gg} and, finally, the two-photon transition probability Γ_g is:

$$\Gamma_g = -2 \operatorname{Re} \left[\frac{\Omega_e}{2} \right]^T A^{-1} \left[\frac{\Omega_e}{2} \right]. \quad (28)$$

This equation is the equivalent, in the case of the Stark mixing, of equation (9). The two-photon probability is proportional to I^2 and we can separate the frequency and intensity variations:

$$\Gamma_g = I^2 \gamma_g(\omega)$$

where $\gamma_g(\omega)$ describes the line profile. Afterwards we include the light shifts, but we neglect the photoionisation and the saturation of the two-photon transition probability. Strictly speaking, we should replace each atomic frequency ω_i ($i = g, e$ or f) by $\omega_i - c_{ls}(i)I$, where the light shift coefficient depends on the state i . In actual fact, to reduce the calculation time, we assume that all the states e and f have the same light shift coefficient c_{ls} . This is justified for two reasons: (i) the anisotropy of the light shift is small (see Tab. 4); (ii) the light shift coefficients of the levels nP , nD and nF are all very similar. For instance, the light shift coefficients β_e of the states $8P(m_L = 0)$, $8D(m_L = 0)$ and $8F(m_L = 0)$ are respectively 287.78, 285.43 and 281.1 (in atomic units). With this approximation, when we include the light shift, the transition probability becomes:

$$\Gamma_g = I^2 \gamma_g(\omega - \frac{1}{2} c_{ls} I). \quad (29)$$

This equation replaces equation (10). Then we follow the procedure described in Section 3.1 (Eqs. (16–18)). However, we have not summed over the velocity distribution in equation (18) but used instead the mean velocity v_m [11]:

$$1/v_m = \langle 1/v \rangle = \frac{\int_0^\infty \frac{f(v)}{v} dv}{\int_0^\infty f(v) dv}$$

where $f(v)$ is the velocity distribution (Eq. (1)).

In reality, we do not know the orientation of the stray electric fields. Consequently, we have made the line shape calculation for an electric field either parallel or perpendicular to the laser polarisation to obtain the line shapes $L_{\parallel}(\omega, P, E)$ and $L_{\perp}(\omega, P, E)$ ($E = |\mathbf{E}|$). Moreover we have to consider the case of each hyperfine sublevel m_F of the $2S_{1/2}(F = 1)$ level ($2S_{1/2}(F = 3/2)$ for deuterium). Finally, we evaluate the mean of these different profiles:

$$\begin{aligned} L(\omega, P, E) = \frac{1}{2F+1} \sum_{m_F} \left[\frac{1}{3} L_{\parallel, m_F}(\omega, P, E) \right. \\ \left. + \frac{2}{3} L_{\perp, m_F}(\omega, P, E) \right]. \end{aligned}$$

Figure 13 shows an example of this line shape in the case of the $2S_{1/2}(F=3/2)-20D_J$ transition in deuterium for a light power of 20 W and several electric fields (in this calculation we have neglected the quadratic Stark effect between the $J = 3/2$ and $J = 5/2$ levels). For an electric field of 5 mV/cm, the linear Stark structure appears clearly and we see that the $nD_{3/2}$ level is more sensitive to an electric field than the $nD_{5/2}$.

3.3.3 Corrections due to the Stark effect

As the linear Stark effect varies as n^2 , we can estimate the residual electric fields from the widths of the transitions to higher nD levels. During the measurements

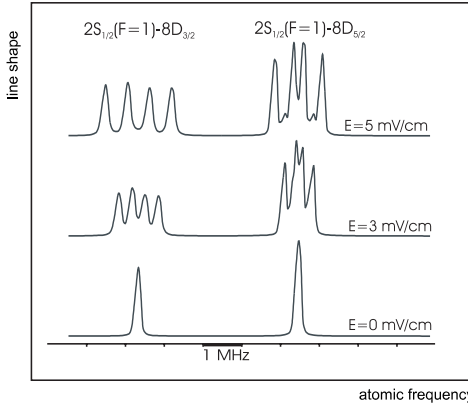


Fig. 13. Stark splitting of the $2S_{1/2}(F = 3/2)-20D_{3/2}$ and $-20D_{5/2}$ transitions for several electric fields.

of the 2S–8S/D frequencies [5,6], we have made several recordings of the $2S_{1/2}-15D_J$ transition. For the 2S–12D measurements [8], we have also observed the $2S_{1/2}-20D_J$ lines. To determine the electric field, we adjust the profile $L(\omega, P, E)$ to the experimental data for several values of the electric field E . We use the procedure described in Section 3.2, but without the Gaussian broadening ($\Delta_\omega = 0$). Two examples are given in Figures 14 and 15. For the $2S_{1/2}-15D_{3/2}$ transition (Fig. 14), the best fit is obtained for an electric field of about 2 mV/cm. Figure 15 shows the fit of the $2S_{1/2}-20D_J$ with an electric field of 3 mV/cm. In this case we see the structure of the theoretical curve (in the experiment, we have in fact a distribution of the amplitude E), but the experimental lines are narrower than the theoretical ones. Finally, we can estimate the residual electric field E_R to be 2.5(1.0) mV/cm during the 2S–8S/D measurements [6] and 2.0(1.0) mV/cm for the 2S–12D ones [8].

The calculation of the quadratic Stark effect is straightforward (see Tab. 11). To evaluate the corrections due to the linear Stark effect, we have fitted all the experimental curves $2S_{1/2}-8D_J$ and $2S_{1/2}-12D_J$ with the theoretical profiles $L(\omega, P, E)$ for the electric field $E = 0$ and $E = E_R$ (for the calculation of $L(\omega, P, E)$ we have used $R_1 = 2$ mm). Then, we make the difference between the two extrapolated values of CLP (obtained for $E = 0$ and $E = E_R$) to obtain the shift due to the linear Stark effect. These corrections are given in Table 12. We can make two comments.

- Contrary to the result of equation (20), the shift due to the linear Stark effect is not zero: the $nD_{5/2}$ level is shifted up, and the $nD_{3/2}$ shifted down. We have the following explanation. Schematically, as the $nD_{5/2}$ level is above the $nF_{5/2}$, the mixing of the two levels divides the two-photon line in two components, a large component above the $nD_{5/2}$ level and a small component below the $nF_{5/2}$ level. Following equation (20), the barycentre of these two components is not shifted. If we take into account the saturation of the two-

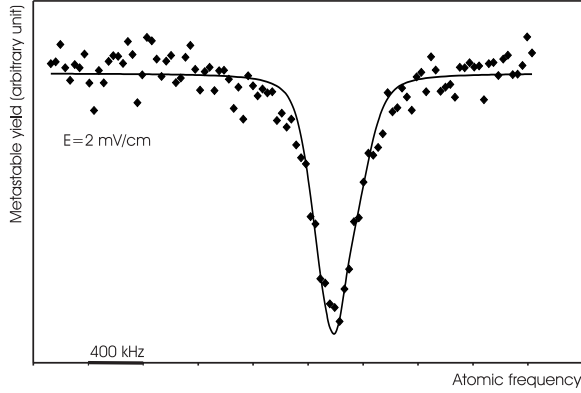


Fig. 14. Fit of the $2S_{1/2}(F = 3/2)-15D_{3/2}$ two-photon transition in deuterium. The theoretical curve (solid) is calculated with an electric field of 2 mV/cm.

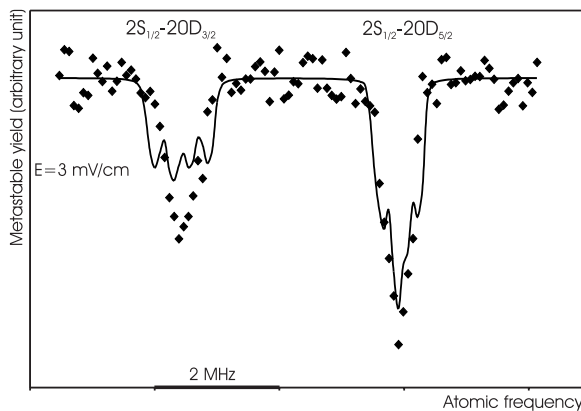


Fig. 15. Fit of the experimental $2S_{1/2}(F = 3/2)-20D_{3/2}$ and $-20D_{5/2}$ profiles in deuterium. The theoretical curve (solid) is calculated with an electric field of 3 mV/cm. For the $2S_{1/2}(F = 3/2)-20D_{3/2}$ transition, the experimental curve is narrower than the theoretical one.

photon transition, the large component is reduced more than the small component and the barycentre should be down shifted. In fact we observe a shift of opposite sign: the adjustment procedure does not give the barycentre of the line, but rather makes the fit to the main component, which is up shifted. The explanation is similar for the $nD_{3/2}$ level but with the signs reversed.

- The total shift is larger for the $nD_{3/2}$ level than for the $nD_{5/2}$, because the quadratic and the linear Stark shift have the same signs in the former case and opposite signs in the latter. This result is important for the 2S–12D transitions: the correction and the uncertainty due to the Stark effect are significant for the $2S_{1/2}-12D_{3/2}$ transition and smaller for the $2S_{1/2}-12D_{5/2}$ one (see Tab. 12).

Table 12. Corrections due to the Stark effect for the 2S–8S/D and 2S–12D transitions (the quadratic Stark corrections are similar for hydrogen and deuterium).

transition	E_R (mV/cm)	quadratic Stark effect (kHz)	linear Stark effect (kHz)	total shift (kHz)
2S _{1/2} –8S _{1/2}	2.5(1.0)	0.56(40)		0.56(40)
hydrogen				
2S _{1/2} –8D _{3/2}	2.5(1.0)	−0.27(19)	−0.24(14)	−0.51(33)
2S _{1/2} –8D _{5/2}	2.5(1.0)	−0.36(25)	0.54(38)	0.18(13)
deuterium				
2S _{1/2} –8D _{3/2}	2.5(1.0)	−0.27(19)	−0.59(43)	−0.86(62)
2S _{1/2} –8D _{5/2}	2.5(1.0)	−0.36(25)	0.38(26)	0.02(1)
hydrogen				
2S _{1/2} –12D _{3/2}	2.0(1.0)	−3.4(2.8)	−2.6(2.1)	−6.0(4.9)
2S _{1/2} –12D _{5/2}	2.0(1.0)	−5.0(4.0)	2.9(2.8)	−2.1(1.2)
deuterium				
2S _{1/2} –12D _{3/2}	2.0(1.0)	−3.4(2.8)	−2.7(2.6)	−6.1(5.4)
2S _{1/2} –12D _{5/2}	2.0(1.0)	−5.0(4.5)	3.9(3.6)	1.1(1.0)

4 Optical frequency measurements

4.1 The rubidium frequency standard

4.1.1 Experimental arrangement and metrological properties

The cornerstone of our optical frequency measurements is a new standard, namely a laser diode at 778 nm (*i.e.* a frequency ν of 385 THz) stabilized to the 5S_{1/2}–5D_{5/2} two-photon transition of rubidium (LD/Rb laser). This standard has been described previously elsewhere [7, 26, 27]. The AlGaAs laser diode is used in an extended cavity configuration to obtain a typical spectral width of 100 kHz. The rubidium cell (temperature of 90 °C and pressure of about 8×10^{-5} torr) is placed in an enhancement cavity (30 cm long with a beam waist of 420 μm) in order to define well the two counterpropagating Gaussian beams and eliminate completely the first order Doppler effect. The optical isolation between the laser and the cavity is provided by a Faraday isolator (isolation of 60 dB) and an acousto-optic modulator (AOM) in a double-pass configuration. To control the light shift, we stabilize with the AOM the intensity of the beam transmitted by the cavity to a reference value I_R . The two-photon transition is monitored *via* the fluorescence at 420 nm due to the cascade 5D–6P–5S. The frequency lock of this system is made with two servo-loops. The laser frequency is modulated at 100 kHz with a peak-to-peak amplitude of 300 kHz. A first error signal is extracted from the intensity of the transmitted beam by the cavity to lock the cavity length to the laser wavelength. We then detect the modulation of the fluorescence signal to lock the laser frequency to the two-photon transition of rubidium.

Three identical systems have been built, two at the LPTF (labelled L₁ and L₂) and a third in *Laboratoire Kastler Brossel* (labelled KB). As the two laboratories are linked by two, 3 km long, optical fibers, we can compare the frequencies of the three systems. To check the frequency shift due to the fiber, we have used our highly

stabilized titanium-sapphire laser. After a round trip of 6 km through the fibers, we have observed a maximum frequency shift of 3 Hz [28]. This shift is completely negligible for our frequency measurements. From these frequency comparisons, we have determined precisely the light shift of each system (−7.32 kHz for the KB system with the intensity reference value I_R). The main metrological features of the LD/Rb laser are a frequency stability (Allan variance) of about $4 \times 10^{-13} \tau^{-1/2}$ per laser over 1000 s and a day-to-day repeatability of 400 Hz.

4.1.2 Optical frequency measurement

The frequencies of the three LD/Rb lasers stabilized on the 5S_{1/2}($F=3$)–5D_{5/2}($F=5$) two-photon transition of ⁸⁵Rb were measured in 1996 at the LPTF with a frequency chain. This frequency chain connects the LD/Rb laser at 385 THz to a standard at 29 THz, namely a CO₂ laser stabilized to an osmium tetroxide line (CO₂/OsO₄) [7]. This standard had been previously measured in 1985 with respect to the Cs clock with an uncertainty of 70 Hz ($\nu = 29\ 096\ 274\ 952\ 340$ (70) Hz) [29, 30]. The optical frequencies of the three LD/Rb systems have been found to lie very close to each other (the maximum difference was 1.1 kHz) and the measured frequency of the system working at LKB was, after correction for the light shift:

$$\nu_{KB} = 385\ 285\ 142\ 377.82 \text{ kHz} \quad (30)$$

with an uncertainty of 1 kHz. This uncertainty was due to the CO₂ laser (13×70 Hz) and the day-to-day repeatability of the LD/Rb standard (400 Hz).

To keep this precision, we have made several frequency comparisons between the L₁, L₂ and KB systems. In 1998, for instance, we have measured the frequency difference $\nu_{KB} - \nu_{L_1}$ and $\nu_{KB} - \nu_{L_2}$. If we suppose that there was no drift of the frequencies ν_{L_1} or ν_{L_2} between 1996 and

1998, we can deduce two values for the frequency of the KB system:

$$\nu_{\text{KB}}(L_1) = 385\ 285\ 142\ 377.53 \text{ kHz},$$

$$\nu_{\text{KB}}(L_2) = 385\ 285\ 142\ 378.32 \text{ kHz}.$$

These values are very close to that of the 1996 measurement (Eq. (30)) so we estimate the frequency shift of the KB system to be smaller than 500 Hz.

In 1998, the measurement of the CO₂/OsO₄ standard with respect to the Cs clock was remade with an uncertainty of 20 Hz (*i.e.* a relative uncertainty of 7×10^{-13}) [31]. This measurement corrects the previous one by -88 Hz. With this correction, the frequency of the LD/Rb standard of LKB becomes:

$$\nu_{\text{KB}} = 385\ 285\ 142\ 376.68 \text{ kHz}.$$

Finally, if we take into account the light shift, the frequency $\nu_{\text{KB}}(I_R)$ of the LD/Rb standard of LKB working with the reference intensity I_R is:

$$\nu_{\text{KB}}(I_R) = 385\ 285\ 142\ 369.4 \text{ (1.0) kHz}. \quad (31)$$

It is this value which has been used for the analysis of the 2S–8S/D and 2S–12D measurements. We have kept a conservative uncertainty of 1 kHz which takes into account the day-to-day repeatability (400 Hz), the long term stability of the LD/Rb standard (500 Hz) and the accuracy of the CO₂/OsO₄ standard (13×20 Hz).

4.2 Optical frequency measurements of the 2S–8S and 2S–8D transitions

4.2.1 The first measurement of the 2S–8S and 2S–8D transitions

In 1993 we carried out a first optical frequency measurement of the 2S–8S and 2S–8D two-photon transitions [5,32]. The principle of this measurement was the near coincidence between the 2S–8S/D frequencies and the frequency difference of two standard lasers, the iodine stabilized (He–Ne/I₂) and the methane stabilized (He–Ne/CH₄) helium-neon lasers (frequencies ν_f and ν_{CH_4} respectively):

$$\nu(2S-8S/D) = \nu_f - \nu_{\text{CH}_4} + \Delta_1$$

where the residual frequency difference Δ_1 is about 89 GHz. After a short description of our experimental scheme, we present an up-to-date analysis of the data which takes into account the recent improvements of the line shape calculations and some optical frequency measurements made subsequently with the LD/Rb standard.

Figure 16 shows the experimental set-up. We use two titanium-sapphire lasers labelled TiS1 and TiS2 which are frequency shifted by about Δ_1 . We observe the two-photon transition in hydrogen with the first titanium-sapphire

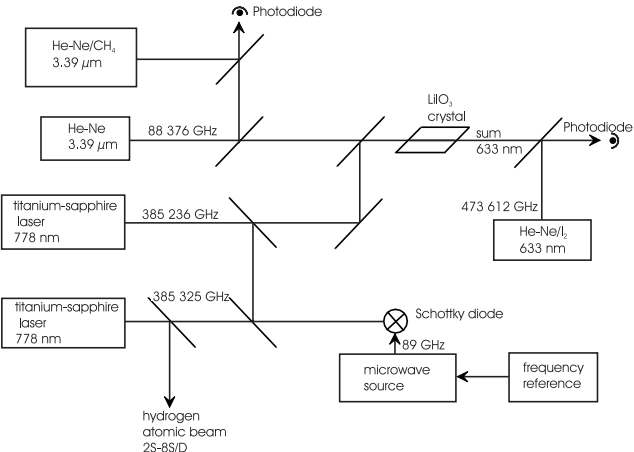


Fig. 16. Experimental set-up for the frequency comparison between the 2S–8S/D transitions in hydrogen and the methane stabilized and iodine stabilized standard lasers.

laser. As the power of the He–Ne/CH₄ laser is only 100 μW, we use a more powerful (about 15 mW) auxiliary He–Ne laser at 3.39 μm, which is frequency locked to the He–Ne/CH₄ standard laser. Then the second titanium-sapphire laser and the auxiliary He–Ne laser are mixed in a LiIO₃ crystal to generate a radiation at 633 nm. This light is heterodyned with that of the He–Ne/I₂ standard laser. Finally, the frequency difference Δ_1 between the two titanium-sapphire lasers is measured with a Schottky diode which is simultaneously illuminated by the two titanium-sapphire lasers and a Gunn diode at 89 GHz. From the frequency Δ_1 and that of the beat notes at 3.39 μm and 633 nm, we deduce the optical frequency of the TiS1 laser. The details of these frequency measurements are given in references [5,15].

The He–Ne/CH₄ standard laser was the laser VB-BIPM from the *Bureau International des Poids et Mesures*. Its frequency is known from previous measurements with an uncertainty of 1 kHz:

$$\nu_{\text{CH}_4} = 88\ 376\ 181\ 602.6 \text{ (1.0) kHz}.$$

The He–Ne/I₂ standard laser was the laser INM12 from the *Institut National de Métrologie*. In 1992, the frequency ν_f of INM12 laser (locked on the f hyperfine component of the ¹²⁷I₂ R11-5 iodine line) was measured in the LPTF with respect to the CO₂/OsO₄ standard [33]. The measured frequency was:

$$\nu_f = 473\ 612\ 353\ 586.9(3.4) \text{ kHz}. \quad (32)$$

In 1993 we used these frequency values to determine the hydrogen frequencies. Today, we can use a more reliable value of the frequency ν_f of the INM12 laser. First, in 1993, promptly after the hydrogen measurements, we measured the frequency $\nu_{\text{Rb}}(5S_{1/2}-5D_{3/2})$ of the 5S_{1/2}–5D_{3/2} two-photon transition of rubidium with the same frequency chain [34]. Indeed, we have a similar coincidence:

$$\nu_{\text{Rb}}(5S_{1/2}-5D_{3/2}) = \nu_f - \nu_{\text{CH}_4} + \Delta_2 \quad (33)$$

Table 13. Experimental determination of the 2S–8S/D transition frequencies from our 1993 measurements (all values in MHz).

transition	2S _{1/2} –8S _{1/2}	2S _{1/2} –8D _{3/2}	2S _{1/2} –8D _{5/2}
1993 analysis [5]	770 649 306.3195	770 649 460.0438	770 649 517.1844
updated analysis	770 649 306.3187	770 649 460.0467	770 649 517.1887
correction of ν_f	0.0070	0.0070	0.0070
2S _{1/2} hyperfine shift	44.3892	44.3892	44.3892
8S _{1/2} hyperfine shift	-0.6936		
$\nu(2S_{1/2}-8S_{1/2}/8D_J)$	770 649 350.0213	770 649 504.4429	770 649 561.5849
8S _{1/2} /8D _{3/2} –8D _{5/2} splitting	211.5621	57.1291	
$\nu(2S_{1/2}-8D_{5/2}) - 770\,649\,000$	561.5834 (143)	561.572 (131)	561.5849 (123)
mean value		770 649 561.580 (11)	

but in this case the residual frequency Δ_2 is only 4 to 7 GHz. For instance, for the 5S_{1/2}(F = 1)–5D_{3/2}(F = 3) hyperfine component in ⁸⁷Rb, we have measured $\Delta_2 = 7\,383\,160.2$ (2.0) kHz. Afterwards, the fine structure 5D_{3/2}–5D_{5/2} in rubidium was measured at the LPTF [35]. The frequency difference between the ⁸⁵Rb 5S_{1/2}(F = 3)–5D_{5/2}(F = 5) (*i.e.* the frequency of the LD/Rb standard) and ⁸⁷Rb 5S_{1/2}(F = 1)–5D_{3/2}(F = 3) hyperfine components was measured to be 41 587 229.1 (2.0) kHz. Finally, if we take into account the frequency measurement of the LD/Rb standard, we can deduce the frequency $\nu_{Rb}(5S_{1/2}-5D_{3/2})$ and use equation (33) to obtain the frequency ν_f of the He–Ne/I₂ INM12 standard. The result is:

$$\nu_f = 473\,612\,353\,590.4(3.5) \text{ kHz.} \quad (34)$$

We have used the mean value of the three LD/Rb standard lasers L₁, L₂ and KB corrected for the recent measurement of the CO₂/OsO₄ standard [7,31] (*i.e.* $\nu(\text{LD/Rb}) = 385\,285\,142\,377.1$ (2.0) kHz). The obtained ν_f value is up shifted (3.5 kHz) with respect to the 1992 measurement (Eq. (32)). Though the uncertainties are similar, the value given by equation (34) seems the most reliable because of the very good reproducibility of the two-photon rubidium lines.

In 1993, we measured the three 2S_{1/2}–8S_{1/2}, 2S_{1/2}–8D_{3/2} and 2S_{1/2}–8D_{5/2} two-photon transitions in hydrogen (see Tab. 2). We have remade the analysis of the data with the line shape calculations presented in Section 3. The hyperfine structure of the 8D levels, the photoionisation of the excited level, the saturation of the two-photon transition as well as the second order Doppler effect are included in the theoretical profile. The details of this analysis are given in Table 13. We recall the results of our first analysis made in 1993 (first row of the table). The results, given in terms of atomic frequency, are corrected for the second order Doppler effect and the hyperfine structure of the D levels (we have detected an error in the reference [5]: the correction due to the second order Doppler effect is not 40.2 kHz, but rather 42.4 kHz, as indicated in Tab. 1). These values can be directly compared with those of our up-to-date analysis (second row of the table). The result is similar for the 2S_{1/2}–8S_{1/2} transition, but is up-shifted by about 3 kHz for the 2S_{1/2}–8D_J ones. After the

Table 14. Theoretical Lamb shifts in hydrogen and deuterium.

level	hydrogen (MHz)	deuterium (MHz)
3S _{1/2}	311.4040 (20)	311.8106 (20)
6S _{1/2}	39.0860 (3)	39.1368 (3)
6D _{5/2}	0.1660 (2)	0.1662 (2)
8S _{1/2}	16.5008 (3)	16.5222 (3)
8D _{3/2}	-0.0607 (2)	-0.0607 (2)
8D _{5/2}	0.0714 (2)	0.0715 (2)
12D _{3/2}	-0.0176 (2)	-0.0176 (2)
12D _{5/2}	0.0215 (2)	0.0215 (2)

correction of the He–Ne/I₂ frequency (see Eqs. (32, 34)) and of the hyperfine structure of the S levels, we obtain the 2S_{1/2}–8S_{1/2} and 2S_{1/2}–8D_J splittings (for this analysis we neglect the Stark effect and the shift due to the black body radiation). For the 2S_{1/2} hyperfine structure, we use the value of reference [36]. We deduce the 8S_{1/2} hyperfine structure with a simple $1/n^3$ scaling law, because at this level of precision the relativistic corrections in $(Z\alpha)^2$ are negligible. The three experimental values of the 2S_{1/2}–8S_{1/2} and 2S_{1/2}–8D_J splittings can be intercompared using the theoretical values of the fine structure and of the Lamb shifts in the $n = 8$ levels. Table 14 gives the theoretical Lamb shifts useful in this paper. We have taken into account the more precise values of the Bethe logarithms [37] and all the recent calculations of the high-order terms following the references [38–40]. For the nuclear charge radii in hydrogen and deuterium, we have used $r_p = 0.862$ fm and $r_d = 2.115$ fm [41,42]. This enables us to deduce three independent values for the 2S_{1/2}–8D_{5/2} splitting which are in good mutual agreement (see Tab. 13). The quoted uncertainties come from the statistics, the second-order Doppler effect (2 kHz), the optical alignment and the theoretical line shape (4 kHz and 2 kHz respectively, see Sect. 3.2) and the He–Ne/I₂ standard laser (2 × 3.5 kHz, see Eq. (34)). Finally, the mean value is:

$$\nu(2S_{1/2}-8D_{5/2}) = 770\,649\,561.580(11) \text{ MHz.}$$

Table 15. Experimental determination of the 2S–8S/D transition frequencies from the measurements made in hydrogen with the rubidium standard. All the values are in MHz and we have subtracted a frequency ν_0 of 770 649 GHz. The values in bold-faced type are the ones used in the 1998 CODATA adjustment of the fundamental constants [44].

transition in hydrogen	2S _{1/2} –8S _{1/2}	2S _{1/2} –8D _{3/2}	2S _{1/2} –8D _{5/2}
result of the extrapolation $-\nu_0$	306.3175 (70)	460.0609 (66)	517.1958 (40)
stark effect	-0.0006 (4)	0.0005 (3)	-0.0002 (1)
black body radiation	-0.0005 (1)	-0.0006 (2)	-0.0006 (2)
2S _{1/2} hyperfine shift	44.3892	44.3892	44.3892
8S _{1/2} hyperfine shift	-0.6936		
$\nu(2S_{1/2}-8S_{1/2}/8D_J)-\nu_0$	350.0120 (86)	504.4500 (83)	561.5842 (64)
8S _{1/2} /8D _{3/2} –8D _{5/2} splitting	211.5621	57.1291	
$\nu(2S_{1/2}-8D_{5/2})-\nu_0$	561.5741 (86)	561.5791 (83)	561.5842 (64)
mean value and χ^2	770 649 561.5811 (59)		$\chi^2 = 1.69$

By comparison with the published value in 1993 ($\nu(2S_{1/2}-8D_{5/2}) = 770\,649\,561.567$ (10) MHz [5]), there is a difference of 13 kHz due to the error in the calculation of the second-order Doppler effect (2.2 kHz), the frequency of the He–Ne/I₂ standard laser (7 kHz), the improvements of the theoretical line shape (2.6 kHz) and the more precise Bethe logarithms (1.2 kHz).

4.2.2 The 1996 measurement using the rubidium standard

To take advantage of the very good long term stability of the LD/Rb standard laser, we have remade the optical frequency measurements of the 2S–8S and 2S–8D transitions in hydrogen and deuterium [6, 25]. In this case, the link between the hydrogen frequencies and the standard laser is straightforward. We have:

$$\nu(2S-8S/D) = \nu(LD/Rb) + \Delta_3$$

where the residual difference Δ_3 is about 40 GHz in hydrogen and 144 GHz in deuterium. To measure this frequency difference, we focus on a Schottky diode the titanium-sapphire laser (used for the observation of the hydrogen lines) and the LD/Rb standard laser. The Schottky diode is simultaneously irradiated by a microwave source at 13 GHz for hydrogen and 48.4 GHz for deuterium. We detect the low frequency beat note between the two optical radiations and the third harmonic of the microwave. Typically, the signal-to-noise ratio is 35 dB with a resolution bandwidth of 300 kHz. A tracking oscillator is phase locked to this beat note, and we count continuously this frequency. The 13 GHz source is the 130th harmonic of a very stable quartz oscillator at 100 MHz (we use a step recovery diode, a YIG filter and a 35 dB amplifier). For deuterium, this microwave source is shifted to 12.1 GHz (on the 121th harmonic of the 100 MHz quartz). Then, a Gunn diode at 48.4 GHz is phase locked on the fourth harmonic of the 12.1 GHz source. The frequency of the 100 MHz quartz oscillator is continuously compared to a high stability quartz oscillator at 10 MHz (stability of 4×10^{-9} during four months), which has been measured with a hydrogen maser several times. Finally, the uncertainty on the Schottky diode measurement is about 15 Hz in hydrogen and 50 Hz in deuterium.

We have measured the three 2S_{1/2}–8S_{1/2}, 2S_{1/2}–8D_{3/2} and 2S_{1/2}–8D_{5/2} two-photon transitions in hydrogen and deuterium (see Tab. 2). In hydrogen, the 2S_{1/2}–8D_{5/2} frequency was measured twice, at the beginning and at the end of the experiment. The analysis of the results is made in Tables 15 and 16. We use the same procedure than for the 1993 results, but we include the corrections due to the Stark effect and the black body radiation (see Tabs. 12 and 8). In deuterium, we have used the 2S_{1/2} hyperfine structure given in reference [43]. In addition to the uncertainties quoted in the Tables, the final uncertainties take into account the second-order Doppler effect (1 kHz), the measurement and the long term stability of the LD/Rb standard laser (2 kHz), the optical alignment and the theoretical line shape (4 kHz and 2 kHz respectively, see Sect. 3.2). The three transition frequencies in hydrogen and deuterium, in bold-faced type in the tables, were used in the 1998 CODATA adjustment of the fundamental constants [44]. As in Table 13, we use the theoretical values of the fine structure between the 8D_{5/2} level and the 8S_{1/2} or 8D_{3/2} ones to obtain three independent values of the 2S_{1/2}–8D_{5/2} interval. These values are in good agreement with each other, especially these for deuterium. The comparison with the results of 1993 in hydrogen (see Tab. 13) shows an improvement of the accuracy by about a factor 2 and a perfect agreement between the mean values of the 2S_{1/2}–8D_{5/2} frequencies. The results given in the Tables 15 and 16 are slightly different from the ones published previously [6] (for the mean values, -3.9 kHz and -3.2 kHz in hydrogen and deuterium). These differences are due to the new measurement of the CO₂/OsO₄ laser (-2.3 kHz), the corrections due to the Stark effect and the black body radiation (about -0.6 kHz) and some improvements of the theoretical line shape. With respect to reference [6], the uncertainties are also more conservative.

4.3 Optical frequencies measurements of the 2S–12D transitions

In order to test the measurements of the 2S–8S and 2S–8D transitions, we have built a new frequency chain to measure the frequencies of the 2S–12D intervals [8, 45].

Table 16. Experimental determination of the 2S–8S/D transition frequencies from the measurements made in deuterium with the rubidium standard. All the values are in MHz and we have subtracted a frequency ν_0 of 770 859 GHz. The values in bold-faced type are the ones used in the 1998 CODATA adjustment of the fundamental constants [44].

transition in deuterium	$2S_{1/2}$ – $8S_{1/2}$	$2S_{1/2}$ – $8D_{3/2}$	$2S_{1/2}$ – $8D_{5/2}$
result of the extrapolation $-\nu_0$	27.8184 (47)	182.0600 (38)	239.2086 (32)
stark effect	-0.0006 (4)	0.0009 (6)	$\simeq 0$
black body radiation	-0.0005 (1)	-0.0006 (2)	-0.0006 (2)
$2S_{1/2}$ hyperfine shift	13.6415	13.6415	13.6415
$8S_{1/2}$ hyperfine shift	-0.2131		
$\nu(2S_{1/2}$ – $8S_{1/2}$) $-8D_J$ $-\nu_0$	41.2457 (69)	195.7018 (63)	252.8495 (59)
$8S_{1/2}$ – $8D_{3/2}$ – $8D_{5/2}$ splitting	211.6027	57.1448	
$\nu(2S_{1/2}$ – $8D_{5/2}$) $-\nu_0$	252.8484 (69)	252.8466 (63)	252.8495 (59)
mean value and χ^2	770 859 252.8483 (55)		$\chi^2 = 0.34$

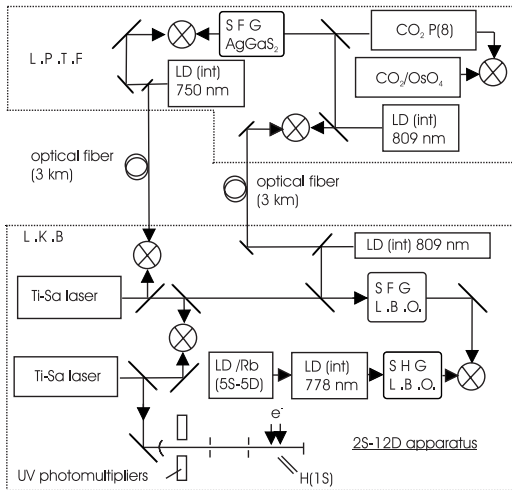


Fig. 17. Outline of the frequency chain between the 2S–12D hydrogen frequencies and the LD/Rb and CO_2/OsO_4 standards. The details are explained in the text (Ti-Sa: titanium sapphire laser, LD/Rb: rubidium stabilized laser diode, LD(int): intermediate laser diode, CO_2/OsO_4 : osmium tetroxyde stabilized CO_2 laser, SHG: second harmonic generation, SFG: sum frequency generation).

This transition yields complementary information, because the 12D levels are very sensitive to the stray electric fields (the quadratic Stark shift varies as n^7 , see Sect. 3.3), and so such a measurement provides a stringent test of Stark corrections to the Rydberg levels.

4.3.1 The experimental scheme

The frequency difference between the 2S–12D transitions ($\lambda \approx 750$ nm, $\nu \approx 399.5$ THz) and the LD/Rb standard laser is about 14.2 THz, *i.e.* the half of the frequency of the CO_2/OsO_4 standard. To bisect this frequency we use an optical divider [2,46]. The frequency chain (see Fig. 17) is split between the LPTF and the LKB: the two optical fibers are used to transfer the CO_2/OsO_4 standard

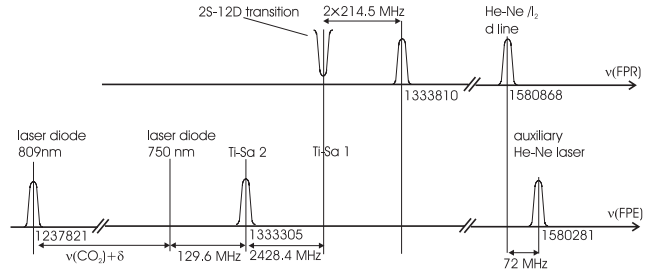


Fig. 18. Example of the position of the laser frequencies with respect to the FPR and FPE cavities during the measurements of the 2S–12D transitions. The fringe 1 580 868 of the FPR cavity is locked on the d line of the He–Ne/ I_2 standard laser. The first titanium sapphire laser (Ti-Sa1) is locked on the fringe 1 333 810 of the FPR cavity with an offset of 2×214.5 MHz. The 809 nm laser diode, the second titanium sapphire laser (Ti-Sa2) and the auxiliary He–Ne laser are respectively locked on the fringes 1 237 821, 1 333 305 and 1 580 281. The laser diode at 750 nm is frequency shifted by $\nu(\text{CO}_2) + \delta$ with respect to the one at 809 nm.

from the LPTF to the LKB, where we observe the hydrogen transitions. This chain includes an auxiliary source at 809 nm ($\nu \approx 370.5$ THz) such that the laser frequencies satisfy the equations:

$$\begin{aligned} \nu(2S-12D) + \nu(809) &= 2\nu(LD/Rb), \\ \nu(2S-12D) - \nu(809) &= \nu(\text{CO}_2). \end{aligned}$$

The first equation is realized at the LKB while the second one is carried out at the LPTF. For this experiment we use two-titanium-sapphire lasers. Figure 18 shows an example of the positions of the laser frequencies with respect to the FPR and FPE cavities in the case of the $2S_{1/2}$ – $12D_{5/2}$ transition in hydrogen. We observe the hydrogen transitions with a first titanium-sapphire laser (TiS1). It is locked on the fringe 1 333 810 of the FPR cavity with a frequency shift due to the AOM1 (see Fig. 2). The source at 809 nm (a laser diode in an extended cavity configuration with a power of about 30 mW) and the second titanium-sapphire laser (TiS2) are frequency modulated

Table 17. Experimental determination of the 2S–12D transition frequencies in hydrogen. All the values are in MHz and we have subtracted a frequency ν_0 of 799 191 GHz. The values in bold-faced type are the ones used in the 1998 CODATA adjustment of the fundamental constants [44].

transition in hydrogen	2S _{1/2} –12D _{3/2}	2S _{1/2} –12D _{5/2}
result of the extrapolation $-\nu_0$	666.0796 (62)	683.0145 (47)
stark effect	0.0060 (49)	0.0021 (12)
black body radiation	-0.0021 (5)	-0.0021 (5)
2S _{1/2} hyperfine shift	44.3892	44.3892
$\nu(2S_{1/2}-12D_J)-\nu_0$	710.4727 (93)	727.4037 (70)
12D _{3/2} –12D _{5/2} splitting	16.9272	
$\nu(2S_{1/2}-12D_{5/2})-\nu_0$	727.3999 (93)	727.4037 (70)
mean value ($\chi^2 = 0.26$)	799 191 727.4028 (67)	

and locked on the fringes 1 237 821 and 1 333 305 of the FPE cavity. A laser diode (power of 50 mW) is injected by the LD/Rb standard and frequency doubled in a LiB₃O₅ crystal (LBO) placed in a ring cavity. This cavity is similar to the one described in reference [13]. We obtain about 10 μ W in the UV. At the same time, the TiS2 laser (about 300 mW) and the source at 809 nm are summed in an other LBO crystal to obtain a second UV beam. A tracking oscillator is phase locked on the beat note between the two UV beams (frequency δ_1). A part of the 809 nm source is sent *via* one fiber to the LPTF. There, a 809 nm local laser diode is phase locked to the one at LKB. A frequency sum of this 809 nm laser diode and of an intermediate CO₂ laser in an AgGaS₂ crystal produces a wave at 750 nm. This wave is used to phase lock, with a frequency shift δ , a laser diode at 750 nm which is sent back to the LKB by the second optical fiber. This 750 nm laser diode is frequency shifted by $\nu(\text{CO}_2) + \delta$ with respect to the one at 809 nm. Then we use a second tracking oscillator to count the beat note (frequency δ_2) between the 750 nm laser diode and the TiS2 laser. Finally, we measure the frequency δ_3 between the two titanium-sapphire lasers. For the hydrogen measurements, the CO₂ auxiliary laser uses the P(8) line (CO₂ R(4) line for deuterium) and the frequency δ_3 is about 2.4 GHz (41.3 GHz in deuterium). The frequency δ_3 is mixed with two times the frequency which drives the AOM1, in order to eliminate the variation of the measured frequency when we scan the TiS1 frequency to observe the hydrogen lines. The 2.4 GHz frequency beat notes is detected with a fast photodiode. For deuterium, we measure the 41.3 GHz frequency with a Schottky diode. As for the hydrogen measurements of the 2S–8S/D transitions (see Sect. 4.2.2), the Schottky diode is irradiated with the two titanium-sapphire lasers and a microwave source at 13.9 GHz and we detect the beat note between the TiS1 and TiS2 lasers and the third harmonic of this microwave radiation (for this measurement we use also a tracking oscillator). Then, from the frequencies δ_1 , δ_2 and δ_3 , we can deduce the frequency $\nu(\text{TiS1})$ of the TiS1 laser. Specifically, we have:

$$\nu(\text{TiS1}) = \nu(\text{LD/Rb}) + \frac{1}{2} (\nu(\text{CO}_2) + \delta + \delta_1 + \delta_2) + \delta_3.$$

The advantage of this scheme is that all the frequency counting is performed at the LKB.

4.3.2 Results and uncertainties

We have measured the two 2S_{1/2}($F=1$ or 3/2)–12D_{3/2} and 2S_{1/2}($F=1$ or 3/2)–12D_{5/2} two-photon transitions in hydrogen and deuterium. We have not studied the 2S_{1/2}–12S_{1/2} transition because of the low signal-to-noise ratio. For each transition, the signal is recorded for about 50 light powers (see Table 2). The extrapolated frequencies and the analysis of the data are shown in Tables 17 and 18.

For these transitions, the corrections due to the black body radiation and to the Stark effect are not negligible (several kHz), especially the Stark correction of the 2S_{1/2}–12D_{3/2} (6 kHz). In Tables 17 and 18, these transition frequencies are corrected for the hyperfine structure and compared by taking into account the theoretical value of the fine structure 12D_{3/2}–12D_{5/2}. We obtain two independent values of the 2S_{1/2}–12D_{5/2} interval which are in good agreement for hydrogen and deuterium. As for the 2S–8S/D results, the final uncertainty takes into account the second order Doppler effect (1 kHz), the accuracy of the LD/Rb standard (2 kHz) and the uncertainties due to the alignment and the theoretical line shape (4 kHz and 2 kHz). Ultimately, these measurements are slightly less precise than those for the 2S–8S/D transitions, owing to the smaller signal-to-noise ratio and the larger Stark shifts.

5 Comparison of the 1S–3S and 2S–6S/D transitions

In this experiment our purpose is the determination of the 1S Lamb shift. This Lamb shift is difficult to measure, because the 1S level is isolated. Up to this experiment, all the measurements of the 1S Lamb shift have been obtained from the study of the 1S–2S two-photon transition by subtracting the 1S–2S Dirac and recoil energies from the experimental value of the 1S–2S interval [47, 48]. In the most recent experiments [49, 50], this subtraction is made

Table 18. Experimental determination of the 2S–12D transition frequencies in deuterium. All the values are in MHz and we have subtracted a frequency ν_0 of 799 409 GHz. The values in bold-faced type are the ones used in the 1998 CODATA adjustment of the fundamental constants [44].

transition in deuterium	2S _{1/2} –12D _{3/2}	2S _{1/2} –12D _{5/2}
result of the extrapolation $-\nu_0$	154.3925 (44)	171.3263 (45)
stark effect	0.0061 (54)	0.0011 (10)
black body radiation	-0.0021 (5)	-0.0021 (5)
2S _{1/2} hyperfine shift	13.6415	13.6415
$\nu(2S_{1/2}-12D_J)-\nu_0$	168.0380 (86)	184.9668 (68)
12D _{3/2} –12D _{5/2} splitting	16.9318	
$\nu(2S_{1/2}-12D_{5/2})-\nu_0$	184.9698 (86)	184.9668 (68)
mean value ($\chi^2 = 0.28$)	799 409	184.9676 (65)

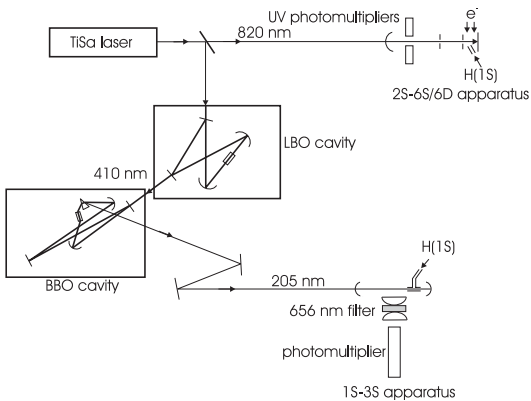


Fig. 19. Experimental setup for the frequency comparison between the 1S–3S and 2S–6S/D transitions (TiSa: titanium sapphire laser, LBO: lithium tri-borate crystal, BBO: β -barium borate crystal).

in a simple way by comparison of the 1S–2S frequency with four times the 2S–4S, 2S–4P or 2S–4D frequencies. Indeed, in the Bohr model, these frequencies lie exactly in a ratio 4:1, and the deviation from this factor is mainly due to the Lamb shifts which vary as $1/n^3$. The principle of our measurement is similar, except that we compare the 1S–3S and 2S–6S/D frequencies, which, for the same reason, are also in a ratio 4:1. This experiment has been described briefly elsewhere [9]. Here we provide some additional details and an updated analysis of the results.

5.1 The 1S–3S transition

Figure 19 shows the general scheme of the experiment. The same titanium-sapphire laser is used to observe, alternately, the 2S–6S or 2S–6D transitions at 820 nm and the 1S–3S transition at 205 nm. The 2S–6S/D apparatus is the one described in Section 2. The UV radiation at 205 nm is obtained from two successive doubling stages with a LBO crystal and a β -barium borate crystal (BBO). Both steps have been described elsewhere [13,51]. Each

crystal is placed in an enhancement ring cavity. The first frequency doubling produces up to 500 mW at 410 nm for a pump power of 2.3 W at 820 nm. The second harmonic generation at 205 nm is far more challenging. To avoid rapid degradation of the faces of the BBO crystal, the second enhancement cavity is placed inside a clean chamber filled with oxygen. Moreover, the length of this enhancement cavity is modulated (modulation frequency of 15 kHz) so as to be resonant only some of the time. We work in an intermediate regime in which the UV intensity consists of 3 μ s pulses at a frequency of 30 kHz. This method prevents the generation, in the ring cavity, of a counterpropagating wave at 410 nm, probably due to a photorefractive effect in the BBO crystal. This modulation produces a frequency shift, the UV frequency being upshifted (downshifted) by about 120 kHz when the length of the BBO cavity decreases (increases). In this regime, a UV power of about 1 mW (peak power) can be obtained for several hours using the same point of the crystal.

To observe the 1S–3S transition, we use a second atomic beam. Atomic hydrogen is produced by a radiofrequency discharge similar to the one described in Section 2.3.1. The discharge is off-axis with respect to the atomic beam, and linked to the vacuum chamber by a 9 cm length of Teflon tube. The atomic hydrogen flows through a Teflon nozzle (3 cm long, 3 mm in diameter) into the vacuum chamber which is evacuated by an oil diffusion pump (Alcatel 6250). Under running conditions, the pressures in the discharge tube and the vacuum chamber are 0.4 mbar and 9×10^{-5} mbar respectively. With the method described in reference [52], we have measured the angular width of the profile of the effusive atomic beam to be about 8° (full width at the half maximum). By comparison with a previous version of the experiment where the discharge was on the axis of the atomic beam (there was only the Teflon nozzle), we have also found that the atomic flux is reduced by about a factor 4. This effect shows that the recombination of the hydrogen atoms in the Teflon tube is significant. The atomic beam is carefully delimited by two diaphragms (diameter of 2 mm and 3 mm successively) to eliminate the stray light coming from the hydrogen discharge. The atomic beam is also placed inside a linear

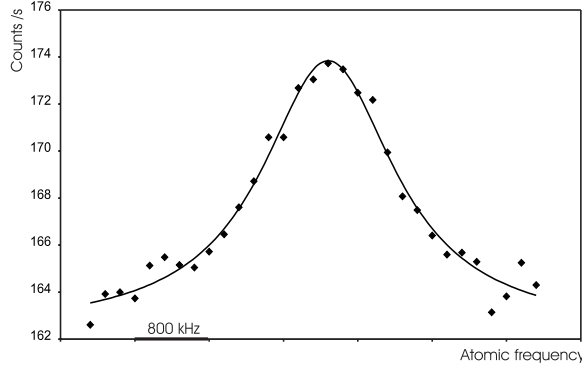


Fig. 20. Spectrum of the $1S_{1/2}(F = 1)$ – $3S_{1/2}(F = 1)$ transition detected by Balmer- α fluorescence. The total acquisition time is about 14 hours. The signal is fitted with a Lorentzian curve (solid).

buildup cavity formed by two spherical mirrors (radius of curvature 25 cm). The UV beam emerging from the BBO crystal is corrected for astigmatism with a spherical lens (focal length 87 mm) and a cylindrical lens (focal length 290 mm) and mode matched into the cavity with two more lenses. Inside the cavity, the UV power is typically 10 mW and the UV beam is focused at a distance of 12 cm from the Teflon nozzle with a waist of about 48 μm . At this distance, we estimate the density of hydrogen atoms to be about 3×10^{10} atoms/ cm^3 . The two cavity mirrors are mounted on PZT stacks and the length of the cavity is locked to the UV frequency so that successive UV pulses have the same intensity inside the cavity. In these conditions, the frequency shifts of two successive UV pulses cancel each other and the residual frequency shift is estimated to be less than 3 kHz. The two-photon transition is detected by monitoring the Balmer- α fluorescence due to the radiative decay $3S$ – $2P$. This fluorescence is collected with a spherical mirror and a $f/0.5$ aspheric lens system, selected with an interference filter and detected with a cooled photomultiplier (EMI 9658R).

The data acquisition is similar to the one described in Section 2.4. Each scan is divided in 31 frequency points. For each point, the photomultiplier signal is counted during 1 s and we make 10 scans of the line to achieve a 7 minute run. As the signal-to-noise ratio is small, we take the mean of several runs to obtain an observable signal. Figure 20 shows the mean of 102 runs. The total background is about 160 counts/s and the $1S$ – $3S$ signal 10 counts/s. In Figure 20, the signal is fitted with a Lorentzian curve. The observed line width (1.7 MHz in terms of atomic frequency) is mainly due to the natural width of the $3S$ level (1 MHz), transit time broadening (200 kHz) and broadening due to the modulation of the UV light (about 500 kHz). We can compare the signal amplitude with a theoretical estimate. The two-photon transition probability Γ_g is given by equation (9). As the value of the matrix element $\langle 3S | Q_{\text{tp}} | 1S \rangle$ of the two-photon operator is 2.14 in atomic units [53], we obtain for a UV power of 10 mW: $\Gamma_g = 2 \times 10^{-2} \text{ s}^{-1}$. If we take into account the

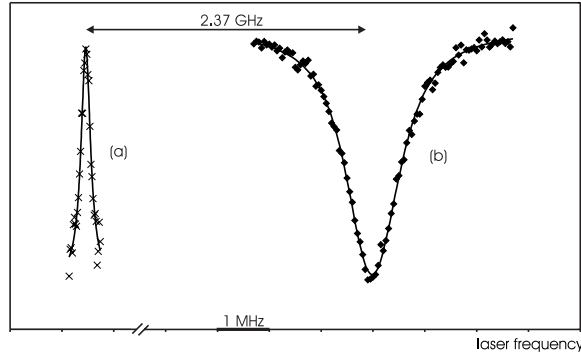


Fig. 21. Hydrogen two-photon spectra. (a) $1S_{1/2}(F = 1)$ – $3S_{1/2}(F = 1)$ transition. (b) $2S_{1/2}(F = 1)$ – $6D_{5/2}$ transition. The two signals are shifted by about 2.37 GHz in terms of laser frequency at 820 nm.

effective linewidth (1.7 MHz), the atomic density in front of the photomultiplier (3×10^{10} atoms/ cm^3), the observation length (12 mm because of the transmission of the interference filter), the detection solid angle ($\Omega/4\pi = 0.24$), the transmission of the detection optics (about 66%), the photomultiplier quantum efficiency (8%), the population of the $F = 1$ hyperfine level (3/4) and the modulation of the UV light (reduction of the excitation time by a factor 0.066), we estimate the signal to be about 20 counts/s. This value is in fair agreement with the experiment if we consider the uncertainties in the UV power and the atomic density.

5.2 Comparison of the $1S$ – $3S$ and $2S$ – $6S/D$ frequencies

We have compared the $1S_{1/2}$ – $3S_{1/2}$ frequencies with those of the $2S_{1/2}$ – $6D_{5/2}$ and $2S_{1/2}$ – $6S_{1/2}$ transitions. To do this, we have measured alternately the $1S$ – $3S$ and $2S$ – $6S/D$ line positions with respect to the fringes 1 219 477 (transition $1S_{1/2}$ – $3S_{1/2}$) and 1 219 485 (transition $2S_{1/2}$ – $6D_{5/2}$) or 1 219 484 (transition $2S_{1/2}$ – $6S_{1/2}$) of our very stable FPR cavity. For the first comparison, we collected the data for the $2S_{1/2}$ – $6D_{5/2}$ transition (1 day), the $1S_{1/2}$ – $3S_{1/2}$ (3 days), then $2S_{1/2}$ – $6D_{5/2}$ once again (2 days). The procedure was similar for the $2S_{1/2}$ – $6S_{1/2}$ transition, but, because of its lower intensity, longer acquisition times were required (4, 3 and 4 days respectively). Figure 21 shows, on the same frequency scale, the recordings of the $1S_{1/2}$ – $3S_{1/2}$ and $2S_{1/2}$ – $6D_{5/2}$ lines. As the $2S$ – $6S/D$ linewidth is larger than the $1S$ – $3S$ one, the accuracy is mainly limited by the uncertainty in the $2S$ – $6S/D$ line positions.

The results are given in Table 19. For the $2S$ – $6S/D$ transitions, we have used our updated analysis of the data: the second-order Doppler effect and the 6D hyperfine structure are included in the theoretical line shape. The quoted uncertainties of the second row of the table (8.8 kHz and 20 kHz for each measurement) are mainly due to the uncertainties in the positions of the $1S$ – $3S$ line

Table 19. Comparison between the $1S_{1/2}-3S_{1/2}$ and $2S_{1/2}-6D_{5/2}/6S_{1/2}$ frequencies. All the values are in MHz. The values in bold-faced type are the ones used in the 1998 CODATA adjustment of the fundamental constants [44].

comparison with	$2S_{1/2}-6D_{5/2}$	$2S_{1/2}-6S_{1/2}$
laser frequency splitting	2370.1140 (44)	2120.188 (10)
laser frequency splitting $\times 2$	4740.2280 (88)	4240.377 (20)
$1S-3S$ second-order Doppler effect	-0.0310 (25)	-0.0310 (25)
hyperfine structure corrections	-41.0981	-42.7421
$\nu(2S-6S/D) - \nu(1S-3S)/4$	4699.099 (11)	4197.604 (21)
$6S_{1/2}-6D_{5/2}$ splitting		501.5051
$\nu(2S_{1/2}-6D_{5/2}) - \nu(1S-3S)/4$	4699.099 (11)	4699.109 (21)
mean value		4699.1006 (98)

(4.7 kHz and 6 kHz for each measurement) and of the $2S-6D$ or $2S-6S$ lines (7.1 kHz and 19 kHz). For the $1S$ atomic beam, the velocity distribution is that of a thermal beam, *i.e.* $f(v) \sim v^3 \exp(-v^2/2\sigma^2)$ and the second-order Doppler shift of the $1S-3S$ line is $-3/2(\sigma/c)^2\nu_{1S-3S}$ (see Eq. (2)). The analysis of the features of the metastable atomic beam shows that the heating due to the discharge is typically 30 K. As the two discharges of the two atomic beams are of identical design, we can assume that the temperature of the beam is in the range 280–330 K and we obtain a second-order Doppler shift of $-124(10)$ kHz for the $1S-3S$ transition in terms of atomic frequency, *i.e.* $-31.0(2.5)$ kHz for the comparison with the $2S-6S/D$ frequencies. Because of the $1S$ and $3S$ hyperfine structures, there is a quadratic Zeeman effect of the $F = 1, m_F = 0$ sublevels. For the $1S-3S$ line this effect introduces a mean shift of 11.9 kHz/G² (in terms of atomic frequency). In our experiment, the Earth's magnetic field is about 260 mG and the Zeeman shift of the $1S-3S$ transition 800 Hz. We have neglected this effect and several other small effects: the shifts due to the black body radiation (see Tab. 8), the residual Stark shifts (smaller than 300 Hz for the $2S-6S/D$ transition) and the light shift of the $1S-3S$ transition. For this transition, the light shift coefficients β_i (see Eq. (11)) are -6.445 and 20.926 (atomic units) for the $1S$ and $3S$ level respectively [19]. With a UV power of 10 mW, the light shift is about 740 Hz for an atom at the center of the laser beam. As previously, the final uncertainties (11 kHz and 21 kHz for the two measurements, see Tab. 19) take into account the uncertainty of the second-order Doppler effect of the $2S-6S/D$ lines (2 kHz), and the uncertainties due to the alignment and the theoretical line shape (4 kHz and 2 kHz).

Finally, if we use the theoretical value of the $6S_{1/2}-6D_{5/2}$ splitting, we can compare the two measurements. We obtain two independent values of the frequency difference $\nu(2S_{1/2}-6D_{5/2}) - \nu(1S-3S)/4$ which are in fair agreement. By comparison with the results published previously [9], these values are shifted by 6 kHz and -3.7 kHz for the $2S_{1/2}-6D_{5/2}$ and $2S_{1/2}-6S_{1/2}$ measurements because of the new theoretical line shape. Finally we obtain an uncertainty of 9.8 kHz for the difference $\nu(2S_{1/2}-6D_{5/2}) - \nu(1S-3S)/4$.

6 Determination of the Rydberg constant and Lamb shifts

6.1 Method and analysis of the data

6.1.1 Theoretical background

The aim of this section is to extract from our measurements the values of Rydberg constant and Lamb shifts. More details of the theory of atomic hydrogen can be found in the review articles [38–40]. The hydrogen level energy is conventionally expressed as the sum of three terms: the energy given by the Dirac equation for a particle with the reduced mass, the first relativistic correction due to the recoil of the proton, and the Lamb shift. The energy $E_H(nLJ)$ of the level $|nLJ\rangle$ of hydrogen is:

$$E_H(nLJ) = d_H(nLJ)hcR_\infty + r_H(n)hcR_\infty + hL_H(nLJ) \quad (35)$$

where $d_H(nLJ)hcR_\infty$ and $r_H(nLJ)hcR_\infty$ describe the Dirac and recoil energies. The coefficients $d_H(nLJ)$ and $r_H(n)$ can be expressed exactly as a function of the fine structure constant α and the electron to proton mass ratio m_e/m_p . Moreover, the coefficient $r_H(n)$ does not depend on the quantum numbers L and J [20]. The Lamb shift $L_H(nLJ)$ is expressed in terms of frequency. It contains all the theoretical corrections, *i.e.* the QED corrections, the other relativistic corrections due to the proton recoil and the effect of the proton charge distribution. For deuterium, the energy $E_D(nLJ)$ is given by a similar equation with the subscripts D. Equation (35) shows that, to extract the Rydberg constant from our measurements, we need to know the Lamb shifts. For the upper levels of the transitions, we can use the theoretical values of the Lamb shift (see Tab. 14), because the theoretical uncertainties (only a few hundred hertz) are far smaller than those of our measurements (typically 6 kHz). On the other hand, for the $1S$ and $2S$ levels, this is not the case. The one-loop QED corrections are now calculated with an accuracy of 1 Hz [54]. By contrast, for the calculations of the higher order terms, the QED uncertainties are typically 5 kHz and 40 kHz for the $2S$ and $1S$ levels [55–57]. Moreover, the disagreement between the two determinations

of the charge radius of the proton ($r_p = 0.805(11)$ fm [58] and $r_p = 0.862(12)$ fm [41]) corresponds to a difference of 18 kHz and 149 kHz respectively for the 2S and 1S Lamb shifts. Consequently, in our data analysis, we shall consider that the 1S and 2S Lamb shifts are unknowns to be determined by the experiment. Nevertheless, since several terms of the Lamb shift calculations vary with the principal quantum number exactly as $1/n^3$ (for instance the effect of the charge distribution of the nucleus), the deviation from this scaling law as been calculated precisely by Karshenboim [59]. For the 1S and 2S levels of hydrogen and deuterium the results are:

$$L_H(1S_{1/2}) - 8L_H(2S_{1/2}) = -187.232(5) \text{ MHz} \quad (36)$$

$$L_D(1S_{1/2}) - 8L_D(2S_{1/2}) = -187.225(5) \text{ MHz} \quad (37)$$

as one might expect, there are similar equations for the other $nS_{1/2}$ levels.

6.1.2 Experimental data

To determine the Rydberg constant and the Lamb shifts, we use the mean values of the frequencies $\nu_A(2S_{1/2}-nD_{5/2})$ ($A = \text{H or D}$ and $n = 8$ or 12) and of the frequency difference $\nu_H(2S_{1/2}-6D_{5/2}) - \nu_H(1S_{1/2}-3S_{1/2})/4$ which are given at the end of the Tables 15–19. We have introduced the subscripts H and D to distinguish the hydrogen and deuterium cases. If we define the coefficient $a_A(2S_{1/2}-nD_{5/2}) = d_A(nD_{5/2}) + r_A(nD_{5/2}) - d_A(2S_{1/2}) - r_A(2S_{1/2})$ we deduce from our experimental results five equations:

$$\begin{aligned} \nu_A(2S_{1/2}-nD_{5/2}) &= a_A(2S_{1/2}-nD_{5/2})cR_\infty \\ &+ L_A(nD_{5/2}) - L_A(2S_{1/2}) \quad (4 \text{ equations}). \end{aligned} \quad (38)$$

And we obtain from the 1S–3S and 2S–6S/D comparison:

$$\begin{aligned} \nu_H(2S_{1/2}-6D_{5/2}) - \frac{1}{4}\nu_H(1S_{1/2}-3S_{1/2}) &= \\ \left[a_H(2S_{1/2}-6D_{5/2}) - \frac{1}{4}a_H(1S_{1/2}-3S_{1/2}) \right] cR_\infty \\ + L_H(6D_{5/2}) - L_H(2S_{1/2}) - \frac{1}{4}(L_H(3S_{1/2}) - L_H(1S_{1/2})) &. \end{aligned} \quad (39)$$

We will use also several other precise measurements in hydrogen and deuterium, at first the measurements of the 2S Lamb shift in hydrogen. This Lamb shift (in fact the difference between the $2S_{1/2}$ and $2P_{1/2}$ Lamb shifts) is deduced from radiofrequency measurements of the $2P_{1/2}-2S_{1/2}$ splitting, the first by Lamb and Rutherford [60]. The most precise direct determination of this splitting is the one by Lundeen and Pipkin (1057.845(9) MHz [61]). We have also used two other indirect determinations deduced from the $2S_{1/2}-2P_{3/2}$ splitting (1057.842(12) MHz [62, 63]) and obtained by the anisotropy method (1057.852(15) MHz

[64]). From the weighted mean value of these three results (1057.8454(65) MHz) and the theoretical value of the $2P_{1/2}$ Lamb shift ($-12.83599(8)$ MHz [63]) we deduce the $2S_{1/2}$ Lamb shift:

$$L_H(2S_{1/2}) = 1045.0094(65) \text{ MHz}. \quad (40)$$

We have not taken into account the determination of Pal'chikov *et al.* (1057.8514(19) MHz [65]) who measured in fact the ratio between the $2S_{1/2}$ Lamb shift and the natural width of the $2P_{1/2}$ level. Since there is an ongoing discussion about the theoretical value of this natural width [66, 67], we have not used this result.

The frequency and the isotope shift of the 1S–2S transition have been measured very accurately by Hänsch and coworkers [2, 3]. Their results provide us with equations:

$$\begin{aligned} \nu_H(1S_{1/2}-2S_{1/2}) &= a_H(1S_{1/2}-2S_{1/2})cR_\infty \\ &+ L_H(2S_{1/2}) - L_H(1S_{1/2}), \end{aligned} \quad (41)$$

$$\begin{aligned} \nu_D(1S_{1/2}-2S_{1/2}) - \nu_H(1S_{1/2}-2S_{1/2}) &= \\ [a_D(1S_{1/2}-2S_{1/2}) - a_H(1S_{1/2}-2S_{1/2})] cR_\infty \\ + L_D(2S_{1/2}) - L_H(2S_{1/2}) - L_D(1S_{1/2}) + L_H(1S_{1/2}). \end{aligned} \quad (42)$$

Lastly, we will use also the measurements of the $1S_{1/2}$ Lamb shift made by comparison of the 1S–2S frequency with the 2S–4S/D frequencies [42, 49] or with the 2S–4P frequencies [50]. If we use the theoretical values of the Lamb shifts for the $n = 4$ levels, the analysis of these data gives two experimental values of the linear combination of the Lamb shifts:

$$L_H(1S_{1/2}) - 5L_H(2S_{1/2}) = 2947.831(37) \text{ MHz} \quad (1S\text{--}2S \text{ and } 2S\text{--}4S/D \text{ comparison}), \quad (43)$$

$$L_H(1S_{1/2}) - 5L_H(2S_{1/2}) = 2947.787(34) \text{ MHz} \quad (1S\text{--}2S \text{ and } 2S\text{--}4P \text{ comparison}). \quad (44)$$

These two measurements are in fair agreement with each other.

To conclude, we obtain a set of 12 equations where the 5 unknowns are the Rydberg constant and the Lamb shifts of the 1S and 2S levels in hydrogen and deuterium: 2 theoretical equations (36, 37), 5 equations given by our experimental results (38, 39) and 5 equations which resume the accurate measurements made in hydrogen or deuterium by several other groups (40–44). This set of equations give us the possibility, with least squares procedures, to extract the Rydberg constant and the Lamb shifts by different ways. We present several approaches below. For these calculations, we use the value of the fine structure constant given by the last adjustment of the fundamental constants $\alpha^{-1} = 137.035\,999\,76(50)$ [44]. This choice is justified because, in this adjustment, the hydrogen measurements have no significant influence on the determination of the fine structure constant. For the proton-to-electron and deuteron-to-proton mass ratios, we use the values taken from references [68, 69]: $m_p/m_e = 1\,836.152\,666\,5(40)$ and $m_d/m_p = 1.999\,007\,501\,3(14)$.

Table 20. Determination of the Rydberg constant.

method and transitions involved	equations	$(R_\infty - 109\,737) \text{ cm}^{-1}$
determination of R_∞ from the 2S–nD and 2S–2P measurements		
2S–2P and 2S–8S/D in hydrogen	(38, 40)	0.315 6861(13)
2S–2P and 2S–12D in hydrogen	(38, 40)	0.315 6848(13)
2S–2P, 2S–8S/D and 2S–12D in hydrogen	(38, 40)	0.315 6855(11)
determination of R_∞ from linear combination of optical frequencies measurements		
2S–8S/D, 1S–2S and $1/n^3$ law in hydrogen	(36, 38, 41)	0.315 6865(16)
2S–12D, 1S–2S and $1/n^3$ law in hydrogen	(36, 38, 41)	0.315 6842(17)
2S–8S/D, 2S–12D, 1S–2S and $1/n^3$ law in hydrogen	(36, 38, 41)	0.315 6854(13)
2S–8S/D, 2S–12D, 1S–2S and $1/n^3$ law in deuterium	(37, 38, 41, 42)	0.315 6854(12)
2S–8S/D, 2S–12D, 1S–2S and $1/n^3$ law in hydrogen and deuterium	(36–38, 41, 42)	0.315 6854(10)
general least squares adjustment in hydrogen and deuterium		
2S–2P, 2S–8S/D, 2S–12D, 1S–2S and $1/n^3$ law	(36–44)	0.315 685 50(84)

6.2 Rydberg constant

We can extract the Rydberg constant from only our results by considering the $8D_{5/2}-12D_{5/2}$ splitting, which is obtained by difference between our $2S_{1/2}-8D_{5/2}$ and $2S_{1/2}-12D_{5/2}$ measurements. Nevertheless, since this splitting is small (about 30 THz), the relative accuracy of this method is only 2×10^{-10} . A first precise method is to use the experimental determination of the $2S_{1/2}$ Lamb shift in hydrogen (Eq. (40)). The first part of Table 20 gives the values of the Rydberg constant deduced from our $2S_{1/2}-8D_{5/2}$ and $2S_{1/2}-12D_{5/2}$ measurements in hydrogen. These two values have a similar precision and are in an acceptable agreement (they differ by about 1 standard deviation). This agreement shows that the corrections due to the Stark effect are well analyzed (these corrections are about 10 times larger for the 12D than for the 8D levels, see Tab. 12). Table 20 gives the average of these results ($R_\infty = 109\,737.315\,685\,5(11) \text{ cm}^{-1}$). The relative uncertainty (about 10^{-11}) comes from the optical frequency measurements (6.1×10^{-12}), the $2S_{1/2}$ Lamb shift (8.3×10^{-12}) and the proton-to-electron mass ratio (1.2×10^{-12}). The uncertainty due to the fine structure constant is negligible (1.3×10^{-13}). This result is the most precise if we make no theoretical assumptions concerning the $1S_{1/2}$ and the $2S_{1/2}$ Lamb shifts. Unfortunately, this method is not appropriate for deuterium, because, for this isotope, no comparably accurate determination of the $2S_{1/2}$ Lamb shift has been performed.

If we use the $1/n^3$ scaling law for the Lamb shifts (Eqs. (36, 37)), we can form the linear combination of the $1S_{1/2}-2S_{1/2}$ and $2S_{1/2}-nD_{5/2}$ frequencies:

$$7\nu_H(2S_{1/2}-nD_{5/2}) - \nu_H(1S_{1/2}-2S_{1/2}).$$

In this way, we can eliminate from the equations (38, 41) the Lamb shift combination $L_H(1S_{1/2}) - 8L_H(2S_{1/2})$ (Eq. (36)) and we deduce the Rydberg constant without the microwave measurements of the $2S_{1/2}$ Lamb shift. Moreover, this method is applicable to both hydrogen and

deuterium. The results are given in the second part of Table 20. The values obtained for hydrogen and deuterium are in perfect agreement. If we use all the precise optical frequency measurements in hydrogen and deuterium (transitions $1S_{1/2}-2S_{1/2}$, $2S_{1/2}-8D_{5/2}$ and $2S_{1/2}-12D_{5/2}$), we obtain a value of R_∞ more precise than the previous ones ($R_\infty = 109\,737.315\,685\,4(10) \text{ cm}^{-1}$). This value is also in perfect agreement with the one deduced *via* the measurements of the $2S_{1/2}$ Lamb shift.

To make an average of these different determinations of R_∞ , we have performed a least squares adjustment which takes into account all the precise measurements described by the equations (36–44): the measurements of the $2S_{1/2}$ Lamb shift, the optical frequency measurements of the $1S-2S$ and $2S-nD$ transitions in hydrogen and deuterium, and also the measurements of the $1S$ Lamb shift which will be described in Section 6.3. This result ($R_\infty = 109\,737.315\,685\,50(84) \text{ cm}^{-1}$) is similar to the one of the 1998 adjustment of the fundamental constant [44], with a relative uncertainty of 7.7×10^{-12} . By comparison with the 1986 adjustment [70], the uncertainty is reduced by a factor of about 150. Figure 22 compares the recent determinations of the Rydberg constant and shows the different steps of this improvement since 1986.

The values of Table 20 are slightly different from the ones published previously [8], because for the fine structure constant α we had used the value of the 1986 CODATA adjustment, which differs from the new value by about 7.5×10^{-8} [70]. To obtain these results, we have chosen to leave out our first determination of the $2S_{1/2}-8D_{5/2}$ frequency (see Tab. 13), because this measurement has no significant bearing upon the final result: if we included this value, the uncertainty in R_∞ would be reduced to only $83 \times 10^{-8} \text{ cm}^{-1}$.

6.3 Lamb shifts

We can deduce the $1S_{1/2}$ Lamb shift from the comparison of the $1S_{1/2}-3S_{1/2}$ and $2S_{1/2}-6D_{5/2}$ frequencies

Table 21. Determination of the $1S_{1/2}$ Lamb shift in hydrogen.

method and transitions involved	equations	$L_H(1S_{1/2})$ (MHz)
comparison of transition frequencies lying in a ratio 4:1		
2S–2P, 1S–3S and 2S–6S/D	(39, 40)	8 172.825(47)
2S–2P, 1S–2S and 2S–4S/D	(43, 40)	8 172.878(51)
2S–2P, 1S–2S and 2S–4P	(44, 40)	8 172.834(48)
comparison of the 1S–2S and 2S–nD frequencies using the $2S_{1/2}$ Lamb shift		
2S–2P, 1S–2S and 2S–8S/D	(38, 40, 41)	8 172.854(33)
2S–2P, 1S–2S and 2S–12D	(38, 40, 41)	8 172.825(34)
2S–2P, 1S–2S, 2S–8S/D and 2S–12D	(38, 40, 41)	8 172.840(31)
comparison of the 1S–2S and 2S–nD frequencies using the $1/n^3$ scaling law		
2S–8S/D, 2S–12D, 1S–2S and $1/n^3$ law in hydrogen	(36, 38, 41)	8 172.837(32)
2S–8S/D, 2S–12D, 1S–2S and $1/n^3$ law in hydrogen and deuterium	(36–38, 41, 42)	8 172.837(26)
general least squares adjustment in hydrogen and deuterium		
2S–2P, 2S–8S/D, 2S–12D, 1S–2S and $1/n^3$ law	(36–44)	8 172.840(22)
theory $r_p = 0.862(12)$ fm [56]		8 172.731(40)
theory $r_p = 0.805(11)$ fm [56]		8 172.582(40)

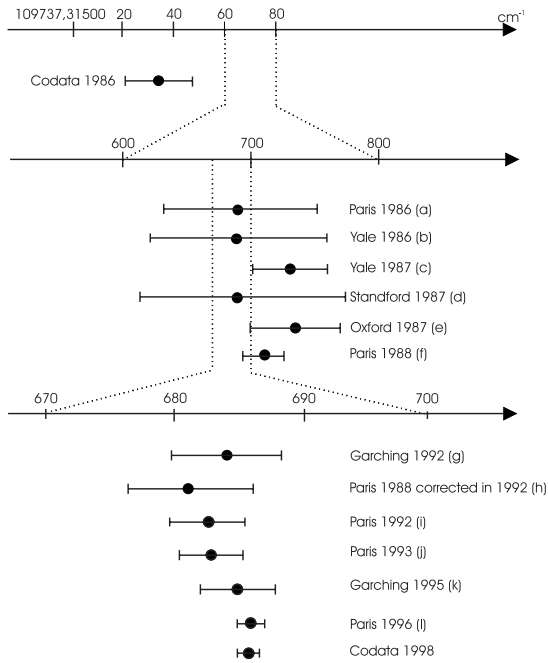


Fig. 22. Comparison of various determinations of the Rydberg constant since the 1986 adjustment of the fundamental constants; Codata 1986 [70], a [71], b [72], c [73], d [74], e [48], f [75], g [76], h: reference [75] corrected for the new measurement of the He–Ne/I₂ standard laser [33], i [4], j [5], k [42], l [6], Codata 1998 [44].

(see Eq. (39)). The value of the term $[a_H(2S_{1/2} - 6D_{5/2}) - a_H(1S_{1/2} - 3S_{1/2})/4]cR_\infty$ is 3 778.5887 MHz. If we use the theoretical values of the $2S_{1/2}$ and $6D_{5/2}$ Lamb shift, we obtain the linear combination of the $1S_{1/2}$ and $2S_{1/2}$ Lamb

shifts:

$$L_H(1S_{1/2}) - 4L_H(2S_{1/2}) = 3 992.787(39) \text{ MHz.} \quad (45)$$

Finally, thanks to the experimental value of the $2S_{1/2}$ Lamb shift (Eq. (40)) we deduce the value $L_H(1S_{1/2}) = 8 172.825(47)$ MHz. This value differs from the one published previously by 27 kHz. This is due to a different value of the $2S_{1/2}$ Lamb shift (10 kHz) and to our new theoretical line shape (17 kHz). This result is compared in the first part of Table 21 with the determinations obtained by comparison of the 1S–2S and 2S–4S/D or 2S–4P frequencies (Eqs. (43, 44); with respect to references [42, 50], these two values are updated by taking into account the different values of the $2S_{1/2}$ Lamb shift and of the fine structure constant). The three results have a similar precision and are in good agreement.

Another way to obtain the $1S_{1/2}$ Lamb shift is to use the precise optical frequency measurements of the $1S_{1/2}$ – $2S_{1/2}$ and $2S_{1/2}$ – $nD_{5/2}$ transitions. A first method uses the experimental value of the $2S_{1/2}$ Lamb shift (Eq. (40)) to extract R_∞ from the $2S_{1/2}$ – $nD_{5/2}$ splitting (see the first part of Tab. 20). Then the $1S_{1/2}$ Lamb shift is deduced from the $1S_{1/2}$ – $2S_{1/2}$ frequency. The results are given in the second part of Table 21. The final result ($L_H(1S_{1/2}) = 8 172.840(31)$ MHz) is more precise than the precedent ones because of the very high accuracy of the optical frequency measurements. The 31 kHz uncertainty is due to the optical frequency measurements (15 kHz) and, mainly, to the measurement of the $2S_{1/2}$ Lamb shift (27 kHz). In a second method, we can avoid this limitation by using the $1/n^3$ scaling law of the Lamb shift. The values obtained by this way are slightly more precise (see the third part of Tab. 21). Moreover, this method provides the $2S_{1/2}$ Lamb shift and is reliable in the case of deuterium. Finally, we give the result of the general

Table 22. Determination of the $1S_{1/2}$ Lamb shift in deuterium.

method and transitions involved	equations	$L_D(1S_{1/2})$ (MHz)
comparison of transition frequencies lying in a ratio 4:1		
$1S-2S$, $2S-4S/D$ and theoretical value of $L_D(2S_{1/2})$ [42]		8 183.807(78)
comparison of the $1S-2S$ and $2S-nD$ frequencies using the $1/n^3$ scaling law		
$2S-8S/D$, $2S-12D$, $1S-2S$ and $1/n^3$ law in deuterium	(37, 38, 41, 42)	8 183.968(31)
$2S-8S/D$, $2S-12D$, $1S-2S$ and $1/n^3$ law in hydrogen and deuterium	(36–38, 41, 42)	8 183.967(26)
general least squares adjustment in hydrogen and deuterium		
$2S-2P$, $2S-8S/D$, $2S-12D$, $1S-2S$ and $1/n^3$ law	(36–44)	8 183.970(22)

Table 23. Determination of the $2S_{1/2}$ Lamb shift in hydrogen.

method and transitions involved	equations	$\nu_H(2S_{1/2}-2P_{1/2})$ (MHz)
direct measurement of the $2S_{1/2}-2P_{1/2}$ splitting		
$2S_{1/2}-2P_{1/2}$, Newton <i>et al.</i> [77]		1 057.862(20)
$2S_{1/2}-2P_{1/2}$, Lundeen <i>et al.</i> [61]		1 057.845(9)
$2S_{1/2}-2P_{3/2}$, Hagley <i>et al.</i> [62, 63]		1 057.842(12)
$2S-2P$, Wijngaarden <i>et al.</i> [64]		1 057.852(15)
comparison of transition frequencies lying in a ratio 4:1		
$1S-3S$, $2S-6S/D$ and $1/n^3$ scaling law	(36, 39)	1 057.841(10)
$1S-2S$, $2S-4S/D$ and $1/n^3$ scaling law	(36, 43)	1 057.857(12)
$1S-2S$, $2S-4P$ and $1/n^3$ scaling law	(36, 44)	1 057.842(11)
comparison of the $1S-2S$ and $2S-nD$ frequencies using the $1/n^3$ scaling law		
$2S-8S/D$, $2S-12D$, $1S-2S$ and $1/n^3$ law in hydrogen	(36, 38, 41)	1 057.8446(42)
$2S-8S/D$, $2S-12D$, $1S-2S$ and $1/n^3$ law in hydrogen and deuterium	(36–38, 41, 42)	1 057.8447(34)
general least squares adjustment in hydrogen and deuterium		
$2S-2P$, $2S-8S/D$, $2S-12D$, $1S-2S$ and $1/n^3$ law	(36–44)	1 057.8450(29)
theory $r_p = 0.862(12)$ fm [56]		1 057.836(6)
theory $r_p = 0.805(11)$ fm [56]		1 057.812(6)

adjustment ($L_H(1S_{1/2}) = 8 172.840(22)$ MHz) with a relative uncertainty of 2.7×10^{-6} .

Table 22 gives the results for the $1S_{1/2}$ Lamb shift in deuterium. First, we recall the value of reference [42] which was obtained by comparison of the $1S-2S$ and $2S-4S/D$ frequencies, but which used the theoretical value of the $2S_{1/2}$ Lamb shift. Afterwards, we give the results of the comparison of the $1S-2S$ and $2S-nD$ frequencies and we conclude with the general least square adjustment in hydrogen and deuterium. This last value ($L_D(1S_{1/2}) = 8 183.970(22)$ MHz) has the same uncertainty as that for hydrogen.

Several values of the $2S_{1/2}$ Lamb shift in hydrogen and deuterium are given in Tables 23 and 24. The first part of these tables displays the determinations deduced from the $2S-2P$ splitting by microwave spectroscopy or by level crossing or anisotropy methods [61, 62, 64, 77, 78]. For hydrogen, the combination of the equations (43, 44, 45) with the $1/n^3$ scaling law of the Lamb shift (Eq. (36)) yields three determinations of the $2S_{1/2}$ Lamb shift (second part of Tab. 23) with a precision equivalent to that

of the direct measurements. For deuterium, a first value of the $2S_{1/2}$ Lamb shift is deduced from the isotope shift of the $2S_{1/2}-8D_{5/2}$ and $2S_{1/2}-12D_{5/2}$ transitions. These isotope shifts are mainly a mass effect. Thanks to the precise determination of the mass ratios m_p/m_e and m_d/m_p , the uncertainty in the mass effect is only 0.5 kHz. Then, from these isotope shifts, we deduce the difference between the $2S_{1/2}$ Lamb shift in deuterium and hydrogen. By using the experimental value of the $2S_{1/2}$ Lamb shift in hydrogen, we obtain finally the $2S_{1/2}$ Lamb shift in deuterium (second part of Tab. 24). To obtain the $2S_{1/2}-2P_{1/2}$ splitting, we use the theoretical value of the $2P_{1/2}$ Lamb shift ($L_D(2P_{1/2}) = -12.8350(3)$ MHz). These results are in very good agreement with the first measurement of Coseens [78].

Next we give the values deduced from the $1S-2S$ and $2S-nD$ optical frequency measurements. These results for the $2S_{1/2}$ Lamb shift ($L_H(2S_{1/2}) = 1 057.8447(34)$ MHz and $L_D(2S_{1/2}) = 1 059.2338(34)$ MHz) are independent and more precise than the direct determinations made by microwave spectroscopy. Lastly, we make

Table 24. Determination of the $2S_{1/2}$ Lamb shift in deuterium.

method and transitions involved	equations	$\nu_D(2S_{1/2}-2P_{1/2})$ (MHz)
direct measurement of the $2S_{1/2}-2P_{1/2}$ splitting $2S_{1/2}-2P_{1/2}$, Cossens [78]		1 059.240(33)
determination from the $2S_{1/2}-nD_{5/2}$ isotope shift 2S-2P in H and 2S-8S/D in H and D 2S-2P in H and 2S-12D in H and D 2S-2P in H, 2S-8S/D and 2S-12D in H and D	(38, 40)	1 059.234(10) 1 059.235(11) 1 059.234(8)
comparison of the 1S-2S and 2S- nD frequencies using the $1/n^3$ scaling law 2S-8S/D, 2S-12D, 1S-2S and $1/n^3$ law in deuterium 2S-8S/D, 2S-12D, 1S-2S and $1/n^3$ law in hydrogen and deuterium	(37, 38, 41, 42)	1 059.234(4) 1 059.2338(34)
general least squares adjustment in hydrogen and deuterium 2S-2P, 2S-8S/D, 2S-12D, 1S-2S and $1/n^3$ law	(36-44)	1 059.2341(29)

an average of all these determinations: the results ($L_H(2S_{1/2}) = 1 057.8450(29)$ MHz and $L_D(2S_{1/2}) = 1 059.2341(29)$ MHz), with an uncertainty of 2.9 kHz, are the most precise to date.

For hydrogen, we compare the values of the $1S_{1/2}$ and $2S_{1/2}$ Lamb shift with theory [56] (see Tabs. 21 and 23). There is a large discrepancy, which varies from 2.4 to 5.6 standard deviations according to which value of the proton charge radius one adopts ($r_p = 0.862(12)$ fm [41] or $r_p = 0.805(11)$ fm [58]). This discrepancy is perhaps due to the calculation of the two-loop corrections [57]. Conversely, if we believe the calculations of the reference [56], we can deduce the radius of the proton charge distribution $r_p = 0.901(16)$ fm.

6.4 Proton-to-electron mass ratio

In a first approximation, the isotope shift of an optical transition is proportional to $(m_e/m_p)(1 - m_p/m_d)cR_\infty$. Since the deuteron-to-proton mass ratio is known with a high accuracy (relative uncertainty of 7×10^{-10}), we could deduce the proton-to-electron mass ratio from the value of the isotope shift. In actual fact, this method is not reliable, because the corrections due to the charge distribution of the proton and deuteron are not well known. To avoid this difficulty, we consider the isotope shift Δ_{H-D} on the linear frequency combination $7\nu(2S_{1/2}-nD_{5/2}) - \nu(1S_{1/2}-2S_{1/2})$, where the Lamb shifts are eliminated using equations (36, 37). From the measurements of the $1S_{1/2}-2S_{1/2}$, $2S_{1/2}-8D_{5/2}$ and $2S_{1/2}-12D_{5/2}$ frequencies, we deduce the values:

$$\Delta_{H-D}(n = 8) = 796\,844.536(50) \text{ MHz}$$

$$\Delta_{H-D}(n = 12) = 851\,208.619(59) \text{ MHz}$$

where the uncertainties are mainly due to the measurements of the $2S_{1/2}-nD_{5/2}$ frequencies.

To sum up, we can obtain two independent values of the proton-to-electron mass ratio which are given

Table 25. Determination of the proton-to-electron mass ratio.

	m_p/m_e	relative uncertainty
van Dyck <i>et al.</i> [79]	1 836.152 701(37)	2×10^{-8}
Garreau <i>et al.</i> [12]	1 836.152 59(24)	1.3×10^{-7}
Gabrielse <i>et al.</i> [80]	1 836.152 680(88)	4.8×10^{-8}
Farnham <i>et al.</i> [68]	1 836.152 6665(40)	2.2×10^{-9}
this work		
$\Delta_{H-D}(n = 8)$	1 836.152 668(115)	6.3×10^{-8}
$\Delta_{H-D}(n = 12)$	1 836.152 666(128)	7×10^{-8}
weighted mean	1 836.152 667(85)	4.6×10^{-8}

in Table 25. The weighted mean value is $m_p/m_e = 1 836.152 667(85)$ with a relative uncertainty of 4.6×10^{-8} . This value is in perfect agreement with the far more precise determination of Farnham *et al.* [68], and also with other previous measurements [12, 79, 80] (see Tab. 25).

7 Conclusion

Thanks to a detailed analysis of the lineshapes of the $2S-nS/D$ transitions, we have obtained more reliable values of the $1S_{1/2}$ Lamb shift and of the $2S_{1/2}-nS_{1/2}$, $-nD_J$ frequencies. These results have been analyzed with a least squares procedure, by taking into account several precise measurements from other groups. If we do not use the $1/n^3$ scaling law for the Lamb shift, the relative uncertainties in the Rydberg constant and the $1S_{1/2}$ Lamb shift are 10^{-11} and 3.8×10^{-6} respectively. In this case, the accuracy is limited mainly by the uncertainty in the $2S_{1/2}$ Lamb shift. To avoid this problem, we make theoretical assumptions concerning the Lamb shift. By using the $1/n^3$ scaling law between the $1S_{1/2}$ and $2S_{1/2}$ Lamb shifts, the very precise optical frequency measurements reduce the uncertainties to 9.1×10^{-12} and 3.2×10^{-6} for R_∞ and the Lamb shifts. By this means, we obtain a value of the $2S_{1/2}$ Lamb shift which is about 2.6 times more precise than the direct microwave measurement. Moreover, the same method can

be applied to deuterium. Finally, we average these different results to reduce the uncertainties in R_∞ and in the Lamb shifts to 7.7×10^{-12} and 2.7×10^{-6} . The precision is now limited by the uncertainties in the 2S–nS/D frequencies, which, in our experiment, are mainly due to the light shifts. To obtain more accurate values of these frequencies, a first possibility is to use ultracold hydrogen to increase the interaction time and decrease the light shifts [81]. In our group, we intend to measure the optical frequency of the 1S–3S transition. In this case, as the number of atoms in the 1S atomic beam is about 10^8 times larger than in the metastable atomic beam, we can observe the transition with a very small light power and, consequently, with negligible light shifts. For this experiment, we plan to compensate the second-order Doppler effect using a magnetic field perpendicular to the atomic beam [82]. As a last word, we note that a new determination of the proton radius r_p is highly desirable. The future measurement of r_p , being prepared at the Paul Scherrer Institute by spectroscopy of muonic hydrogen, should provide the opportunity to test even further the theoretical calculations of the Lamb shift [83].

The authors thank S. Bourzeix, M.D. Plimmer, F. de Tomasi and D.N. Stacey for their essential contribution to the first step of the 1S–3S experiment. They are indebted to B. Cagnac for many stimulating discussions as well as his constant interest in these projects. They thank also M. Pinard for fruitful discussions on the calculation of the theoretical line shape and D. Delande for his help in the use of the Sturmian functions and the calculation of several matrix elements of the two-photon and light shift operators. Finally, they thank again M.D. Plimmer for critical reading of manuscript. This work was partially supported by the Bureau National de Métrologie, by the Direction des Recherches et Études Techniques and by the European Community (SCIENCE cooperation Contract No. SCI*-CT92-0816 and network Contract No. CHRX-CT93-0105).

References

1. B. Cagnac, M.D. Plimmer, L. Julien, F. Biraben, Rep. Prog. Phys. **57**, 853 (1994).
2. Th. Udem, H. Huber, B. Gross, J. Reichert, M. Prevedelli, M. Weitz, T.W. Hänsch, Phys. Rev. Lett. **79**, 2646 (1997); note added in proof: a more accurate result has been recently published: J. Reichert, M. Niering, R. Holwarth, M. Weitz, Th. Udem, T.W. Hänsch, Phys. Rev. Lett. **84**, 3232 (2000).
3. A. Huber, Th. Udem, B. Gross, J. Reichert, M. Kourogi, K. Pachucki, M. Weitz, T.W. Hänsch, Phys. Rev. Lett. **80**, 468 (1998).
4. F. Nez, M.D. Plimmer, S. Bourzeix, L. Julien, F. Biraben, R. Felder, O. Acef, J.J. Zondy, P. Laurent, A. Clairon, M. Abed, Y. Millerioux, P. Juncar, Phys. Rev. Lett. **69**, 2326 (1992).
5. F. Nez, M.D. Plimmer, S. Bourzeix, L. Julien, F. Biraben, R. Felder, Y. Millerioux, P. de Natale, Europhys. Lett. **24**, 635 (1993).
6. B. de Beauvoir, F. Nez, L. Julien, B. Cagnac, F. Biraben, D. Touahri, L. Hilico, O. Acef, A. Clairon, J.J. Zondy, Phys. Rev. Lett. **78**, 440 (1997).
7. D. Touahri, O. Acef, A. Clairon, J.J. Zondy, R. Felder, L. Hilico, B. de Beauvoir, F. Biraben, F. Nez, Opt. Commun. **133**, 471 (1997).
8. C. Schwob, L. Jozefowski, B. de Beauvoir, L. Hilico, F. Nez, L. Julien, F. Biraben, O. Acef, A. Clairon, Phys. Rev. Lett. **82**, 4960 (1999).
9. S. Bourzeix, B. de Beauvoir, F. Nez, M.D. Plimmer, F. de Tomasi, L. Julien, F. Biraben, D.N. Stacey, Phys. Rev. Lett. **76**, 384 (1996).
10. J.C. Garreau, M. Allegrini, L. Julien, F. Biraben, J. Phys. France **51**, 2263 (1990).
11. J.C. Garreau, M. Allegrini, L. Julien, F. Biraben, J. Phys. France **51**, 2275 (1990).
12. J.C. Garreau, M. Allegrini, L. Julien, F. Biraben, J. Phys. France **51**, 2293 (1990).
13. S. Bourzeix, M.D. Plimmer, F. Nez, L. Julien, F. Biraben, Opt. Commun. **99**, 89 (1993).
14. R.W.P. Drever, J.L. Hall, F.V. Kowalski, J. Hough, G.M. Ford, A.J. Munley, H. Ward, Appl. Phys. B **31**, 97 (1983).
15. F. Nez, Thèse de doctorat de l'université Pierre et Marie Curie, Paris, 1993.
16. F. Biraben, J.C. Garreau, L. Julien, M. Allegrini, Rev. Sci. Instrum. **61**, 1468 (1990).
17. T.W. Hänsch, B. Couillaud, Opt. Commun. **41**, 441 (1980).
18. B. Cagnac, G. Grynberg, F. Biraben, J. Phys. France **34**, 845 (1973).
19. D. Delande, private communication.
20. H.A. Bethe, E.E. Salpeter, in *Quantum mechanics of one- and two-electron atoms* (Springer-Verlag, Berlin, 1957).
21. W.J. Karzas, R. Latter, Astrophys. J. Suppl. Ser. **6**, 167 (1961).
22. G. Grynberg, B. Cagnac, F. Biraben, in *Coherent Nonlinear Optics*, edited by M.S. Feld, V.S. Letokhov (Springer-Verlag, 1980).
23. F. Biraben, M. Bassini, B. Cagnac, J. Phys. France **40**, 445 (1979).
24. J.W. Farley, W.H. Wing, Phys. Rev. A **23**, 2397 (1981).
25. B. de Beauvoir, Thèse de doctorat de l'université Pierre et Marie Curie, Paris, 1996.
26. Y. Millerioux, D. Touahri, L. Hilico, A. Clairon, R. Felder, F. Biraben, B. de Beauvoir, Opt. Commun. **103**, 91 (1994).
27. L. Hilico, R. Felder, D. Touahri, O. Acef, A. Clairon, F. Biraben, Eur. Phys. J. AP **4**, 219 (1998).
28. B. de Beauvoir, F. Nez, L. Hilico, L. Julien, F. Biraben, B. Cagnac, J.J. Zondy, D. Touahri, O. Acef, A. Clairon, Eur. Phys. J. D **1**, 227 (1998).
29. A. Clairon, B. Dahmani, A. Filimon, J. Rutman, IEEE Trans. Inst. Meas. **IM34**, 265 (1985).
30. A. Clairon, B. Dahmani, O. Acef, M. Granveaud, Y.S. Dominin, S.B. Pouchkine, V.M. Tatarenkov, R. Felder, Metrologia **25**, 9 (1988).
31. G.D. Rovera, O. Acef, IEEE Trans. Inst. Meas. **48**, 571 (1999).
32. F. Nez, M.D. Plimmer, S. Bourzeix, L. Julien, F. Biraben, R. Felder, Y. Millerioux, P. de Natale, IEEE Trans. Inst. Meas. **44**, 568 (1995).
33. O. Acef, J.J. Zondy, M. Abed, G.D. Rovera, A.H. Gerard, A. Clairon, P. Laurent, Y. Millerioux, P. Juncar, Opt. Commun. **97**, 29 (1993).
34. F. Nez, F. Biraben, R. Felder, Y. Millerioux, Opt. Commun. **102**, 432 (1993).

35. R. Felder, D. Touahri, O. Acef, L. Hilico, J.J. Zondy, A. Clairon, B. de Beauvoir, F. Biraben, F. Nez, L. Julien, Y. Millerioux, Proc. SPIE **2378**, 52 (1995).
36. J.W. Heberle, H.A. Reich, P. Kusch, Phys. Rev. **101**, 612 (1956).
37. G.W.F. Drake, R.A. Swainson, Phys. Rev. A **41**, 1243 (1990).
38. J.R. Sapirstein, D.R. Yennie, in *Quantum Electrodynamics*, edited by T. Kinoshita (World Scientific, Singapore, 1990).
39. P.J. Mohr, in *Atomic, Molecular and Optical Physics Handbook*, edited by G.W.F. Drake (AIP, New-York, 1996).
40. K. Pachucki, D. Leibfreid, M. Weitz, A. Huber, W. König, T.W. Hänsch, J. Phys. B **29**, 177 (1996).
41. G.G. Simon, C. Schmitt, F. Borkovski, V.H. Walther, Nucl. Phys. A **333**, 381 (1980).
42. M. Weitz, A. Huber, F. Schmidt-Kaler, D. Leibfreid, W. Vassen, C. Zimmermann, K. Pachucki, T.W. Hänsch, L. Julien, F. Biraben, Phys. Rev. A **52**, 2664 (1995).
43. H.A. Reich, J.W. Heberle, P. Kusch, Phys. Rev. **104**, 1585 (1956).
44. P.J. Mohr, B.N. Taylor, Rev. Mod. Phys. **72** (to be published, 2000).
45. C. Schwob, L. Jozefowski, O. Acef, L. Hilico, B. de Beauvoir, F. Nez, L. Julien, A. Clairon, F. Biraben, IEEE Trans. Inst. Meas. **48**, 178 (1999).
46. H.R. Telle, D. Meschede, T.W. Hänsch, Opt. Lett. **15**, 532 (1990).
47. T.W. Hänsch, S.A. Lee, R. Wallenstein, C. Wieman, Phys. Rev. Lett. **34**, 307 (1975).
48. M.G. Boshier, P.E.G. Baird, C.J. Foot, E.A. Hinds, M.D. Plimmer, D.N. Stacey, J.B. Swan, D.A. Tate, D.M. Warrington, G.K. Woodgate, Nature **330**, 463 (1987); Phys. Rev. A **40**, 6169 (1989).
49. M. Weitz, A. Huber, F. Schmidt-Kaler, D. Leibfreid, T.W. Hänsch, Phys. Rev. Lett. **72**, 328 (1994).
50. D.J. Berkeland, E.A. Hinds, M.G. Boshier, Phys. Rev. Lett. **75**, 2470 (1995).
51. S. Bourzeix, B. de Beauvoir, F. Nez, F. de Tomasi, L. Julien, F. Biraben, Opt. Commun. **133**, 239 (1997).
52. K.C. Harvey, C. Fehrenbach, Rev. Sci. Instrum. **54**, 1117 (1983).
53. Y. Gontier, M. Trahin, Phys. Lett. A **36**, 463 (1971).
54. U.D. Jentschura, P.J. Mohr, G. Soff, Phys. Rev. Lett. **82**, 53 (1999).
55. K. Pachucki, Phys. Rev. Lett. **72**, 3154 (1994).
56. S. Mallampalli, J. Sapirstein, Phys. Rev. Lett. **80**, 5297 (1998).
57. I. Goidenko, L. Labzowsky, A. Nefiodov, G. Plunien, G. Soff, Phys. Rev. Lett. **83**, 2312 (1999).
58. L.N. Hand, D.J. Miller, R. Wilson, Rev. Mod. Phys. **35**, 335 (1963).
59. S.G. Karshenboim, J. Phys. B **29**, L29 (1996); Z. Phys. D **39**, 109 (1997).
60. W.E. Lamb, R.C. Rutherford, Phys. Rev. **72**, 241 (1947).
61. S.R. Lundeen, F.M. Pipkin, Phys. Rev. Lett. **46**, 232 (1981).
62. E.W. Hagley, F.M. Pipkin, Phys. Rev. Lett. **72**, 1172 (1994).
63. U. Jentschura, K. Pachucki, Phys. Rev. A **54**, 1853 (1996).
64. A. van Wijngaarden, F. Holuj, G.F.W. Drake, Can. J. Phys. **76**, 95 (1998).
65. V.G. Pal'chikov, Y.L. Sokolov, V.P. Yakovlev, Metrologia **21**, 99 (1985); Phys. Scripta **55**, 33 (1997).
66. V.G. Pal'chikov, Y.L. Sokolov, V.P. Yakovlev, Sov. Phys. JETP Lett. **38**, 419 (1983).
67. S.G. Karshenboim, Sov. Phys. JETP **79**, 230 (1994).
68. D.L. Farnham, R.S. van Dyck Jr, P.B. Schwinberg, Phys. Rev. Lett. **75**, 3598 (1995).
69. G. Audi, A.H. Wapstra, Nucl. Phys. A **565**, 1 (1993).
70. E.R. Cohen, B.N. Taylor, Rev. Mod. Phys. **59**, 1121 (1987).
71. F. Biraben, J.C. Garreau, L. Julien, Europhys. Lett. **2**, 925 (1986).
72. P. Zhao, W. Lichten, H.P. Layer, J.C. Bergquist, Phys. Rev. A **34**, 5138 (1986).
73. P. Zhao, W. Lichten, H.P. Layer, J.C. Bergquist, Phys. Rev. Lett. **58**, 1293 (1987).
74. D.H. Mc Intyre, R.G. Beausoleil, C.J. Foot, E.A. Hildum, B. Couillaud, T.W. Hänsch, Phys. Rev. A **39**, 4591 (1989).
75. F. Biraben, J.C. Garreau, L. Julien, M. Allegrini, Phys. Rev. Lett. **62**, 621 (1989).
76. T. Andreae, W. König, R. Wynands, D. Leibfried, F. Schmidt-Kaler, C. Zimmermann, D. Meschede, T.W. Hänsch, Phys. Rev. Lett. **69**, 1923 (1992).
77. G. Newton, D.A. Andrews, P.J. Unsworth, Philos. Trans. R. Soc. Lond. **290**, 373 (1979).
78. B.L. Cosen, Phys. Rev. **173**, 49 (1968).
79. R.S. van Dyck, F.L. Moore, D.L. Farnham, P.B. Schwinberg, Bull. Am. Phys. Soc. **31**, 244 (1986).
80. G. Gabrielse, X. Fei, L.A. Orozco, R.L. Tjoelker, J. Haas, H. Kalinowsky, T.A. Trainor, W. Kells, Phys. Rev. Lett. **65**, 1317 (1990).
81. C.L. Cesar, D.G. Fried, T.C. Killian, A.D. Polcyn, J.C. Sandberg, I.A. Yu, T.J. Greytak, D. Kleppner, J.M. Doyle, Phys. Rev. Lett. **77**, 255 (1996).
82. F. Biraben, L. Julien, J. Plon, F. Nez, Europhys. Lett. **15**, 831 (1991).
83. D. Taqqu, F. Biraben, C.A.N. Conde, T.W. Hänsch, F.J. Hartmann, P. Hauser, P. Indelicato, P. Knowles, F. Kottmann, F. Mulhauser, C. Petitjean, R. Pohl, P. Rabinowitz, R. Rosenfelder, J.M.F. Santos, W. Schott, L.M. Simons, J. Veloso, Hyperfine Interact. **119**, 311 (1999).

Chapitre 4

Oscillations de Bloch et détermination de la constante de structure fine

4.1 Introduction

En 1999, mettant à profit une expérience préliminaire réalisée dans le groupe de Christophe Salomon au LKB [45], l'équipe de Métrologie des Systèmes Simples se lance dans la mesure de haute précision de la constante de structure fine.

La constante de structure fine α , qui caractérise l'amplitude du couplage électromagnétique, a initialement été introduite par Sommerfeld dans le cas de l'atome d'hydrogène de la façon suivante : l'énergie d'ionisation de l'atome d'hydrogène, donnée par la constante de Rydberg, est égale à l'énergie cinétique d'un électron se déplaçant à la vitesse αc . Soit,

$$hcR_\infty = \frac{1}{2}m(\alpha c)^2 \quad (4.1)$$

où h est la constante de Planck, c la vitesse de la lumière dans le vide, R_∞ la constante de Rydberg et m la masse de l'électron.

En introduisant $A_r(e)$ la masse relative de l'électron et $A_r(X)$ celle de la particule X de masse m_X dans l'expression (4.1), on obtient :

$$\alpha^2 = \frac{2R_\infty}{c} \frac{A_r(X)}{A_r(e)} \frac{h}{m_X} \quad (4.2)$$

La relation (4.2) est le point de départ de notre expérience : nous mesurons h/m_X , m_X étant la masse de l'atome de rubidium. Actuellement, les grandeurs R_∞ , $A_r(e)$ et

$A_r(X)$ étant connues avec de très faibles incertitudes relatives, c'est la précision sur le rapport $\frac{h}{m_X}$ qui limite la précision sur α (7×10^{-12} pour R_∞ [46] [43], $4,4 \times 10^{-10}$ pour $A_r(e)$ [47] et moins de $2,0 \times 10^{-10}$ pour $A_r(Cs)$ et $A_r(Rb)$ [48]).

Notre objectif est de déterminer ce rapport à partir de la mesure de la vitesse de recul qu'acquiert un atome lorsqu'il absorbe un photon de vecteur d'onde k ($v_r = \frac{\hbar k}{m_X}$).

4.1.1 Le contexte

La constante de structure fine apparaît dans de nombreux domaines de la physique et a été, à ce titre, déterminée par différentes méthodes sur lesquelles je reviendrai brièvement dans le paragraphe suivant. En 1999, l'état des lieux des différentes déterminations de α avait été établi par le CODATA 98 (voir figure (4.1)). L'importante dispersion des mesures, de l'ordre de 10^{-7} , a motivé le développement de notre expérience. Entre les deux ajustements réalisés en 98 et en 2002 par le CODATA [49] [50],

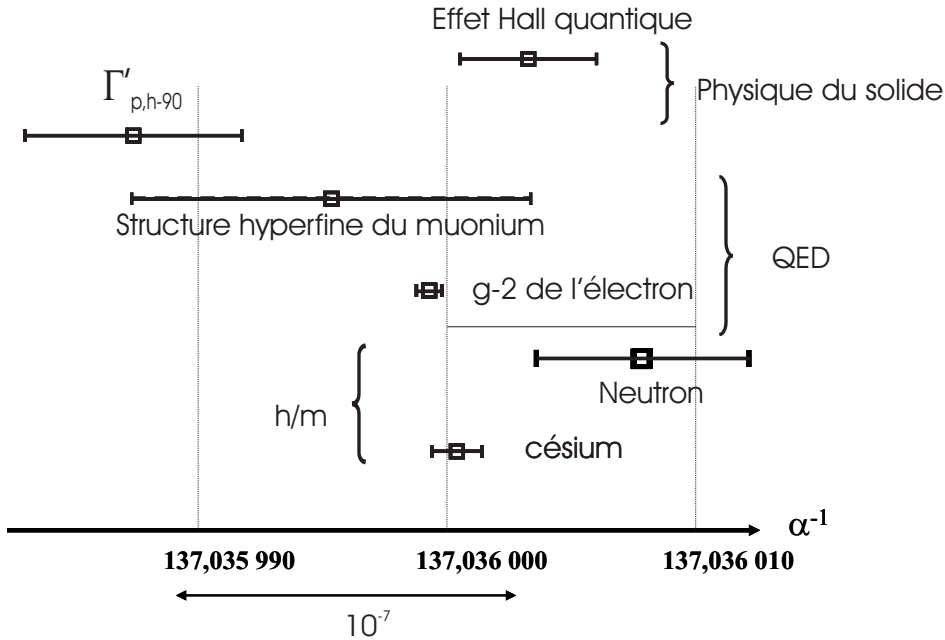


FIG. 4.1 – Les différentes déterminations de α (CODATA 98).

la situation a bien évolué, réduisant la dispersion des valeurs comme le montre la figure (4.2). Cependant, la valeur recommandée étant calculée à partir d'un ajustement du type moindres carrés, seules les déterminations entachées d'une très faible incertitude relative contribuent. Actuellement, la valeur recommandée de α est déduite de deux mesures : du rapport $\frac{h}{m_{Cs}}$ [51] et, principalement, de l'anomalie du moment gyromagnetic

gnétique de l'électron [52]. Il est à noter que cette dernière valeur diffère de celle du CODATA 98 à cause d'une erreur décelée dans les calculs des termes QED.

L'équipe de S. Chu annonce une mesure encore plus précise de $\frac{h}{m(Cs)}$ dans un futur proche [53]. D'autre part, le groupe de G. Gabrielse ayant très récemment publié une nouvelle détermination du $g - 2$ de l'électron à 0,7 ppb [54], cette dernière valeur sera prépondérante lors du prochain ajustement. C'est pourquoi il paraît indispensable de disposer d'autres déterminations de α , peu dépendantes de la QED, avec des incertitudes suffisamment faibles pour être prises en compte de façon significative dans l'ajustement.

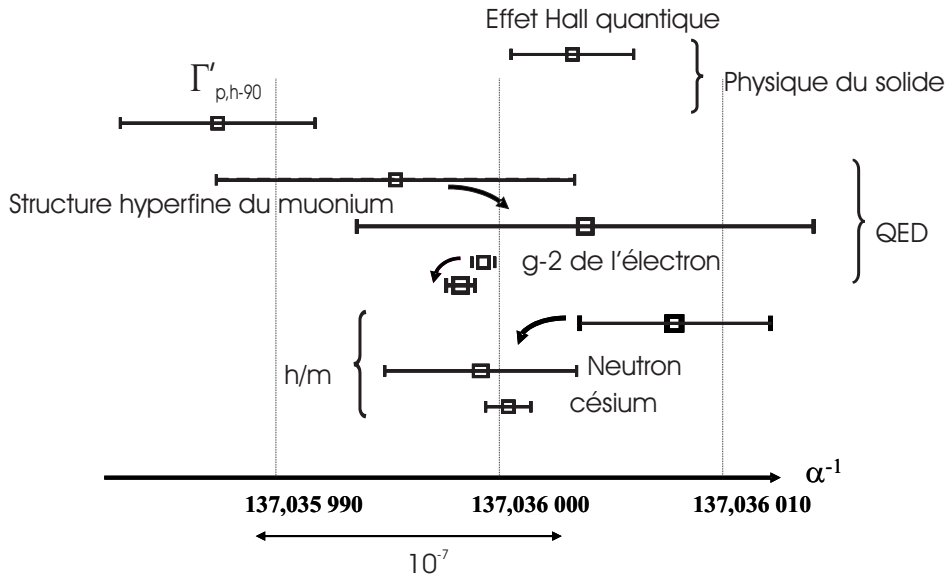


FIG. 4.2 – Les différentes déterminations de α : évolution entre le CODATA 98 et le CODATA 02.

4.1.2 Les différentes déterminations de α

L'anomalie du moment gyromagnétique de l'électron

L'anomalie du moment gyromagnétique de l'électron a_e traduit la correction à la théorie de Dirac due à l'électrodynamique quantique. Elle introduit une différence entre la vitesse angulaire de précession du spin de l'électron autour d'un champ magnétique ($\omega_{spin} = |\gamma|B$ où γ est le facteur gyromagnétique et B le champ magnétique) et la vitesse angulaire orbitale de l'électron soumis à ce champ ($\omega_{orb} = \frac{eB}{m}$ où e est la charge

et m la masse de l'électron) :

$$a_e = \frac{g - 2}{2} = \frac{\omega_{spin}}{\omega_{orb}} - 1 \quad (4.3)$$

où g est le facteur de Landé de l'électron. La théorie de Dirac prévoit $g = 2$.

a_e se développe en puissance de $\frac{\alpha}{\pi}$ en sommant des diagrammes de Feynman. Le dernier terme calculé numériquement est le terme d'ordre 4 qui fait intervenir 891 diagrammes. La constante de structure fine est alors obtenue à partir de ce développement et de la mesure de a_e . C'est une erreur décelée dans un diagramme qui explique le décalage de la valeur du $g - 2$ entre le CODATA de 98 et celui de 02 [55].

La mesure de a_e est réalisée à partir d'électrons piégés dans un piège de Penning et soumis à un champ magnétique de plusieurs teslas. Les mesures des vitesses angulaires orbitale et de précession du spin sont des mesures de fréquences et, de ce fait, potentiellement très précises.

L'incertitude relative sur α est de $3,8 \times 10^{-9}$ pour l'expérience menée à l'Université de Washington (CODATA 98 et 02) [52] et de $0,7 \times 10^{-9}$ pour celle de Harvard [54].

La structure hyperfine du muonium

L'autre méthode de détermination de la constante de structure fine dépendant de la QED est basée sur la mesure de la structure hyperfine du muonium. Le muonium est un atome d'hydrogène dans lequel le proton a été remplacé par un muon μ^+ .

L'expression théorique de la structure hyperfine du muonium s'exprime de la façon suivante :

$$\Delta\nu_{Mu} = \frac{16}{3}cR_\infty\alpha^2\frac{m}{m_\mu}(1 + \frac{m}{m_\mu})^{-3}f(\alpha, \frac{m}{m_\mu}) \quad (4.4)$$

où m est la masse de l'électron, m_μ celle du muon et $f(\alpha, \frac{m}{m_\mu})$ une fonction qui représente les corrections QED et qui dépend faiblement de α et de $\frac{m}{m_\mu}$.

La structure hyperfine du muonium est obtenue par la détection de résonances magnétiques en spectroscopie micro-onde à Los Alamos [56]. Pour en déduire une valeur de α , il est nécessaire de déterminer le rapport $\frac{m}{m_\mu}$ en le mesurant sur une autre transition du muonium. L'incertitude sur α obtenue par cette méthode est de $5,8 \times 10^{-8}$. On remarque sur la figure (4.2) que la valeur publiée a bougé entre les CODATA 98 et 02. Ceci s'explique par la révision des calculs des corrections QED.

Il est à noter qu'une mesure du même type avec l'atome d'hydrogène serait beaucoup moins précise. Ceci est dû au fait que le proton, contrairement au muon, n'est pas une particule élémentaire. Il faudrait prendre en compte sa distribution de charge et de moment magnétique, quantités mal connues.

L'effet Hall quantique

Les deux déterminations de α que je vais mentionner à présent, sont issues de la physique du solide.

L'effet Hall quantique est caractérisé par la constante de von Klitzing R_K qui s'exprime de la façon suivante :

$$R_K = \frac{h}{e^2} = \frac{\mu_0 c}{2\alpha} \quad (4.5)$$

La mesure de R_K est issue de celle d'une chaîne d'impédances, avec comme source primaire un condensateur calculable.

Une moyenne réalisée sur l'ensemble des mesures de R_K publiées dans différents laboratoires conduit à une incertitude relative de $1,8 \times 10^{-8}$ sur α [57], [58], [59], [60].

Le moment gyromagnétique du proton et l'effet Josephson

Cette méthode est basée sur la mesure du rapport gyromagnétique du proton γ_p ou plus précisément du rapport $\frac{\gamma_p}{K_J R_K}$ (où K_J est la constante de Josephson).

γ_p s'écrit en fonction du rapport gyromagnétique de l'électron γ_e :

$$\gamma_p = \frac{\mu_p}{\mu_e} \gamma_e = \frac{\mu_p g}{\mu_e 2m} e \quad (4.6)$$

où μ_p et μ_e sont respectivement les moments magnétiques du proton et de l'électron, g le facteur de Landé de l'électron et m sa masse.

En utilisant les expressions de R_K et K_J : $R_K = \frac{h}{e^2}$ et $K_J = \frac{2e}{h}$, on obtient

$$\frac{\gamma_p}{K_J R_K} = \frac{\mu_p g}{\mu_e 4m} e^2 \quad (4.7)$$

A partir des expressions de α , $\alpha = \frac{e^2}{4\pi\epsilon_0\hbar c}$ et $\alpha^2 = \frac{2hR_\infty}{mc}$, on peut relier la constante de structure fine au rapport $\frac{\gamma_p}{K_J R_K}$.

$$\frac{\gamma_p}{K_J R_K} = \frac{\mu_p g}{\mu_e 4} \frac{\alpha^3}{\mu_0 R_\infty} \quad (4.8)$$

La détermination du rapport gyromagnétique du proton est basée sur la mesure de la fréquence de précession du spin. Il est donc nécessaire de connaître précisément le champ magnétique B . Dans la configuration expérimentale de la mesure la plus précise, le champ magnétique est créé à partir d'un solénoïde parcouru par un courant I . Ce courant est mesuré à partir d'un étalon de tension (effet Josephson) et d'un étalon de résistance (effet Hall quantique).

Dans cette expérience, l'incertitude obtenue sur le rapport $\frac{\gamma_p}{K_J R_K}$ est de $1,1 \times 10^{-8}$ [61]. En reportant les incertitudes relatives des différentes grandeurs apparaissant dans l'expression (4.8) (10^{-8} sur $\frac{\mu_p}{\mu_e}$, 4×10^{-12} sur g et 7×10^{-12} sur R_∞), on obtient finalement une incertitude de $3,1 \times 10^{-8}$ sur la détermination de α par cette méthode.

La mesure du rapport h/m_n

Les méthodes mentionnées ci-après utilisent l'expression de α donnée par l'équation (4.2) et visent donc à mesurer le rapport $\frac{h}{m_X}$ de la particule X .

Historiquement, la première mesure de ce type est basée sur la diffraction de Bragg d'un faisceau de neutrons par un cristal de silicium.

$$\frac{h}{m_n} = \lambda v \quad (4.9)$$

où λ est la longueur d'onde de de Broglie du neutron et v sa vitesse. La vitesse est mesurée par temps de vol et la longueur d'onde de de Broglie à partir de la connaissance de la distance inter-réticulaire du cristal de silicium, donnée qui constitue la principale limitation de cette méthode. L'incertitude obtenue sur α est de $3,4 \times 10^{-8}$ [62].

Le décalage de la valeur de $\frac{h}{m_n}$ entre le CODATA 98 et 02 ([62], [63]) s'explique principalement par une réévaluation de la distance inter-réticulaire [64].

La mesure du rapport h/m_{Cs}

Cette expérience, développée à Stanford dans l'équipe de S. Chu, est proche de la nôtre puisqu'elle consiste à mesurer le rapport h/m où m est la masse de l'atome de césium. Son principe, détaillé dans le paragraphe 4.4, est basé sur la mesure de l'énergie de recul qu'acquiert un atome qui absorbe un photon de vecteur d'onde k ($E_r = \frac{\hbar^2 k^2}{2m_{Cs}}$ où m_{Cs} est la masse de l'atome de césium), ou, plus précisément, sur la mesure du déphasage de la fonction d'onde atomique induit par ce changement d'énergie. Ce déphasage est obtenu en faisant interférer deux trajectoires différentes au sein d'un interféromètre atomique. En mesurant de plus le vecteur d'onde k du photon, on peut en déduire le rapport $\frac{h}{m_{Cs}}$. L'incertitude ainsi obtenue sur α est de $7,7 \times 10^{-9}$ [51].

4.1.3 Le principe de notre mesure

Dans notre expérience, le rapport $\frac{h}{m_{Rb}}$, et donc α sont déduits de la mesure de la vitesse de recul de l'atome de rubidium.

$$v_r = \frac{\hbar k}{m_{Rb}} \quad (4.10)$$

L'effet de recul a été observé pour la première fois sur le dédoublement des raies d'absorption saturée du méthane [65]. Il est de l'ordre de $6 \text{ mm} \cdot \text{s}^{-1}$ dans le cas du rubidium. Pour mesurer de façon précise la vitesse de recul, il faut transférer un grand nombre de fois cette vitesse aux atomes de façon cohérente, c'est-à-dire sans émission spontanée. Nous utilisons pour celà des transitions Raman contra-propageantes appliquées sans changement de niveau atomique interne¹. A chaque transition, l'atome acquiert exactement deux fois la vitesse de recul en absorbant un photon dans une onde et en ré-émettant un photon stimulé dans l'autre onde. Afin qu'il reste à résonance avec les faisceaux, on compense l'effet Doppler en balayant continûment la différence de fréquence entre les deux ondes. Cette méthode a été développée dans l'équipe de C. Salomon [45] et est bien connue en physique du solide sous le nom d'oscillations de Bloch. Elle permet de transférer un grand nombre de reculs de façon très efficace, en un temps très court. Nous avons pu mesurer une efficacité de 99,95% par oscillation.

La valeur du recul est déduite de la mesure de la variation de vitesse induite par l'accélération cohérente. Pour mener à bien l'expérience, il est nécessaire, d'une part de réaliser les oscillations de Bloch sur une classe de vitesses atomiques subrecul préalablement sélectionnée et d'autre part, de pouvoir mesurer la vitesse finale des atomes. Nous réalisons les phases de sélection et de mesure à l'aide de transitions Raman sélectives en vitesse entre les deux sous niveaux hyperfins $F = 1$ et $F = 2$ du fondamental.

En résumé, partant d'atomes froids piégés dans un piège magnéto-optique, suivi d'une phase de mélasse à l'issue de laquelle les atomes sont dans l'état $F=2$, une séquence de l'expérience comporte trois parties (voir figure (4.3)) :

- sélection d'une classe de vitesse subrecul, centrée sur la vitesse nulle au moyen d'une

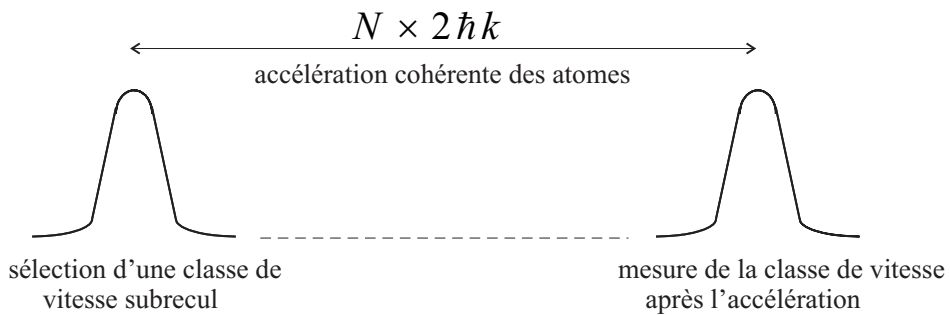


FIG. 4.3 – Principe de l'expérience de mesure de la vitesse de recul de l'atome de rubidium.

transition entre $F=2$ et $F=1$,

¹Ce type de processus a été étudié en détail par Ch.J. Bordé pour expliquer les formes de raie d'absorption saturée [66].

- accélération cohérente des atomes sélectionnés au moyen d'oscillations de Bloch dans l'état $F=1$,

- mesure de la vitesse finale grâce à une transition de $F=1$ vers $F=2$.

On mesure finalement par temps de vol le nombre d'atomes ayant effectué la dernière transition normalisé au nombre d'atomes total. La technique de détection est similaire à celle développée au BNM-SYRTE sur les horloges atomiques [67]. Elle permet de mesurer le nombre d'atomes dans les états $F=1$ et $F=2$ et ainsi d'en déduire la fraction du nombre total d'atomes ayant effectué la dernière transition². Son schéma de principe est représenté sur la figure (4.4). Les atomes en chute libre sont éclairés par un faisceau rétro-réfléchi, polarisé circulairement et résonant avec la transition $F = 2 \rightarrow F' = 3$. Le signal de fluorescence détecté est proportionnel à la fraction d'atomes dans $F=2$. Un cache placé sur la partie basse du faisceau permet de pousser les atomes détectés dans $F=2$. Ceux de $F=1$ continuent de tomber et atteignent une seconde nappe lumineuse où le faisceau résonant avec la transition $F = 2 \rightarrow F' = 3$ est superposé avec un faisceau repompeur, résonant avec $F = 1 \rightarrow F' = 2$. Les atomes de $F=1$ sont donc repompés vers $F=2$, puis détectés comme précédemment.

Cette séquence est reproduite en changeant la fréquence de la transition Raman de

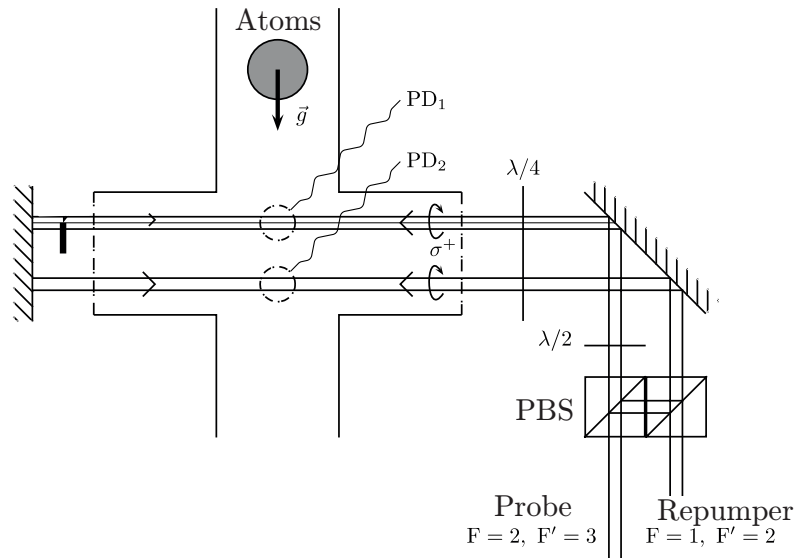


FIG. 4.4 – Schéma de principe de la détection.

²On s'affranchit ainsi des fluctuations du nombre total d'atomes entre les séquences expérimentales successives.

mesure afin de réaliser un spectre correspondant à la distribution finale de vitesse. La vitesse de recul se déduit de la variation de vitesse, soit

$$\Delta v = 2Nv_r = \frac{\delta_{sel} - \delta_{mes}}{k_1 + k_2} \quad (4.11)$$

où Δv est la variation de vitesse, N le nombre d'oscillations de Bloch, δ_{sel} la fréquence centrale de la distribution de vitesse initiale, δ_{mes} celle de la distribution de vitesse finale, k_1 et k_2 les vecteurs d'onde des faisceaux de sélection et de mesure.

Le rapport $\frac{\hbar}{m_{Rb}}$ est obtenu à partir de la conservation de l'impulsion ($m_{Rb}\Delta v = 2N\hbar k_B$ où k_B est le vecteur d'onde du faisceau utilisé pour accélérer les atomes). On a donc finalement :

$$\frac{\hbar}{m_{Rb}} = \frac{\delta_{sel} - \delta_{mes}}{2Nk_B(k_1 + k_2)} \quad (4.12)$$

L'incertitude obtenue sur la vitesse de recul dépend de l'incertitude sur le pointé du centre de la distribution de vitesse finale et du nombre d'oscillations de Bloch réalisées.

$$\sigma_{v_r} = \frac{\sigma_v}{2N} \quad (4.13)$$

4.2 Le dispositif expérimental

L'objectif de ce paragraphe est de décrire brièvement les principaux ingrédients du dispositif expérimental, en mettant l'accent sur ses particularités. Il s'agit d'un montage complexe et sophistiqué dont la mise en oeuvre a nécessité de gros moyens humains. Ce travail a débuté en 1999 et les premiers signaux expérimentaux ont été obtenus en 2003. L'essentiel du montage a été développé durant la thèse de Rémy Battesti [68]. Des modifications et astuces expérimentales ont été apportées au cours de celle de Pierre Cladé [69]. L'ensemble du dispositif est piloté par le logiciel Labview : une grande partie de mon activité lors des débuts de cette expérience a consisté à programmer la séquence temporelle et l'acquisition de données.

Les deux principaux éléments du dispositif sont le senseur inertiel (sélection et mesure des distributions de vitesse) et le potentiel lumineux (oscillations de Bloch).

4.2.1 Le senseur inertiel

Le senseur inertiel est l'ensemble des deux impulsions π sélectives en vitesse qui permettent de sélectionner et de mesurer une classe de vitesse atomique. Pour cela, nous utilisons deux faisceaux contrapropageants de fréquence ω_1 et ω_2 , de vecteurs d'onde \vec{k}_1 et \vec{k}_2 , désaccordés par rapport à la raie D₂ pour éviter l'émission spontanée

(je les appellerai dans la suite "faisceaux Raman" pour les différentier des faisceaux utilisés pour les oscillations de Bloch, pour lesquels j'utilisera le terme de "faisceaux Bloch").

Le désaccord à résonance δ ($\delta = \omega_1 - \omega_2 - \omega_{SHF}$ où ω_{SHF} représente l'écart de structure hyperfine entre les sous niveaux $F = 1$ et $F = 2$, $\omega_{SHF} \sim 6,8$ GHz) s'écrit :

$$\delta = \Delta_1 - \Delta_2 + (\vec{k}_1 - \vec{k}_2)(\vec{v}_i + \frac{\hbar}{m_{Rb}}(\vec{k}_1 - \vec{k}_2)) \quad (4.14)$$

où \vec{v}_i est la vitesse centrale de la distribution que l'on sélectionne ou que l'on mesure et Δ_1 (respectivement Δ_2) un éventuel déplacement de niveau de $F=1$ (respectivement $F=2$).

La largeur de la classe de vitesse sélectionnée ou mesurée est uniquement limitée par la durée de l'impulsion. Nous sélectionnons typiquement des classes de vitesse de largeur $\frac{v_r}{50}$, ce qui correspond à une impulsion de 3,4 ms.

Le dispositif expérimental

Les faisceaux Raman sont produits par deux diodes laser à 780 nm injectées par deux diodes laser en cavité étendue dans la configuration maître-esclave. Les diodes maîtres sont asservies en phase à environ 6,8 GHz l'une de l'autre au moyen d'une chaîne micro-onde accordable. Cette chaîne comprend, entre autres, un quartz à 100 MHz, très stable, référencé sur l'horloge à césum du BNM-SYRTE grâce à la fibre optique qui relie nos deux laboratoires. La fréquence de l'une des diodes maîtres est stabilisée sur une cavité Fabry Perot ultrastable en zérodur et on compte le battement entre la fréquence de cette diode et celle de notre standard de fréquence réalisé à partir d'une diode laser stabilisée sur la transition à deux photons 5S-5D du rubidium.

L'inversion du sens des faisceaux Raman

On voit dans l'expression (4.14) qu'il est nécessaire de bien contrôler les déplacements de niveaux différentiels pour réaliser une mesure de vitesse précise. Les déplacements de niveaux sont principalement dus à deux effets : les déplacements lumineux et l'effet Zeeman quadratique ³. Les effets de déplacements de niveaux induits par un

³L'effet Zeeman du premier ordre est éliminé par le fait que nous travaillons uniquement avec les sous niveaux hyperfins $m_F = 0$ grâce à l'application d'un champ magnétique directeur parallèlement à la direction de propagation des faisceaux.

champ constant s'éliminent entre la sélection et la mesure. Néanmoins, on conserve un effet résiduel dû aux fluctuations de l'intensité lumineuse et aux inhomogénéités spatiales du champ magnétique. Pour limiter cet effet, nous avons développé un protocole expérimental basé sur le fait que l'erreur sur la mesure de vitesse due aux déplacements de niveaux change de signe lorsque l'on inverse les sens de propagation des faisceaux Raman. L'effet est fortement diminué en réalisant deux séquences expérimentales, une pour chaque sens de propagation, et en faisant la moyenne des deux spectres comme le montre la figure (4.5). Il n'est pas complètement annulé, principalement à cause de la dépendance temporelle des fluctuations du champ magnétique.

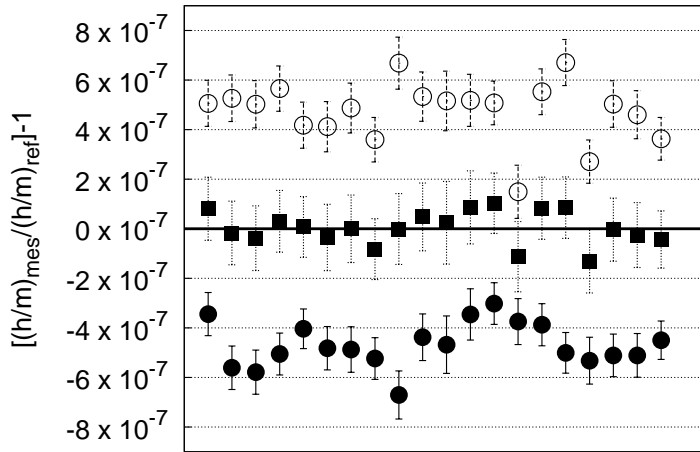


FIG. 4.5 – Mesures de h/m_{Rb} comparées à la valeur du CODATA 98, réalisées en inversant le sens des faisceaux Raman. La moyenne des mesures dans les deux sens est de $-0,63 \pm 0,17$ ppm. Le champ magnétique appliqué est de 150 mG.

Les performances du senseur inertiel

Durant sa thèse, Pierre Cladé a étudié dans le détail les sources de bruit limitant la sensibilité du senseur inertiel [70]. Le bruit de phase dû aux fibres optiques amenant les faisceaux Raman jusqu'à l'enceinte à vide a été réduit en utilisant, à la place de deux fibres indépendantes, une seule fibre et un miroir de rétroréflexion. Nous sommes à présent limités par les vibrations. Une solution visant à mettre en place une plateforme anti-vibrations pourvue d'un asservissement actif est en cours d'étude. Une autre limitation à la sensibilité du senseur inertiel est due au bruit de détection. Nous sommes néanmoins actuellement capables de pointer le centre de la distribution de vitesse au hertz, ce qui correspond à une incertitude meilleure que $10^{-4}v_r$ pour un temps d'intégration de 5 minutes.

4.2.2 L'accélération cohérente des atomes

Interprétation du phénomène

L'accélération cohérente des atomes est réalisée au moyen de transitions Raman n'impliquant qu'un seul sous niveau hyperfin. De cette façon, l'état d'énergie interne de l'atome reste le même tandis que sa quantité de mouvement augmente de $2\hbar k$ à chaque transition. Afin d'effectuer un grand nombre de transitions, l'effet Doppler est compensé en faisant varier continûment la différence de fréquence δ' entre les deux faisceaux (voir figure (4.6)).

$$\delta' = \omega_1 - \omega_2 = 2k_B at \quad (4.15)$$

où k_B est la norme du vecteur d'onde des faisceaux Bloch.

Dans le référentiel du laboratoire, l'atome est donc soumis à une accélération constante :

$$a = \frac{1}{2k_B} \frac{d\delta'}{dt} = \frac{1}{m_{Rb}} \frac{dp}{dt} = \frac{2\hbar k_B}{m_{Rb}} \frac{dN}{dt} \quad (4.16)$$

Cette interprétation en termes de transition à deux photons est bien adaptée au cas des

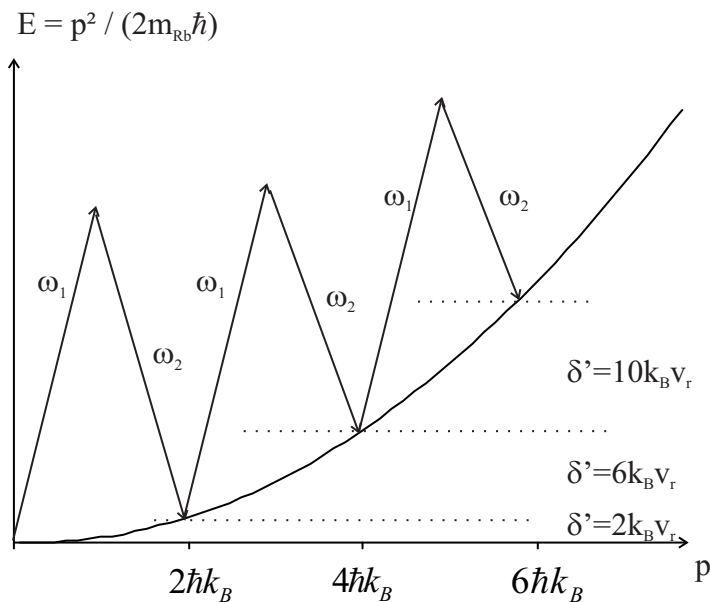


FIG. 4.6 – Parabole énergie-impulsion.

liaisons faibles, c'est-à-dire au cas où la profondeur U_0 du potentiel lumineux créé par l'interférence entre les deux faisceaux est faible devant l'énergie de recul ($E_r = \frac{\hbar^2 k^2}{2m}$).

L'atome perçoit alors l'onde comme une perturbation, sauf au moment où il est à résonance et effectue une transition. Son impulsion évolue donc par sauts de $2\hbar k_B$.

Le phénomène d'accélération cohérente peut également être interprété en termes d'oscillations de Bloch [71]. La périodicité du potentiel lumineux auquel est soumis l'atome induit une structure de bande. La différence de fréquence $\delta'(t)$ se traduit par une accélération uniforme du potentiel lumineux dans le référentiel du laboratoire. Si $\delta'(t)$ varie de façon adiabatique, les atomes suivent le mouvement de l'onde stationnaire et sont donc soumis à une force d'inertie constante $\vec{F} = m \vec{a}$.

Le mouvement des atomes est analogue à celui d'électrons placés dans un réseau cristallin parfait et soumis à une force constante (produite par un champ électrique). Les électrons oscillent sur place, sans changer de bande d'énergie : ce sont les oscillations de Bloch [72].

Cette seconde interprétation est mieux adaptée à la limite des liaisons fortes ($U_0 \gg 4E_r$) dans laquelle les atomes sont piégés au fond d'un puit de potentiel. La vitesse moyenne des atomes suivant celle du réseau lumineux, leur impulsion évolue de façon continue et non par sauts comme dans le cas des liaisons faibles.

Expérimentalement, le potentiel lumineux est obtenu au moyen de deux faisceaux contrapropageants, de polarisations linéaires parallèles, produits par un laser Ti :Sa pompé par un laser Nd :YAG doublé (Millenia, Spectra Physics). La fréquence du laser Ti :Sa est stabilisée sur la même cavité Fabry Perot que les faisceaux Raman. A la fin du processus d'accélération, l'intensité de l'onde stationnaire est diminuée de façon adiabatique afin de ramener les atomes dans un état d'impulsion bien défini.

Le schéma de double accélération

Dans la pratique, la séquence "sélection d'une classe de vitesse - accélération - mesure" décrite précédemment, n'est pas appliquée telle quelle. Un schéma de double accélération s'est avéré nécessaire lorsque nous avons débuté l'expérience en accélérant les atomes suivant la direction horizontale. En effet, à partir de quatre oscillations de Bloch, à cause de la vitesse acquise, les atomes "rataient" la zone de détection placée à la verticale du piège. Le schéma de double accélération, décrit ci-dessous, permet de les ramener à vitesse nulle afin qu'ils tombent selon la verticale. Nous l'avons conservé lorsque nous sommes passés à la configuration verticale pour éviter que les atomes n'atteignent la paroi supérieure de la cellule. Comme le montre la figure (4.7), on

opère donc une pré-accelération avant de sélectionner une classe de vitesse. La phase d'oscillations de Bloch consiste finalement à décélérer les atomes qui se retrouvent donc à vitesse nulle au moment de la mesure finale. Le faisceau appelé "pousseur" sur la figure (4.7), résonant avec la transition $F = 2 \rightarrow F' = 3$, permet d'éliminer les atomes non sélectionnés.

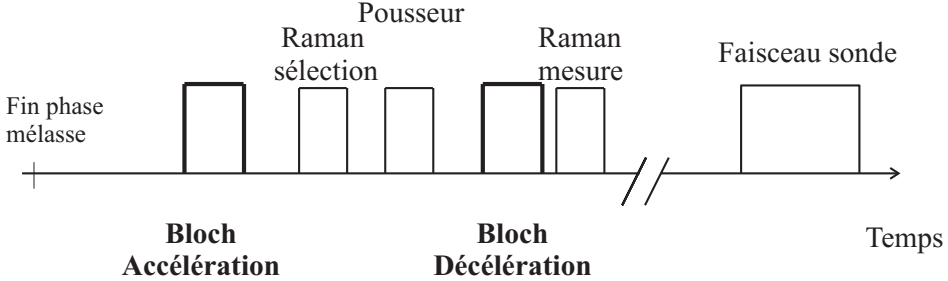


FIG. 4.7 – Schéma expérimental de double accélération.

La mesure différentielle

Une autre astuce expérimentale consiste à accélérer les atomes dans les deux sens (droite et gauche avec des faisceaux horizontaux, haut et bas avec des faisceaux verticaux). En configuration horizontale, ce procédé permet d'éliminer un certain nombre d'effets systématiques comme les défauts d'horizontalité des faisceaux et les déplacements lumineux indépendants du temps. En configuration verticale, il nous autorise de plus à annuler l'effet de la gravité au premier ordre. Une mesure de la vitesse de recul est alors obtenue en faisant la moyenne entre les fréquences centrales des spectres obtenus dans les deux sens. Le rapport $\frac{\hbar}{m_{Rb}}$ est alors donné par l'expression suivante :

$$\frac{\hbar}{m_{Rb}} = \frac{(\delta_{sel} - \delta_{mes})^+ - (\delta_{sel} - \delta_{mes})^-}{2(N^+ + N^-)k_B(k_1 + k_2)} \quad (4.17)$$

où N^+ (respectivement N^-) est le nombre d'oscillations de Bloch réalisé dans le sens noté + (respectivement -).

4.3 Les résultats

4.3.1 La configuration horizontale

Chronologiquement, nous avons démarré l'expérience en accélérant les atomes suivant la direction horizontale. Cette situation correspond à la configuration expéimen-

tale la plus simple, puisque que la gravité ne contribue pas au mouvement des atomes dans la direction des faisceaux. En revanche, elle réduit notablement le temps d'interaction des atomes avec la lumière. Les premiers résultats ont été obtenus en 2003, à la fin de la thèse de Rémy Battesti [68] et sont publiés dans la référence [73]. Dans cette première configuration expérimentale, nous avons réalisé 50 oscillations de Bloch dans chaque sens et ainsi déterminé la vitesse de recul avec une incertitude relative de $1,5 \times 10^{-6}$ (ce qui correspond à une résolution en vitesse de $2 \times 10^{-4}v_r$ pour 10 minutes d'enregistrement par spectre). Une série de $n = 43$ mesures de v_r ($\frac{\chi^2}{n-1} \simeq 2,4$) nous a permis de réaliser une détermination préliminaire de $\frac{h}{m_{Rb}}$ avec une incertitude relative de $4,2 \times 10^{-7}$. Cependant, comme le montre la figure (4.8), la valeur obtenue est décalée de $6,1 \times 10^{-7}$ au-dessus de la valeur déduite du CODATA 98. Nous avons imputé cette différence principalement à la coupure brutale du potentiel lumineux à la fin de la phase d'accélération (la coupure adiabatique du potentiel n'avait alors pas encore été mise en place) ainsi qu'à l'effet Zeeman quadratique (la méthode d'inversion du sens des faisceaux Raman n'était pas encore mise en oeuvre non plus).

Le principal résultat de cette mesure préliminaire a été de mettre en évidence l'énorme

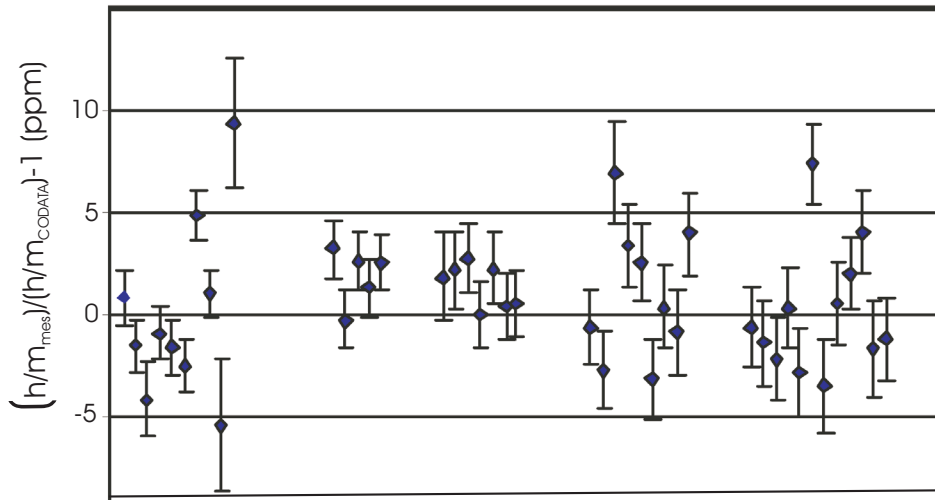


FIG. 4.8 – Les 43 déterminations de h/m_{Rb} dans l'ordre chronologique pour $N = 50$ oscillations dans chaque sens.

potentiel de cette méthode. En effet, nous avons démontré expérimentalement une efficacité de transfert de 99,5% par oscillation de Bloch, efficacité que nous avons pu augmenter par la suite jusqu'à 99,95% au fur et à mesure des améliorations du dispositif expérimental.

4.3.2 La configuration verticale stationnaire : mesure de la période de Bloch

Avant de passer aux résultats expérimentaux les plus précis, obtenus en configuration verticale accélérée, je voudrais mentionner la mesure préliminaire de la constante de gravité g que nous avons réalisée. Cette mesure est détaillée dans l'article [74] joint à la fin de ce chapitre.

Les oscillations de Bloch ont été introduites comme les oscillations d'un état atomique, placé dans un potentiel périodique et soumis à une force constante. Cette force peut être créée par l'accélération du réseau lumineux, comme dans le cas précédent, ou bien par la gravité. C'est ce qui se passe lorsque l'atome est placé dans une onde stationnaire verticale. Il oscille alors à la période de Bloch, τ_B , donnée par :

$$\nu_B = \frac{1}{\tau_B} = \frac{m_{Rb}g}{2\hbar k_B} \quad (4.18)$$

Notre dispositif expérimental nous permet de mesurer τ_B , et connaissant $\frac{\hbar}{m_{Rb}}$, d'en déduire une valeur de g . Le principe de la mesure est illustré par la figure (4.9). Après la phase de sélection et l'élimination des atomes non sélectionnés par le faisceau pousseur, on branche le potentiel lumineux pendant un temps T_{Bloch} variable, puis on mesure la distribution de vitesse finale à l'aide d'une deuxième transition Raman. Il faut noter qu'il s'écoule quelques millisecondes entre l'impulsion de sélection et l'allumage des faisceaux Bloch : les atomes du centre de la distribution sélectionnée ont donc une vitesse non nulle (correspondant à plusieurs vitesses de recul) au moment de la mise en place du potentiel lumineux. Afin de réaliser les oscillations dans la première bande d'énergie, on utilise en fait une onde quasi-stationnaire de vitesse correspondant à celle qu'avaient les atomes lorsqu'elle a été mise en place.

La variation de la vitesse finale des atomes (en unité de $2v_r$) en fonction de la durée

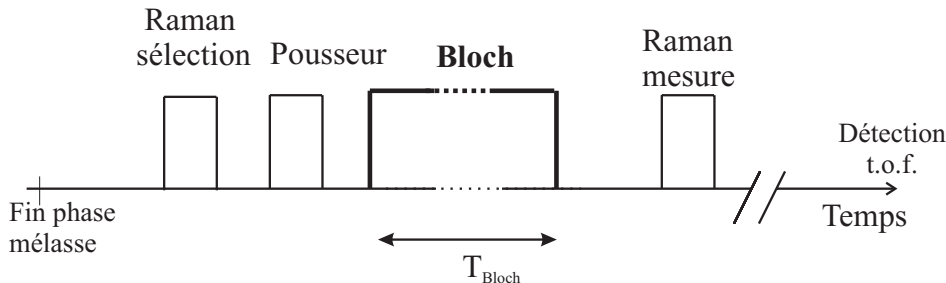


FIG. 4.9 – Séquence temporelle pour la mesure de ν_B .

T_{Bloch} est représentée par la figure (4.10). L'évolution en dent de scie est caractéristique

des oscillations de Bloch. Afin de réduire les effets systématiques, on réalise une mesure de τ_B en deux points (t_1, v_1) et (t_2, v_2) correspondants à la même vitesse finale (c'est-à-dire deux points séparés par un multiple de la période de Bloch). La période de Bloch est alors donnée par :

$$\frac{1}{\tau_B} = \frac{N_2 - N_1}{t_2 - t_1} + \frac{v_2 - v_1}{2v_r(t_2 - t_1)} \quad (4.19)$$

où N_1 (respectivement N_2) est le nombre d'oscillations correspondant au temps t_1 (respectivement t_2).

La précision obtenue sur τ_B pour 50 oscillations, est de 2×10^{-6} , ce qui conduit à 10^{-6}

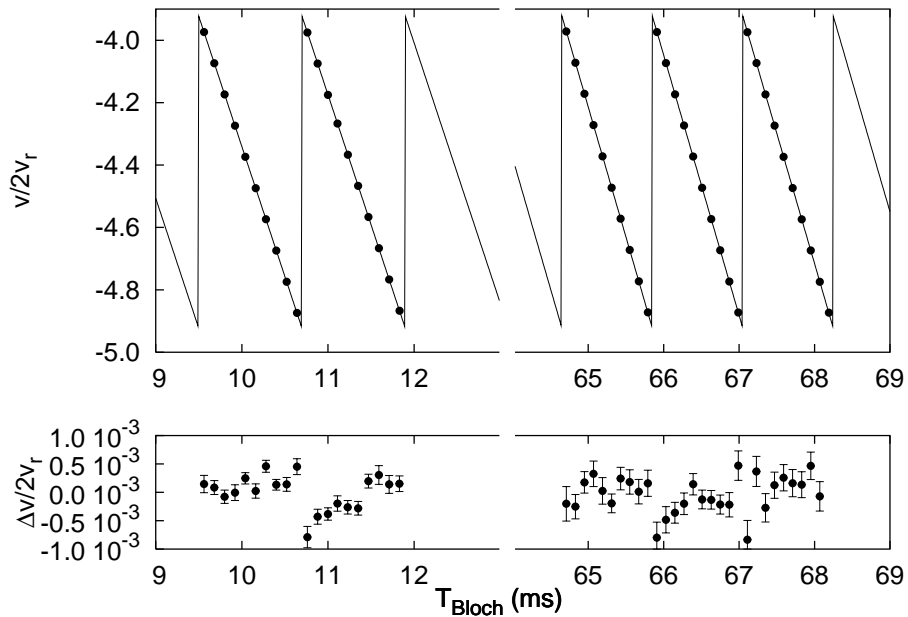


FIG. 4.10 – Oscillations de Bloch dans l'onde stationnaire : les points expérimentaux sont ajustés par un ajustement de type moindres carrés. En-dessous : les écarts résiduels entre les valeurs expérimentales et l'ajustement.

sur g [74]. Cette expérience de démonstration n'est absolument pas compétitive avec les gravimètres (2×10^{-9} pour les gravimètres à "coin de cube"). Cependant, ces résultats préliminaires pourraient être nettement améliorés en augmentant le nombre d'oscillations et ainsi la résolution sur la mesure de τ_B . En effet, nous avons constaté que le rapport signal à bruit des spectres obtenus diminuait notablement avec l'augmentation du nombre d'oscillations ⁴. Nous avons pu montrer que les pertes par oscillation ne

⁴Il est à noter que, dans cette expérience, la durée d'une oscillation est fixée à environ 1,2 ms par l'équation (4.18) alors que l'on peut faire beaucoup plus d'oscillations en moins de temps en

s'expliquaient pas seulement par les transitions interbandes et l'émission spontanée. Il est nécessaire de prendre en compte également les collisions avec la vapeur de rubidium présente dans l'enceinte à vide. Cet effet devrait être notablement réduit dans la prochaine version de l'expérience, dans laquelle le piège magnéto-optique sera chargé à partir d'un jet atomique ralenti produit par un piège à deux dimensions.

4.3.3 La configuration verticale accélérée : mesure de h/m_{Rb}

La configuration la plus favorable pour réaliser un grand nombre d'oscillations en un temps court consiste à placer les atomes dans un potentiel lumineux vertical accéléré. C'est dans cette situation qu'en 2005, nous avons réalisé une mesure compétitive de $\frac{h}{m_{Rb}}$. Les résultats correspondants s'inscrivent dans le travail de thèse de Pierre Cladé, Malo Cadoret et Estéfania de Mirandes. Ils sont publiés dans la référence [75] jointe à la fin du chapitre (pour plus de détails, voir la référence [76], également jointe au manuscrit).

La procédure expérimentale est celle décrite dans le paragraphe 4.2. J'en rappelle ici les points importants :

- réalisation d'une double accélération (accélération puis décélération) pour éviter que les atomes ne heurtent le haut de la cellule.
- réalisation d'une accélération dans les deux sens suivant la direction verticale et mesure différentielle pour éliminer la contribution de g .
- inversion du sens des faisceaux Raman pour réduire les effets de déplacement de niveaux.

Finalement, une mesure de $\frac{h}{m_{Rb}}$ se déduit de quatre spectres expérimentaux, comme ceux représentés sur la figure (4.11).

De façon générale, il est nécessaire de désaccorder les faisceaux Bloch (de quelques dizaines de GHz) par rapport à la résonance à un photon, afin d'éviter l'émission spontanée. Une particularité de cette mesure, par rapport aux précédentes, a été de se placer dans la limite des liaisons fortes ($U_0 \simeq 70E_r$) et de désaccorder les faisceaux vers le bleu de la transition. En effet, on peut montrer que dans ce cas, le taux d'émission spontanée est réduit d'un facteur $\frac{1}{2}\sqrt{\frac{E_r}{|U_0|}}$ par rapport à un désaccord vers le rouge [69]. De plus, dans nos conditions expérimentales, l'effet de la force dipolaire transverse qui pousse les atomes vers l'extérieur des faisceaux dans le cas d'un désaccord vers le bleu, est négligeable.

Finalement, pendant une phase d'accélération de 3 ms, les atomes réalisent environ

configuration accélérée. Nous sommes donc ici beaucoup plus sensibles à tous les effets systématiques, en particulier aux vibrations.

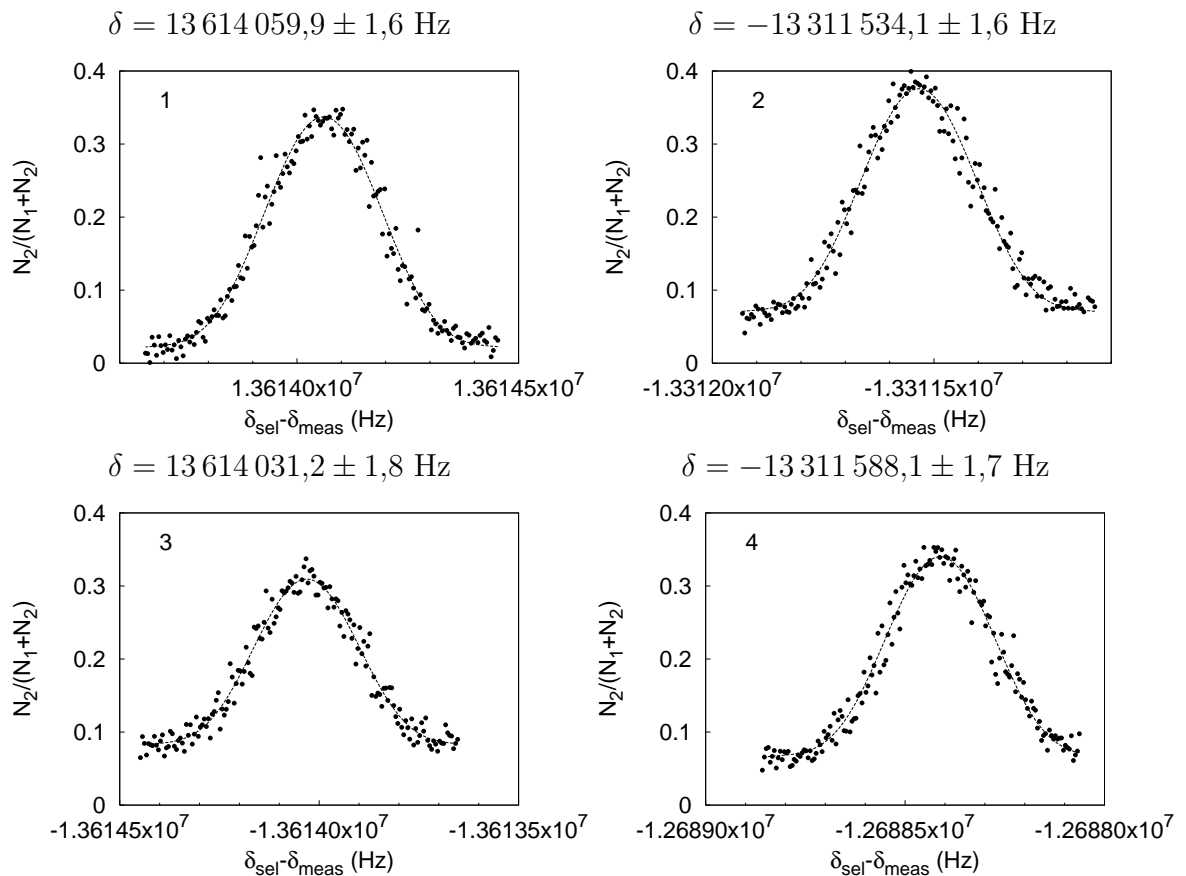


FIG. 4.11 – Spectres expérimentaux. En abscisse figure la différence entre la fréquence Raman à la sélection et à la mesure ; en ordonnée se trouve la proportion d'atomes ayant effectué la seconde transition Raman. L'incertitude sur le pointé de la fréquence centrale de chaque spectre est d'environ 1,7 Hz. De ces quatre spectres on peut déduire une détermination de α avec une incertitude de $3,3 \times 10^{-8}$.

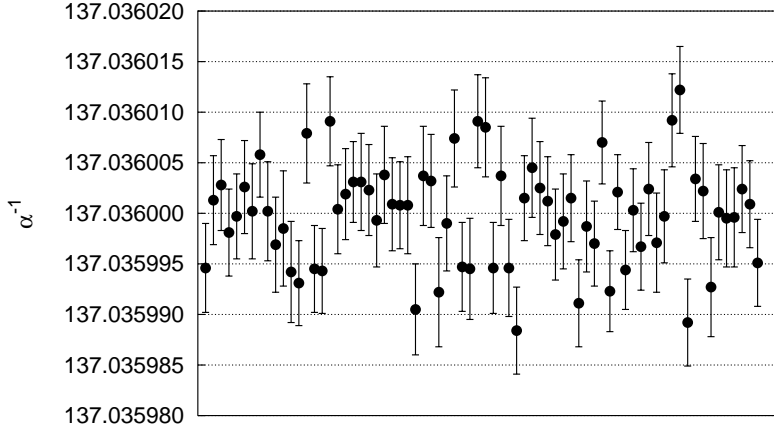


FIG. 4.12 – Ensemble des mesures prises en avril 2005. Chaque point correspond à 4 spectres. On a $\chi^2/(n - 1) \simeq 1,3$. L'incertitude statistique finale sur α vaut $4,4 \times 10^{-9}$.

450 oscillations de Bloch. Chaque spectre (voir figure (4.11)) comporte 160 points et est obtenu en 5 minutes. Sa fréquence centrale est pointée avec une incertitude de 1,7 Hz, ce qui correspond à environ $10^{-4}v_r$. A partir d'un ensemble de quatre courbes expérimentales, nous obtenons une valeur de $\frac{h}{m_{Rb}}$ entachée d'une incertitude relative de $6,6 \times 10^{-8}$.

Une série de 72 mesures (voir figure (4.12)) nous a permis de déterminer α avec une incertitude statistique égale à $4,4 \times 10^{-9}$. Les valeurs obtenues sont :

$$\frac{h}{m_{Rb}} = 4,591359237(40) \times 10^{-9} [8,8 \times 10^{-8}] \text{ m}^2 \cdot \text{s}^{-1} \quad (4.20)$$

pour l'isotope 87 du rubidium.

et

$$\alpha^{-1} = 137,03599959(60) [4,4 \times 10^{-9}] \quad (4.21)$$

Dans le cadre des résultats expérimentaux présentés ci-dessus, nous avons réalisé une analyse la plus exhaustive possible des effets systématiques susceptibles de décaler notre mesure. Leurs contributions sont détaillées dans la référence [76] ci-jointe. Le tableau 4.1 résume les corrections et les incertitudes associées que nous avons appliquées à notre mesure. Avec l'incertitude statistique, nous obtenons finalement une incertitude relative de $6,7 \times 10^{-9}$ sur α^{-1} .

En définitive, les valeurs de h/m_{Rb} et de α^{-1} sont :

$$\frac{h}{m_{Rb}} = 4,59135929(6) \times 10^{-9} [1,3 \times 10^{-8}] \text{ m}^2 \cdot \text{s}^{-1} \quad (4.22)$$

TAB. 4.1 – Bilan des effets systématiques et des incertitudes associées.

effet sur la mesure de α^{-1}	correction (α^{-1}) (ppb)	incertitude (α^{-1}) (ppb)
Fréquence des lasers		0,8
Parallélisme des faisceaux	-2	2
Phase de Gouy et courbure du front d'onde	-8,2	4
Déplacement Zeeman quadratique	6,6	2
Force Zeeman quadratique	-1,3	0,4
Gradient de gravité	-0,18	0,02
Déplacement lumineux 1 photon		0,2
Déplacement lumineux 2 photons	-0,5	0,2
Déplacement lumineux oscillation de Bloch	0,46	0,2
Indice de réfraction (nuage d'atomes)	<0,1	0,3
Indice de réfraction (vapeur résiduelle)	-0,37	0,3
Total	-5,49	5,0

pour l'isotope 87 du rubidium.

et

$$\alpha^{-1} = 137,03599884(91) [6,7 \times 10^{-9}] \quad (4.23)$$

Cette valeur est en bon accord avec celle recommandée par le CODATA 2002.

Le tableau 4.2 récapitule les différentes déterminations prises en compte dans le CODATA 2002 auquelles j'ai ajouté la nôtre ainsi que la dernière valeur publiée de a_e . Notre mesure est compétitive avec les meilleures valeurs déduites de l'interférométrie atomique. La très grande efficacité des oscillations de Bloch, associée à des améliorations du dispositif expérimental détaillées dans le chapitre suivant, pourrait nous permettre d'atteindre une précision au niveau du ppb, et donc comparable à celle déduite de la mesure de $g - 2$.

4.4 Comparaison avec l'expérience de Stanford

Ce paragraphe est dédié à la comparaison entre l'expérience d'interférométrie atomique menée à Stanford dans l'équipe de S. Chu et la nôtre. Cette comparaison est d'autant plus pertinente que les méthodes utilisées sont très proches (il s'agit dans les

TAB. 4.2 – Les différentes déterminations de α (CODATA 2002 et dernières publications).

	α^{-1}	Incertitude
$a_e(2006)$	137,035 999 710(96)	$0,7 \times 10^{-9}$
a_e	137,035 99880(52)	$3,8 \times 10^{-9}$
$h/m(Rb)$	137,035 99878(91)	$6,7 \times 10^{-9}$
$h/m(Cs)$	137,036 0001(11)	$7,7 \times 10^{-9}$
R_K	137,036 0030(25)	$1,7 \times 10^{-8}$
Γ'_{90}	137,035 9875(43)	$3,1 \times 10^{-8}$
h/m_n	137,036 0015(47)	$3,4 \times 10^{-8}$
$\Delta\nu_{\text{Mu}}$	137,036 0017(80)	$5,8 \times 10^{-8}$

deux cas de mesurer la vitesse de recul d'un alcalin) et les incertitudes obtenues sur α comparables.

Après quelques rappels sur le principe de l'interférométrie atomique, je discuterai les performances des deux expériences en termes d'incertitude statistique et d'effets systématiques.

4.4.1 L'interférométrie atomique

L'interféromètre de Ramsey à deux impulsions

Le point de départ de l'interféromètre développé par l'équipe de S. Chu est l'interféromètre de Ramsey à deux impulsions dont le principe est illustré par la figure (4.13). Partant d'atomes de vitesse v_0 , initialement dans l'état $|a\rangle$, une première impulsion $\pi/2$ les transfèrent dans l'état $(|a\rangle + |b\rangle)/\sqrt{2}$. Cette transition accélère l'atome dans l'état $|b\rangle$ d'une quantité bien définie et égale à $2v_r$. Une seconde impulsion $\pi/2$ recombine les états atomiques. Il existe quatre chemins possibles, les chemins correspondant au même état final interférant à l'infini. Pour calculer la probabilité qu'a un atome de se trouver dans l'un ou l'autre des deux états, il faut calculer la différence de phase due à l'énergie cinétique, accumulée entre les deux impulsions $\pi/2$, soit

$$\Delta\phi_c = \frac{T_{\text{Ramsey}}}{\hbar} (E_c^{|b\rangle} - E_c^{|a\rangle}) = 2kT_{\text{Ramsey}}(v_0 + v_r) \quad (4.24)$$

où T_{Ramsey} est l'intervalle de temps entre les deux impulsions $\pi/2$ et k le vecteur d'onde du photon. Il faut rajouter à ce déphasage, le déphasage du laser qui dépend du désaccord entre la fréquence du laser et celle de la transition atomique. En mesurant le déphasage total en fonction de ce désaccord, on a accès à la valeur de la quantité

$$2k(v_0 + v_r).$$

Le principal inconvénient de ce dispositif est que le déphasage final dépend de la vitesse initiale des atomes. Ce problème peut être surmonté en couplant deux interféromètres à deux impulsions, c'est-à-dire en réalisant un interféromètre de Ramsey Bordé.

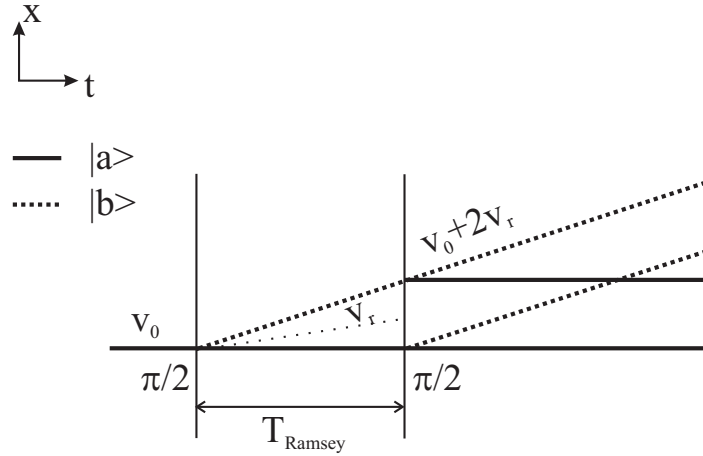


FIG. 4.13 – Interféromètre de Ramsey à deux impulsions.

L'interféromètre de Ramsey Bordé

Le schéma de principe de ce double interféromètre est représenté par la figure (4.14) [77]. Le sens des impulsions $\pi/2$ est inversé entre les deux interféromètres afin de changer le sens du recul transféré aux atomes. Si on calcule par exemple le déphasage dû à l'énergie cinétique correspondant aux deux trajectoires du haut, on obtient :

$$\Delta\phi_c = \frac{T_{Ramsey}}{\hbar} \left[\frac{1}{2}m(v_0+2v_r)^2 - \frac{1}{2}mv_0^2 \right] + \frac{T_{Ramsey}}{\hbar} \left[\frac{1}{2}m(v_0+2v_r)^2 - \frac{1}{2}m(v_0+4v_r)^2 \right] \quad (4.25)$$

où m est la masse de l'atome.

Le premier terme entre crochets de l'expression 4.25 correspond à la différence d'énergie cinétique de chaque état pendant le premier interféromètre, le second terme à la même quantité pendant le deuxième interféromètre.

Finalement, le déphasage $\Delta\phi_c$ vaut

$$\Delta\phi_c = -4kT_{Ramsey}v_r \quad (4.26)$$

et est indépendant de la vitesse initiale v_0 , ce qui autorise à réaliser l'expérience sur des atomes ayant une distribution de vitesse de largeur supérieure à v_r . On peut, de

plus, remarquer que le déphasage accumulé entre les deux impulsions $\pi/2$ de l'un des interféromètres est proportionnel à la moyenne de la vitesse de l'atome entre les deux chemins qui interfèrent. Finalement, la quantité mesurée est la différence entre la vitesse moyenne des atomes au moment du premier interféromètre et au moment du second, c'est-à-dire $2v_r$.

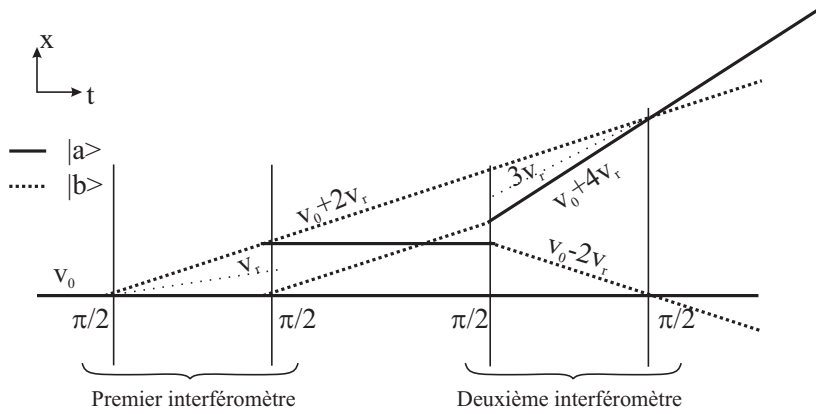


FIG. 4.14 – Interféromètre de Ramsey Bordé (ne sont représentés que les chemins fermés qui interfèrent).

L'interféromètre développé à Stanford

L'interféromètre de Ramsey Bordé mesure donc une variation de vitesse. L'interféromètre développé par l'équipe de S. Chu est basé sur ce dispositif dont la sensibilité est augmentée en accélérant les atomes entre les deux paires d'impulsions $\pi/2$ au moyen d'impulsions π (voir figure (4.15)). Contrairement au cas de notre expérience, ces impulsions π couplent les deux états $|a\rangle$ et $|b\rangle$, le sens des faisceaux étant inversé entre chaque impulsion afin d'accélérer les atomes toujours dans le même sens. La vitesse acquise par impulsion étant égale à $2v_r$, le déphasage accumulé après N impulsions est égal à :

$$\Delta\phi_c = -4k(N+1)T_{Ramsey}v_r \quad (4.27)$$

La contribution de g au premier ordre est éliminée en réalisant une mesure différentielle entre les trajectoires du haut et du bas représentées sur la figure (4.15).

4.4.2 La comparaison des expériences de Stanford et Paris

Les résultats de l'expérience de Stanford sur la détermination de α sont issus de la référence [51]. Il est intéressant de comparer pour les deux expériences, d'une part les

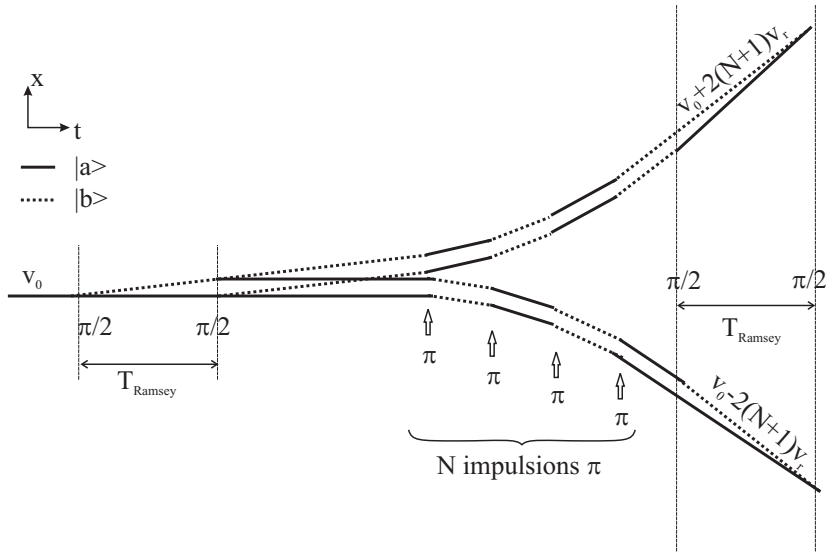


FIG. 4.15 – Interféromètre de l’expérience de Stanford.

sources de limitation de la statistique, d’autre part les effets systématiques prépondérants.

L’incertitude statistique

L’incertitude statistique entachant notre détermination de α est de 4,4 ppb. Elle est de 2,5 ppb pour celle de S. Chu. Dans les deux cas, elle peut s’exprimer comme l’incertitude liée au senseur inertiel divisée par le nombre N de transitions π .

La valeur de N de l’expérience de Stanford est limitée à 30 ($N=450$ dans notre cas). Ceci est dû au fait que les impulsions π induisent des passages adiabatiques résonants. L’efficacité de transfert résultante est limitée à 97% par l’émission spontanée, alors qu’elle atteint 99,95% dans notre cas.

L’incertitude statistique du senseur de Stanford est de $3 \times 10^{-7}v_r$, alors qu’elle est égale à $8 \times 10^{-6}v_r$ sur notre dispositif expérimental. Ceci est dû à la meilleure résolution de l’expérience américaine (la largeur de leurs franges est de 8 Hz à comparer à environ 30 Hz dans notre cas). Cependant le fait que notre séquence temporelle soit beaucoup plus courte (10 ms à comparer à environ 300 ms) rend notre montage potentiellement beaucoup moins sensible aux vibrations. Mais, il faut avoir à l’esprit la grande expérience sur la réduction des vibrations qu’a acquise l’équipe de Stanford à travers la gravimétrie.

Un autre aspect favorable à la méthode américaine est le fait qu’il ne leur est pas né-

cessaire de sélectionner une classe de vitesses sub-recul : tous les atomes sont utilisés dans l'interféromètre. Le rapport signal à bruit est donc potentiellement bien meilleur que dans notre expérience où son augmentation se fait au détriment de la résolution.

Les effets systématiques

L'incertitude liée aux effets systématiques est évaluée à 5 ppb dans notre expérience et à 7,7 ppb dans celle de S. Chu.

La principale contribution aux effets systématiques de cette dernière provient des effets d'indice et est estimée à 7 ppb. Ceux-ci sont notablement plus importants que dans notre expérience car le processus d'accélération est réalisé avec un laser résonant. Il n'y a donc a priori pas d'effet de dispersion. Néanmoins, les atomes qui manquent une transition peuvent peupler des sous niveaux Zeeman hors résonance. Dans ce cas, l'indice devient important. Dans notre expérience, la valeur de l'indice reste toujours très faible et aux désaccords auxquels nous travaillons, l'effet est négligeable, en tout cas en ce qui concerne l'indice du nuage atomique (voir tableau 4.1).

Les effets prépondérants dans notre expérience sont liés d'une part aux déplacements Zeeman quadratiques, d'autre part à la phase de Gouy et à la courbure des fronts d'onde. En ce qui concerne les déplacements Zeeman, ils devraient être a priori plus faibles dans notre cas, car l'effet doit être divisé par le nombre de reculs transmis aux atomes. Leur importance s'explique par un mauvais contrôle du champ magnétique dans notre cellule qui n'est pas pourvue de blindage magnétique. Les effets de phase de Gouy et de courbure du front d'onde ont été amplifiés lors de nos mesures à cause d'un faisceau mal collimaté. Cependant, ils sont a priori plus importants que dans l'expérience de Stanford. En effet, l'utilisation d'un laser résonant avec la transition atomique requiert une intensité lumineuse plus faible et permet donc de travailler avec des faisceaux de plus grand diamètre dont la courbure est plus facile à contrôler⁵.

Finalement, je voudrais insister sur le fait que nos mesures ont été réalisées sur un dispositif expérimental préliminaire. Plusieurs améliorations, détaillées dans la première partie du chapitre 5, seront apportées dans la prochaine version.

De plus, notre montage peut être aisement adapté à des mesures interférométriques. Cette possibilité a été testée pendant la thèse de Rémy Battesti et des mesures sont actuellement en cours (voir également la chapitre 5).

⁵Nos faisceaux ont un col de l'ordre de 2 mm, ceux de Stanford un col de l'ordre de 1 cm.

Articles joints

P. Cladé, S. Guellati-Khélifa, C. Schwob, F. Nez, L. Julien et F. Biraben, Europhys. Lett, **71** (2005) p.730 : "A promising method for the measurement of the local acceleration of gravity using Bloch oscillations of ultracold atoms in a vertical standing wave".

P. Cladé, E. de Mirandes, M. Cadoret, S. Guellati-Khélifa, C. Schwob, F. Nez, L. Julien et F. Biraben, Phys. Rev. Lett. **96**, (2006), p.033001 : "A new determination of the fine structure constant based on Bloch oscillations of ultracold atoms in a vertical optical lattice".

P. Cladé, E. de Mirandes, M. Cadoret, S. Guellati-Khélifa, C. Schwob, F. Nez, L. Julien et F. Biraben, accepté à Phys. Rev. A : "A precise measurement of h/m_{Rb} using Bloch oscillations of ultracold atoms in a vertical optical lattice : determination of the fine structure constant".

A promising method for the measurement of the local acceleration of gravity using Bloch oscillations of ultracold atoms in a vertical standing wave

P. CLADÉ¹, S. GUELLATI-KHÉLIFA², C. SCHWOB¹, F. NEZ¹,
L. JULIEN¹ and F. BIRABEN¹

¹ Laboratoire Kastler-Brossel, École Normale Supérieure, CNRS, UPMC

4 place Jussieu, 75252 Paris Cedex 05, France

² CNAM-INM, Conservatoire National des Arts et Métiers

292 rue Saint Martin, 75141 Paris Cedex 03, France

received 17 March 2005; accepted in final form 11 July 2005

published online 5 August 2005

PACS. 32.80.Pj – Optical cooling of atoms; trapping.

PACS. 42.50.Vk – Mechanical effects of light on atoms, molecules, electrons, and ions.

PACS. 04.80.-y – Experimental studies of gravity.

Abstract. – An obvious determination of the local acceleration of gravity g can be deduced from the measurement of the velocity of falling atoms using a π - π pulses sequence of stimulated Raman transitions. By using a vertical standing wave to hold atoms against gravity, we expect to improve the relative accuracy by increasing the upholding time in the gravity field and to minimize the systematic errors induced by inhomogeneous fields, owing to the very small spatial amplitude of the atomic center-of-mass wavepacket periodic motion. We also propose to use such an experimental setup nearby a Watt balance. By exploiting the g/h (h is the Planck constant) dependence of the Bloch frequency, this should provide a way to link a macroscopic mass to an atomic mass.

Introduction. – The dynamics of an atomic wave packet in a periodic potential under the influence of a static force has been extensively analyzed using different physical approaches: in terms of Wannier-Stark resonance states [1], Bloch oscillations [2] or macroscopic quantum interferences induced by tunnelling due to the external acceleration [3] (for a review see [4]). An interesting configuration occurs when the external force is induced by the acceleration of gravity. In this case the Bloch frequency is equal to $\nu_B = \frac{mg\lambda}{2h}$ and depends only on the local acceleration of the gravity g , the wavelength of the light λ and some fundamental constants. This frequency is typically in the range 100 Hz–2000 Hz, and its measurement allows the determination of g . Previous experiments have already been realized using the dynamics of BEC [3, 5] or degenerated Fermi gas [5] in vertical 1D optical lattice. Kasevich's group has observed the interference between macroscopic quantum states of BEC atoms confined in a vertical array of optical traps. This interference arises from the tunneling induced by the acceleration of gravity and appears as a train of falling atomic pulses. The acceleration of gravity

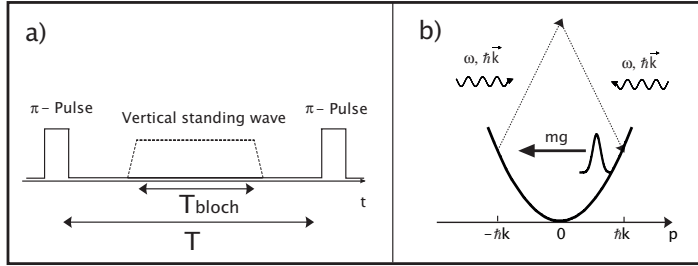


Fig. 1 – a) Experimental pulses sequence. b) A narrow velocity class is selected by the first Raman pulse. When the vertical standing wave is switched on, atoms fall until they are resonant with the Λ transition: they absorb a photon from the upward wave and emit a stimulated photon in the downward wave. This induces a momentum exchange of $2\hbar k$.

g was determined by measuring the spatial period of the pulses train. In Inguscio's group [5], the Bloch period is straightforwardly deduced from the evolution of the momentum in the trap by adiabatically releasing the cloud from the lattice. In both experiments the detection is performed by imaging the falling atomic cloud using absorption imaging techniques and the uncertainty on the g determination did not exceed 10^{-4} dominated by the imaging system.

Our experimental approach is based on the precise determination of the velocity distribution of atoms along the vertical axis using Doppler-sensitive Raman transitions. An obvious determination of the acceleration of gravity is possible by measuring the atomic velocity variation after a given falling time T . This is performed by applying a π - π pulses sequence with a spacing time T : the first pulse defines an initial velocity by selecting a narrow velocity class from an ultracold atomic sample. Atoms are then in a well-defined internal state. The second pulse measures the final velocity distribution of the atoms after the fall by transferring a resonant velocity slice to another internal state. This so-called velocity sensor allows us to locate the center of the velocity distribution with high accuracy and is now limited by the experimental setup platform's vibrations [6]. We could substantially improve the relative uncertainty on the measurement of g by increasing the falling time T , but this parameter is swiftly limited by the dimension of the vacuum chamber. In our experiment we suggest to hold the atoms against gravity by applying between the two Raman pulses a far resonant standing wave, during an interrogation time T_{Bloch} (fig. 1a). In the non-dissipative case, atoms fall until they absorb a photon from the upward wave and emit a stimulated photon in the downward wave. The atoms make a succession of Λ transitions (fig. 1b) inducing a momentum exchange of $2\hbar k$ (k is a wave vector of the standing wave) with the cycling frequency $\nu_B = \frac{mg\lambda}{2\hbar}$. This evolution is equivalent to the dynamics of the Bloch oscillations [7]. In a previous work [8], we have measured a transfer efficiency of 99.5% per cycle. This result promises a large number of Bloch oscillations. Another particular interesting aspect of our method is the small spatial amplitude of the atomic wavepacket motion, during the oscillations⁽¹⁾, therefore the selection (first Raman pulse) and measurement (second Raman pulse) are done in a small volume allowing a better control of systematic effects arising from inhomogeneous fields. In this letter we investigate the possibility to make a high precise measurement of the acceleration of gravity g using Bloch oscillations of cold atoms in a vertical standing wave. Such accurate measurements have important repercussions on geophysical applications including earthquake

⁽¹⁾The amplitude of the oscillation of atomic wavepacket is given by $\Delta z = \Delta_n/2|F|$, where Δ_n is the energy width of the n -th band [2]. In our experiment only the fundamental band is considered $\Delta_0 < E_r$, $F = mg$. Then $\Delta z < 1\mu\text{m}$ which is very small compared to the size of the atomic cloud (1 mm).

predictions, locating oil and studies of the global warming. We first describe our measurement method, then we present a preliminary measurement of g , and finally we discuss the signal losses observed when we increase the number of Bloch oscillations.

Experimental set-up. – The main experimental apparatus has already been described in ref. [8]. Briefly, ^{87}Rb atoms are captured, from a background vapor, in a $\sigma^+ \text{-} \sigma^-$ configuration magneto-optical trap (MOT). The trapping magnetic field is switched off and the atoms are cooled to about $3\mu\text{K}$ in an optical molasses. After the cooling process, we apply a bias field of $\sim 100\text{mG}$. The atoms are then optically pumped into the $F = 2$, $m_F = 0$ ground state. The determination of the velocity distribution is performed using a $\pi\text{-}\pi$ pulses sequence of two vertical counter-propagating laser beams (Raman beams): the first pulse with a fixed frequency ν_{sel} , transfers atoms from $5S_{1/2}$, $|F = 2, m_F = 0\rangle$ state to $5S_{1/2}$, $|F = 1, m_F = 0\rangle$ state, into a velocity class of about $v_r/15$ centered around $(\lambda\nu_{select}/2) - v_r$, where λ is the laser wavelength and v_r is the recoil velocity. To push away the atoms remaining in the ground state $F = 2$, we apply after the first π -pulse, a laser beam resonant with the $5S_{1/2}$ ($F = 2$) to $5P_{3/2}$ ($F = 3$) cycling transition. Atoms in the state $F = 1$ fall under the acceleration of gravity during T . We then perform the final velocity measurement using the second Raman π -pulse, whose frequency is ν_{meas} . The population transfer from the hyperfine state $F = 1$ to the hyperfine state $F = 2$ due to the second Raman pulse is maximal when $2\pi(\nu_{sel} - \nu_{meas}) = g \times T \times \|(\mathbf{k}_1 - \mathbf{k}_2)\|$, where $\mathbf{k}_1, \mathbf{k}_2$ are the wave vectors of the Raman beams. The populations ($F = 1$ and $F = 2$) are measured separately by using the one-dimensional time-of-flight technique developed for atomic clocks and depicted in [9]. To plot the final velocity distribution we repeat this procedure by scanning the Raman beam frequency ν_{meas} of the second pulse.

The two Raman beams are generated using two diode lasers injected by two extended-cavity diode lasers (ECLs). To drive the velocity-sensitive Raman transition, the frequency difference of the master lasers must be precisely resonant with ^{87}Rb ground-state hyperfine transition ($\sim 6.8\text{ GHz}$). The frequency of one ECL is stabilized on a high stable Zerodur Fabry-Perot (ZFP) cavity. The second ECL is then phase-locked to the other using the beat note technique (see fig. 2b). The very stable RF source is performed by mixing the 62th harmonic of a 100 MHz quartz oscillator with different digital synthesizers (SRS DS345). They are used to tune finely the frequency of the RF source. A YIG oscillator is phase-locked onto the central line of the source in order to reject completely the residual sidebands of the different mixings. A multiplexer switches between two synthesizers to generate the frequency offset for the velocity selection or measurement. The frequency of a third synthesizer is linearly swept during the selection and the measurement pulses to compensate the Doppler shift during the fall of the atoms (fig. 2a). The time interval between the two Raman pulses is precisely defined by the delay between the triggering signal of the two-frequency sweeps. Each laser beam passes through an acousto-optic modulator ($\sim 80\text{ MHz}$) for timing (switch on and off) and intensity control. The two beams have linear orthogonal polarizations and are coupled into the same polarization maintaining optical fiber. The pair of Raman beams is sent through the vacuum cell. The counter-propagating configuration is achieved using a polarizing beam-splitter cube and an horizontal retroreflection mirror placed above the exit window of the cell. The standing wave used to create the 1D optical lattice is generated by a Ti:Sapphire laser, whose frequency is stabilized on the same highly stable ZFP cavity. This laser beam is splitted into two parts. To perform the timing sequence, each one passes through an acousto-optic modulator to control its intensity and frequency. The beams are detuned by 260 GHz from the $5S_{1/2}$ - $5P_{3/2}$ resonance line to avoid spontaneous emission. With these laser parameters, the optical potential depth U_0 equals to $2.7 E_R$ ($E_R = \frac{\hbar^2 k^2}{2m}$ is the recoil energy).

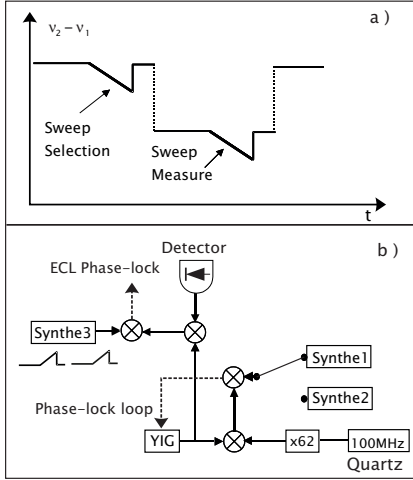


Fig. 2

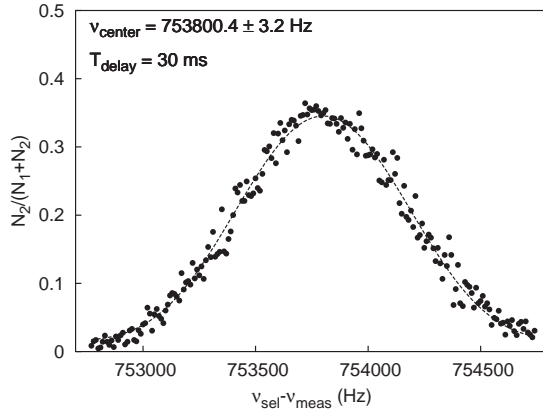


Fig. 3

Fig. 2 – a) Temporal variation of the frequency difference of the two Raman beams. b) The synthe1 and the synthe2 allow us to switch between the selection and a measurement steps. To compensate the Doppler shift during the falling of the atoms, the frequency of the synthe3 is swept linearly during the Raman pulses.

Fig. 3 – The final distribution velocity of atoms after a free fall of 30 ms. The center of the velocity distribution is located with an uncertainty of 3.2 Hz, corresponding to a relative uncertainty of 4×10^{-6} on the measurement of the acceleration of the gravity.

For this value, when the external acceleration is due to gravity, the transfer of atoms to the higher bands remains insignificant for several periods of Bloch oscillations.

Results. – In a first experiment, we determine g by measuring the atomic velocity variation after the free fall of atoms during 30 ms, using the $\pi-\pi$ Raman pulses sequence described previously. The typical final velocity distribution is shown in fig. 3. The center of this distribution is located with an uncertainty of 3.2 Hz (corresponding to $v_r/5000$) in an average time of 20 min, allowing a measurement of g with a relative uncertainty of 4×10^{-6} . This uncertainty is limited by many systematic errors. These errors may occur due to the vibration noise of the retroreflecting mirror [6], the fluctuation of the number of detected atoms and the atomic motion between the two pulses (effect of inhomogeneous fields).

In a second experiment, we apply between the two π -pulses a standing wave during an interrogation time T_{Bloch} . We then study the evolution of the final momentum distribution by changing T_{Bloch} . Before analyzing the experimental results, we briefly recall the relevant results of Bloch's theory. The energy spectrum of the particle presents a band structure (indexed by n) arising from the periodicity of the potential (optical lattice with period $d = \lambda/2$). The corresponding eigenenergies $E_n(q)$ and the eigenstates $|n, q\rangle$ (Bloch states) are periodic functions of the continuous quasi-momentum q , with a period $2k = 2\pi/d$. The quasi-momentum q is conventionally restricted to the first Brillouin zone $[-\pi/d, \pi/d]$. If we apply a constant force F , sufficiently weak in order to avoid interband transitions, a given Bloch state $|n, q(0)\rangle$ evolves (up to a phase factor) into the state $|n, q(t)\rangle$ according to

$$q(t) = q(0) + 2k \frac{t}{\tau_B} \pmod{2\pi/d}. \quad (1)$$

When the atoms are only submitted to the gravity force, the Bloch period τ_B is given

by $\frac{2\hbar}{mg\lambda}$. This period corresponds to the time required for the quasi-momentum to scan a full Brillouin zone. In our experiment, first we prepare Bloch states around $q = 0$ (in lattice frame) at the bottom of the fundamental energy band ($n = 0$) by turning on adiabatically the standing wave (rise time of $300 \mu\text{s}$): this avoids a transfer of population into the higher energy band. We point out that just before turning on the Bloch potential, selected atoms reach a mean velocity of about $10 v_r$. In order to compensate this velocity drift, the upward beam's frequency is shifted by $\sim 150 \text{ kHz}$ (in the laboratory frame the standing wave is then moving with a constant velocity of about $10 v_r$). To use a pure standing wave, we should launch atoms in ballistic atomic-fountain trajectories either from a moving molasses [10] or with Bloch oscillations [8], and turn on the Bloch potential when they reach their summit. After time T_B we suddenly switch off the optical potential and we measure the final momentum distribution in the first Brillouin zone. In fig. 4a we report the center of the measured peak as a function of the holding time T_B . The observed sawtooth shape is the signature of Bloch oscillations (eq. (1)). We observe more than 60 Bloch periods corresponding to the longest lived Bloch oscillator observed in bosonic systems. To determine the Bloch period τ_B , we measure the time interval between the centers of the two extreme slopes of sawtooth. We extract the value of τ_B by dividing this time interval by the number of periods. This measurement leads to a determination of the local acceleration of gravity with a relative uncertainty of 1.1×10^{-6} as $\frac{\hbar}{m}$ ratio [11] and the wavelength λ are known with a better accuracy. The linear fit of the experimental data in (fig. 4a) is performed by fixing the value of the recoil velocity. In fig. 4b we present the residuals of the fit; they increase when we move away from the center of the Brillouin zone. That reveals that there is a difference between the quasi-momentum

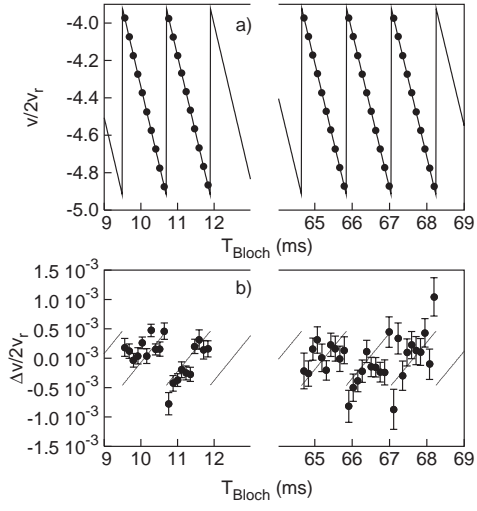


Fig. 4

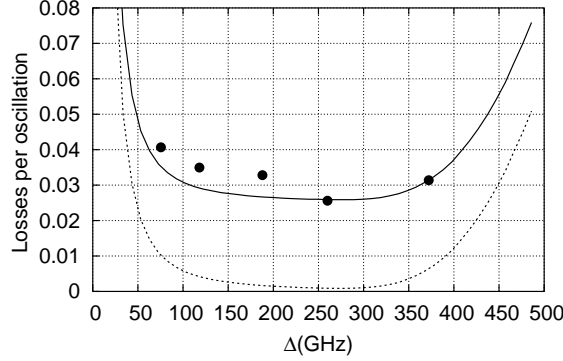


Fig. 5

Fig. 4 – a) The center of the final velocity distribution *vs.* the duration of the standing wave. The dot represents the experimental data and the line the least-square fit performed by fixing the recoil velocity. b) The residuals of the fit.

Fig. 5 – The losses per oscillation *vs.* detuning Δ . These losses are obtained by comparing the number of atoms measured after N oscillations to those measured after $N = 10$ oscillations. The relevant advantage of this presentation is to take into account only the losses during the Bloch oscillations process. Dot: the experimental data. Dotted line: theory. Solid line: theory including the interparticle collisions.

and the measured momentum of about $10^{-3} \times \hbar k$. The momentum spectrum $\Psi_{0,q}(p)$ can be calculated by projecting the Bloch state $|0, q\rangle$ onto plane-wave components $|p\rangle$ (measurement basis). Using analytic properties of the Bloch wave functions one obtains

$$\Psi_{0,q}(p) = \sqrt{\frac{2\pi}{d}} \tilde{\Phi}_0(p) \times \sum_l \delta(p - q - 2\pi l/d), \quad l \in \mathbb{Z}, \quad (2)$$

where $\tilde{\Phi}_0(p)$ is the Fourier transform of the Wannier function of the fundamental energy band [12]: the momentum spectrum is composed of peaks separated by the reciprocal-lattice vector, $2k = 2\pi/d$, with an amplitude given by the envelope function $\tilde{\Phi}_0(p)$. This function is not constant along the width of the selected velocity class. Thus the center of the measured momentum distribution is shifted with respect to the quasi-momentum $q(t)$ (eq. (1)) by a factor depending on the momentum spread. The data analysis allowing the determination of the Bloch period is performed in order to reduce substantially the systematic error induced by this effect.

When we increase the interrogation time of the standing wave up to 100 ms, the signal is significantly degraded (the loss rate becomes larger than 50%). In order to understand the origin of this losses, we have measured, for a given laser intensity, the losses per oscillation *vs.* the detuning Δ , relative to $F = 2 \rightarrow F = 3$ transition (fig. 5). These losses are obtained by comparing the number of atoms measured after N oscillations to those measured after $N = 10$ oscillations. The choice of the parameter Δ allows us to estimate the effects of the spontaneous photon scattering and the interband transitions which depend both on Δ (for interband transition see [7]). We observe that the losses exceed 3%; they are more important than the 0.5% rate losses measured using an accelerated standing wave [8]. This results from the slowness of the Bloch oscillations, since in a vertical standing wave the Bloch period is ~ 1.2 ms, when in ref. [8] the period was only ~ 0.1 ms.

For the experimental values of the standing-wave parameters, the losses induced by the spontaneous emission and the interband transitions in the weak binding limit do not match with the experimental data (dotted line in (fig. 5)). Performing a least-square fit based on this model and including collisions with the residual Rb vapor, we extract a characteristic time constant of the damping due to the collisions of about 70 ms. This value corresponds to the lifetime of the molasses for the residual vapor pressure in the cell. Therefore, we think that the number of Bloch oscillations in our experiment could be increased by reducing the pressure in the vacuum chamber.

Conclusion and prospects. – We have described an experimental method to measure the vertical velocity distribution of atoms by using a $\pi-\pi$ pulses sequence of Doppler-sensitive Raman transitions. We have performed a preliminary determination of the local acceleration of gravity with a relative accuracy of 10^{-6} by measuring the Bloch period. We have also demonstrated that the number of Bloch oscillations is not yet limited by either the interband transitions or the spontaneous emission, but only by collisions with the background atomic vapor. To overcome this limit, we are now building a new ultrahigh vacuum chamber where the magneto-optical trap will be loaded by an atomic slow beam. In order to improve the accuracy of the velocity measurement, a vibration-isolation system is also in implementation. These improvements should allow us to take a better benefit of the Bloch oscillations.

An attractive possibility consists in replacing the $\pi-\pi$ velocity measurement by a two $\pi/2$ Ramsey-Bordé sequence. We obtain then a $\pi/2-\pi/2$ -Bloch oscillation- $\pi/2-\pi/2$ atom-interferometer. Comparing this scheme to the $\pi/2-\pi-\pi/2$ atom-interferometer used in gravimetry [13, 14], where the pulses spacing time is limited by the effects related to the spatial position, the advantage would be to increase the measurement time thanks to Bloch oscillations

for a similar phase difference between the two paths. This way, we could reduce significantly the uncertainty of the gravity interferometric measurement. Finally, we suggest to use such experiment nearby a Watt balance site [15, 16]. In the dynamics mode of the balance the relation which equates the mechanical power and the electrical power is given by [16]

$$Mgv = CF_J F'_J h, \quad (3)$$

where M is the standard mass, v is the velocity of the vertical moving coil, h the Planck constant, C represents a dimensionless constant and F_J , F'_J denote the frequencies applied to a Josephson device. Using the g/h -dependence of the Bloch period we obtain

$$\frac{M}{m} = \frac{CF_J F'_J}{2} \frac{\lambda}{\nu_B} \frac{1}{v}. \quad (4)$$

In conclusion, associating our Bloch oscillations experiment to a Watt balance could be used to link a macroscopic mass to an atomic mass.

* * *

We thank A. CLAIRON and C. SALOMON for valuable discussions. This experiment is supported in part by the Bureau National de Métrologie (Contrats 993009 and 033006) and by the Région Ile de France (Contrat SESAME E1220).

REFERENCES

- [1] WILKINSON S. R., BHARUCHA C. F., MADISON K. W., QIAN NIU and RAIZEN M. G., *Phys. Rev. Lett.*, **76** (1996) 4512.
- [2] BEN DAHAN M., PEIK E., REICHEL J., CASTIN Y. and SALOMON C., *Phys. Rev. Lett.*, **76** (1996) 4508.
- [3] ANDERSON B. P. and KASEVICH M. A., *Science*, **282** (1998) 1686.
- [4] RAIZEN M. G., SALOMON C. and NIU Q., *Phys. Today*, **50** (1997) 30.
- [5] ROATI G., DE MIRANDES E., FERLAINO F., OTT H., MODUNGNO G. and INGUSCIO M., *Phys. Rev. Lett.*, **92** (2004) 230402-1.
- [6] CLADÉ P., GUELLATI-KHÉLIFA S., SCHWOB C., NEZ F., JULIEN F. and BIRABEN F., *Eur. Phys. J. D*, **33** (2005) 173.
- [7] PEIK E., BEN DAHAN M., BOUCHOULE I., CASTIN Y. and SALOMON C., *Phys. Rev. A*, **55** (1997) 2989.
- [8] BATTESTI R., CLADÉ P., GUELLATI-KHÉLIFA S., SCHWOB C., GRÉMAUD B., NEZ F., JULIEN L. and BIRABEN F., *Phys. Rev. Lett.*, **92** (2004) 253001-1.
- [9] CLAIRON A., LAURENT P., SANTARELLI G., GHEZALI S., LEA N. and BAHOURA M., *IEEE Trans. Instrum. Meas.*, **44** (1995) 128.
- [10] CLAIRON A., SALOMON C., GUELLATI S. and PHILLIPS W. D., *Europhys. Lett.*, **16** (1991) 165.
- [11] MOHR P. and TAYLOR B., *Rev. Mod. Phys.*, **72** (2000) 351.
- [12] KOHN W., *Phys. Rev.*, **115** (1959) 809.
- [13] PETERS A., CHUNG K. Y. and CHU S., *Metrologia*, **38** (2001) 25.
- [14] MCGUIRK J. M., FOSTER G. T., FIXLER J. B., SNADDEN M. J. and KASEVICH M., *Phys. Rev. A*, **65** (2002) 033608.
- [15] KIBBLE B. P., *Atomic Mass and Fundamental Constants*, Vol. 5, edited by SANDERS J. H. and WAPSTRA A. H. (Plenum, New York) 1976, p. 545.
- [16] EICHENBERGER A., JECKELMANN B. and RICHARD P., *Metrologia*, **40** (2003) 356.

Determination of the Fine Structure Constant Based on Bloch Oscillations of Ultracold Atoms in a Vertical Optical Lattice

Pierre Cladé,¹ Estefania de Mirandes,¹ Malo Cadoret,¹ Saïda Guellati-Khélifa,² Catherine Schwob,¹ François Nez,¹ Lucile Julien,¹ and François Biraben¹

¹Laboratoire Kastler Brossel, Ecole Normale Supérieure, CNRS, UPMC, 4 place Jussieu, 75252 Paris Cedex 05, France

²INM, Conservatoire National des Arts et Métiers, 292 rue Saint Martin, 75141 Paris Cedex 03, France

(Received 26 July 2005; published 23 January 2006)

We report an accurate measurement of the recoil velocity of ^{87}Rb atoms based on Bloch oscillations in a vertical accelerated optical lattice. We transfer about 900 recoil momenta with an efficiency of 99.97% per recoil. A set of 72 measurements of the recoil velocity, each one with a relative uncertainty of about 33 ppb in 20 min integration time, leads to a determination of the fine structure constant α with a statistical relative uncertainty of 4.4 ppb. The detailed analysis of the different systematic errors yields to a relative uncertainty of 6.7 ppb. The deduced value of α^{-1} is 137.035 998 78(91).

DOI: 10.1103/PhysRevLett.96.033001

PACS numbers: 32.80.Pj, 06.20.Jr, 32.80.Qk, 42.65.Dr

The fine structure constant α plays an important role among all the physical constants because it sets the scale of electromagnetic interactions. Therefore, it can be measured in different fields of physics and so be used to test the consistency of the physics. In the Committee on Data for Science and Technology (CODATA) adjustment [1], all accurate known determinations of α are used to give the best estimate of α (labeled α_{2002} for 2002 adjustment). But as pointed out in [1], the actual estimate α_{2002} is only determined by two data points and in fact mainly by the electron magnetic moment anomaly a_e experiment. This lack of redundancy in input data is a key weakness of the CODATA adjustment. For example, α_{2002} differs from α_{1998} by more than one sigma mainly because of some revisions in the complicated theoretical expression of a_e from which α is deduced [1]. Accurate determinations of α by completely different methods are absolutely needed. A competitive determination of α with respect to the a_e experiment is actually the measurement of the ratio h/m_{Cs} (where h is the Planck constant and m_{Cs} is the mass of the cesium atom) using ultracold atom interferometry [2]. The fine structure constant is related to the ratio h/m_X by [3]

$$\alpha^2 = \frac{2R_\infty}{c} \frac{A_r(X)}{A_r(e)} \frac{h}{m_X}, \quad (1)$$

where several terms are known with a very small uncertainty: 8×10^{-12} for the Rydberg constant R_∞ [4,5] and 4.4×10^{-10} for the electron relative mass $A_r(e)$ [1]. The relative atomic mass of X is known with relative uncertainty less than 2.0×10^{-10} for Cs and Rb atoms [6].

In this Letter, we report a new determination of the fine structure constant α deduced from the measurement of the ratio h/m_{Rb} based on Bloch oscillations. We describe a sophisticated experimental method to measure accurately the recoil velocity of a rubidium atom when it absorbs or emits a photon. The principle of this experiment is already

described in a previous Letter [7]: by using velocity-selective Raman transitions, we measure the variation of the atomic velocity induced by a frequency-chirped standing wave. This coherent acceleration arises from a succession of stimulated Raman transitions where each Raman transition modifies the atomic momentum by $2\hbar k$ ($k = 2\pi/\lambda$, λ is the laser wavelength), leaving the internal state unchanged. The acceleration process can also be interpreted in terms of Bloch oscillations in the fundamental energy band of an optical lattice created by the standing wave [8]: the atomic momentum evolves by steps of $2\hbar k$, each one corresponding to a Bloch oscillation. After N oscillations, we release adiabatically the optical lattice and we measure the final velocity distribution which corresponds to the initial one shifted by $2Nv_r$ ($v_r = \hbar k/m$ is the recoil velocity). In comparison with our prior setup [7], the Bloch beams (optical lattice) and the Raman beams (velocity measurement) are now in vertical geometry (Fig. 1, left). This scheme is more suitable to achieve a high precision measurement of the recoil velocity, because it allows us to increase significantly the number of transferred momenta.

An atomic sample of 3×10^7 atoms (^{87}Rb) is produced in a magneto-optical trap (MOT), followed by a $\sigma^+ - \sigma^-$ optical molasses. The final temperature of the cloud is $3 \mu\text{K}$, its radius at $1/\sqrt{e}$ is $\sim 600 \mu\text{m}$ and all the atoms are in the hyperfine state $F = 2$. An optical Zeeman re-pumper (resonant with the $F = 2, F' = 2$ transition) transfers the atoms to the $F = 2, m_F = 0$ hyperfine state.

Then, a narrow velocity class is selected to $F = 1, m_F = 0$ by using a counterpropagating Raman π pulse. The nonselected atoms are blown away using a resonant laser beam. After the acceleration process described later, the atomic velocity distribution is probed using a second Raman π pulse from $F = 1$ to $F = 2$ (Fig. 1, right). The population in both levels is detected using a time of flight technique [9]. The Raman beams are produced by two

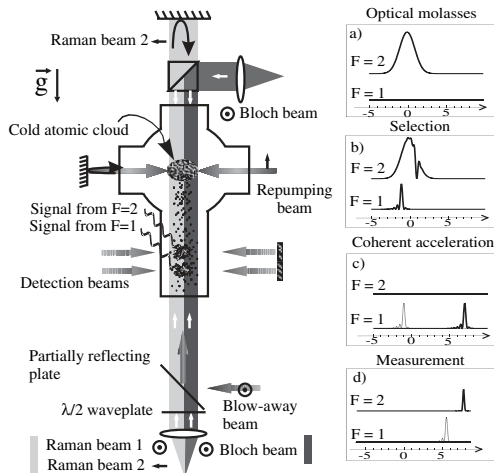


FIG. 1. Left: Experimental setup. The cold atomic cloud is produced in a MOT (the cooling laser beams are not shown); the Raman and the Bloch beams are in vertical geometry and the detection zone is at 15 cm below the MOT. Right: Evolution of the velocity distribution (in v_r unit) during one experimental cycle providing one point in the final velocity distribution shown in Fig. 3 (see the text and [7]).

stabilized laser diodes. Their beat frequency is precisely controlled by a frequency chain that allows us to easily switch the Raman frequency detuning from the selection (δ_{sel}) to the measurement (δ_{meas}). One of the lasers is stabilized on a highly stable Fabry-Perot cavity and its frequency is measured by counting the beatnote with a two-photon Rb standard [10]. The frequency of one Raman beam is linearly swept in order to compensate the Doppler shift induced by the fall of the atoms (Fig. 2) (with the same slope for the selection and the measurement). The Raman beams power is 8 mW and their waist is 2 mm. To reduce photon scattering and light shifts, they are blue detuned by 1 THz from the D2 line. The duration of the

π pulse is 3.4 ms: thus, the width of the selected velocity class is $v_r/50$. In order to reduce the phase noise, the Raman beams follow the same optical path: they come out from the same fiber and one of them is retroreflected (Fig. 1, left).

Coherent acceleration.—As shown in our previous Letter [7], Bloch oscillations of atoms in an optical lattice are a very efficient tool to transfer a large number of recoil momenta to the selected atoms in a short time. The optical lattice results from the interference of two counterpropagating beams generated by a Ti:sapphire laser (waist of 2 mm), whose frequency is stabilized on the same Fabry-Perot cavity used for the Raman beams and is blue detuned by ~ 40 GHz from the one-photon transition. The optical lattice is adiabatically raised in 500 μ s in order to load all the atoms into the first Bloch band. To perform the coherent acceleration, the frequency difference of the two beams is swept linearly within 3 ms using acousto-optic modulators. Then, the lattice intensity is adiabatically lowered in 500 μ s to bring atoms back in a well-defined momentum state. The optical potential depth is $70E_r$ ($E_r = \hbar^2 k^2 / 2m$ is the recoil energy). With these parameters the spontaneous emission is negligible. For an acceleration of 2000 ms^{-2} we transfer 900 recoil momenta in 3 ms with an efficiency of 99.97% per recoil. To prevent the atoms reaching the upper windows of the vacuum chamber, we use a double acceleration scheme (see Fig. 2): instead of selecting atoms at rest, we first accelerate them using Bloch oscillations and then we perform the three steps sequence: selection-acceleration-measurement. In this way the atomic velocity at the measurement step is close to zero.

In the vertical direction, an accurate determination of the recoil velocity would require a measurement of the gravity g . In order to get rid of gravity, we make a differential measurement by accelerating the atoms in opposite directions (up and down trajectories) keeping the same delay between the selection and the measurement π pulses. The ratio \hbar/m can then be deduced from

$$\frac{\hbar}{m} = \frac{(\delta_{\text{sel}} - \delta_{\text{meas}})^{\text{up}} - (\delta_{\text{sel}} - \delta_{\text{meas}})^{\text{down}}}{2(N^{\text{up}} + N^{\text{down}})k_B(k_1 + k_2)}, \quad (2)$$

where $(\delta_{\text{meas}} - \delta_{\text{sel}})^{\text{up/down}}$ corresponds, respectively, to the center of the final velocity distribution for the up and the down trajectories, $N^{\text{up/down}}$ are the number of Bloch oscillations in both opposite directions, k_B is the wave vector of the Bloch beams, and k_1 and k_2 are the wave vectors of the Raman beams. In Fig. 3 we present two typical velocity distributions for $N^{\text{up}} = 430$ and $N^{\text{down}} = 460$. The effective recoil number is then $2(N^{\text{up}} + N^{\text{down}}) = 1780$. The center of each spectrum is determined with an uncertainty of 1.7 Hz ($\sim v_r/10\,000$) for an integration time of 5 min.

The contribution of some systematic effects (energy level shifts) to δ_{sel} or δ_{meas} is inverted when the directions of the Raman beams are exchanged. To improve the ex-

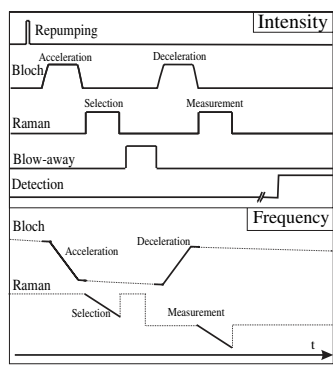


FIG. 2. Intensity and frequency timing of the different laser beams for the acceleration-deceleration sequence. (The scale of the frequency is not the same for the Bloch and the Raman beams).

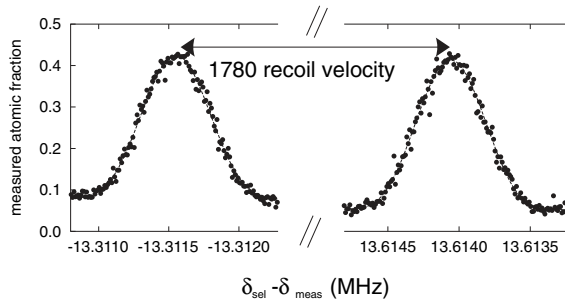


FIG. 3. Typical final velocity distribution for the up and down trajectories.

perimental protocol, for each trajectory, the Raman beams directions are reversed leading to the record of two velocity spectra. When the atoms follow exactly the same up or down trajectories, these systematic effects are cancelled by taking the mean value of these two measurements. Finally, one determination of α is obtained from four velocity spectra (20 min of integration time).

The Fig. 4 presents a set of 72 determinations of the fine structure constant α . From the uncertainty of each spectrum center we deduce the standard deviation of the mean. For these $n = 72$ measurements this relative uncertainty is 3.9 ppb with $\chi^2 \approx 90$. Consequently, the resulting statistical relative uncertainty on α is $3.9 \times \sqrt{\chi^2/(n-1)} = 4.4$ ppb.

Systematic effects analysis.—We detail now all the different systematic effects taken into account to determine the final value of α^{-1} and its uncertainty.

Laser frequencies: The frequency of the reference Fabry-Perot cavity on which the Bloch and the Raman lasers are stabilized is checked several times during the 20 min measurement, with respect to the Rb standard. The frequency drift is 1 MHz and we deduce the mean laser frequency with an uncertainty smaller than 100 kHz. Thus, we assume a conservative uncertainty of 300 kHz for the absolute determination of the different laser frequencies, which corresponds to 0.8 ppb on α^{-1} .

Beams alignment: We have measured the fiber-fiber coupling of the counterpropagating Bloch and Raman

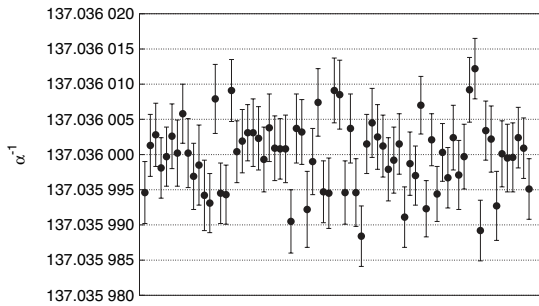


FIG. 4. Chronological display of 72 determinations of α^{-1} .

beams. It varies by less than 10% with respect to the maximum coupling. That corresponds to a maximum misalignment of 3.1×10^{-5} rad between the Raman beams and of 1.6×10^{-4} rad between the Bloch beams. The maximum systematic effect on α^{-1} is of -4×10^{-9} . Thus, we correct α^{-1} by (-2 ± 2) ppb.

Wave front curvature and Gouy phase: As the experimental beams are not plane waves, we have to consider the phase gradient in (2) instead of wave vectors k . For a Gaussian beam, the phase gradient along the propagation axis is

$$\frac{d\phi}{dz} = k - \frac{2}{kw^2(z)} - k \frac{r^2}{2R^2(z)} \frac{dR}{dz}, \quad (3)$$

where r is the radial distance from the propagation axis, $w(z)$ is the beam radius and $R(z) = z[1 + (z_r/z)^2]$ is the curvature radius. The first corrective term (Gouy phase) originates from the spread on the transverse momenta, which is inversely proportional to the beam transverse spatial confinement. The second term comes from the spatial variation of the phase due to the curvature radius. We have measured $w(z)$ and $R(z)$ with a wave front analyzer. The effective radial distance from the propagation axis is determined by the size of the atomic cloud (600 μ m) and a possible misalignment of the Bloch beam with respect to the atomic cloud. This misalignment is at maximum estimated at 500 μ m. The correction to α^{-1} is (-8.2 ± 4) ppb. This is our dominant systematic effect.

Magnetic field: Residual magnetic field gradients contribute to the systematics in two ways. First, there is a second order Zeeman shift of the energy levels which induces an error in the Raman velocity measurement. Second, the quadratic magnetic force modifies the atomic motion between the selection and the measurement. We have precisely measured the spatial magnetic field variations using copropagating Raman transitions. The Zeeman level shift is not totally compensated by changing the direction of the Raman beams because the two up (or down) trajectories are not completely identical. They differ by about 300 μ m, leading to a differential level shift of about (0.3 ± 0.1) Hz and a α^{-1} correction of (6.6 ± 2) ppb. The magnetic force changes the atomic velocity by $(2.3 \pm 0.7) \times 10^{-6}$ recoil velocity. We correct α^{-1} by (-1.3 ± 0.4) ppb.

Gravity gradient: Gravity is not totally compensated between up and down trajectories because they differ by about 10 cm. The correction to α^{-1} is (0.18 ± 0.02) ppb.

Light shifts: In principle, light shifts are compensated in three ways: between the selection and the measurement Raman pulses, between the upward and downward trajectories, and when the Raman beams direction is changed. However, this effect is not totally cancelled. This is firstly due to a different intensity at the selection and at the measurement because of the expansion of the cloud, sec-

A precise measurement of h/m_{Rb} using Bloch oscillations in a vertical optical lattice : determination of the fine structure constant

Pierre Cladé*, Estefania de Mirandes, Malo Cadoret, Saïda Guellati-Khélifa†,
 Catherine Schwob, François Nez, Lucile Julien, and François Biraben
*Laboratoire Kastler Brossel, Ecole Normale Supérieure, CNRS,
 UPMC, 4 place Jussieu, 75252 Paris Cedex 05, France*

Bloch oscillations in a frequency chirped optical lattice are a powerful tool to transfer coherently many photon momenta to the atoms. We have used this method to measure accurately the ratio h/m_{Rb} . In this paper we detail the experimental procedure and we present a complete analysis of the different systematic effects. They yield to a global relative uncertainty of 13 ppb. The measured value of h/m_{Rb} is $4.591\,359\,29(6) \times 10^{-9} \text{ m}^2 \cdot \text{s}^{-1}$. The deduced value of the fine structure constant is $\alpha^{-1} = 137.035\,998\,84(91)$ with a relative uncertainty of 6.7 ppb.

I. INTRODUCTION

The fine structure constant α is defined as

$$\alpha = \frac{e^2}{4\pi\epsilon_0\hbar c} \quad (1)$$

where ϵ_0 is the permittivity of vacuum, c is the speed of light, e is the electron charge and $\hbar = h/2\pi$ is the reduced Planck constant. The fine structure constant sets the scale of the electromagnetic interaction, which is one of the four fundamental interactions. It appears and so can be determined in different domains of physics, which spread from atomic physics to mesoscopic and macroscopic condensed matter physics and elementary particle physics. The relevance of the fine structure constant is that it is dimensionless, and therefore it does not depend on any unit system. Hence, this allows the comparison of all the various accurate measurements of α , which constitutes an interesting test of the consistency of physics. This comparison is regularly made by the international committee CODATA (Committee on Data for science and technology), which determines the recommended values of all the physical constants from an adjustment of all the relevant data available [1]. One key weakness of the last adjustment made in 2002 is the lack of redundancy in the input data for α . The estimation of this constant by CODATA2002 is essentially determined only by two data, from the measurement of h/m_{Cs} where m_{Cs} is the atomic mass of Cesium (relative uncertainty of 7.7 ppb)[2], and mainly by the electron magnetic moment anomaly a_e (relative uncertainty of 3.8 ppb).

This situation has been modified recently : after almost two decades of work, a new experimental measurement of a_e [3], along with an impressive improvement of the QED calculation [4] have lead to a new determination of α with a relative uncertainty of 0.70 ppb. This important result renews the need of other determinations

of α at 1 ppb level for several reasons : i) For the next CODATA adjustment, α will be mainly determined from only one measurement and this will be a true weakness. ii) To test more stringently the QED calculations of a_e , an independent determination of α is needed. iii) If we assume the accuracy of the QED calculation of a_e , another determination of α will give a limit upon a possible internal electron structure [5].

The recent proposal of a redefinition of the kilogram by fixing the value of the Planck constant h [6, 7] has also renewed the interest of having an accurate determination of the fine structure constant. The realization of h with the watt balance [7] relies on the validity of the expression $R_K = h/e^2 = \mu_0 c/(2\alpha)$ where R_K is the von Klitzing constant from the quantum Hall effect. At present time there is a minor difference (24 ± 18 ppb) between the determination of α deduced from R_K [8] and the one deduced from the recent measurement of a_e [5]. For a redefinition of the kilogram, a good alternative is to use the value of α issued from the a_e to define R_K , much more accurately than it can be measured from the quantum Hall effect. In this case, it seems prudent to independently check the used value of α as accurately as possible.

In this paper, we report a new determination of the fine structure constant with a relative uncertainty of 6.7 ppb which is a first step towards a 1 ppb measurement. This experiment takes benefit of 20 years of research on atom-light interaction. Nowadays, laser cooling techniques enable a precise and easy control of the atomic motion [9]. Many applications of those technics have been developed in metrology such as the realization of microwave and optical clocks [10, 11] or inertial sensors [12, 13]. One of the earliest applications to the measurement of fundamental constants has been the determination of the fine structure constant α using atom interferometry by S. Chu's group at Stanford, in 1991 [14]. This experimental determination of α is deduced from the measurement of h/m_{Cs} [2]. Indeed, the fine structure constant can be related to the ratio h/m_X [15] by

$$\alpha^2 = \frac{2R_\infty}{c} \frac{A_r(X)}{A_r(e)} \frac{h}{m_X} \quad (2)$$

where R_∞ is the Rydberg constant, $A_r(e)$ is the relative

*present adress : National Institute of Standards and Technology
 100 Bureau Drive, Stop 8424 Gaithersburg, MD 20899-8424

†INM, Conservatoire National des Arts et Métiers, 61, rue du
 Landy, 93210 La plaine Saint Denis, France

atomic mass of the electron and $A_r(X)$ the relative mass of the particle X with mass m_X . These factors are known with a relative uncertainty of 7×10^{-12} for R_∞ [16, 17], 4.4×10^{-10} for $A_r(e)$ [18] and less than 2.0×10^{-10} for $A_r(Cs)$ and $A_r(Rb)$ [19]. Hence, the factor limiting the accuracy of α is the ratio h/m_X .

In the present review we report a new determination of the fine structure constant α deduced from the measurement of h/m_{Rb} [20]. The principle of the experiment consists in determining h/m_{Rb} through the accurate measurement of the Rubidium recoil velocity $v_r = \hbar k/m_{Rb}$ when the atom absorbs or emits a photon of wavevector k .

To determine precisely the recoil velocity, we transfer to the atoms a very high number of photon momenta without spontaneous emission and then we measure their velocity variation. The induced acceleration arises from a succession of stimulated two-photon transitions using two counterpropagating laser beams. Each transition modifies the atomic velocity by $2v_r$ leaving the internal state unchanged. This acceleration process can also be interpreted in terms of Bloch oscillations in the fundamental energy band of the periodic potential created by an optical standing wave. Bloch oscillations are a powerful tool to transfer to the atoms a very high number of recoil velocities in a short time with a high efficiency [21].

To measure accurately the atomic velocity variation, we prepare a narrow and well determined initial velocity distribution. For this purpose we use two counter-propagating laser beams to induce a velocity selective Raman transition. This first step defines the initial velocity class. After the acceleration process, the final atomic velocity is determined by measuring the Doppler effect by a second counter-propagating velocity selective Raman transition. To determine the whole velocity profile the second Raman transition is scanned in frequency. The final uncertainty in the measurement of the recoil velocity σ_{v_r} will therefore depend on two factors : i) the uncertainty σ_v of the *Raman inertial sensor* which measures the atomic velocity variation and ii) the number $2N$ of photon momenta transferred to the atoms : $\sigma_{v_r} = \sigma_v/2N$.

The discussion is organized as follows. First, the Raman velocity sensor is described in Sec.(II) along with the noise sources which limit its sensitivity. Next, in Sec.(III), we study the physical processus used to transfer to the atoms a high number of recoil velocities, i.e. Bloch oscillations in a frequency chirped standing wave. In Sec.(IV) we present our experimental setup and in Sec.(V) our determination of the fine structure constant. Finally, in Sec. (VI) we detail the systematic effects which limit the accuracy on h/m_{Rb} and α .

II. THE VELOCITY SENSOR

In this section we introduce the velocity sensor used to select and measure a narrow atomic velocity class. We also discuss the noise and error sources limiting the ac-

curacy of the velocity sensor.

A. Accurate selection and measurement of a narrow velocity class

The principle of the velocity sensor is described in Fig.(1). The main tool is the velocity selective Raman transition between two hyperfine levels $|a\rangle$, $|b\rangle$ of the ground state, with energies E_a and E_b . This transition is realized by using two counterpropagating laser beams with frequencies ω_1, ω_2 and wavevectors $\mathbf{k}_1, \mathbf{k}_2$. After the cooling process, the atoms are all in a well defined internal state $|b\rangle$. We apply a first velocity selective Raman π pulse ($|b\rangle \rightarrow |a\rangle$) to define an initial velocity class centered on v_i . At resonance :

$$\delta_{sel} = \Delta_l + (\mathbf{k}_1 - \mathbf{k}_2) \cdot \left(\mathbf{v}_i + \frac{\hbar}{2m}(\mathbf{k}_1 - \mathbf{k}_2) \right) \quad (3)$$

where $\delta_{sel} \equiv \omega_1 - \omega_2 - \omega_{HFS}$ is the Raman detuning from the atomic resonance ($\hbar\omega_{HFS} = E_b - E_a$) and Δ_l is a differential shift of the atomic levels. This level shift takes into account a possible light shift and quadratic Zeeman level shifts. To cancel the associated systematic effects we use an experimental procedure described in the next section. The second term corresponds to the Doppler effect and to the atomic recoil. After this first step, we push away the remaining atoms in $|b\rangle$ by using a resonant beam tuned to the one-photon transition. Then an acceleration changes the atomic velocity from v_i to v_f (see section III). Finally, to measure the final velocity, we apply a second π pulse ($|a\rangle \rightarrow |b\rangle$) with a detuning δ_{meas} . To reconstruct the final velocity distribution, we repeat all the precedent steps by scanning the detuning δ_{meas} . The variation of velocity Δv is given by

$$\Delta \mathbf{v} \cdot (\mathbf{k}_1 - \mathbf{k}_2) = (\delta_{meas}^{max} - \delta_{sel}) \quad (4)$$

where δ_{meas}^{max} is the detuning at the maximum of the velocity distribution.

The final populations in both states $|a\rangle$ and $|b\rangle$ are measured by fluorescence using the time of flight technique (see section IV). We emphasize that, even if the time of flight technique was initially developed for measuring the temperature of the cold atomic sample [22], we only use this method to extract information about the fraction of atoms in each hyperfine level.

As mentioned before, in such experiments, Raman transitions involve two hyperfine levels of the ground state. Therefore the width of the resonant velocity class Δv is only determined by the photon coupling and the duration of the Raman pulse τ . In particular, for a π pulse

$$\Delta v \simeq \frac{1}{\tau(k_1 + k_2)} \quad (5)$$

As an example, for Rubidium $(k_1 + k_2)v_r \simeq 15$ kHz, one selects an atomic velocity class of width $\Delta v \simeq \frac{v_r}{15}$ for $\tau=1$ ms.

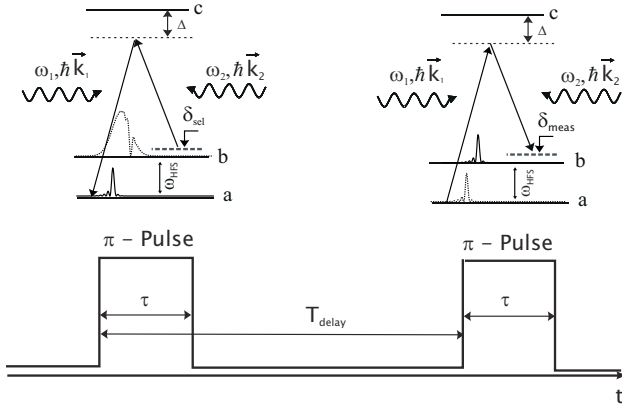


FIG. 1: Principle of the velocity sensor : The first Raman π pulse drives a narrow velocity class of atoms from initial internal state $|b\rangle$ to state $|a\rangle$. The remaining atoms in $|b\rangle$ are pushed away. To measure the final velocity of atoms in $|a\rangle$ we use a second Raman π pulse. This pulse transfers from $|a\rangle$ to $|b\rangle$ a velocity dependent fraction of atoms.

B. Error sources and noise of the velocity sensor

Eq.(3) shows that we have to control carefully the frequency difference between the two laser beams $\omega_1 - \omega_2$ and the differential atomic level shifts Δ_l in order to ensure a good accuracy in the velocity measurement.

We are mainly concerned by two level shifts : light shifts and quadratic Zeeman shifts. In principle, level shifts are compensated between the selection and the measurement if they are induced by a constant field. However there is a residual effect due to laser intensity fluctuations and spatial inhomogeneities of the magnetic field.

Nevertheless, the corresponding error in the determination of the recoil velocity changes sign when the direction of the Raman beams is reversed. Thus, the velocity is obtained from the mean value of two velocity measurements exchanging the Raman beams. This idea is reflected writing the resonance condition for the two configurations :

$$\delta = \Delta_l(z, t) - \epsilon_R(k_1 + k_2)(v_i + \epsilon_R \frac{\hbar}{2m}(k_1 + k_2)) \quad (6)$$

with $\epsilon_R = +1(-1)$ for the configuration defined I (II) when the Raman recoil is upward (downward). From the two measurements of δ , we obtain

$$\frac{\delta^{II} - \delta^I}{2} = \frac{\Delta_l(z^{II}, t^{II}) - \Delta_l(z^I, t^I)}{2} + (k_1 + k_2)v_i \quad (7)$$

Assuming that both measurements take place at the same spatial point and that the magnetic field has a periodic dependence with the experimental sequence we have : $\Delta_l(z^{II}, t^{II}) \simeq \Delta_l(z^I, t^I)$. Hence, the atomic velocity can be written as

$$v_i = \frac{\delta^{II} - \delta^I}{2(k_1 + k_2)} \quad (8)$$

which is free from the systematic effect $\Delta_l(z, t)$.

The noise sources limiting the sensitivity of our velocity sensor have been widely studied in a previous paper [23]. At present, we are limited by the noise on the detection setup and the vibration noise of the retroreflecting mirror. The last can be reduced by an actively stabilized anti-vibrations platform.

From all these considerations we are able to define the center of the atomic velocity distribution with an statistical uncertainty better than $v_r/10000$ in 5 min of integration time.

III. COHERENT ACCELERATION OF THE ATOMS : BLOCH OSCILLATIONS

In this section we describe the physical process to accelerate the atoms transferring them a well defined number of recoil momenta by means of Bloch oscillations [24]. We also discuss some systematic effects that may arise from the modification of the velocity distribution of atoms in the optical lattice when we switch off the optical potential and we justify the choice of a blue detuning for the Bloch laser beams.

A. Atoms in a periodic optical potential

The atoms are coherently accelerated by using two counter-propagating laser beams inducing a succession of two photon Raman transitions. Each transition modifies the atomic velocity by $2v_r$ leaving the internal state unchanged. In order to compensate the Doppler shift the frequency difference of the two laser beams is linearly swept. A more suitable approach based on Bloch formalism allows a more subtle description of the process : the interference of the two laser beams leads to a periodic light shift of the atomic energy levels. Thus, the atoms feel a periodic potential

$$U(x) = U_0 \cos^2(kx) \quad (9)$$

where $U_0 = \frac{\hbar\Gamma}{2} \frac{I}{I_s} \frac{\Gamma}{\Delta}$, Γ being the natural width of the transition, Δ the detuning from the one photon transition, I the laser intensity of each beam and I_s the saturation intensity.

The periodicity of the potential leads to the well known energy band structure, historically developed to describe the dynamics of electrons in a perfect crystal [25]. Bloch theorem introduces two quantum numbers to solve this problem : n , the band index and the wavevector q (quasi-momentum) which plays the same role in the motion of a particle in a periodic potential as the free particle wavevector p (true momentum) in the absence of any external potential.

The eigenstates solution of the corresponding Bloch Hamiltonian for a stationary periodic potential can be

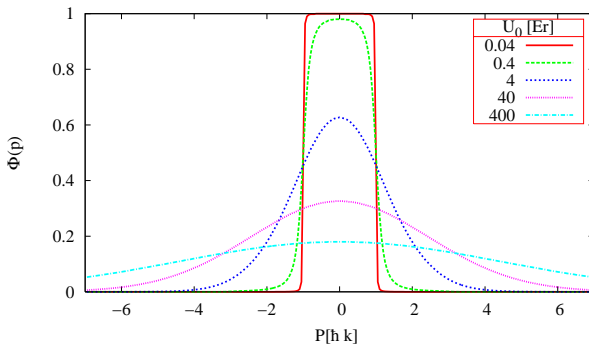


FIG. 2: (color online). Wannier function in momentum space $\phi(p)$ for different potential heights U_0 . When the potential depth is close to zero, the Wannier function is constant all over the first Brillouin zone and tends to 1.

written in momentum space as

$$|\psi_{n,q}\rangle = |n, q\rangle = \sum_l \phi_n(q + 2lk)|q + 2lk\rangle \quad (10)$$

with $l \in \mathbb{Z}$. Here $|q\rangle$ designs the ket associated to a plane wave of quasimomentum q and the amplitudes ϕ_n correspond to the Wannier function [26] in momentum space. From eq.(10) we see that the only states coupled by the potential $U(x)$ are the plane waves with a momentum differing by a multiple of $2\hbar k$. The Wannier function ϕ_0 for the fundamental energy band is shown in Fig.(2) for various potential depths U_0/E_r ($E_r = \hbar^2 k^2 / 2m$ is the recoil energy).

Now we consider a linear frequency chirp between the two laser beams $\Delta\omega(t)$. From the laboratory frame, the periodic potential $U(x)$ is now moving with a velocity $v(t) = \frac{\Delta\omega(t)}{2k}$. If $\Delta\omega(t)$ is adiabatically swept the atoms evolve in the same energy band i.e. the fundamental band. The temporal evolution of the atomic wavefunction in momentum space is then given by

$$|\Psi'(t)\rangle = \sum_l \phi_n(q(t) + 2lk)|q_0 + 2lk\rangle \quad (11)$$

where q_0 is the quasimomentum associated to the center of the initial atomic velocity distribution and $q(t) = q_0 + mv(t)/\hbar$. Consequently, only the enveloping Wannier function ϕ_n is time dependent. The atomic momentum distribution is periodic in time because it is described as the product of a Dirac comb with a time translated envelop.

From the reference frame of the moving potential the atomic momentum distribution is now written as the product of a stationary enveloping Wannier function (centred in $q = 0$) by a time translated Dirac comb. Therefore $q(t)$ scans periodically the Brillouin zone giving rise to the well known Bloch oscillations.

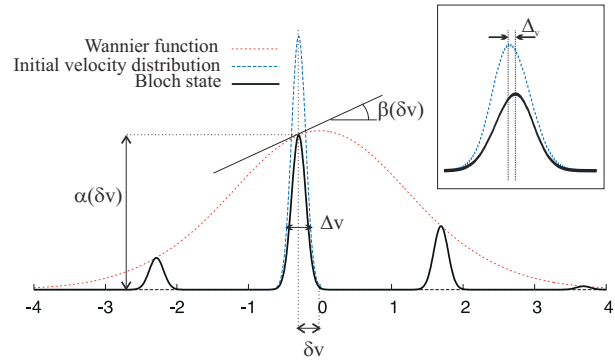


FIG. 3: (color online). In this figure the envelop (dotted curve) corresponds to the Wannier function in momentum space $\phi_0(p)$. This function modulates the Bloch states (solid line). Δv is the width of the velocity distribution and δv is the difference between the atomic velocity and the center of the first Brillouin zone. $\alpha(\delta v)$ is the value of the Wannier function for a given δv and $\beta(\delta v)$ is the derivative of the Wannier function normalized with respect to v_r . The inset is a zoom of the center of the Brillouin zone. It shows the shift Δ_v due to the Wannier function.

B. Analysis of the final velocity distribution : effect of the optical potential

In this section we discuss the displacement of the center of the final velocity distribution when the optical potential is switched off non adiabatically. This effect was briefly described in a previous paper [27] where we presented a measurement of the Bloch oscillation frequency of atoms in standing wave in the presence of the gravity field. In that experiment the effect induces a modification of the amplitude of the oscillations but does not give rise to a systematic effect in the Bloch frequency. This is not the case for the measurement presented in this paper.

We start from a selected narrow velocity class $\eta_{sel}(p)$ centered around $p = 0$. Then we load the atoms in the fundamental energy band $n = 0$. By linearly chirping the frequency difference of the laser beams the atoms are subjected to perform N Bloch oscillations acquiring $2\hbar k$ per oscillation. At the end of this process if the potential is switched off in a sudden way, non adiabatically, the final momentum distribution $\eta_{fin}(p + 2N\hbar k)$ can be obtained projecting the atomic wavefunction $\Psi(t)$ in p space. We find that the final momentum distribution, around the peak at $2N\hbar k$, is given by

$$\eta_{fin}(p + 2N\hbar k) = |\phi_0(p + m\delta v)|^2 \eta_{sel}(p) \quad (12)$$

where δv is the difference between the average velocity of the cloud and the velocity of the optical lattice, i.e. the velocity of the cloud is $2Nv_r + \delta v$. The final distribution η_{fin} is given by the initial one η_{sel} modulated by the enveloping Wannier function $\phi_0(p)$. This leads not only to a reduction of the signal but also to a shift of the center of the distribution which depends on δv (see Fig.(3)). Let

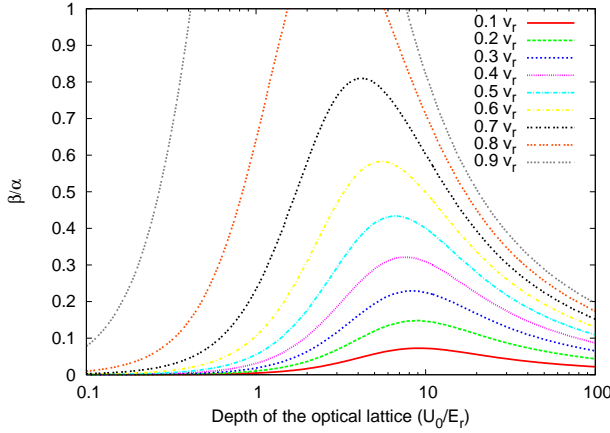


FIG. 4: (color online). Numerical simulation of the ratio β/α versus the potential depth for different values of δv . This ratio increases fast when getting away from the center of the Brillouin zone.

we estimate the corresponding systematic effect Δ_v in the measurement of the velocity. Assuming that the initial momentum distribution is $\Delta p \ll \hbar k$, one can develop $|\phi_0|^2$ to the first order. Then eq.(12) becomes :

$$\eta_{fin}(p + 2N\hbar k) = \left(\alpha(m\delta v) + \beta(m\delta v) \times \frac{p}{\hbar k} \right) \eta_{sel}(p) \quad (13)$$

where $\alpha(v) \equiv |\phi_0(v)|^2$ and $\beta(v) \equiv v_r \frac{d\alpha}{dv}$.

Consequently, if the initial velocity distribution $\eta_{sel}(p)$ is centered around $p = 0$, the final velocity distribution $\eta_{fin}(p)$ is not centered on $2N\hbar k$ but shifted by $m\Delta_v$ because of the first factor of eq.(13) (see the inset of Fig.(3)). Close to the maximum of $\eta_{sel}(p)$ we obtain the following order of magnitude for this effect

$$\frac{\Delta_v}{v_r} \propto \frac{\beta(\delta v)}{\alpha(\delta v)} \left(\frac{\Delta p}{\hbar k} \right)^2 \quad (14)$$

Fig.(4) shows the numerical calculation of the ratio of coefficients β/α as a function of the potential depth U_0 for different values of δv . This ratio is maximal at the edge of the first Brillouin zone.

As an example, for a 1.2 ms π pulse, with $U_0 = 10E_r$ and $\delta v = 0.3v_r$ the systematic effect on the velocity measurement (evaluated from a numerical calculation of the coefficients of eq.(14)) is about $7 \times 10^{-5}v_r$.

Instead, if the potential is adiabatically lowered, the Wannier function, which depends strongly on U_0 (see Fig.(2)), tends to a square function over the first Brillouin zone and thus $\alpha(v) \rightarrow 1$ and $\beta(v) \rightarrow 0$ for $|\delta v| \leq v_r$. No systematic effect in the measurement of the final velocity profile is then derived. Hence, in the experiment to determine h/m_{Rb} the optical potential has been switched off adiabatically.

C. Choice of blue detuning of the potential to reduce spontaneous emission

In this section we discuss the effect of a red or blue detuning Δ of the optical potential in the spontaneous emission rate. Indeed, spontaneous emission limits the number N of Bloch oscillations the atoms are able to perform. Let us derive an expression comparing the rate of spontaneous emission for a red and a blue detuned potential. For our periodic potential (9) the spontaneous emission rate is given by

$$P_{sp}(x) = \frac{U_0}{\hbar} \frac{\Gamma}{\Delta} \cos^2(kx) \quad (15)$$

In particular, for a Bloch state $|\Psi_{n,q}(x)\rangle$ the average spontaneous emission rate can be derived from $\langle \Psi_{n,q}(x) | P_{sp}(x) | \Psi_{n,q}(x) \rangle$. One can write

$$\langle \cos^2(kx) \rangle = \frac{1}{2} c(U_0, q) \quad (16)$$

where $c(U_0, q)$ is a corrective factor which considers the beams interference. Therefore,

$$c(U_0, q) = 1 + \langle \Psi_{n,q}(x) | \cos(2kx) | \Psi_{n,q}(x) \rangle \quad (17)$$

In the tight binding limit $|U_0| \gg E_r$, the atoms can be well described by particles trapped in a single lattice well. Let us now distinguish two cases : red and blue detuning of the potential.

1. Red detuning of the potential $\Delta < 0$.

If $\Delta < 0$, the atoms are trapped in the spatial region x_0 where the intensity of the field is the highest. Hence, we can approximate $\langle \cos(2kx) \rangle \simeq 1 + \langle -2k^2 x^2 \rangle$ assuming $x_0 = 0$. To calculate $\langle -2k^2 x^2 \rangle$ we recall the expression of the mean value of a harmonic potential for the ground state $\langle -U_0 k^2 x^2 \rangle = \frac{1}{2} \sqrt{|U_0| E_r}$. We find

$$c(U_0, q)_{red} = 2 - \sqrt{\frac{E_r}{|U_0|}} \simeq 2 \quad (18)$$

We conclude that for a red detuning the atoms are lead to the trap center seeking the highest field, and the spontaneous emission rate increases by a factor of 2 with respect to two non-interfering beams.

2. Blue detuning of the potential $\Delta > 0$

If $\Delta > 0$ the atoms are trapped at the spatial regions with minimum intensity. Therefore, the proper assumption now is $\langle \cos(2kx) \rangle \simeq -1 + \langle +2k^2 x^2 \rangle$. An identical

calculation as in the previous section leads to

$$c(U_0, q)_{blue} = 1 + \langle \cos(2kx) \rangle = \sqrt{\frac{E_r}{|U_0|}} \quad (19)$$

As a consequence, the ratio between the spontaneous rate in a blue detuned lattice to a red detuned one is

$$\frac{P^{blue}}{P^{red}} = \frac{1}{2} \sqrt{\frac{E_r}{|U_0|}} \quad (20)$$

Notice that this result can also be expressed in terms of the Lamb-Dicke parameter η [28] equal, in our case, to $(E_r/4U_0)^{1/4}$.

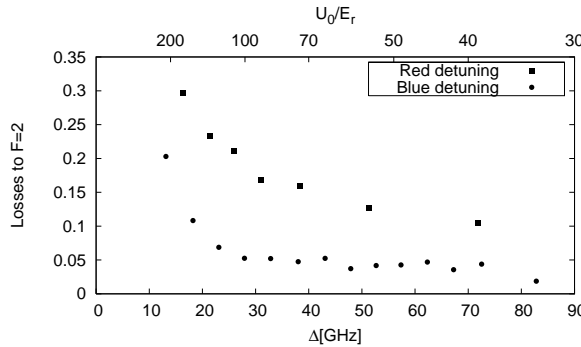


FIG. 5: Losses to $F=2$ induced by spontaneous emission versus the detuning Δ . A blue detuning of the potential (circles) leads to less atomic losses than a red detuning (squares). As the intensities of the two Bloch beams are slightly different, the ratio between the losses (for red and blue detuning) does not verify the quantitative behavior predicted by the model described in this section.

Hence, for $U_0 \gg E_r$ a blue detuned potential causes less spontaneous emission than a red detuned one. These results have been confirmed by the following experiment (see Fig.(5)) : after the selection step we accelerate the atoms in $F=1$ during a given time. We evaluate the losses by measuring the fraction of atoms transferred to $F=2$ by spontaneous emission. As predicted, we see that a blue detuned potential induces less losses than a red detuned one. However, the ratio between the losses (for red and blue detuning) does not verify the quantitative behavior predicted by eq.(20). This is probably due to intensity imbalance the two laser beams. The ratio of losses for a blue and a red detuning that we measure is about 4 compared to 10 expected by eq.(20). This corresponds to an intensity imbalance of about 15% between the two laser beams.

D. Effect of the transverse dipolar force on the width of the atomic velocity distribution

Up to now, we have neglected the atomic transverse degree of freedom. The finite size of the laser beams gives

rise to a transverse dipolar force that pushes the atoms to (away from) the center of the beam in case of red (blue) detuning. In the next paragraph we calculate this force and the associated acceleration focusing in the tight binding regime and with a blue detuning of the potential.

We want to evaluate the potential energy $E(r)$ of an atom subjected to the potential $U(r, x)$ as a function of its distance r from the propagation axis. We use a classical treatment for the transverse variable r and the Bloch formalism for the propagation axis variable x . The optical potential can be written as

$$U(r, x) = U_0 \cos^2(kx) e^{-2r^2/w_0^2} \quad (21)$$

where w_0 is the beam waist. We consider an atom in the fundamental energy band. The average atomic energy is therefore

$$E(r) = U_0 e^{-2r^2/w_0^2} \langle \cos^2(kx) \rangle \quad (22)$$

The transverse dipolar force is then

$$F = E_r \frac{2r}{w_0^2} \frac{U_0}{E_r} e^{-2r^2/w_0^2} c(U_0, q) \quad (23)$$

where $c(U_0, q)$ is defined in eq.(17). In Sec.(III.D) we showed that in the tight binding regime and for a blue detuning of the potential, $c(U_0) = \sqrt{\frac{E_r}{|U_0|}}$. Thus, the transverse acceleration for $r \ll w_0$ is given by

$$a_\perp = \frac{E_r}{m} \frac{2r}{w_0^2} \sqrt{\frac{|U_0|}{E_r}} \quad (24)$$

As an example, for typical parameters $w_0 = 2$ mm and $r = 500 \mu\text{m}$, $a_\perp \approx 4,3 \sqrt{\frac{|U_0|}{E_r}}$ ($\text{mm} \cdot \text{s}^{-2}$). For 10 ms of Bloch oscillations and $U_0 \approx 100E_r$, we find a variation of the atomic transverse velocity of $0.43 \text{ mm/s} \approx v_r/10$. This shift is negligible compared to the spread of the transversal atomic velocity distribution. In conclusion, a blue-detuning of the Bloch laser beams does not induce a significative transverse broadening of the atomic cloud.

IV. EXPERIMENTAL SETUP

In this section we detail the experimental protocol and we present our results in the determination of the ratio h/m_{Rb} and the fine structure constant α along with their statistical uncertainty.

The experimental sequence begins with the loading of a standard magneto-optical trap (MOT) from a Rubidium vapor. After a few seconds the magnetic field is switched off and the atoms equilibrate in an optical molasses, reaching a temperature of $3 \mu\text{K}$. Then the experiment develops in three steps : i) we select a narrow subrecoil velocity class using a Raman velocity selective π pulse ; ii) we accelerate coherently the atoms transferring

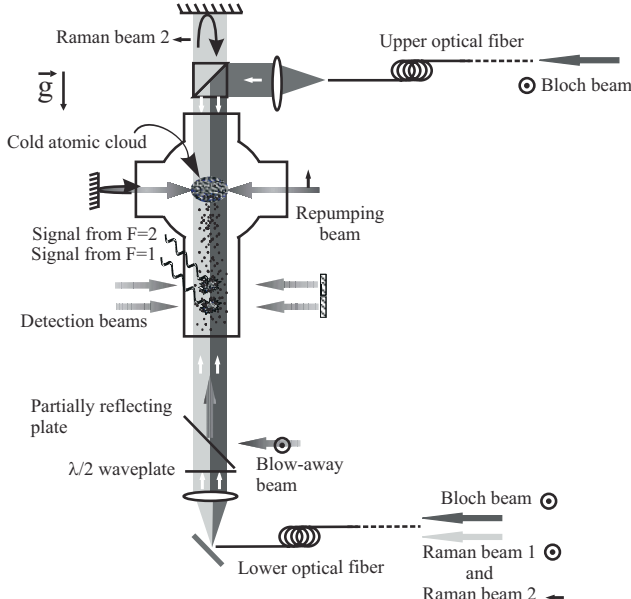


FIG. 6: Scheme of the experimental setup : the cold atomic cloud is produced in a MOT (the cooling laser beams are not shown). The Raman and the Bloch beams are in vertical geometry. The Raman beams and the upward Bloch beam are injected into the same optical fiber. The "blow-away" beam is tuned to the one photon transition and allows us to clear the atoms remaining in $F=2$ after the selection step. The populations in the hyperfine levels $F=1$ and $F=2$ are detected by fluorescence at 15 cm below the MOT using a time of flight technique.

to them $2N$ photon momenta by means of Bloch oscillations; iii) we probe the final velocity distribution using another Raman π pulse. Then we measure the proportion of atoms in the different hyperfine states. The Bloch and Raman beams are in vertical configuration. The detailed procedure is the following :

A. Zeeman repumper

At the end of the optical molasses phase, 3×10^7 ^{87}Rb atoms are in $F = 2$ state, equally distributed among all m_F sublevels. In the experiment we address only the atoms in $m_F = 0$ state. Hence, to pump the atoms to $|F = 2, m_F = 0\rangle$, we shine during $50\ \mu\text{s}$ a laser beam (Zeeman repumper) linearly polarized, parallel to the quantification axis and resonant with the $F = 2 \rightarrow F' = 2$ transition. The Clebsch-Gordan coefficient between $|F = 2, m_F = 0\rangle \rightarrow |F' = 2, m'_F = 0\rangle$ is zero, so after many cycles, the atoms will be optically pumped to $|F = 2, m_F = 0\rangle$ state. The repumper beam increases the atomic fraction in $|m_F = 0\rangle$ state, but it transfers momentum to the atoms broadening the velocity distribution. Experimentally, the $|F = 2, m_F = 0\rangle$ density in momentum space increases by a factor of two.

B. Selection of a sub-recoil velocity class

In order to select a narrow subrecoil velocity distribution we use a square counter-propagating Raman pulse in $\text{lin} \perp \text{lin}$ configuration, with a frequency detuning fixed at δ_{sel} . A bias vertical magnetic field of 150 mG parallel to the propagation axis of the Raman beams is applied so that only the $m_F = 0$ sublevel takes part in the Raman transition. The Raman pulse transfers atoms from $5S_{1/2} |F = 2, m_F = 0\rangle$ to $5S_{1/2} |F = 1, m_F = 0\rangle$ state. To reduce photon scattering and light shifts the Raman lasers are blue detuned by 1 THz from the D2 line. This detuning is chosen so that the Raman frequencies are close to the two-photon ^{85}Rb standard [29]. For a power of 8 mW and a beam waist of 2 mm, the π condition is achieved using a $\tau = 3.4$ ms pulse. The width of the selected velocity class is $v_r/50$.

In order to reduce the phase noise, the two Raman beams follow the same optical path. They reach the lower part of the cell by the same fiber and to achieve a counter-propagating configuration one of them is retro-reflected in the upper part of the cell. During the Raman pulse, the frequency of one Raman beam is linearly swept in order to compensate the Doppler shift induced by the fall of the atoms under the gravity field.

We generate the Raman beams by phase-locking two extended cavity diode lasers (ECL). Their frequencies and phase difference are then referenced to a stable frequency source and can be controlled precisely. The beat note of the two overlapped beams ($f_{\text{Raman}} \simeq 6.834$ GHz) is detected by a fast photodiode, amplified and mixed down with a local oscillator (YIG) at a frequency $f_{\text{YIG}} \simeq 6.409$ GHz to a more convenient intermediate frequency 425 MHz. This frequency is mixed with a frequency ramp around 25 MHz generated by a modulated synthesizer (SRS DS345). This ramp compensates the Doppler effect of the free falling atoms and can be used both for the selection and the measurement. An adjustable band-pass filter keeps only the beatnote at 400 MHz which is again divided by 4 and compared to the signal at 100 MHz from a referenced quartz. The frequency of this quartz is referenced to the Cs clock thanks to our optical fiber link with the LNE-SYRTE (Primary French Time Frequency Laboratory) [30]. Their beat note is amplified once again and used as the input for three feedback paths. The fastest path acts directly on the diode. The second path uses the modulation input of the diode laser current controller. The slowest path uses a piezo-electric transducer to adjust the length of the ECL cavity.

The lasers are amplified in master-slave configurations with the slave being a high power diode laser. Amplitude control of the laser light is achieved using 80 MHz acousto-optic modulators (AOM) whose radio frequencies are also referenced to the same stable 100 MHz quartz oscillator. The frequencies of the Raman and Bloch beams are stabilized onto an ultrastable zerodur Fabry-Perot cavity. We measure precisely one of the Raman beams frequency by counting its beatnote with a

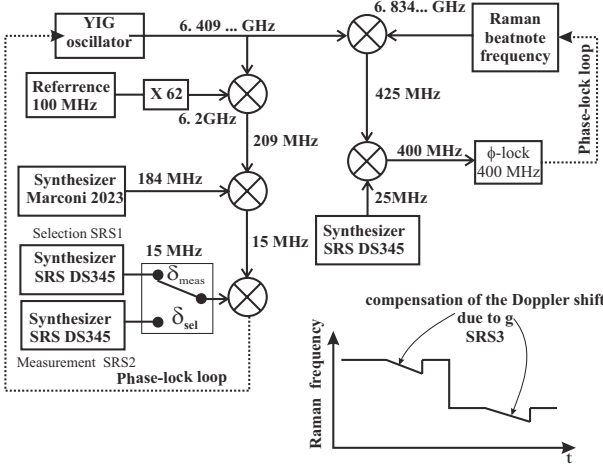


FIG. 7: Phase locking scheme for the Raman beams. The YIG oscillator is phase locked at 6.409..GHz by mixing it down with the 62th harmonic of the quartz oscillator and with two synthesizers (Marconi 2030 and SRS DS345). All the synthesizers are referenced to the Cs clock. To perform the selection or the measurement, we switch between the two SRS DS345 synthesizers. A third SRS synthesizer is used to compensate the Doppler shift induced by the local acceleration of gravity.

standard : the two-photon $5S_{1/2}(F=3) - 5D_{1/2}(F=5)$ transition of ^{85}Rb at $\nu_{2ph} = 385285142378(2)$ kHz [29, 31] (see Fig.(8)). From the beatnote we can determine the Raman beams wavelength, the free spectral range of the cavity and hence the Bloch beams wavelength. We use this optical reference to calibrate continuously the thermal drift of the cavity. The laser wavelengths can be thus determined with an uncertainty of 300 kHz.

C. Push beam

After the Raman selection, the non-selected atoms remaining in $F = 2$ are removed by a 3 ms laser pulse resonant with the $F = 2 \rightarrow F' = 3$ transition. This beam is 6.8 GHz out of resonance from the atoms in $F=1$ and could exert a dipolar force on the Raman selected cloud. To avoid this force the push beam is placed parallel to the Raman beams. Thus, the gradient of the dipolar force is transversal and there is no effect on the atoms longitudinal velocity.

D. Coherent acceleration

The optical lattice is the result of the interference of two counter-propagating laser beams in $lin||lin$ configuration. They are blue detuned by 40 GHz from the one photon transition $5^2S_{1/2} \rightarrow 5^2P_{3/2}$. The optical lattice is raised adiabatically in 500 μs to load all the selected atoms in the fundamental Bloch band. The final poten-

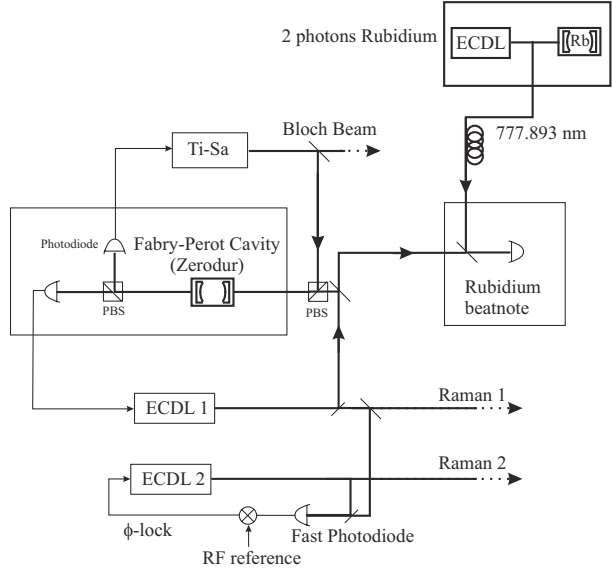


FIG. 8: Setup to stabilize and measure the Bloch and Raman beams frequencies. One of Raman lasers and a Ti-Sa laser are stabilized on a highly stable Fabry-Perot cavity. Their frequencies are measured by counting the beatnote with a two-photon Rb standard.

tial depth is $70 E_r$. In order to perform a coherent acceleration of the atoms, we sweep linearly in time the frequency difference between the two Bloch beams $\Delta\nu(t)$ using acousto-optic modulators : $\Delta\nu(t) = 2at/\lambda$, where a is the effective acceleration. In a 3 ms frequency sweep the atoms are accelerated at 1800 ms^{-2} receiving 900 photon momenta. The efficiency per oscillation (taking into account spontaneous emission and non-adiabatic transitions) is 99.95%.

Finally, the lattice intensity is adiabatically lowered in 500 μs to bring the atoms back to a well defined momentum state. Note that during the 500 μs of both adiabatic ramps, the optical lattice is constantly accelerated in order to compensate the gravity acceleration.

The Bloch lasers are issue of a Ti : Sapphire laser pumped by a 10W doubled Neodimium-Yag at 532 nm (Millenia, Spectra Physics). The Ti : Sapphire laser is frequency stabilized on the same Fabry-Perot cavity used for the Raman beams. The output power is 2 W with a tunability of some nanometers around 780 nm. The output is divided in two beams, each one controlled in frequency and amplitude by an independent AOM. The two beams reach the cell by two different fibers.

One of the Bloch beams is injected in the Raman beams fiber using the following trick : we place an AOM before the fiber and the Bloch beam is aligned into it with the AOM off while the first diffracted order of the Raman beams is aligned into the fiber with the AOM on. Hence, for each state of the AOM only one of the beams is selected into the fiber. The frequency difference between the Bloch beams is controlled by a frequency generator

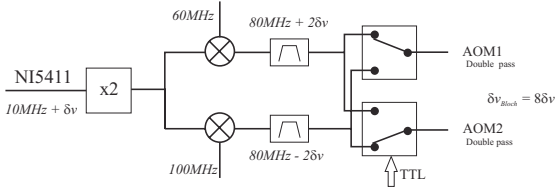


FIG. 9: Frequency control of the two AOMs for the Bloch beams

(NI5411) with a rate of 40 million points per second. We program on it a frequency ramp around 10MHz : $f(t)=10\text{ MHz}+\delta\nu(t)$. The output $f(t)$ is frequency doubled and divided in two paths (see Fig.(9)). One path mixes the signal with 60 MHz coming from a synthesiser and the other path mixes it with 100 MHz from another synthesiser in order to obtain two opposite frequency ramps around 80 MHz to control each one of the Bloch AOM's and accelerate the atoms. As the AOM modulators are used in double pass configuration, the acceleration of the lattice is then given by $a_{lat} = \frac{8}{(k_{B2}+k_{B1})} \frac{d\delta\nu}{dt}$ (k_{B1} , k_{B2} are the wavevectors of the Bloch beams). Using the frequency control scheme depicted in Fig.(9), the sum of this wavevectors does not vary at the first order during the acceleration process.

E. Velocity measurement

After the coherent Bloch acceleration, we measure the final atomic velocity by means of a second Raman π pulse with frequency δ_{meas} . It transfers the atomic population from $|F=1, m_F=0\rangle$ to $|F=2, m_F=0\rangle$ satisfying the relation (10). δ_{meas} is scanned in frequency in order to shape accurately the final velocity distribution. We are able to determine the center of the final distribution with an uncertainty on the order of 1 Hz, corresponding to about $7 \times 10^{-5} v_r$ in 10 minutes.

F. Detection

The experimental method to detect the fraction of atoms in each hyperfine level ($F=1$ and $F=2$) reminds the one used in atomic clock systems [32]. We shine to the free falling atoms at 15 cm below the trapping zone two parallel beams separated by 10 mm (see fig.(10)). The first one is a retro-reflected circularly polarized laser beam resonant with the closed transition $F=2 \rightarrow F'=3$ leaving the $F=1$ population unaffected. From the fluorescence signal in a photodiode we detect the atomic fraction in $F=2$. To avoid a decay in $F=1$ we add a magnetic bias field parallel to the detection beams propagation. Thus, the atoms will be fastly pumped to $|F=2, m_F=2\rangle$ state. On the retro-reflecting mirror of the first detection beam there is a small stain

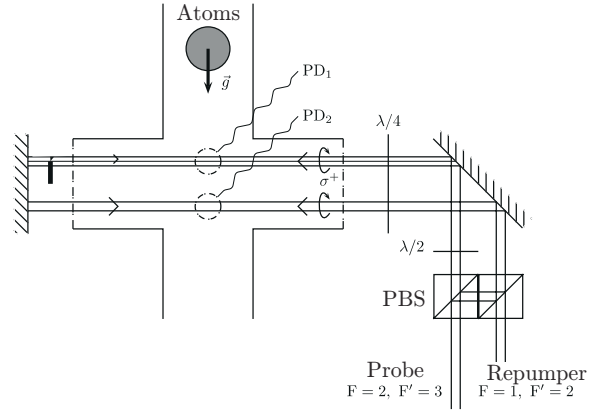


FIG. 10: Detection scheme

which avoids the lowest part of the beam to come back. In this way, the atoms detected in $F=2$ are subsequently pushed far away from the detection zone. The atomic fraction in $F=1$ continues to fall freely and is detected by the second laser beam placed below. This beam is a superposition of $F=2 \rightarrow F'=3$ resonant light with a repumper beam resonant with $F=1 \rightarrow F'=2$ transition. The atoms in $F=1$ are hence pumped to $F=2$ state and then detected following the previous procedure.

G. Further improvements of the experimental protocol

The final sequence is strongly improved from the one described above in order to meet some experimental requirements and to reach a competitive uncertainty. The complete temporel sequence of both the intensity and the frequency of the different lasers is described in Fig.(11).

1. Double acceleration

After the Bloch acceleration, the atoms can reach the upper window of the vacuum chamber. To avoid it, we have implemented a double acceleration scheme. At the end of the optical molasses phase, when all the atoms are in $F=2$, we effectuate a first acceleration of the cloud by means of N_{first} Bloch oscillations (see Fig.(11)). The first Raman transition selects a narrow velocity class from the accelerated cloud. Then, the push beam eliminates the non-selected atoms. We apply the second acceleration, N_{second} Bloch oscillations in the opposite direction to decelerate the atoms to $v \simeq 0$. Finally, the second Raman pulse measures the final velocity distribution. We emphasize that the velocity shift between the selection and the measurement is only due to the second Bloch acceleration, which is the one referred as "Bloch acceleration" everywhere in the text.

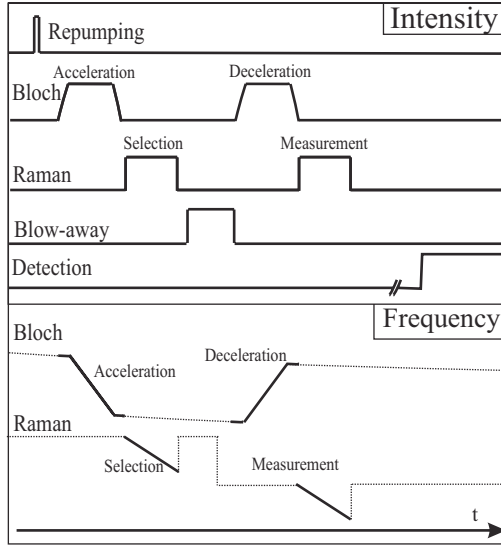


FIG. 11: Intensity and frequency timing of the different laser beams for the acceleration-deceleration sequence.

2. Differential measurement and Raman beams inversion

In this vertical configuration, we should know precisely the value of the local acceleration of gravity g to measure accurately the ratio h/m_{Rb} . In order to cancel the effect of gravity we effectuate two identical measurements of h/m_{Rb} with opposite directions of the Bloch acceleration (up/down) keeping constant the delay between the selection and measurement π pulses [45]. The ratio \hbar/m_{Rb} can be then determined from :

$$\frac{\hbar}{m_{Rb}} = \frac{(\delta_{sel} - \delta_{meas})^{up} - (\delta_{sel} - \delta_{meas})^{down}}{2(N^{up} + N^{down})k_B(k_1 + k_2)} \quad (25)$$

where $N^{up/down}$ corresponds respectively to the number of Bloch oscillations in both opposite directions, k_B is the Bloch wavevector and k_1 and k_2 are the wavevectors of the two Raman beams.

As discussed in Sec.(II), the contribution of some systematic effects to the determination of h/m_{Rb} changes sign when the direction of the Raman beams is exchanged (see Fig.(12)). Hence, for each up or down trajectory the Raman beams are reversed, we record two velocity spectra and we take the mean value of these two measurements. Finally, each determination of h/m_{Rb} and α is obtained from 4 velocity spectra (see Fig.(13)).

V. EXPERIMENTAL RESULTS. DETERMINATION OF h/m_{Rb} AND THE FINE STRUCTURE CONSTANT

Here we present our final determinations of h/m_{Rb} and α . They have been derived from 72 experimental

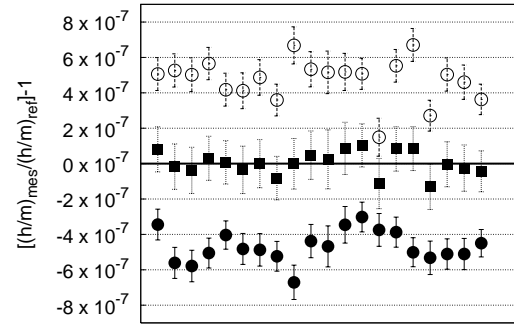


FIG. 12: h/m_{Rb} measurements are obtained by inverting the Raman beams (circles). $B \simeq 150$ mG. The mean value of each pair of measurements (squares) cancels out systematic effects, as light shifts and quadratic Zeeman shifts. For clarity, we plot the ratio of the measured $(h/m)_{mes}$ to $(h/m)_{ref}$, where $(h/m)_{ref}$ is the value derived from the α_{2002} .

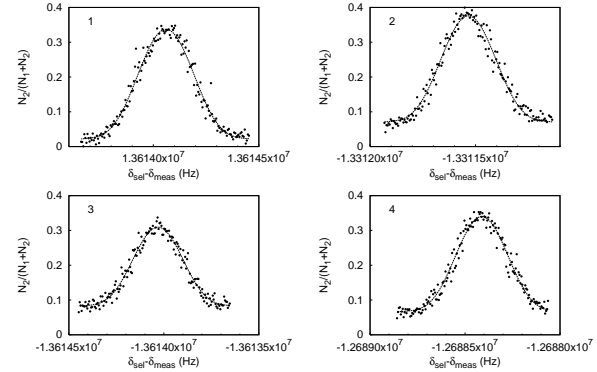


FIG. 13: Sequence of four spectra used for each determination of α . Here N_1 and N_2 are respectively the number of atoms in $F=1$ and $F=2$ after the acceleration process. They are obtained exchanging the Raman beams direction and performing the Bloch acceleration upwards or downwards. The used parameters for each spectrum are summarized in Table(II). The relative uncertainty for each spectrum is about 1.7 Hz. From the four spectra, h/m_{Rb} can be determined with an uncertainty of 6.6×10^{-8} .

data point taken during four days.

Each determination of h/m_{Rb} is obtained from four spectra as detailed in the previous section. Each spectrum contains 160 points and is obtained in 5 minutes. The uncertainty in the determination of the central frequency of each spectrum is about 1.7 Hz, ($\simeq 10^{-4}v_R$). We show in Fig.(13) four typical velocity distributions for $N^{up} = 430$ Bloch oscillations and $N^{down} = 460$ oscillations. The effective recoil number is here $2(N^{up} + N^{down}) = 1780$.

In Table(I) we present the parameters for the Bloch and Raman beams in all our determinations of α .

The parameters of the four spectra of each measu-

	Raman beams	Bloch beams
P	10 mW	115 mW
I	150 mW/cm ²	1800 mW/cm ²
Detuning	1THz	40GHz

TAB. I: Power, intensity and detuning of the Bloch and Raman beams in the measurements.

	spec.1	spec.2	spec.3	spec.4
N_{first}	-450	390	-450	390
N_{second}	460	-430	460	-430
ϵ_R	-1	-1	1	1
ν_{sel} [Hz]	-13956985	11455931	13926651	-11486265
ν_{mes} [Hz]	-342932	-1855606	312598	1825272

TAB. II: Parameters of the four spectra used for each determination of α . N_{first} and N_{second} are defined in section (IV-G-1).

rement are summarized in Table(II), where N_{first} and N_{second} are the number of Bloch oscillations in the acceleration-deceleration process of each measurement of h/m_{Rb} . The sign of ϵ_R represents the inversion of the Raman beams.

Fig.(14) presents the set of 72 determinations of the fine structure constant α . In each one of them, we have transferred to the atoms up to 460 Bloch oscillations, with an efficiency of 99.95% per oscillation. Each determination is obtained after 20 minutes of integration time. The corresponding relative uncertainty in h/m_{Rb} is around 6.6×10^{-8} and hence α is deduced with a relative uncertainty of 3.3×10^{-8} . The dispersion of these $n=72$ measurements is $\chi^2/(n-1) = 1.3$ and the resulting statistical relative uncertainty on h/m_{Rb} is 8.8 ppb.

The experimental value of h/m_{Rb} , taking into account only the statistical uncertainty without any correction is for the isotope ^{87}Rb :

$$\frac{h}{m_{Rb}} = 4.591359237(40) \times 10^{-9} \quad [8.8 \times 10^{-9}] \text{ m}^2 \cdot \text{s}^{-1} \quad (26)$$

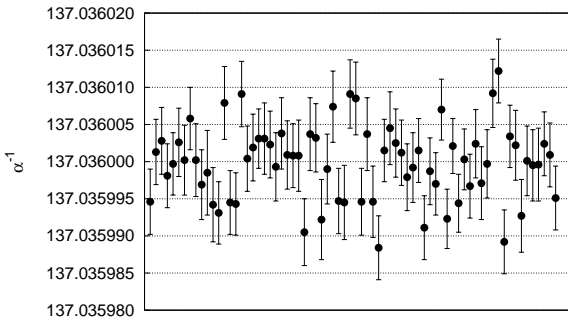


FIG. 14: Chronologically, our 72 determinations of the fine structure constant.

The deduced value of α^{-1} is then

$$\alpha^{-1} = 137.03599959(60) \quad [4.4 \times 10^{-9}] \quad (27)$$

In the next section, all systematic effects affecting the experimental measurement will be analyzed and taken into account to determine the final values of h/m_{Rb} and α .

VI. SYSTEMATIC EFFECTS

In this section we present the different systematic effects limiting the measurement of the ratio h/m_{Rb} and the associated uncertainties. The resulting relative uncertainty on the fine structure constant is derived.

A. Wavefront curvature and Gouy phase

The relation $p = h\nu/c$ for the impulsion of a photon as a function of its frequency is only valid for a plane wave. In the more realistic case of a beam of finite waist, there are corrections to this relation which can be characterized by the Gouy phase shift [33] and the wavefront curvature. We evaluate these two corrections in the same formulae as a function of the beam's parameters.

Let us first calculate an order of magnitude of the Gouy phase shift. The Gouy phase is the phase describing the π phase shift at the focus of a beam. The laser beam can be described as a sum of plane waves, and the Gouy phase shift is due to the dispersion of the \mathbf{k} wave vectors. Each wave vector has a component along the propagation axis (k_z) and a component orthogonal to this axis (k_\perp). Each plane wave has the same frequency, so we have the relation $k^2 = \omega^2/c^2 = k_z^2 + k_\perp^2$. For a beam of minimal waist w_0 , the dispersion in k_\perp is Fourier limited to $1/w_0$. At the position of the minimal waist, where all the plane waves are in phase, the wave vector is of the order of

$$k_z = \sqrt{k^2 - k_\perp^2} \simeq k \left(1 - \frac{k_\perp^2}{2k^2} \right) \quad (28)$$

The correction is thus of the order of $1/k^2 w_0^2$. The effect of the Gouy phase shift is to reduce the effective wave vector. This effect is very similar to the reduction of the speed of an electromagnetic wave confined in a wave guide. On the other hand, the conservation of momentum implies that a beam passing through a lens (and then having a different waist w_0) will exert onto it a force. This force has been in fact known for a long time and it is used, for example, for trapping dielectric particle in optical tweezers [34].

In order to calculate the exact effect at a position z from the minimal waist and r from the axis, we have to take into account the phase between the different plane waves interfering at that point. This will lead to the Gouy effect (dependance upon z) and the wave front curvature (dependance upon r). The effective wave vector resulting

TAB. III: Wavefront parameters of the Raman and Bloch laser beams.

	$w(z)$ [mm]	$R(z)$ [m]	$k_z^{\text{eff}}/k - 1$ [ppb]
Upward beams	2.1	15.9	-7
Bloch (downward)	2.0	7.0	-14
Raman (downward)	2.4	31.6	-5

from the interference of each plane wave can also be directly obtained from the gradient of the phase of the laser beam [35] :

$$k_z^{\text{eff}} = \frac{d\phi}{dz} = k - \frac{2}{kw(z)^2} \left(1 - \frac{r^2}{w(z)^2} (1 - (z/z_R)^2) \right) \quad (29)$$

where $z_R = \pi w_0^2/\lambda$ is the Rayleigh length and $w(z)^2 = w_0^2(1 + (z/z_R)^2)$. Notice that at $z = z_R$, where the wavefront curvature is maximal, the effective wavevector does not depend upon r .

Eq.(29) gives the effective wavevector as a function of two parameters : $w(z)$ the waist of the beam at the measurement point and z/z_R . To evaluate these two parameters, we have used a Shack-Hartmann wave front analyzer (HASO 64, Imagine Optic) which measures the wavefront curvature radius $R(z)$ and the waist $w(z)$ at a given position. Assuming that our beam is a gaussian beam, and thus using the relation $R(z) = z[1 + (z_R/z)^2]$, we obtain that

$$\frac{z}{z_R} = \left[\frac{\pi w(z)^2}{\lambda R(z)} \right] \quad (30)$$

The wavefront curvature effect depends upon the distance r from the propagation axis. To calculate the effect, we need to know the mean value of r^2 . The diameter of the atomic cloud measured using absorption imaging is $\langle r^2 \rangle \simeq (800 \mu\text{m})^2$. The light beams were centered on the atomic cloud by using copropagating Raman transitions and maximizing the number of transferred atoms. We estimate that the cloud is in the center of the Raman beams with a precision better than $500 \mu\text{m}$, leading to $\langle r^2 \rangle \simeq (950 \mu\text{m})^2$.

Table III gives the wavefront parameters of the different beams involved in our experiment. Using the fact that $h/m_{Rb} \propto (k_R k_B)^{-1}$ (see eq.(25)), where k_R and k_B are the mean value of the effective wave vector for the Raman and the Bloch beams, the final relative correction on h/m_{Rb} is -16.4 ppb. The uncertainty of the measured wavefront curvature is quite high. We thus took a conservative uncertainty of 50%, leading to a relative uncertainty of 8 ppb.

B. Laser beams alinement

In eq. (25) we supposed that both Raman and Bloch beams are counterpropagating. Rigorously, one should replace the term $2k_B(k_1 + k_2)$ by $(\mathbf{k}_R^U - \mathbf{k}_R^D) \cdot (\mathbf{k}_B^U - \mathbf{k}_B^D)$,

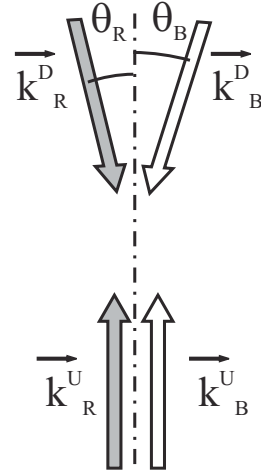


FIG. 15: Laser beam alinement : in our geometry, the two upwards propagating beams come from the same fiber and thus are parallel. We denote by θ_R (θ_B) the angle between the two Raman (Bloch) beams.

where $(\mathbf{k}_R^U, \mathbf{k}_R^D)$ and $(\mathbf{k}_B^U, \mathbf{k}_B^D)$ are respectively the wavevectors of the Raman and the Bloch beams defined in Fig.(15). The two upwards propagating wavevectors are parallel because the beams come out from the same fiber. The correction to apply will then depend only upon the angle θ_R and θ_B between the upward and downward Bloch and Raman beams (see Fig. (15)). If all four wavevectors are in the same plane, and in the limit θ_R and $\theta_B \ll 1$, the relative correction to h/m_{Rb} is given by $(\theta_B^2 + \theta_R^2 - \theta_B \theta_R)/4$.

The alinement of the counterpropagating beams was done by maximizing the coupling of the downwards propagating beams into the lower fiber. For the Raman beam, we measured a reduction of the coupling by a factor of 2 when we tilted the mirror of 7×10^{-5} rad. Assuming that the coupling was within 10% of the optimum, we find $\theta_R \approx 3 \times 10^{-5}$ rad. Similarly, $\theta_B \approx 1.6 \times 10^{-4}$ for the Bloch beam.

In the worst case where θ_B and θ_R have opposite sign, we obtain a systematic effect of 8×10^{-9} . Thus, we assume a relative systematic effect on h/m_{Rb} of 4×10^{-9} , with a relative uncertainty of 4×10^{-9} .

C. Gravity gradient

The local acceleration of gravity g induces an atomic velocity variation of gT_{delay} , where T_{delay} is the time between the selection and measurement pulses. However, to cancel the effect of this velocity shift we use the same temporal sequence for the upper and lower atomic trajectories. Nevertheless, gravity will be slightly different for the two trajectories because of the gravity gradient $\partial_z g$. (see Fig.16). The atomic velocity variation due to

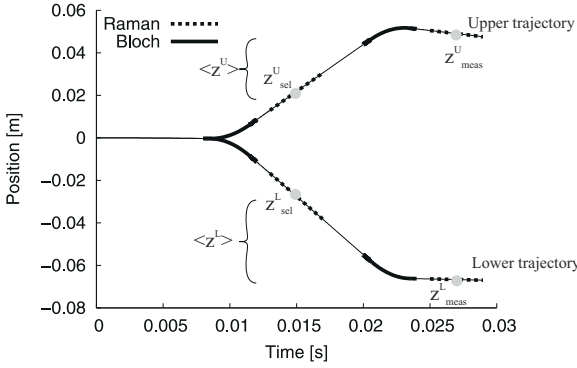


FIG. 16: Position of atoms for the upper and lower trajectories

this gradient is then proportional to the mean value of z during the flight. The correction on h/m_{Rb} is thus

$$\frac{m_{Rb}}{h} \Delta \left(\frac{h}{m_{Rb}} \right)_{\text{grav.grad.}} = \frac{T_{\text{delay}} (\langle z \rangle^U - \langle z \rangle^L) \partial_z g}{2v_r (N^{up} + N^{down})} \quad (31)$$

where $\langle z \rangle^U - \langle z \rangle^L$ is the difference of the mean position of the upper and lower trajectories (see Fig.(16)) and $N^{up} + N^{down}$ is the total number of Bloch oscillations done for the two trajectories. We calculate $\langle z \rangle^U - \langle z \rangle^L = 10 \text{ cm}$. The gravity gradient is, neglecting effects due to earth rotation, $\partial_z g = -2g/R_T \simeq 3.1 \times 10^{-7} \text{ g} \cdot \text{m}^{-1}$ (R_T is the radius of earth). With $T_{\text{delay}} = 12 \text{ ms}$, we obtain a relative correction for h/m_{Rb} of 3.5×10^{-10} .

D. Index of refraction

In this section, we first calculate the refractive index for the Raman and Bloch beams due to both the vapor background and the atomic cloud. In a second part, using simple arguments of momentum conservation, we explain how this refractive index may induce an effect on the recoil measurement.

1. Measurement of the refractive index

For a detuning Δ larger than the natural linewidth Γ of the atomic transition, the refractive index is given by :

$$n = 1 + f \frac{3\pi}{2} \rho \frac{\Gamma}{\Delta} \left(\frac{\lambda}{2\pi} \right)^3 \quad (32)$$

where λ is the wavelength of the transition, ρ is the atomic density and f the oscillator strength. In our case the detuning is larger than the hyperfine splitting (500 MHz), but smaller than the fine structure (7 THz), hence $f=2/3$ for the D2 line.

Our magneto-optical trap is loaded from a Rubidium vapor. To measure the density of this vapor, we looked at

TAB. IV: Refractive index for the different steps of the experiment

	Detuning $\rho [\text{at} \cdot \text{cm}^{-3}]$	$n - 1$
Cold atom cloud		
Raman selection	1 THz	$1 \times 10^{10} - 3.5 \times 10^{-10}$
Bloch	40 GHz	$2 \times 10^8 - 1.7 \times 10^{-10}$
Raman measurement	1 THz	$2 \times 10^8 - 7 \times 10^{-12}$
Background vapor		
Raman	1 THz	$8 \times 10^8 - 2.9 \times 10^{-11}$
Bloch	40 GHz	$8 \times 10^8 - 7.2 \times 10^{-10}$

the absorption of a probe beam through the cell. Because the Doppler effect is larger than the hyperfine splitting, the cross section is calculated without hyperfine splitting : $\sigma = f3\lambda^2/2\pi$. By taking into account that only 1/4 of the atoms are ^{87}Rb , 5/8 of them are in $F=2$ state, and that because of the Doppler effect, only a small proportion (the natural linewidth divided by the Doppler width) are resonant, we find that the total density of the background vapor is $8 \times 10^8 \text{ at/cm}^3$.

The cold atom density is measured just after the optical molasses phase using absorption imaging on the $F=2$ to $F'=3$ transition. By integrating the attenuation of the probe beam over the cloud one can calculate the total number of atoms. Assuming a gaussian isotropic density distribution, we obtain a density of $\rho = 1.1 \times 10^{10} \text{ at/cm}^3$. However, we have to take into account the fact that less than 2% of the atoms remain after the first selection. The resulting refractive index are summarized on table IV.

2. Photon recoil in a dispersive media A simple theoretical approach

The problem of the momentum of a photon in dispersive media is quite an old question ; classically it can be expressed as the momentum of a wave packet of given energy E . Almost a century ago, this question lead to a controversial between Abraham [36, 37], who affirmed that the photon momentum in a medium of refractive index n was E/nc and Minkowski [38, 39], who affirmed that it should be En/c . Later work due to R. Peierls gave other values [40]. A precise calculation of the recoil induced by the reflection of a light pulse, done by J.P. Gordon [41] confirmed Minkowski formula. This formula, applied for a quantum of light, says that the recoil of a photon of wavevector k in the vacuum is $n\hbar k$. Recently, W. Ketterle's group [42] measured the recoil energy of atoms diffracted by a standing wave in an atom interferometer. The result obtained is in agreement with Minkowski formula.

This result can be obtained using the following argument : in a refractive medium of index n , the phase of the electric field varies as nkx . When the atoms interact with this field, this phase will be added to the initial phase of

the atomic wavefunction. For a one photon transition, this means that the momentum of the atoms increases by $n\hbar k$.

However, in the case of Bloch oscillations we know that for each atom transferred, an incoming photon (of momentum $\hbar k$ before any interaction) will leave the medium in the opposite direction, with the same frequency and so a momentum $-\hbar k$. Consequently, for a complete Bloch oscillation, a total momentum of $2\hbar k$ will be transmitted to each atom.

As pointed out in [42], to understand the phenomenon we have to take into account the motion of the refractive medium. This can be done using the following argument : in order to calculate the recoil due to the diffraction of atoms by light, we need to calculate the phase of the light at the position of the atoms. Because we are doing a two photon transition only the difference $\Phi = \phi_1 - \phi_2$ between the phase of the two beams is involved.

Using the facts that, (i) without dispersive media the phase would be $\Phi(x) = 2kx$, (ii) inside the medium we have the relation $d\Phi/dx = 2nk$ and, (iii) at the position $\langle x \rangle$ of the center of the medium the effect due to the refractive index cancels from the first and second beams, we obtain that

$$\Phi(x) = 2(n-1)k(x - \langle x \rangle) + 2kx \quad (33)$$

By assuming that the medium is uniform, we have $\langle x \rangle = \sum_i x_i/N$, where x_i ($i = 1 \dots N$) is the position of the atoms in the dispersive medium. The function $\Phi(x)$ depends on the position of all the atoms. Consequently, when an atom is transferred, it acquires the momentum $\hbar d\Phi(x_i)/dx_i = 2n\hbar k + 2(1-n)\hbar k/N \simeq 2n\hbar k$ and each other atom j ($j \neq i$) acquires a momentum of $\hbar d\Phi(x_j)/dx_j = 2(1-n)\hbar k/N$. The approach described in this paragraph is not a full quantum approach of the refractive index, but more a mean field approach. However, this simple calculation leads both to the result of Minkowski and respects momentum conservation.

a. Bloch Let us consider the problem of Bloch oscillations in a more general way as a process transferring a fraction ϱ of atoms with a two photon transition. We obtain that the momentum of the transferred atoms is $2(n + \varrho(1-n))\hbar k$ (each atom is transferred one time and is ϱN times in the dispersive medium when another atom is transferred). The momentum of non transferred atoms is $2\varrho(1-n)\hbar k$ [46].

So for an efficiency of 100%, there is no effect due to the refractive index. In our experiment, where the efficiency per oscillation is $\varrho > 99.95\%$, the correction due to refractive index is less than two orders of magnitude lower than the correction given by the Minkowski formula, and thus negligible.

b. Raman One way to calculate the Doppler effect of a non relativistic atom is to consider the time derivative of the phase at the position $x(t) = vt$ of the atom : $\omega' = d\Phi(x(t), t)/dt$. To calculate the derivative of eq.(33), we have to take into account the motion of the cloud. By

assuming that the cloud is moving at a speed v_0 , the value of the Raman frequency δ' for an atom moving at a speed v is :

$$\delta' = \delta - 2kv + 2(n-1)k(v_0 - v) \quad (34)$$

In the experiment, the mean velocity of the cloud at the selection is about $2Nv_r$. We select atoms in such a way that their velocity differs from this mean velocity by less than one recoil. As a consequence, the relative effect of the refractive index is of the order of $(n-1)/(2N)$ where $N \simeq 500$ is the velocity of the atoms in units of $2v_r$. With $n-1 \simeq 3 \times 10^{-10}$, the effect is then completely negligible.

c. Background vapor We have seen that the momentum transferred to the atoms is given by $2(1+(1-\varrho)(n-1))\hbar k$ where $(1-\varrho)$ is the fraction of non-transferred atoms. This equation can be interpreted using the Minkowski formula in which the refractive index n is replaced by the refractive index due only to non-transferred atoms $(1+(1-\varrho)(1-n))$. Consequently, because the hot atoms from the background are out of resonance and do not perform Bloch oscillations, we have to take them into account as non-transferred atoms. This results in a relative correction of 0.75 ppb on h/m_{Rb} .

E. Quadratic Zeeman effect

Residual magnetic field gradients contribute to the systematics in two ways. Firstly there is a second order Zeeman shift of the energy levels which induces an error in the Raman velocity measurement. Secondly, the quadratic magnetic force modifies the atomic motion between the selection and the measurement.

1. Zeeman shift in the Raman process

As explained in section II, by exchanging the direction of propagation of the two Raman beams used for the selection and the measurement of the velocity of atoms, one can change the sign of the effect due to level shifts. This assumes that between two consecutive measurements the magnetic field and the atomic position are the same. The temporal sequence being the same for the two directions of propagation, there is no reason for a systematic effect due to a temporal variation of the magnetic field. However, the position of atoms is not exactly the same because the directions of the recoils given at the first Raman transition are opposite. For the timing used in our experiment, this difference is about $\delta z = 300 \mu\text{m}$.

The systematic effect arising from the position shift depends only on the gradient of Zeeman shift ($\partial_z \Delta_{\text{Zee}}$) at the position of the atoms at the second Raman pulse for the upper and lower trajectories. In order to measure this gradient, we perform copropagating Raman transitions. The sequence is the following : we keep the same first

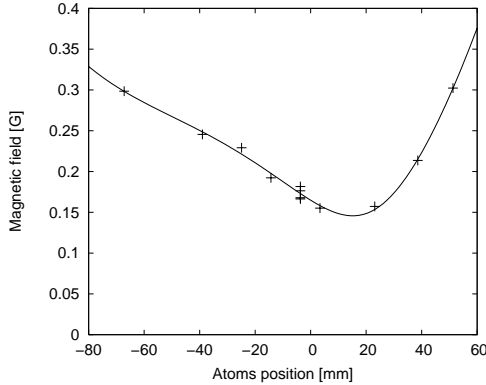


FIG. 17: Experimental determination of the magnetic field along the atomic trajectory. The zero of the atomic position corresponds to the center of the molasses.

three steps : initial acceleration with Bloch oscillations, selection of a subrecoil velocity class and deceleration of this velocity class. The last step is a copropagating Raman transition, between the same $|F = 1, m_F = 0\rangle$ and the $|F = 2, m_F = 0\rangle$ states - we can then measure the hyperfine splitting between the two states. This measurement includes many shifts : the Zeeman shift (~ 10 Hz for a magnetic field of 150 mG), the light shifts (~ 3.5 Hz) and the Doppler shift (~ 5 Hz). Indeed, for a copropagating transition, the Doppler effect, given by $(k_1 - k_2)v$, is about 10^5 times smaller than for a counterpropagating transition - but not negligible. We thus take care to make the same number of oscillations in the accelerating and decelerating processes. The final atomic velocity is then only due to the gravitational fall and can be calculated. Furthermore both Doppler shift and light shift can be canceled out by calculating the gradient from measurements at different positions. This is done by changing the number of Bloch oscillations.

The experiment is realized in a non-magnetically-shielded stainless steel vacuum chamber. The deduced Zeeman shift gradients (see Fig.(17)) are $\partial_z \Delta_{\text{Zee}}^U = 1.85 \text{ Hz} \cdot \text{mm}^{-1}$ and $\partial_z \Delta_{\text{Zee}}^L = -0.52 \text{ Hz} \cdot \text{mm}^{-1}$ respectively for the upper and lower trajectories.

From Eq.(25), we can estimate the correction to the value of h/m_{Rb} :

$$\Delta \left(\frac{\hbar}{m_{Rb}} \right)_{\text{Zeeman}} = \frac{\partial_z \Delta_{\text{Zee}}^U - \partial_z \Delta_{\text{Zee}}^L}{8(N^{up} + N^{down})k_B k_R} \delta z \quad (35)$$

The resulting relative correction on h/m_{Rb} for our parameters is -13.2 ppb. Taking into account the uncertainty of the magnetic field measurement, we estimate the corresponding uncertainty at 4 ppb.

2. Quadratic magnetic force

Second order Zeeman effect induces a shift in the energy levels of an atom in the magnetic field. If this magnetic field is not homogenous, the kinetic energy of the atoms will be modified. The variation of velocity of an atom with velocity v enduring a variation of energy ΔE is $\Delta v = \Delta E/mv$. We obtain that the relative correction on h/m_{Rb} due to this effect is :

$$\frac{h}{2(N^{up} + N^{down})v_r} \left(\frac{\Delta_{\text{Zee}, F=1}^U}{mv_{sel}^U} - \frac{\Delta_{\text{Zee}, F=1}^L}{mv_{sel}^L} \right) \quad (36)$$

where $\Delta_{\text{Zee}, F=1}^{U/L}$ is the variation of Zeeman shift between the selection and the measurement for the upper and lower trajectories. We emphasize that only the $F = 1$ hyperfine level is involved in the Bloch oscillations process.

As shown in Fig.(17), the minimum of the measured magnetic field is in the center of the chamber and therefore the induced force opposes to the second Bloch acceleration. The corresponding correction to h/m_{Rb} is positive. For a typically measured Zeeman shift of 30 Hz, we obtain that the relative correction on h/m_{Rb} is 2.6 ppb. We estimate our knowledge of the magnetic field within 30% corresponding to an uncertainty of 0.8 ppb.

F. Light shift

In the same way that second order Zeeman effect gives two different systematic effects, light shifts can induce an error in the Raman velocity selection and measurement and can also induce a force to atoms in between, during Bloch oscillations.

1. One photon light shift

For atoms in $|F, m_F = 0\rangle$, the light shift induced by a laser beam of intensity I and detuned by Δ from the D2 line is, in the case where Δ is larger than the hyperfine splitting but smaller than the fine structure :

$$\delta_{l.s.} = \frac{\Gamma^2}{8I_S} \frac{I}{\Delta} \quad (37)$$

where Γ is the linewidth of the $5P_{3/2}$ state and I_S is the saturation intensity of the D2 line.

However, for a Raman transition, only the differential effect from the light shift of the $|F = 1, m_F = 0\rangle$ and $|F = 2, m_F = 0\rangle$ states is important. In the case where Δ is larger than the hyperfine splitting ω_{HFS} of the ground state, the differential effect is obtain by derivating eq.(37). We obtain

$$\delta_{l.s.}^{|F=2\rangle} - \delta_{l.s.}^{|F=1\rangle} = - \frac{\Gamma^2 I}{8I_S} \frac{\omega_{\text{HFS}}}{\Delta^2} \quad (38)$$

The light intensity at the position of the atoms is easily measured by looking to the π condition of a copropagating Raman transition. Indeed, the effective Raman coupling Ω , in the case of a $\text{lin} \perp \text{lin}$ transition is equal to

$$\Omega = \frac{I}{I_S} \frac{\Gamma^2}{16 |\Delta|} \quad (39)$$

Combining eq.(38) and eq.(39), and using the fact that we have to add the light shift of three beams (one of the Raman is retroreflected), we obtain that

$$\delta_{l.s.}^{[F=2]} - \delta_{l.s.}^{[F=1]} = -\frac{6\pi}{\tau} \frac{\omega_{\text{HFS}}}{|\Delta|} \quad (40)$$

With our parameters, one can calculate that the light shift will shift the transition by 75 Hz - leading to a change in velocity by about $5 \times 10^{-3} v_r$. This effect is important. However, one can expect to cancel it in many ways : between the selection and measurement (constant effect is cancelled), upper and lower trajectories (time dependant effect is then cancelled) and by reversing the direction of propagation of the Raman beam (position dependant effect is cancelled). The inversion of the direction of the Raman beams, which should result in the cancellation of level shifts (up to the systematic shift in the position of atoms) does not work well for light shifts, because of a possible systematic change in the intensity of light when the direction of propagation is changed. Thus, we do not compensate neither the effect resulting from spatial variations of light nor the effect due to the fact that because of the spread of the atomic cloud and the finite size of the laser beam. The intensity at the measurement will be, in average, less than the intensity at the selection.

Let us call $\Delta_{l.s.}^0$, the light shift for the selection, ξ a parameter such that the residual light shift due to the spread of the cloud is $\Delta_{l.s.}^0(1-\xi)$ at the measurement, R a typical length for the variation of intensity and β the relative difference of intensity between the Raman beams when we exchange their direction of propagation.

The correction to apply to h/m_{Rb} is then :

$$\frac{\beta}{R} \frac{\Delta_{d.l.}^0(z_{\text{sel}}^U - z_{\text{sel}}^L) - \Delta_{d.l.}^0(1-\xi)(z_{\text{meas}}^U - z_{\text{meas}}^L)}{8(N^{up} + N^{down})k_R k_B} \quad (41)$$

where $z_{\text{sel}/\text{meas}}^{U/L}$ are the positions of atoms during the selection and measurement for the upwards and downwards trajectories (see Fig.(16)).

We measure $\beta < 10\%$ and estimate $R \gtrsim 10$ m. Consequently, the effect, of the order of 2×10^{-10} for h/m_{Rb} , is negligible and we decide not to apply any correction.

2. Two photon light shift

There is a two photon light shift induced by the copropagating Raman beams coming out of the same fiber

(afterwards one of them will be retroreflected in order to form the counterpropagating beam). The experiment is based on the fact that, because we are addressing moving atoms, only the velocity selective transition is resonant. However, the copropagating one will induce a light shift given by :

$$\delta_{l.s. \text{ 2ph.}} = -\frac{\Omega^2}{2\delta} \quad (42)$$

This light shift, inversely proportional to the detuning δ of the transition – and thus to the velocity of atoms – is larger during the second Raman pulse. It does not cancel between the upward and downward trajectories because we are not using a totally symmetric scheme (due especially to gravity and a different number of transmitted recoils). Finally we obtain that the relative effect on h/m_{Rb} is

$$\frac{\Omega^2}{2} \frac{(\delta_{\text{sel}}^U)^{-1} - (\delta_{\text{meas}}^U)^{-1} - (\delta_{\text{sel}}^L)^{-1} + (\delta_{\text{meas}}^L)^{-1}}{\delta_{\text{sel}}^U - \delta_{\text{meas}}^U - \delta_{\text{sel}}^L + \delta_{\text{meas}}^L} \quad (43)$$

With our experimental parameters, the corresponding correction to h/m_{Rb} is 1 ppb with an uncertainty of 0.4 ppb.

3. Light shift gradient during Bloch oscillation

Another important systematic effect induced by a spatial variation of the light intensity is the dipolar electric force. This force modifies the atomic velocity during Bloch oscillations. A rough calculation based on light shifts considering about $U_0 = 100 E_r$ and a typical length for the variation of light shift $R = 10$ m leads to a force $F = U_0/R$ giving an acceleration of $3 \times 10^{-5} v_r/\text{ms}$. This effect is then non-negligible.

However, this force cannot be calculated by adding the force due to the gradient of each beam : we have to take into account both the interference of the lasers and the fact that the wavefunction of atoms is not uniform. Especially, in the case of a deep blue-detuned lattice, atoms are located in spatial positions where the light intensity is minimal. The effect is then highly reduced. Furthermore, only the spatial variation of this force is important, because any constant force (such as gravity) will cancel out from the upper and lower trajectories.

To evaluate this effect, we calculate the energy of an atom in the fundamental band of the lattice as a function of its position. The energy level in the tight binding limit is then given by :

$$U = \frac{U_0}{4} \frac{(\mathcal{E}_U - \mathcal{E}_D)^2}{\mathcal{E}_U \mathcal{E}_D} + \sqrt{U_0 E_r} \quad (44)$$

where $\mathcal{E}_{U/D}$ are the amplitudes of the electromagnetic field of the upward and downward propagating beams which form the optical lattice. The first term of Eq.(44) corresponds to the minimum energy in the lattice potential and the second term is the energy of the harmonic

TAB. V: Error budget on the determination of h/m_{Rb} (Systematic effect and relative uncertainty in ppb).

Source	Correction (ppb)	Relative uncertainty (ppb)
Laser frequencies		1.6
Beams alignment	4	4
Wavefront curvature and Gouy phase	16.4	8
2nd order Zeeman effect	-13.2	4
Quadratic magnetic force	2.6	0.8
Gravity gradient	0.36	0.04
light shift (one photon transition)		0.4
light shift (two photon transition)	1.0	0.4
light shift (Bloch oscillation)	-0.92	0.4
Index of refraction atomic cloud		0.6
Index of refraction background vapor	0.75	0.6
Global systematic effects	10.98	10.0

oscillator in the potential well. It is important to notice that this formula is valid only for a blue-detuned lattice. This energy shift induces a force $F = -\frac{\partial U}{\partial z}$.

In the tight binding limit, because $U_0 \gg 16E_r$ the contribution of the second term of Eq.(44) is small. As mentioned above, all constant forces cancel out between the upper and lower trajectories and only the gradient of the force $\frac{\partial}{\partial z}F(z)$ contributes to the systematics. By neglecting the second term in Eq.(44), we obtain that

$$\frac{\partial F(z)}{\partial z} = 2\frac{U_0}{\kappa} \left[(\kappa - 1) \left(\frac{\gamma_U}{R_U^2} - \kappa \frac{\gamma_D}{R_D^2} \right) - \left(\frac{1}{R_U} - \frac{\kappa}{R_D} \right)^2 \right] \quad (45)$$

where $\kappa = \frac{\varepsilon_D}{\varepsilon_U}$, $R_{U/D}$ are the curvature radius of the upwards and downwards propagating beams and $\gamma_{U/D}$ are dimensionless factor given by the relations :

$$\gamma_{U/D} = 2 - \left(\frac{\lambda R_{U/D}}{\pi w_{U/D}^2} \right)^2 \quad (46)$$

Because our measurement was done with beams of different curvature radius, the force gradient is not null, even for beams of equal intensity ($\kappa = 1$). Using the parameters of the table III, we obtain a systematic correction on h/m_{Rb} of -9.2×10^{-10} . The uncertainty, coming mainly from the uncertainty on the wavefront curvature is of 4×10^{-10} . We did not take into account this effect in our previous publication [20]. Therefore the value of the fine structure constant α is slightly different than that published in this reference.

G. Final results and uncertainty budget

We summarize on table V the different systematic effects and their contributions to the uncertainty on the

TAB. VI: Constants used for the determination of α from h/m_{Rb} .

	Value (ppb)	Relative uncertainty (ppb)
Rydberg constant [1]	10 973 731.568 525 (73) m ⁻¹	0.0006
Rubidium mass [19]	86.909 180 520 (15) amu	0.2
Electron mass [1]	5.485 799 0945(24) 10 ⁻⁴ amu	0.44

determination of the ratio h/m_{Rb} . All the uncertainties are added in quadrature. The largest uncertainty comes from the laser geometric parameters (wavefront curvature, waist, alignment) (9 ppb). All these parameters were measured a posteriori. The contribution of the magnetic field to the systematics was experimentally determined by mapping the magnetic field gradient seen by the atoms. Those uncertainties can be reduced by using appropriate technics. More fundamental uncertainties come from the different light shifts in the experiment (0.7 ppb). Finally concerning the index of refraction effect, we have assumed a conservative uncertainty of 0.85 ppb derived from the calculation of the Bloch and Raman wavelengths in the medium.

Table (VI) shows the different constants used for the determination of α from our measurement. Their uncertainties are negligible. Taking into account the corrections, we obtain that

$$\frac{h}{m_{Rb}} = 4.591 359 29 (6) \times 10^{-9} \quad [1.3 \cdot 10^{-8}] \quad m^2 \cdot s^{-1} \quad (47)$$

$$\alpha^{-1} = 137.035 998 84 (91) \quad [6, 7 \cdot 10^{-9}] \quad (48)$$

VI. CONCLUSION AND PROSPECTS

Thanks to the high efficiency of the Bloch oscillations process (99.97% per recoil), we are able to transfer to the atoms about 900 photon momenta. This method combined with a precise velocity sensor leads to a measurement of the ratio h/m_{Rb} with a relative uncertainty of 1.3×10^{-8} . This non interferometric measurement achieves a precision comparable to the best measurement provided by an atomic interferometry experiment [2]. A comparison of our determination of α with other determinations is presented in Fig.18. Except for the more recent value of α obtained from the Harvard measurement of a_e , all the values used for this comparison come from the last

	α^{-1}	Uncertainty (ppb)
a_e (Harvard)	137.035 999 710(96)	0.7
a_e (UW)	137.035 99880(52)	3.8
$h/m(Rb)$	137.035 99884(91)	6.7
$h/m(Cs)$	137.036 0001(11)	7.7
R_K	137.036 0030(25)	17
Γ'_{90}	137.035 9875(43)	31
h/m_n	137.036 0015(47)	34
$\Delta\nu_{Mu}$	137.036 0017(80)	58

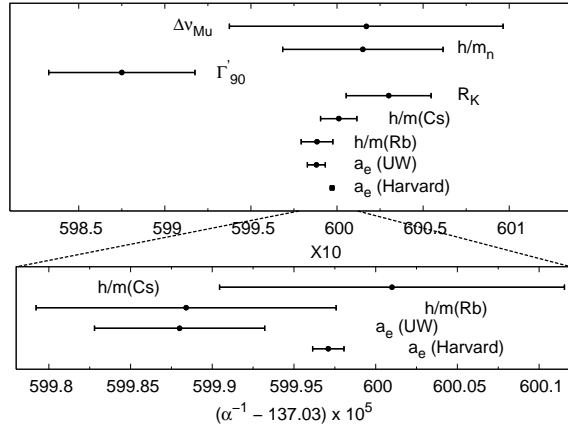


FIG. 18: Comparison of our measurement ($h/m(Rb)$) with the measurements used for the 2002 CODATA adjustment[1] and the new measurement from Harvard [5].

CODATA report. This new determination of α with an uncertainty below 10 ppb, will increase the confidence on α value at this level of uncertainty.

We plan several improvements in order to achieve a one ppb level uncertainty on α . The statistical uncertainty of our current measurement (4.4 ppb) arises from the signal to noise ratio on the velocity sensor. We expect to improve this ratio by a factor of 4, first, by increasing significantly the initial density of atoms in velocity space, and second, by implementing a vibration isolation platform on our experimental set-up. On the other hand increasing the number of recoils transmitted to the atoms (using a much larger cell and a more powerful laser), we plan to reduce the statistical uncertainty significantly below 1ppb.

We need also to control more carefully systematic effects (5ppb, in the current measurement). For this purpose, we consider several enhancements : *i)* a better control of the geometrical parameters of the Raman and Bloch laser beams will allow us to reduce the uncertainty coming from the wavefront curvature. *ii)* a magnetic shielding of the vacuum chamber, associated to the differential measurement currently used to bring down systematics, will probably reduce by one order of magnitude effects due to magnetic field. *iii)* laser frequency stabilisation and measurement can easily be improved to neglect the associated systematic effect at the ppb level. *iv)* a better determination and control of experimental parameters involved in the light shift and the refractive index will be required to reduce the uncertainty on their estimations.

Furthermore, improvements in the statistical uncertainty (due to the reduction of integration time) may allow us to place experimental error bars on systematic effects by making measurements with different parameters. These major improvements should lead to a measurement of α below the ppb level.

A new measurement of the fine structure constant at the ppb level would have an important consequence not only in metrology but also in fundamental physics. Indeed, with the recent 0.7 ppb determination of α from the measurement of a_e , such determination which is almost independent to the QED would lead to an unprecedented test of the QED and of the internal structure of the electron [5].

VII. ACKNOWLEDGEMENTS

We wish to thank A. Clairon, C. Salomon, S. Reynaud and P. Wolf for valuable discussions. This experiment is supported in part by the Laboratoire National de Métrologie et d'Essais (Ex. Bureau National de Métrologie) (contract 033006) and by the Région Ile de France (contract SESAME E1220). The work of E. de Mirandes is supported by IFRAF (Institut Francilien de Recherches sur les Atomes Froids).

-
- [1] P. Mohr and B.N. Taylor, *Rev. Mod. Phys.* **77**, 1 (2005).
 - [2] A. Wicht *et al.*, *Physica Scripta* **T102**, 82 (2002).
 - [3] B. Odom, D. Hanneke, B. D'Urso and G. Gabrielse, *Phys. Rev. Lett.* **97**, 030801 (2006).
 - [4] T. Kinoshita and M. Nio, *Phys. Rev. D* **7**, 013003 (2006).
 - [5] G. Gabrielse, D. Hanneke, T. Kinoshita, M. Nio and B. Odom, *Phys. Rev. Lett.* **97**, 030802 (2006).
 - [6] C. J. Bordé, *Phil. Trans. R. Soc. A* **363**, 2177 (2005).
 - [7] I. M. Mills, P. J. Mohr, T. J. Quinn, B. N. Taylor and E. R. Williams, *Metrologia* **43**, 227 (2006).
 - [8] A. Jeffery *et al.*, *Metrologia* **35**, 83 (1998).
 - [9] S. Chu, C. Cohen-Tannoudji, W.D. Phillips, *Rev. Mod. Phys.* **70**, 685-741 (1998).
 - [10] G. Santarelli *et al.*, *Phys. Rev. Lett.* **82**, 4619 (1999).
 - [11] C.W. Oates, K.R. Vogel and J.L. Hall, *Phys. Rev. Lett.* **76**, 2866 (1996).
 - [12] A. Peters, K. Y. Chung and S. Chu, *Metrologia* **38**, 25 (2001).
 - [13] T. L. Gustavson, P. Bouyer and M. A. Kasevich, *Phys. Rev. Lett.* **78**, 2046 (1997).

- [14] D.S. Weiss and B.C. Young and S. Chu, Phys. Rev. Lett. **70**, 2706 (1992).
- [15] B. Taylor, *Metrologia*. **31**, 181 (1994).
- [16] Th. Udem *et al.*, *Phys. Rev. Lett.* **79**, 2646 (1997).
- [17] C. Schwob *et al.*, *Phys. Rev. Lett.* **82**, 4960 (1999).
- [18] T. Beir *et al.*, *Phys. Rev. Lett.* **88**, 011603 (2002).
- [19] M.P. Bradley *et al.*, *Phys. Rev. Lett.* **83**, 4510 (1999).
- [20] P. Cladé *et al.*, *Phys. Rev. Lett.* **96**, 033001-1 (2006).
- [21] R. Battesti *et al.*, *Phys. Rev. Lett.* **92**, 253001-1 (2004).
- [22] P. Lett, R. Watts, C. Westbrook, W. Phillips, P. Gould and H. Metcalf, *Phys. Rev. Lett.* **61**, 169 (1988).
- [23] P. Cladé, S. Guellati-Khélifa, C. Schwob, F. Nez, L. Julien and F. Biraben, *Euro. Phys. J. D.* **33**, 173 (2005).
- [24] M. Ben Dahan *et al.* *Phys. Rev. Lett.* **76**, 4508 (1996).
- [25] F. Bloch, *Z. Phys.* **52**, 555 (1928).
- [26] G. H. Wannier, *Phys. Rev.* **52**, 191 (1937).
- [27] P. Cladé, S. Guellati-Khélifa, C. Schwob, F. Nez, L. Julien and F. Biraben, *Europhy. Lett.*, **71**, 730 (2005).
- [28] G. Morigi, J. Eschner, J. I. Cirac and P. Zoller, *Phys. Rev. A*, **59** 3797, (1999).
- [29] D. Touahri *et al.*, *Opt. Comm.* **133**, 471 (1997).
- [30] B. de Beauvoir, F. Nez, L. Hilico, L. Julien, F. Biraben, B. Cagnac, J.J. Zondy, D. Touahri, O. Acef et A. Clairon, *Eur. Phys. J. D.* **1** 227, (1998).
- [31] B. De Beauvoir , C. Schwob, O. Acef , L. Jozefowski , L. Hilico, F. Nez, L. Julien, A. Clairon et F. Biraben , *Eur. Phys. J. D* **12** 61 (2000).
- [32] A. Clairon *et al.*, *IEEE Trans. Instrum. Meas.* **44**, 128 (1995).
- [33] A. Wicht, E. Sarajlic, J. M. Hensley and S. Chu , *Phys. Rev. A*, **72**, 023602 (2005).
- [34] A. Ashkin, J. M. Dziedzic, J. E. Bjorkholm and S. Chu, *Optics Letters*. **11**, 288 (1986)
- [35] H. Kogelnik and T. Li, *Applied Optics* **5**, 1550 (1966).
- [36] M. Abraham, *Rc. Circ. Mat. Palermo* **28**, 1 (1909).
- [37] M. Abraham, *Rc. Circ. Mat. Palermo* **30**, 33 (1910).
- [38] H. Minkowski, *Nachr. Ges. Wiss. Göttingen*, 53 (1908).
- [39] H. Minkowski, *Math. Annalen* **68** 472 (1910).
- [40] R. Peierls, *Proceedings of Scuola Normale Superiore, Pisa*, 187 (1987).
- [41] J. P. Gordon, *Phys. Rev. A* **8**, 14 (1073).
- [42] G. K. Campbell *et al.*, *Phys. Rev. Lett.* **94**, 170403 (2005).
- [43] B. Jeckelmann *et al.*, *IEEE. Trans. Instr. Meas* **44**, 269 (1995).
- [44] J. Tsai *et al.*, *Phys. Rev. Lett* **51**, 316 (1983).
- [45] We emphasize that both the trigger generator and the synthesizer making the sweep to compensate g are not reprogrammed
- [46] For $\varrho = 1/2$, this prediction differs by a factor of two from Ref.[42].

Chapitre 5

Perspectives

Ce dernier chapitre se décompose en trois parties. Tout d'abord, je mentionnerai les différentes améliorations que nous allons prochainement apporter à notre montage expérimental dans le but de déterminer α au ppb. Je décrirai ensuite un dispositif permettant d'associer la sensibilité de l'interférométrie à l'efficacité des oscillations de Bloch. Finalement, j'aborderai le rôle du rapport h/m dans le cadre d'une éventuelle redéfinition du kilogramme.

5.1 Améliorations sur l'expérience actuelle

Afin d'améliorer la précision de notre détermination de α , nous pouvons agir sur deux plans : l'augmentation de la sensibilité du senseur inertiel et la réduction des effets systématiques.

5.1.1 Augmenter la sensibilité du senseur inertiel

L'enceinte à vide utilisée jusqu'à présent nous a été prêtée par l'INM et n'a donc pas été conçue spécifiquement pour notre expérience. En particulier, le petit diamètre de ses hublots, et donc des faisceaux laser, ne nous permet pas de piéger plus de 3×10^7 atomes sur environ 1 mm^3 . Dans la prochaine version de l'expérience, nous utiliserons une cellule en titane¹ pourvue de hublots plus grands, et dessinée pour répondre à nos besoins. Nous espérons ainsi augmenter le rapport signal à bruit au niveau de la détection.

Le piège magnéto-optique réalisé dans cette nouvelle cellule sera chargé à partir d'un

¹Le titane est plus amagnétique que l'inox.

piège magnéto-optique à deux dimensions [78]. Du point de vue de la statistique, ceci devrait nous permettre d'augmenter la vitesse de chargement du piège 3D, et ainsi de diminuer notablement la durée d'une séquence temporelle.

De plus, en réduisant la densité de vapeur résiduelle et donc le taux de collisions, l'utilisation du piège 2D devrait conduire à une amélioration notable de la précision sur la mesure de la période de Bloch en onde stationnaire.

La sensibilité du senseur inertiel est actuellement limitée par les vibrations. Afin de les réduire, nous avons fait l'acquisition de pieds anti-vibrations actifs. Ceux-ci ont été testés par Benjamin Besga pendant son stage de L3 [79].

5.1.2 Réduire les effets systématiques

Une autre conséquence de la diminution de la densité de vapeur résiduelle sera de réduire l'effet systématique lié à l'indice de cette vapeur.

Les deux effets prépondérants dans notre expérience sont liés d'une part aux déplacements Zeeman quadratiques, d'autre part à la courbure des fronts d'onde et à la phase de Gouy.

Afin de mieux contrôler le champ magnétique, la cellule en titane sera entourée d'un blindage en mumétal.

Une meilleure collimation des faisceaux sera obtenue grâce à l'utilisation d'un analyseur de fronts d'onde de type Shack-Hartmann (HASO 64 Imagine Optics).

Nous espérons ainsi atteindre une incertitude relative de 10^{-9} sur α .

5.2 Interférométrie avec des oscillations de Bloch

La modification à apporter à notre expérience pour réaliser des mesures interféro-métriques consiste à remplacer les impulsions π de sélection et de mesure par deux paires d'impulsions $\pi/2$. On dispose alors de deux paramètres indépendants : la durée τ d'une impulsion et l'intervalle de temps T_{Ramsey} séparant les deux impulsions $\pi/2$.

Le nombre d'atomes sélectionnés varie en $1/\tau$ et la distance entre deux franges en $1/T_{Ramsey}$. La résolution de l'interféromètre ne dépend que de ce dernier paramètre. Il est donc a priori possible d'augmenter la résolution sans perte d'atomes.

Avec notre méthode expérimentale actuelle (impulsions π de sélection et de mesure et oscillations de Bloch), on ne peut jouer que sur le paramètre τ . De ce fait, si l'on choisit d'augmenter la résolution du senseur inertiel en sélectionnant une classe de vitesse plus étroite (c'est-à-dire en augmentant la valeur de τ), on sélectionne moins d'atomes, et

finalement on ne gagne pas en précision sur la mesure de v_r .

Il semble donc qu'en réalisant des mesures interférométriques, on puisse gagner à la fois sur la résolution et sur le rapport signal à bruit.

Le principe de notre interféromètre est illustré par la figure (5.1). A la différence de l'interféromètre de Ramsey Bordé (figure 4.14), nous n'inversons pas le sens des faisceaux entre les deux paires d'impulsions $\pi/2$. La vitesse moyenne des atomes étant la même pour le premier et le second interféromètre, ce dispositif ne permet pas de mesurer directement la vitesse de recul. Il est nécessaire d'accélérer les atomes entre les deux interféromètres, ce que nous réalisons au moyen d'oscillations de Bloch (figure 5.2).

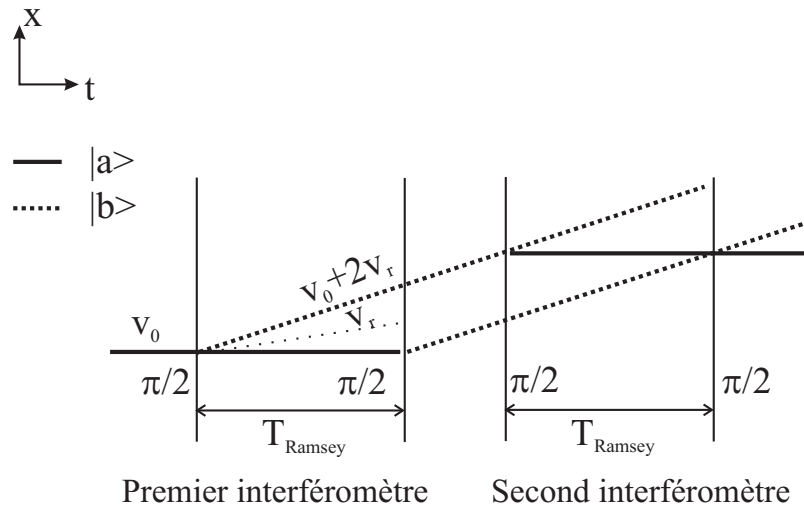


FIG. 5.1 – Schéma de principe de notre interféromètre

Si l'on effectue N oscillations de Bloch entre les deux interféromètres, le déphasage dû à l'énergie cinétique est identique à celui donné par l'expression 4.27 en remplaçant $N + 1$ par N , soit :

$$\Delta\phi_c = -4kNT_{Ramsey}v_r \quad (5.1)$$

et la sensibilité du dispositif croît linéairement avec N . De la même façon que précédemment, la contribution de la gravité est éliminée au premier ordre en réalisant une mesure différentielle entre les trajectoires du haut et du bas.

Du point de vue des effets systématiques, cette méthode est très similaire à celle développée à Stanford. En ce qui concerne la sensibilité du senseur, on peut tout de même noter quelques différences. Comme cela a été discuté dans le chapitre précédent, notre dispositif nous permet de réaliser plus d'oscillations en mettant à profit le caractère non résonant des impulsions π . Cependant, contrairement au cas de l'expérience américaine,

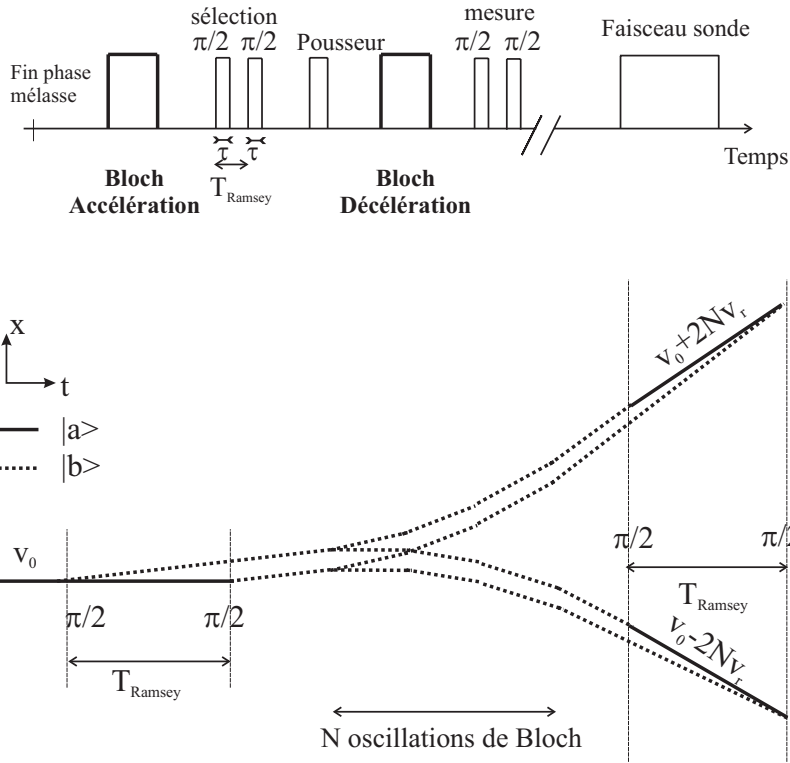


FIG. 5.2 – Mesure de v_r par interférométrie. En haut, la séquence temporelle. En bas, le schéma de principe de l'interféromètre (les chemins représentés correspondent aux accélérations vers le haut et vers le bas).

il nécessite la sélection d'une classe de vitesse initiale, de largeur égale à quelques v_r , correspondant à la première zone de Brillouin, et donc réduit le nombre d'atomes qui participent au processus. Cet inconvénient devrait être partiellement compensé grâce à l'utilisation de la nouvelle enceinte à vide (voir paragraphe 5.1.1).

Des mesures de α , basées sur cette méthode, sont actuellement en cours sur le montage expérimental préliminaire. Les premiers résultats semblent prometteurs, puisque nous parvenons à pointer la fréquence centrale des spectres avec une incertitude sub-hertz.

5.3 Vers une redéfinition du kilogramme

Le kilogramme est la dernière unité de base du système international définie par un artefact matériel. La comparaison de différents étalons a montré que leur masse a dérivé de plusieurs dizaines de microgrammes, c'est-à-dire de quelques 10^{-8} en valeur relative.

Des débats animent actuellement la communauté des métrologistes au sujet d'une éventuelle redéfinition du kilogramme. Ces discussions interviennent dans le cadre plus général du rattachement des unités de base aux constantes fondamentales, qui, grâce aux avancées technologiques et au développement de dispositifs expérimentaux de plus en plus sophistiqués, sont mesurées de plus en plus précisément [80] [81] [82].

5.3.1 Propositions de redéfinition du kilogramme

Redéfinir le kilogramme en fixant h

Une possibilité avancée pour redéfinir le kilogramme consiste à fixer la constante de Planck h , ce qui revient à relier les unités de masse et de temps ($E = h\nu = mc^2$). La réalisation du kilogramme serait alors obtenue à partir de la balance du watt, qui permet de comparer une puissance mécanique et une puissance électrique [83].

L'expérience de la balance du watt comporte deux étapes. Une première étape, appelée phase statique, permet de comparer la force de Laplace exercée sur une bobine, parcourue par un courant continu et placée dans le champ créé par un aimant, au poids d'une masse M reliée au kilogramme. La seconde étape, ou phase dynamique, consiste à mesurer la tension induite aux extrémités de la bobine lorsque celle-ci est déplacée dans le même champ à une vitesse v connue. Les mesures des quantités électriques sont ramenées aux constantes de von Klitzing (R_K) et de Josephson (K_J).

La balance du watt permet finalement de relier une masse macroscopique au produit $R_K K_J^2$ sous la forme :

$$MK_J^2 R_K = \frac{A}{gv} \quad (5.2)$$

où A est une grandeur proportionnelle au produit des fréquences Josephson correspondant aux mesures de tension lors des phases statique et dynamique et g l'accélération de la pesanteur subie par la masse M .

En écrivant $R_K = \frac{h}{e^2}$ et $K_J = \frac{2e}{h}$, on obtient :

$$\frac{4M}{h} = \frac{A}{gv} \quad (5.3)$$

La quantité $4/K_J^2 R_K$, c'est-à-dire h , a été déterminée avec une incertitude relative de 5×10^{-8} dans l'expérience de balance du watt américaine [84].

Si h est fixé, la mesure des grandeurs A , g et v permet la réalisation du kilogramme. Il est important de noter que cette réalisation repose sur la validité des relations $R_K = \frac{h}{e^2}$ et $K_J = \frac{2e}{h}$. Or, le manque de consistance entre certaines données expérimentales

a été à l'origine d'un test de l'exactitude de ces relations lors du dernier CODATA [50]. A l'issue de ce test, l'introduction de deux constantes ϵ_J et ϵ_K prenant en compte l'existence d'éventuels facteurs correctifs, a cassé l'égalité stricte qui existait entre K_J , R_K et leurs expressions théoriques, soit :

$$K_J = \frac{2e}{h}(1 + \epsilon_J) \quad (5.4)$$

et

$$R_K = \frac{h}{e^2}(1 + \epsilon_K) \quad (5.5)$$

avec $\epsilon_J = -126 (81) \times 10^{-9}$ et $\epsilon_K = 23 (19) \times 10^{-9}$ [50]. Il apparait donc nécessaire de développer des protocoles expérimentaux permettant de tester R_K et K_J .

Redéfinir le kilogramme en fixant N_A

Une autre possibilité avancée pour la redéfinition du kilogramme consiste à fixer la constante d'Avogadro N_A [80].

Le kilogramme serait alors défini par :

$$1 \text{ kg} = 10^3 N_A m_u \quad (5.6)$$

où m_u est l'unité de masse atomique ($m_u = \frac{1}{12}m(^{12}\text{C})$).

Pour rendre cette méthode compétitive, il faudrait déterminer N_A à 10^{-8} .

A l'heure actuelle, N_A est mesuré à $3,1 \times 10^{-7}$ à partir du volume molaire d'une sphère de silicium [85]. Plus précisément, N_A s'exprime comme le rapport entre le volume molaire et le volume atomique [86] :

$$N_A = \frac{V_{mol}}{V_{at}} = n \frac{M(Si)}{m} \frac{v}{V_0} \quad (5.7)$$

avec m et v , la masse et le volume de l'échantillon de Si, $M(Si)$ la masse molaire moyenne du Si, V_0 le volume d'une maille élémentaire et n le nombre d'atomes composant une maille élémentaire ($n = 8$). La détermination de N_A implique donc de mesurer la densité macroscopique de l'échantillon, la masse molaire moyenne et le volume de la maille.

Le volume de la maille se déduit du pas du réseau cristallin (noté d_{220}) mesuré par diffraction X. Cette grandeur dépend fortement de la présence d'impuretés et de défauts dans la maille cristalline et sa détermination est entachée d'effets systématiques liés au système de mesure. Elle est mesurée à quelques 10^{-8} par différentes équipes dans le monde, en particulier à la PTB (Physikalisch- Technische Bundesanstalt), à l'IMGC

(Istituto di Metrologia "G. Colonnetti", Turin) et au NRLM (National Research Laboratory of Metrology, Japon).

La masse molaire du silicium est déterminée par spectrométrie de masse. Les résultats obtenus dépendent de la composition isotopique de l'échantillon et certaines équipes travaillent actuellement sur la fabrication de sphères de silicium enrichi (99% de ^{28}Si au lieu de 92% en abondance naturelle).

Il faut enfin mesurer la densité macroscopique de l'échantillon en la comparant à un standard de 1 kg. La difficulté réside alors dans la fabrication de sphères dont le diamètre et l'état de surface sont connus avec une incertitude sub-nanométrique. Le volume de la sphère est déterminé via son diamètre par interférométrie.

La réalisation expérimentale de N_A à partir du silicium est donc extrêmement délicate. Néanmoins, les différents groupes impliqués dans ce projet espèrent atteindre une incertitude relative de 2×10^{-8} dans un futur proche.

5.3.2 Notre expérience de mesure de h/m associée à la balance du watt

Notre expérience d'oscillations de Bloch avec des atomes froids de rubidium, décrite dans le chapitre 4 de ce mémoire, pourrait jouer un rôle dans cette dynamique. En effet, notre équipe, associée à celle de Gérard Genevès, chargée de l'expérience de balance du watt au Laboratoire National de Métrologie et d'Essais, propose un rapprochement des deux expériences, soit pour réaliser N_A , soit pour tester la validité des expressions de R_K et K_J [87].

Réalisation de N_A

La constante d'Avogadro s'écrit sous la forme :

$$N_A = \frac{M_u}{m_u} = \frac{1}{h} \frac{h}{A_r(X)m_u} A_r(X)M_u = \frac{1}{h} \frac{h}{m(X)} A_r(X)M_u \quad (5.8)$$

où M_u est la constante de masse molaire ($M_u = 10^{-3} \text{ kg mol}^{-1}$), m_u , l'unité de masse atomique, $A_r(X)$ la masse atomique relative de la particule X et $m(X)$, la masse atomique de la particule X .

Dans notre expérience, nous mesurons soit la quantité $\frac{h}{m_{Rb}g^{(a)}}$ (où $g^{(a)}$ est la gravité locale subie par les atomes) en plaçant les atomes dans l'onde stationnaire verticale (voir paragraphe 4.3.2), soit la quantité $\frac{h}{m_{Rb}}$ en accélérant les atomes vers le haut puis vers le bas pour éliminer $g^{(a)}$ (voir paragraphe 4.3.3).

L'expérience de balance du watt permet de mesurer la quantité $R_K K_J^2 g^{(w)}$ (où $g^{(w)}$ est

la gravité locale subie par la masse macroscopique) ou bien la quantité $R_K K_J^2$ si elle est associée à un gravimètre absolu permettant de mesurer $g^{(w)}$ indépendamment.

Si on suppose que les expressions théoriques de R_K et K_J sont exactes, on dispose alors, en utilisant l'expression (5.8), de deux possibilités de réalisations de N_A .

$$N_A^{(1)} = \left\{ \frac{K_J^2 R_K g^{(w)}}{4} \right\} \left\{ \frac{h}{m_{Rb} g^{(a)}} \right\} \left\{ \frac{g^{(a)}}{g(w)} \right\} A_r(Rb) M_u \quad (5.9)$$

dans le cadre de l'expérience des oscillations de Bloch en onde stationnaire. Si les deux montages sont suffisamment proches l'un de l'autre, les deux accélérations locales $g^{(a)}$ et $g^{(w)}$ peuvent être comparées précisément avec des gravimètres relatifs.

Si on mesure le rapport h/m_{Rb} , N_A peut être réalisé sous la forme suivante :

$$N_A^{(2)} = \left\{ \frac{K_J^2 R_K}{4} \right\} \left\{ \frac{h}{m_{Rb}} \right\} A_r(Rb) M_u \quad (5.10)$$

L'incertitude relative que l'on pourrait attendre sur $N_A^{(1)}$ est limitée actuellement par l'incertitude sur le rapport $\frac{h}{m_{Rb} g^{(a)}}$ (de l'ordre de 10^{-6} dans l'expérience préliminaire que nous avons réalisée). Les autres quantités apparaissant dans l'expression (5.9) sont mieux connues : 4×10^{-8} sur $R_K K_J^2 g^{(w)}$ en extrapolant les résultats de la référence [84], mieux que 2×10^{-10} pour $A_r(Rb)$ et le transfert de la mesure de g peut être réalisé à 10^{-9} si les deux expériences sont assez proches l'une de l'autre.

En ce qui concerne la réalisation $N_A^{(2)}$, notre mesure du rapport h/m_{Rb} à $1,3 \times 10^{-8}$ [75] permet d'espérer une incertitude relative de $5,3 \times 10^{-8}$, a priori plus faible que celle obtenue jusqu'à présent sur le silicium.

Test de la validité de l'expression théorique de $K_J^2 R_K$

En tenant compte des deux paramètres ϵ_J et ϵ_K qui corrige les valeurs de K_J et R_K par rapport à leurs expressions théoriques, les expressions de $N_A^{(1)}$ et $N_A^{(2)}$ deviennent :

$$N_A^{(1)} = \left\{ \frac{K_J^2 R_K g^{(w)}}{4} \right\} \left\{ \frac{h}{m_{Rb} g^{(a)}} \right\} \left\{ \frac{g^{(a)}}{g(w)} \right\} \frac{A_r(Rb) M_u}{(1 + \epsilon_J)^2 (1 + \epsilon_K)} \quad (5.11)$$

et

$$N_A^{(2)} = \left\{ \frac{K_J^2 R_K}{4} \right\} \left\{ \frac{h}{m_{Rb}} \right\} \frac{A_r(Rb) M_u}{(1 + \epsilon_J)^2 (1 + \epsilon_K)} \quad (5.12)$$

L'une ou l'autre des deux propositions de réalisation de N_A , associée à une détermination indépendante constituerait un test de la validité des relations $R_K = \frac{h}{e^2}$ et $K_J = \frac{2e}{h}$. Plus précisément, des incertitudes relatives de $5,3 \times 10^{-8}$ sur $N_A^{(2)}$ et de 2×10^{-8} sur

N_A du projet "silicium" aboutiraient à un test à $5,7 \times 10^{-8}$.

Ces perspectives montrent bien que les possibilités de notre expérience d'oscillations de Bloch avec des atomes froids dépassent largement le cadre de la détermination de la constante de structure fine. En effet, associée à l'expérience de la balance du watt, elle pourrait contribuer au projet de redéfinition du kilogramme qui agite le monde de la métrologie.

Bibliographie

- [1] Astrid Lambrecht, *Atomes froids et fluctuations quantiques*, Thèse de doctorat de l'université Pierre et Marie Curie, 1995. Cité p. 9
- [2] A. Lambrecht, T. Coudreau, A.M. Steinberg, and E. Giacobino, Euro. Phys. Lett. **36** (1996), 93. Cité p. 9
- [3] A.Z. Khouri, T. Coudreau, C. Fabre, and E. Giacobino, Phys. Rev. A **57** (1770), 1238. Cité p. 9
- [4] Valéry Jost, *Réduction du bruit dans les lasers : applications aux lasers à semi-conducteur et aux minilasers solides*, Thèse de doctorat de l'université Pierre et Marie Curie, 1997. Cité p. 9
- [5] Alberto Bramati, *Etude du bruit quantique dans les lasers à semi-conducteur et à solide*, Thèse de doctorat de l'université Pierre et Marie Curie, 1998. Cité p. 9
- [6] T.C. Zhang, J.P. Poizat, P. Grelu, J.F. Roch, P. Grangier, F. Marin, A. Bramati, V. Jost, M.D. Levenson, and E. Giacobino, Quantum and Semiclass Optics **7** (1995), 601. Cité p. 9
- [7] E. Giacobino, A. Bramati, and F. Marin, J. of Nonlinear Optical Physics and Materials **5** (1996), 863. Cité p. 9
- [8] F. Marin, A. Bramati, E. Giacobino, T.C. Zhang, J.P. Poizat, J.F. Roch, and P. Grangier, Phys. Rev. Lett. **75** (1995), 4606. Cité p. 9
- [9] Jean-Pierre Hermier, *Etude du bruit quantique dans les microlasers semi-conducteurs à cavité verticale (VCESLs) et les lasers à solide Nd : YVO₄*, Thèse de doctorat de l'université Pierre et Marie Curie, 2000. Cité p. 9
- [10] J.P. Hermier, A. Bramati, A.Z. Khouri, E. Giacobino, J.P. Poizat, T.C. Chang, and P. Grangier, J. Opt. Soc. Am. B **16** (1999), 2140. Cité p. 9
- [11] J.P. Hermier, A. Bramati, A.Z. Khouri, E. Giacobino, J.P. Poizat, P. Grangier, P. Schnitzer, R. Michalzik, and K.J. Ebeling, Optics Lett. **24** (1999), 893. Cité p. 9

- [12] Gaëtan Messin, *Luminescence, bruit et effets non linéaires dans les microcavités*, Thèse de doctorat de l'université Pierre et Marie Curie, 2000. Cité p. 9
- [13] Jean-Philippe Karr, *Effets non linéaires et quantiques dans les microcavités semi-conductrices*, Thèse de doctorat de l'université Pierre et Marie Curie, 2001. Cité p. 9
- [14] Augustin Baas, *Amplification paramétrique et réduction du bruit quantique dans les microcavités semi-conductrices*, Thèse de doctorat de l'université Pierre et Marie Curie, 2003. Cité p. 9
- [15] G. Messin, J.P. Karr, A. Baas, G. Khitrova, R. Houdré, R.P. Stanley, U. Oesterle, and E. Giacobino, Phys. Rev. Lett. **87** (2001), 127403. Cité p. 9
- [16] E.S. Polzik, J. Carri, and H.J. Kimble, Phys. Rev. Lett. **68** (1992), 3020. Cité p. 9
- [17] P.H. Souto Ribeiro, C. Schwob, A. Maître, and C. Fabre, Optics Lett. **22** (1997), 1893. Cité p. 10, 14, 17
- [18] J. Mertz, T. Debuisschert, A. Heidmann, C. Fabre, and E. Giacobino, Optics Letters **16** (1991), 1234. Cité p. 12
- [19] Catherine Schwob, *Utilisation des faisceaux corrélés au niveau quantique produits par un oscillateur paramétrique optique en spectroscopie de grande sensibilité*, Thèse de doctorat de l'université Pierre et Marie Curie, 1997. Cité p. 13
- [20] J. Gao, F. Cui, C. Xue, C. Xie, and P. Kunchi, Opt. Lett. **23** (1998), 870. Cité p. 17
- [21] J. Laurat, T. Coudreau, N. Treps, A. Maître, and C. Fabre, Phys. Rev. A **69** (2004), 033808. Cité p. 18
- [22] C. Fabre, A. Maître, and J.-B. Fouet, Optics Lett. **25** (2000), 76. Cité p. 18
- [23] N. Treps, U. Andersen, B. Buchler, P.K. Lam, A. Maître, H.-A. Bachor, and C. Fabre, Phys. Rev. Lett. **88** (2002), 203601. Cité p. 18
- [24] N. Treps, N. Grosse, W.P. Bowen, C. Fabre, H.-A. Bachor, and P.K. Lam, *A quantum laser pointer*, Science (August 2003), 940–943. Cité p. 18
- [25] Béatrice de Beauvoir, *Réalisation d'un étalon de fréquence à 778 nm : mesure absolue des fréquences 2S – 8S/D des atomes d'hydrogène et de deutérium et détermination de la constante de Rydberg*, Thèse de doctorat de l'université Pierre et Marie Curie, 1996. Cité p. 25, 38
- [26] V.A. Yerokhin, P. Indelicato, and V.M. Shabaev, Phys. Rev. A **71** (2005), 040101. Cité p. 28, 29
- [27] I. Sick, Phys. Lett. B **576** (2003), 62. Cité p. 29

- [28] Olivier Arnoult, Thèse de doctorat de l'université Pierre et Marie Curie, 2006. Cité p. 29
- [29] M. Niering, R. Holzwarth, J. Reichert, P. Pokasov, Th. Udem, M. Weitz, T.W. Hänsch, P. Lemonde, G. Santarelli, M. Abgrall, P. Laurent, C. Salomon, and A. Clairon, Phys. Rev. Lett. **84** (2000), 5496. Cité p. 29
- [30] R. Pohl, A. Antognini, F.D. Amaro, F. Biraben, J.M.R. Cardoso, C.A.N. Conde, A. Dax, S. Dhawan, L.M.P. Fernandes, T.W. Hänsch, F.J. Hartmann, V.W. Hughes O. Huot, P. Indelicato, L. Julien, P.E. Knowles, F. Kottmann, Y.-W. Liu, L. Ludhova, C.M.B. Monteiro, F. Mulhauser, F. Nez, P. Rabinowitz, J.M.F. dos Santos, L.A. Schaller, C. Schwob, D. Taqqu, and J.F.C.A. Veloso, Can. J. Phys. **83** (2005), 339. Cité p. 31
- [31] A. Antognini, F.D. Amaro, F. Biraben, J.M.R. Cardoso, C.A.N. Conde, D.S. Co-vita, A. Dax, S. Dhawan, L.M.P. Fernandes, T.W. Hänsch, V.W. Hughes, O. Huot, P. Indelicato, L. Julien, P.E. Knowles, F. Kottmann, Y.-W. Liu, J.A.M. Lopes, L. Ludhova, C.M.B. Monteiro, F. Mulhauser, F. Nez, B.N. Perry, R. Pohl, P. Rabinowitz, J.M.F. dos Santos, L.A. Schaller, C. Schwob, D. Taqqu, and J.F.C.A. Veloso, Opt. Comm. **253** (2005), 362. Cité p. 31
- [32] M. Weitz, F. Schmidt-Kaler, and T.W. Hänsch, Phys.rev. Lett. **68** (1992), 1120. Cité p. 32
- [33] M. Fischer, N. Kolachevsky, M. Zimmermann, R. Holzwarth, Th. Udem, T.W. Hänsch, M. Abgrall, J. Grünert, I. Maksimovic, S. Bize, H. Marion, F. Pereira Dos Santos, P. Lemonde, G. Santarelli, P. Laurent, A. Clairon, C. Salomon, M. Haas, U.D. Jentschura, and C.H. Keitel, Phys. Rev. Lett. **92** (2004), 230802. Cité p. 32
- [34] S. Karshenboim, Z. Phys. D **39** (1997), 109. Cité p. 32
- [35] Sophie Bourzeix, *Laser continu à 205 nm : application à la mesure du déplacement de Lamb dans l'hydrogène*, Thèse de doctorat de l'université Pierre et Marie Curie, 1995. Cité p. 33
- [36] S. Bourzeix, B. de Beauvoir, F. Nez, M.D. Plimmer, F. de Tomasi, L. Julien, F. Biraben, and D.N. Stacey, Phys. Rev. Lett. **76** (1996), 384. Cité p. 33
- [37] Gaëtan Hagel, *Spectroscopie de l'atome d'hydrogène. Vers une mesure absolue de la fréquence de la transition 1S – 3S*, Thèse de doctorat de l'université Pierre et Marie Curie, 2001. Cité p. 33
- [38] F. Biraben, L. Julien, J. Plon, and F. Nez, Europhys. Lett. **15** (1991), 831. Cité p. 33

- [39] G. Hagel, R. Battesti, F. Nez, L. Julien, and F. Biraben, Phys. Rev. Lett. **89** (2002), 203001. Cité p. 33
- [40] François Nez, *Chaîne de fréquence optique pour mesurer les transitions $2S - 8S/D$ dans l'atome d'hydrogène, mesure de la constante de Rydberg en unité de fréquence*, Thèse de doctorat de l'université Pierre et Marie Curie, 1993. Cité p. 34
- [41] F. Nez, M.D. Plimmer, S. Bourzeix, L. Julien, F. Biraben, R. Felder, Y. Milleroux, and P. De Natale, Europhys. Lett. **24** (1993), 635. Cité p. 34
- [42] B. de Beauvoir, F. Nez, L. Hilico, L. Julien, F. Biraben, B. Cagnac, J.-J. Zondy, D. Touhari, O. Acef, and A. Clairon, EPJD **1** (1998), 227. Cité p. 35, 36
- [43] C. Schwob, L. Jozefowski, B. de Beauvoir, L. Hilico, F. Nez, L. Julien, and F. Biraben, Phys. Rev. Lett. **82** (1999), 4960. Cité p. 35, 36, 41, 84
- [44] B. de Beauvoir, C. Schwob, O. Acef, L. Jozefowski, F. Nez, L. Julien, A. Clairon, and F. Biraben, EPJD **12** (2000), 61. Cité p. 38, 40
- [45] M. Ben Dahan, E. Peik, J. Reichel, Y. Castin, and C. Salomon, Phys. Rev. Lett. **76** (1996), 4508. Cité p. 83, 89
- [46] Th. Udem, A. Huber, B. Gross, J. Reichert, M. Prevedelli, M. Weitz, and T.W. Hänsch, Phys. Rev. Lett. **79** (1997), 2646. Cité p. 84
- [47] T. Beir, H. Häffner, N. Hermanspahn, S.G. Karshenboim, H.J. Kluge, W. Quint, S. Stahl, J. Verdú, and G. Werth, Phys. Rev. Lett. **88** (2002), 011603. Cité p. 84
- [48] M.P. Bradley, J.V. Porto, S. Rainville, J.K. Thompson, and D.E. Pritchard, Phys. Rev. Lett. **83** (1999), 4510. Cité p. 84
- [49] P. Mohr and B.N. Taylor, Rev. Mod. Phys. **72** (2000). Cité p. 84
- [50] P. Mohr and B.N. Taylor, Rev. Mod. Phys. **77** (2005). Cité p. 84, 144
- [51] A Wicht, J.M. Hensley, E. Sarajlic, and S. Chu, Physica Scripta **T102** (2002), 82. Cité p. 84, 88, 106
- [52] R.S. Van Dyck, P.B. Schwinberg, and H.G. Dehmelt, Phys. Rev. Lett. **59** (1987), 26. Cité p. 85, 86
- [53] H. Müller, S.-W. Chiow, Q. Long, C. Vo, and S. Chu, Appl. Phys. B **84** (2006), 633. Cité p. 85
- [54] G. Gabrielse, D. Hanneke, T. Kinoshita, M. Nio, and B. Odom, Phys. Rev. Lett. **97** (2006), 030802. Cité p. 85, 86
- [55] T. Kinoshita and M. Nio, Phys. Rev. Lett. **90** (2003), 021803. Cité p. 86

- [56] W. Liu, M.G. Boshier, S. Dhawan, O. van Dyck, P. Egan, X. Fei, M. Grosse Perdekamp, V.W. Hughes, M. Janousch, K. Jungmann, D. Kawall, F.G. Mariam, C. Pillai, R. Prigl, G. zu Putlitz, I. Reinhard, W. Schwarz, P.A. Thompson, and K.A. Woodle, Phys. Rev. Lett. **82** (1999), 711. Cité p. 86
- [57] A.M. Jeffery, R.E. Elmquist, L.H. Lee, J.Q. Shields, and R.F. Dziuba, IEEE Trans. Instrum. Meas. **48** (1997), 356. Cité p. 87
- [58] G.W. Small, B.W. Ricketts, P.C. Coogan, B.J. Pritchard, and M.M.R. Sovierzoski, Metrologia **34** (1997), 241. Cité p. 87
- [59] Z. Zhang, X. Wang, D. Wang, X. Li, Q. He, and Y. Ruan, Acta Metrologia Sinica **16** (1995), 1. Cité p. 87
- [60] G. Trapon, O. Thévenot, J.C. Lacueille, W. Poirier, H. Fhima, and G. Genevès, IEEE Trans. Instrum. Meas. **50** (2001), 572. Cité p. 87
- [61] E.R. Williams, G.R. Jones, S. Ye, R. Liu, H. Sasaki, P.T. Olsen, W.D. Phillips, and H.P. Layer, IEEE Trans. Instrum. Meas. **38** (1989), 233. Cité p. 88
- [62] E. Krüger, W. Nistler, and W. Weirauch, Metrologia **36** (1999), 147. Cité p. 88
- [63] E. Krüger, W. Nistler, and W. Weirauch, Metrologia **32** (1995), 117. Cité p. 88
- [64] G. Cavagnero, H. Fujimoto, G. Mana, E. Massa, K. Nakayama, and G. Zosi, Metrologia **41** (2004), 56. Cité p. 88
- [65] J.L. Hall, C.J. Bordé, and K. Uehara, Phys. Rev. Lett. **37** (1976), 1339. Cité p. 89
- [66] Ch.J. Bordé, *Proceedings of frequency standards and metrology*, p. 196, A. De Marchi Springer-Verlag, 1989. Cité p. 89
- [67] A. Clairon, P. Laurent, G. Santarelli, S. Ghezali, S.N. Lea, and M. Bahoura, IEEE Trans. Instrum. Meas. **44** (1995), 128. Cité p. 90
- [68] Rémy Battesti, *Accélération d'atomes ultrafroids ; mesure de h/M* , Thèse de doctorat de l'université Pierre et Marie Curie, 2003. Cité p. 91, 97
- [69] Pierre Cladé, *Oscillations de Bloch d'atomes ultrafroids et mesure de la constante de structure fine*, Thèse de doctorat de l'université Pierre et Marie Curie, 2005. Cité p. 91, 100
- [70] P. Cladé, S. Guellati-Khélifa, C. Schwob, F. Nez, L. Julien, and F. Biraben, EPJD **33** (2005), 173. Cité p. 93
- [71] E. Peik, M. Ben Dahan, I. Bouchoule, Y. Castin, and C. Salomon, Phys. Rev. A **55** (1997), 2989. Cité p. 95
- [72] F. Bloch, Z. Phys. **52** (1928), 555. Cité p. 95

- [73] R. Battesti, P. Cladé, S. Guellati-Khélifa, C. Schwob, B. Grémaud, F. Nez, L. Julien, and F. Biraben, Phys. Rev. Lett. **92** (2003), 253001. Cité p. 97
- [74] P. Cladé, S. Guellati-Khélifa, C. Schwob, F. Nez, L. Julien, and F. Biraben, Europhys. Lett. **71** (2005), 730. Cité p. 98, 99
- [75] P. Cladé, E. de Mirandes, M. Cadoret, S. Guellati-Khélifa, C. Schwob, F. Nez, L. Julien, and F. Biraben, Phys. Rev. Lett. **96** (2006), 033001. Cité p. 100, 146
- [76] P. Cladé, E. de Mirandes, M. Cadoret, S. Guellati-Khélifa, C. Schwob, F. Nez, L. Julien, and F. Biraben, accepté à Phys. Rev. A. Cité p. 100, 102
- [77] Ch.J Bordé, Phys. rev. A **140** (1989), 10. Cité p. 105
- [78] K. Dieckmann, R.J.C. Spreeuw, M. Weidemüller, and J.T.M. Walraven, Phys. rev. A **58** (1998), 3891. Cité p. 140
- [79] Benjamin Besga, *Isolation active des vibrations basses fréquences, amélioration de la sensibilité d'un senseur inertiel*, Stage de 1ère année, Ecole Normale Supérieure de Lyon, 2006. Cité p. 140
- [80] I.M. Mills, P.J. Mohr, T.J. Quinn, B.N. Taylor, and E.R. Williams, Metrologia **42** (2005), 71. Cité p. 143, 144
- [81] I.M. Mill, P.J. Mohr, T.J. Quinn, B.N. Taylor, and E.R. Williams, Metrologia **43** (2006), 227. Cité p. 143
- [82] Ch.J. Bordé, Cr. Physique 5 (2004), 813. Cité p. 143
- [83] B.P. Kibble, *Atomic masses and fundamental constants 5*, Plenum Press. Cité p. 143
- [84] R.L. Steiner, E.R. Williams, D.B. Newell, and R. Liu, Metrologia **42** (2005), 431. Cité p. 143, 146
- [85] K. Fujii, A. Waseda, N. Kuramoto, S. Mizushima, P. Becker, H. Bettin, A. Nicolaus, U. Kuetgens, S. Valkiers, P. Taylor, P. De Bievre, G. Mana, E. Massa, R. Matyi, E.G. Kessler Jr, and M. Hanke, IEEE Trans. Instr. Meas. **54** (2005), 854. Cité p. 144
- [86] P. Becker, Metrologia **40** (2003), 366. Cité p. 144
- [87] F. Biraben, M. Cadoret, P. Cladé, G. Genevès, P. Gournay, S. Guellati Khélifa, L. Julien, P. Juncar, E. de Mirandes, and F. Nez, *Proposal for new experimental schemes to realize the Avogadro constant.*, accepté à Metrologia, 366. Cité p. 145

Curriculum vitae

Catherine Schwob

Laboratoire Kastler Brossel

Université Pierre et Marie Curie

4, place Jussieu, 75252 Paris cedex 05

01 44 27 72 48

schwob@spectro.jussieu.fr

née le 09 février 1970

Formation

1990 DEUG A physique-mathématiques, Université Paris XI

1991 Licence de physique fondamentale, Université Paris XI

1992 Maîtrise de physique fondamentale, Université Paris XI

1993 DEA Lasers et Matière, Université Paris XI

1997 Doctorat de l'Université Pierre et Marie Curie. Thèse réalisée au Laboratoire Kastler Brossel.

spécialité : Lasers et Matière

sujet : Utilisation de faisceaux corrélés au niveau quantique, produits par un Oscillateur Paramétrique Optique, en spectroscopie de grande sensibilité.

Fonctions

1993-1996 Monitrice à l'Université de Versailles-Saint Quentin en Yvelines

1997-1998 Attachée Temporaire à l'Enseignement et à la Recherche à l'Université Pierre et Marie Curie

Depuis 1998 Maître de conférence à l'Université Pierre et Marie Curie, Paris. Recherche effectuée au Laboratoire Kastler Brossel dans l'équipe de Métrologie des Systèmes Simples et Tests Fondamentaux.

Activités de recherche

07/92-08/92 Stage de maîtrise au CEA Saclay

Réalisation de matériaux supraconducteurs (YBaCuO) par électrolyse et caractérisation de leurs propriétés vis-à-vis de l'application d'un champ magnétique à très basse température.

04/93-07/93 Stage de DEA au Laboratoire Kastler Brossel, dans le groupe d'optique quantique, sous la direction de Claude Fabre

Réalisation d'une diode laser en cavité étendue. Caractérisation du spectre d'émission.

Stabilisation de la fréquence d'émission par absorption saturée sur l'atome de césium.

09/93-07/97 Thèse au Laboratoire Kastler Brossel, dans le groupe d'optique quantique, sous la direction de Claude Fabre.

Développement d'une expérience de spectroscopie de haute sensibilité sur l'atome de potassium. Utilisation des corrélations quantiques apparaissant sur la différence des intensités des faisceaux produits par un oscillateur paramétrique optique pour détecter un signal absorption avec un bruit de fond inférieur à la limite quantique standard ("shot noise").

Développement d'un modèle théorique prenant en compte le caractère gaussien des champs produits par génération paramétrique : analyse du fonctionnement multimode transverse de l'oscillateur paramétrique optique du point de vue de la réduction des fluctuations quantiques.

Depuis 09/97 activité de recherche au Laboratoire Kastler Brossel, dans le groupe de Métrologie des Systèmes Simples et Tests Fondamentaux, sous la direction de François Biraben.

97-98 Mesure absolue de la transition 2S-12D des atomes d'hydrogène et de deutérium dans le cadre de la détermination de la constante de Rydberg. Développement d'une cavité de doublage pour réaliser l'une des équations du schéma de fréquence à partir de la diode laser étalon à 778 nm.

98-99 Traitement des données en ajustant les signaux expérimentaux sur des formes de raie calculées. Affinement des formes de raies théoriques existantes grâce à la prise en compte des champs électriques parasites par effet Stark.

depuis 99 Réalisation d'une expérience d'oscillations de Bloch sur des atomes froids. Détermination de la constante de structure fine.

Encadrement

Dans le cadre des activités de recherche

1999-2000 Christophe Winisdoerffer

Scientifique du contingent, Montage d'un piège magnéto-optique, développement du programme informatique de gestion de l'expérience.

01/00-02/00 Alexis Cothenet

Stage de M1, Refroidissement d'un nuage d'atomes de rubidium dans un piège magnéto-optique.

2000-2001 Sébastien Charnoz

Gestion informatique de la caméra CCD pour la visualisation d'un nuage d'atomes

froids. 2000-2003 **Rémy Battesti**

Thèse de l'Université Pierre et Marie Curie, Accélération d'atomes ultrafroids : mesure de h/M.

04/02-07/02 **Pierre Cladé**

Stage de M2 Physique quantique, Transitions Raman sur des atomes de rubidium froids : vers une mesure de h/M.

depuis 12/04 **Malo Cadoret**

Thèse de l'Université Pierre et Marie Curie, Oscillations de Bloch d'atomes ultrafroids dans un réseau optique vertical : déterminations de h/M par méthodes interférométrique et non interférométrique.

31/01/05-11/02/05 **Daniel Heng et Philippe Phothisaine**

Stage de découverte L3, développement d'un système laser compact pour aligner les fibres optiques.

07/05 **Julien Arminjo**

Stage MIP 1ère année, Montage et caractérisation d'une diode laser couplée sur réseau en vue du piégeage d'atomes ultrafroids.

14/03/06-07/04/06 **Damien Cornu**

Stage ENS 1ère année, Mise en oeuvre d'un analyseur de front d'onde pour le réglage de faisceaux laser destinés à piéger des atomes.

04/06-07/06 **Franck Ferreyrol**

Stage de M1 PHYTEM, Développement de sources laser pour la réalisation d'un piège magnéto-optique à deux dimensions pour la mesure du rapport h/M du rubidium.

06/06-07/06 **Benjamin Besga**

Stage ENS 1ère année, Isolation active des vibrations basses fréquences, amélioration de la sensibilité d'un senseur inertiel.

Dans le cadre des activités d'enseignement

04/03-06/03 **Nicolas Coscas et Guillaume Bouchaud**

Stage de Licence Pro, Réalisation d'un débitmètre laser.

04/05-07/05 **Philippe Llorens**

Stage de Licence Pro, Observation de la rétrodiffusion cohérente dans un milieu désordonné. Développement d'un montage expérimental sur l'adaptation de modes d'une cavité optique.

23/01/06-03/02/06 **Aberzki Merouani et Tony Lefevre**

Stage de découverte L3, Réalisation d'un montage de lecture de code barre.

04/06-07/06 **Yannick Darras et Lionel Tribut**

Stage de Licence Pro, Réalisation d'un montage de transmission d'images par voie op-

tique.

Enseignement

93-96 Travaux Pratiques d'**optique géométrique et de thermométrie** en L1 (monitorat à l'Université de Versailles-Saint Quentin en Yvelines)

96-97 Travaux Dirigés de **physique atomique et moléculaire** en M1 (vacations à l'Université d'Evry-Val d'Essonne)

depuis septembre 97, j'effectue mon enseignement à Paris 6

97-01 préparation au CAPES : épreuve du montage (réécriture de fiches d'utilisation des logiciels)

97-98 Travaux Dirigés sur les **lasers et l'optique non linéaire** en M2 (réécriture des textes de TD)

99-04 Cours, Travaux Dirigés et Travaux Pratiques d'**optique géométrique** en L3 (réécriture du polycopié de cours, des textes de TD et TP)

Travaux Dirigés et Travaux Pratiques d'**optique physique et électromagnétisme** en L3 (réécriture des textes de TD et TP)

01-03 Travaux Dirigés et Travaux Pratiques sur les **ondes** en L2 (réécriture des textes d'examen et de contrôle continu)

02-04 Travaux Dirigés d'**électromagnétisme** en L2 (réécriture des textes de TD et d'examen)

97-02 puis depuis 04 **Centre d'Instrumentation Laser**

- encadrement des Travaux Pratiques sur les lasers en M1 et M2

- développement de montages existants et création de nouveaux TP :

laser hélium néon, manipulation de faisceaux gaussiens (2h de TP), adaptation de modes d'une cavité optique (2h de TP), vélocimétrie Doppler (4h de TP), fibres optiques (6h de TP), expériences de démonstration (mesure de la vitesse de propagation de la lumière dans une fibre optique, transmission d'image par voie optique, lecture de code barre)

- réécriture des polycopiés de TP

- formation des enseignants

- organisation et encadrement de stages de formation continue sur les lasers

- **depuis 04** : gestion complète du Centre d'Instrumentation Laser

depuis 05 : Création et organisation de l'**UE Projet Expérimental** de M1 :

- développement d'un montage sur la rétrodiffusion cohérente de la lumière et encadrement d'étudiants sur ce montage

- coordination des différents projets proposés par les autres enseignants.

Responsabilités universitaires

depuis septembre 2004, responsable de la plate-forme expérimentale du Master de Physique de Paris 6, et en particulier du Centre d'Instrumentation Laser.

Commissions et conseils

2001-2004 membre de la commission de spécialistes 30ème section de l'Université Pierre et Marie Curie

depuis 2001 membre de la commission de spécialistes de physique de l'Université d'Evry-Val d'Essonne

depuis 2001 membre de la commission de spécialistes de physique du Conservatoire National des Arts et Métiers.

depuis 2004 membre de l'équipe de formation universitaire du Master de Physique de l'Université Pierre et Marie Curie.

depuis 2006 membre du conseil de département du Master de Physique de l'Université Pierre et Marie Curie

depuis 2006 membre du conseil du Laboratoire Kastler Brossel.

Publications

Revues internationales avec comité de lecture

- [1] C. Fabre, P.F. Cohadon, C. Schwob, Quantum and Semiclass. Opt., **9** (1997) p165 : "CW optical parametric oscillators : single mode operation and frequency tuning properties".
- [2] P. Souto Ribeiro., C. Schwob, A. Maître, C. Fabre, Optics Letters **22** n°24 (1997) p1893 : "Sub-shot-noise high-sensitivity spectroscopy with optical parametric oscillator twin beams".
- [3] C. Schwob, P.F. Cohadon, C. Fabre, M. Marte, A. Gatti, L. Lugiato, Applied Physics B (Lasers and Optics) **B66** (1998) p685 : "Transverse effects and mode coupling in OPOs".
- [4] G. Hagel, C. Nesi, L. Jozefowski, C. Schwob, F. Nez et F. Biraben, Optics Communications **160** (1999) p1-4 : "Accurate measurement of the frequency of the 2S-8S two-photon transitions in cesium".
- [5] C. Schwob, L. Jozefowski, B. de Beauvoir, L. Hilico, F. Nez, L. Julien, F. Biraben, O. Acef, J.-J. Zondy et A. Clairon, Phys. Rev. Lett. **82** (1999) p.4960-4963 : "Optical frequency measurement of the 2S-12D transitions in hydrogen and deuterium : Rydberg constant and Lamb shift determinations".
- [6] C. Schwob, L. Jozefowski, O. Acef, L. Hilico, B. de Beauvoir, F. Nez, L. Julien, A. Clairon, F. Biraben, IEEE Transactions on Instrumentation and Measurements **48** (1999) p178 : "Frequency measurement of the 2S-12D transitions in hydrogen and deuterium, new determination of the Rydberg constant".
- [7] C. Fabre, M. Vaupel, N. Treps, P.F. Cohadon, C. Schwob, A. Maître, CR Acad Sci Paris 1 série IV (2000) p553 : "CW optical parametric oscillators : single mode or multimode ?".
- [8] B. de Beauvoir, C. Schwob, O. Acef, J.-J. Zondy, L. Jozefowski, L. Hilico, F. Nez, L. Julien, A. Clairon et F. Biraben, Eur. Phys. J. D **12** (2000) p.61-93 : "Metrology of the hydrogen and deuterium atoms : determination of the Rydberg constant and Lamb shifts".
- [9] R. Battesti, P. Cladé, S. Guellati-Khélifa, C. Schwob, B. Grémaud, F. Nez, L. Julien et F. Biraben, J. Opt. B : Quantum Semiclass. Opt. **5** (2003) ppS178-S182 : "Acceleration of ultracold atoms : towards a measurement of h/M_{Rb} ".
- [10] R. Battesti, P. Cladé, S. Guellati-Khélifa, C. Schwob, B. Grémaud, F. Nez, L. Julien et F. Biraben, Phys. Rev. Lett. **92** (2004) p.253001-1 : "Bloch oscillations of ultracold atoms : a tool for metrological determination of h/m_{Rb} ".
- [11] P. Cladé, S. Guellati-Khélifa, C. Schwob, F. Nez, L. Julien et F. Biraben, Europhys. Lett, **71** (2005) p.730 : "A promising method for the measurement of the local

acceleration of gravity using Bloch oscillations of ultracold atoms in a vertical standing wave”.

- [12] A. Antognini, F.D. Amaro, F. Biraben, J.M.R. Cardoso, C.A.N. Conde, D.S. Co-vita, A. Dax, S. Dhawan, L.M.P. Fernandes, T.W. Hänsch, V.W. Hughes, O. Huot, P. Indelicato, L. Julien, P.E. Knowles, F. Kottmann, Y.-W. Liu, J.A.M. Lopes, L. Lud-hova, C.M.B. Monteiro, F. Mulhauser, F. Nez, B.N. Perry, R. Pohl, P. Rabinowitz, J.M.F. dos Santos, L.A. Schaller, C. Schwob, D. Taqqu, J.F.C.A. Veloso, Opt. Comm. **253** (2005) p.362 : ”Powerful fast triggerable $6 \mu\text{m}$ laser for the muonic hydrogen 2S-Lamb shift experiment”.
- [13] P. Cladé, S. Guellati-Khélifa, C. Schwob, B. Grémaud, F. Nez, L. Julien, F. Biraben, EPJD, **33** (2005) p. 173 : ”Noise sensitivity of an atomic velocity sensor”.
- [14] P. Cladé, E. de Mirandes, M. Cadoret, S. Guellati-Khélifa, C. Schwob, F. Nez, L. Julien et F. Biraben, Phys. Rev. Lett. **96**, (2006), p.033001 : ”A new determination of the fine structure constant based on Bloch oscillations of ultracold atoms in a vertical optical lattice”.
- [15] P. Cladé, E. de Mirandes, M. Cadoret, S. Guellati-Khélifa, C. Schwob, F. Nez, L. Julien et F. Biraben, Phys. Rev. A **74**, (2006), p.052109 : ”A precise measurement of h/m_{Rb} using Bloch oscillations of ultracold atoms in a vertical optical lattice : de-termination of the fine structure constant”.
- [16] L. Ludhova, F.D. Amaro, A. Antognini, F. Biraben, J.M.R. Cardoso, C.A.N. Conde, A. Dax, S. Dhawan, L.M.P. Fernandes, T.W. Hänsch, V.W. Hughes, P. Indelicato, L. Julien, P.E. Knowles, F. Kottmann, Y.-W. Liu, J.A.M. Lopes, C.M.B. Monteiro, F. Mulhauser, F. Nez, R. Pohl, P. Rabinowitz, J.M.F. dos Santos, L.A. Schaller, C. Schwob, D. Taqqu, J.F.C.A. Veloso, soumis à PRL : ”Muonic hydrogen cascade time and lifetime of short-lived 2S state”.

Publications dans des actes de colloques

- [1] C. Schwob, C. Richy, C. Fabre, actes de COLOQ 4, Ann. Phys. Fr. **20** (1995) p581. : ”Spectroscopie en lumière comprimée”.
- [2] C. Schwob, P. Souto Ribeiro, A. Maître, C. Fabre, Actes de COLOQ 5, Ann. Phys. Fr. **23** (1998) p277 : ”Au-delà du shot noise : utilisation de faisceaux jumeaux en spec-troscopie de grande sensibilité”.
- [3] C. Schwob, L. Jozefowski, B. de Beauvoir, L. Hilico, F. Nez, L. Julien, F. Biraben, O. Acef et A. Clairon, Proceedings of the XXXIVth Rencontres de Moriond, Gravitationnal Waves and experimental gravity, édité par J. Trần Thanh Vân, J. Dumarchez, S. Reynaud, C. Salomon, S. Thorsett et J.Y. Vinet, World Publishers, Hanoi, Vietnam, p.427-432 : ”Metrology of the hydrogen atom : Rydberg constant determination and

Lamb shift”.

- [4] C. Schwob, L. Masson, B. Grémaud, S. Guellati, F. Nez, L. Julien et F. Biraben, Actes de COLOQ 6, Journal de physique IV **10** (2000) p.153-154 : ”Accélération d’atomes ultrafroids : mesure de h/M_A ”.
- [5] G. Hagel, C. Schwob, L. Jozefowski, B. de Beauvoir, L. Hilico, O. Acef, F. Nez, L. Julien, A. Clairon et F. Biraben, Proceedings SPIE **4269** (San Jose, 2001) pp.25-31 : ”Metrology of hydrogen atom : determination of the Rydberg constant and Lamb shifts”.
- [6] F. Biraben, T.W. Hänsch, M Fischer, M Niering, R. Holzwarth, J. Reichert, Th. Udem, M. Weitz, B. de Beauvoir, C. Schwob, L. Jozefowski, L. Hilico, F. Nez, L. Julien, O. Acef et A. Clairon, Lecture Notes in Physics (Springer), The Hydrogen Atom, Precision Physics of Simple Atomic Systems, édité par S.G. Karshenboïm, F.S. Pavone, G.F. Bassani, M. Inguscio and T.W. Hänsch, LNP **570** (2001) p. 17-41 : ”Precision spectroscopy of atomic hydrogen”.
- [7] G. Hagel, R. Battesti, C. Schwob, F. Nez, L. Julien, F. Biraben, O. Acef, J.J. Zondy, A. Clairon, Lecture Notes in Physics (Springer), The Hydrogen Atom, Precision Physics of Simple Atomic Systems, édité par S.G. Karshenboïm, F.S. Pavone, G.F. Bassani, M. Inguscio and T.W. Hänsch, LNP **570** (2001) sur cdrom : ”Absolute frequency measurement of the 1S-3S transition in hydrogen”.
- [8] G. Hagel, C. Schwob, L. Jozefowski, B. de Beauvoir, L. Hilico, F. Nez, L. Julien, F. Biraben, O. Acef et A. Clairon, Proceedings of the Third international symposium Modern Problems of Laser Physics (Institute of Laser Physics, Novosibirsk, 2000), édité par S.N. Bagayev et V.I. Denisov, pp.40-51 ; publié aussi dans Laser Physics **11** (2001) pp.1076-1082 ”Metrology of hydrogen atom : determination of the Rydberg constant and Lamb shifts”.
- [9] G. Hagel, C. Schwob, L. Jozefowski, B. de Beauvoir, L. Hilico, O. Acef, F. Nez, L. Julien, A. Clairon et F. Biraben, Proceedings of the Conference QED 2000 (Trieste, 2000), Quantum Electrodynamics and Physics of the Vacuum, édité par G. Cantatore, AIP-Conference proceedings **564** (2001) p.231-238 : ”Metrology of hydrogen atom : determination of the Rydberg constant and Lamb shifts”.
- [10] G. Hagel, C. Schwob, L. Jozefowski, B. de Beauvoir, L. Hilico, F. Nez, L. Julien, F. Biraben, O. Acef, J.J. Zondy and A. Clairon, Proceedings of the Sixth Symposium on Frequency Standards and Metrology (St-Andrews, 2001), édité par P. Gill, World Scientific (2002), pp. 222-229 : ”Metrology of hydrogen atom : determination of the Rydberg constant and Lamb shifts”.
- [11] R. Battesti, C. Schwob, B. Grémaud, S. Guellati-Khélifa, F. Nez, L. Julien et F. Biraben : Proceedings of the Sixth Symposium on Frequency Standards and Metrology

- (St-Andrews, 2001), édité par P. Gill, World Scientific (2002), pp. 535-537 : "Acceleration of rubidium cold atoms : determination of α ".
- [12] R. Battesti, P. Cladé, C. Schwob, B. Grémaud, S. Guellati-Khélifa, F. Nez, L. Julien et F. Biraben, actes de COLOQ 8, J. Phys. IV France **119** (2004) pp.157-158 : "Accélération d'atomes ultrafroids : vers une mesure de h/M_A ".
- [13] O. Arnoult, C. Schwob, F. Nez, L. Julien and F. Biraben, Can. J. Phys. **83** (2005) 273-281 : "Absolute frequency measurement of 1S-3S line in atomic hydrogen".
- [14] R. Pohl, A. Antognini, F.D. Amaro, F. Biraben, J.M.R. Cardoso, C.A.N. Conde, A. Dax, S. Dhawan, L.M.P. Fernandes, T.W. Hänsch, F.J. Hartmann, V.W. Hughes, O. Huot, P. Indelicato, L. Julien, P.E. Knowles, F. Kottmann, Y.-W. Liu, L. Ludhova, C.M.B. Monteiro, F. Mulhauser, F. Nez, P. Rabinowitz, J.M.F. dos Santos, L.A. Schaller, C. Schwob, D. Taqqu, and J.F.C.A. Veloso, Can. J. Phys. **83**, (2005) 339-349 : "The muonic hydrogen Lamb-shift experiment".
- [15] P. Cladé, R. Battesti, S. Guellati-Khélifa, C. Schwob, B. Grémaud, F. Nez, L. Julien and F. Biraben, Proceedings of the Fourth international symposium Modern Problems of Laser Physics (Institute of Laser Physics, Novosibirsk, 2004), édité par S.N. Bagayev et P.V. Pokasov, pp. 166-173, publié aussi dans Laser Physics 15, **5** (2005) pp.1-6, "Preliminary measurement of h/M_{Rb} using Bloch oscillations of ultracold atoms".
- [16] A. Antognini, F.D. Amaro, F. Biraben, U. Brauch, J.M.R. Cardoso, C.A.N. Conde, A. Dax, S. Dhawan, L.M.P. Fernandes, A. Giesen, T.W. Hänsch, P. Indelicato, L. Julien, P.E. Knowles, F. Kottmann, Y.-W. Liu, J.A.M. Lopes, L. Ludhova, C.M.B. Monteiro, F. Mulhauser, F. Nez, R. Pohl, P. Rabinowitz, J.M.F. dos Santos, L.A. Schaller, C. Schwob, C. Stolzenburg, D. Taqqu, and J.F.C.A. Veloso, AIP Conf. Proc. **796**, (2005) 253-259 : "The 2S Lamb Shift in Muonic Hydrogen and the Proton rms Charge Radius".
- [17] R. Pohl, A. Antognini, F.D. Amaro, F. Biraben, J.M.R. Cardoso, C.A.N. Conde, A. Dax, S. Dhawan, L.M.P. Fernandes, T.W. Hänsch, F.J. Hartmann, V.W. Hughes, O. Huot, P. Indelicato, L. Julien, P.E. Knowles, F. Kottmann, Y.-W. Liu, L. Ludhova, C.M.B. Monteiro, F. Mulhauser, F. Nez, P. Rabinowitz, J.M.F. dos Santos, L.A. Schaller, C. Schwob, D. Taqqu, and J.F.C.A. Veloso, Proc. of EXA05, International Conference on Exotic Atoms and Related Topics, Feb. 21-25, (2005), Vienna, Austria, ed. by A. Hirtl, J. Marton, E. Widmann, and J. Zmeskal, Austrian Academy of Sciences Press, p. 285-290, Vienna (2005) : "The muonic hydrogen Lamb-shift experiment".
- [18] S. Guellati-Khélifa, P. Cladé, M. Cadoret, E. de Mirandes, C. Schwob, F. Nez, L. Julien and F. Biraben, Proceeding for 17th International Conference on laser spectroscopy (ICOLS'05), Scotland, 19-24 Juin 2005 pp.72-78 : "Bloch oscillations of ultra-cold atoms : a tool for h/m_{Rb} measurement".

[19] T. Nebel, F.D. Amaro, A. Antognini, F. Biraben, J.M.R. Cardoso, C.A.N. Conde, A. Dax, S. Dhawan, L.M.P. Fernandes, A. Giesen, T.W. Hänsch, P. Indelicato, L. Julien, P.E. Knowles, F. Kottmann, E. Le Bigot, Y.-W. Liu, J.A.M. Lopez, L. Ludhova, C.M.B. Monteiro, F. Mulhauser, F. Nez, R. Pohl, P. Rabinowitz, J.M.F. dos Santos, L.A. Schaller, K. Schuhmann, C. Schwob, D. Taqqu, and J.F.C.A. Veloso, soumis à Can. J. Phys. : "Status of the muonic hydrogen Lamb-shift experiment".

Conférences invitées

[1] The 5th international conference on squeezed states and uncertainty relations, Balatonfured, Hongrie, 1997 (actes).

C. Fabre, C. Schwob, P. Souto Ribeiro, A. Maître, G. Gao, K. Kasai : "Two novel experiments with OPOs".

[2] XXXIVth Rencontres de Moriond, Gravitational waves and experimental gravity, Les Arcs, France, 1999 (actes).

C. Schwob, L. Jozefowski, B. de Beauvoir, L. Hilico, F. Nez, L. Julien, F. Biraben, O. Acef et A. Clairon : "Metrology of the hydrogen atom : Rydberg constant determination and Lamb shift".

[3] First Russian-French Workshop, Les Houches, France, 1999.

C. Schwob, L. Jozefowski, B. de Beauvoir, L. Hilico, F. Nez, L. Julien, F. Biraben, O. Acef et A. Clairon : "High resolution spectroscopy of hydrogen atoms".

[4] Third international symposium Modern Problems of Laser Physics, Novosibirsk, Russie, 2000 (actes).

G. Hagel, C. Schwob, L. Jozefowski, B. de Beauvoir, L. Hilico, F. Nez, L. Julien, F. Biraben, O. Acef et A. Clairon : "Metrology of hydrogen atom : determination of the Rydberg constant and Lamb shifts".

[5] Conference QED 2000, Frontier Tests of Quantum Electrodynamics and Physics of the Vacuum, Trieste, Italie, 2000 (actes).

G. Hagel, C. Schwob, L. Jozefowski, B. de Beauvoir, L. Hilico, O. Acef, F. Nez, L. Julien, A. Clairon et F. Biraben : "Metrology of hydrogen atom : determination of the Rydberg constant and Lamb shifts".

[6] Conference SPIE LASE 2001, San Jose, USA, 2001 (actes).

G. Hagel, C. Schwob, L. Jozefowski, B. de Beauvoir, L. Hilico, O. Acef, F. Nez, L. Julien, A. Clairon et F. Biraben : "Metrology of hydrogen atom : determination of the Rydberg constant and Lamb shifts".

[7] Second Russian-French Laser Symposium, Vladimir, Russie, octobre 2001.

G. Hagel, C. Schwob, L. Jozefowski, B. de Beauvoir, L. Hilico, O. Acef, J.-J. Zondy, F. Nez, L. Julien, A. Clairon et F. Biraben : "Precision spectroscopy of hydrogenic

systems”.

- [8] Third Russian-French Laser Symposium, Moscou, Russie, octobre 2003.
R. Battesti, P. Cladé, S. Guellati-Khélifa, C. Schwob, B. Grémaud, F. Nez, L. Julien et F. Biraben : ”Towards a measurement of the fine structure constant using cold atoms”.
- [9] 4th International Symposium Modern Problems of Laser Physics, Novosibirsk, Russie, août 2004.
R. Battesti, P. Cladé, S. Guellati-Khélifa, C. Schwob, B. Grémaud, F. Nez, L. Julien et F. Biraben : ”Preliminary measurement of h/m_{Rb} using Bloch oscillations of ultracold atoms”.
- [10] 17th International Conference on laser spectroscopy (ICOLS’05), Scotland, 19-24 Juin 2005.
P. Cladé, M. Cadoret, E. de Mirandes, S. Guellati-Khélifa, C. Schwob, F. Nez, L. Julien and F. Biraben : ”Bloch oscillations of ultracold atoms : a tool for h/m_{Rb} measurement”.
- [11] COLOQ 9, Dijon, 7-9 Septembre 2005.
P. Cladé, M. Cadoret, E. de Mirandes, S. Guellati-Khélifa, C. Schwob, F. Nez, L. Julien et F. Biraben : ”Oscillations de Bloch d’atomes froids : mesure de h/M_{Rb} ”.
- [12] 7ème Journée des Phénomènes Ultra-rapides (JPU2005), Villeneuve d’Ascq, 5-7 Décembre 2005.
F. Nez, O. Arnoult, C. Schwob, L. Julien, F. Biraben : ”Le laser femtoseconde : un outil pour mesurer des constantes fondamentales”.
- [13] 38ème European Group on Atomic Systems (EGAS), Ischia, Italie, juin 2006.
P. Cladé, O. Arnoult, M. Cadoret, E. de Mirandes, S. Guellati-Khélifa, C. Schwob, F. Nez, L. Julien et F. Biraben : ”From spectroscopy of atomic hydrogen to metrology of fundamental constants”.
- [14] Lepton Moments International Symposium, Cape Cod, USA, juin 2006.
P. Cladé, M. Cadoret, E. de Mirandes, S. Guellati-Khélifa, C. Schwob, F. Nez, L. Julien et F. Biraben : ”A new determination of the fine structure constant based on Bloch oscillations of ^{87}Rb atoms in a vertical optical lattice”.

Conférences

- [1] 5th European Quantum Electronics Conference (EQEC), Amsterdam, Hollande, 1994 (poster).
C. Schwob, C. Richy, K. Petsas, T. Coudreau, E. Giacobino, C. Fabre : ”Observation of instability and delayed bifurcation in a triply resonant optical parametric oscillator”.
- [2] Colloque sur les Lasers et l’Optique Quantique (COLOQ 4), Paris, France, 1995 (poster).
C. Schwob, C. Richy, C. Fabre : ”Spectroscopie en lumière comprimée”.

- [3] Congrès général de la Société Française de Physique, Paris, France, 1997 (poster).
C. Schwob, P. Souto Ribeiro, A. Maître, C. Fabre : "Au delà du shot noise : utilisation de faisceaux jumeaux en spectroscopie de grande sensibilité".
- [4] Colloque sur les Lasers et l'Optique Quantique (COLOQ 5), Strasbourg, France, 1997 (poster).
C. Schwob, P. Souto Ribeiro, A. Maître, C. Fabre : "Au delà du shot noise : utilisation de faisceaux jumeaux en spectroscopie de grande sensibilité".
- [5] Conference on Precision Electromagnetic Measurements (CPEM), Washington, Etats-Unis 1998 (oral, actes).
C. Schwob, L. Jozefowski, O. Acef, L. Hilico, B. de Beauvoir, F. Nez, L. Julien, A. Clairon, F. Biraben : "Frequency measurement of the 2S-12D transitions in hydrogen and deuterium, new determination of the Rydberg constant".
- [6] Colloque sur les Lasers et l'Optique Quantique (COLOQ 6), Talence, France, 1999 (poster).
C. Schwob, L. Masson, B. Grémaud, S. Guellati-Khélifa, F. Nez, L. Julien, F. Biraben : "Accélération d'atomes ultra-froids : mesure de h/M_A ".
- [7] 17th International Conference on Atomic Physics (ICAP), Firenze, Italie, 2000 (poster).
S. Guellati-Khélifa, C. Winisdoerffer, C. Schwob, B. Grémaud, F. Nez, L. Julien, F. Biraben : "Acceleration of ultracold atoms : measurement of h/M_A ".
- [8] Colloque sur les Lasers et l'Optique Quantique (COLOQ 7), Rennes, France, 2001 (poster).
R. Battesti, C. Schwob, B. Grémaud, S. Guellati-Khélifa, F. Nez, L. Julien, F. Biraben : "Accélération d'atomes ultra-froids : mesure de h/M_A ".
- [9] Conference on Precision Electromagnetic Measurements (CPEM), Ottawa, Canada 2002 (poster, actes).
R. Battesti, P. Cladé, C. Schwob, B. Grémaud, S. Guellati-Khélifa, F. Nez, L. Julien, F. Biraben : "Measurement of h/M_{Rb} with ultracold atoms".
- [10] 7th workshop on Atom Optics and Interferometry, Luntheren, Hollande, 2002 (poster).
S. Guellati-Khélifa, C. Schwob, R. Battesti, P. Cladé, B. Grémaud, F. Nez, L. Julien, F. Biraben : "Measurement of h/M_{Rb} with ultracold atoms".
- [11] Conference on Precision Electromagnetic Measurements (CPEM), Londres, Grande-Bretagne, 2004 (oral).
P. Cladé, R. Battesti, S. Guellati-Khélifa, C. Schwob, B. Grémaud, F. Nez, L. Julien, F. Biraben : "A preliminary measurement of h/m_{Rb} using ultracold atoms".
- [12] 8th European Conference on Atomic and Molecular Physics (ECAMP), Rennes,

- France, 2004 (poster).
- P. Cladé, R. Battesti, S. Guellati-Khélifa, C. Schwob, B. Grémaud, F. Nez, L. Julien, F. Biraben : "A preliminary measurement of h/m_{Rb} using ultracold atoms".
- [13] 19th International Conference on Atomic Physics (ICAP), Rio de Janeiro, Brésil, 2004 (poster).
- P. Cladé, R. Battesti, S. Guellati-Khélifa, C. Schwob, B. Grémaud, F. Nez, L. Julien, F. Biraben : "Bloch oscillations of ultracold atoms : a tool for metrological determination of h/m_{Rb} ".
- [14] 3rd Conference on Hydrogen Atom, Rio de Janeiro, Brésil, 2004 (oral).
- O. Arnoult, C. Schwob, F. Nez, L. Julien, F. Biraben : "Absolute frequency measurement of the 1S-3S line in atomic hydrogen".
- [15] Quantum Physics of Nature, Vienne, mai 2005 (oral).
- P. Cladé, M. Cadoret, S. Guellati-Khélifa, C. Schwob, F. Nez, L. Julien and F. Biraben : "Bloch oscillations of ultracold atoms".
- [16] European Quantum Electronic Conference, Munich, 12-17 juin 2005 (oral)
- P. Cladé, M. Cadoret, E. de Mirandes, S. Guellati-Khélifa, C. Schwob, F. Nez, L. Julien and F. Biraben : "Bloch oscillations of ultracold atoms : a tool for h/m_{Rb} measurement".
- [17] workshop du GREX (Gravitation and Experiment in Space), octobre 2005.
- P. Cladé, M. Cadoret, E. de Mirandes, S. Guellati-Khélifa, C. Schwob, F. Nez, L. Julien et F. Biraben : "Nouvelle mesure de la constante de structure fine à l'aide d'oscillations de Bloch d'atomes ultrafroids".
- [18] P. Cladé, M. Cadoret, E. de Mirandes, S. Guellati-Khélifa, C. Schwob, F. Nez, L. Julien and F. Biraben, Séminaire au Max Planck institut für Quantenoptik, Munich, 24 novembre 2005 : "A new determination of the fine structure constant based on Bloch oscillations of ^{87}Rb atoms in a vertical optical lattice".
- [19] Conference on Precision Electromagnetic Measurements, Turin, Italie, juillet 2006 (oral).
- P. Cladé, E. de Mirandes, M. Cadoret, S. Guellati-Khélifa, C. Schwob, F. Nez, L. Julien et F. Biraben : "New determination of the fine structure constant with cold rubidium atoms".
- [20] 20th International Conference on Atomic Physics, Innsbruck, Autriche, juillet 2006 (posters).
- M. Cadoret, E. de Mirandes, P. Cladé, C. Schwob, F. Nez, L. Julien, F. Biraben, S. Guellati-Khélifa : "A measurement of h/M_{Rb} and a determination of the fine structure constant".
- A. Antognini, F.D. Amaro, F. Biraben, J.M.R. Cardoso, C.A.N. Conde, A. Dax, A. Giesen, T.W. Hänsch, O. Huot, P. Indelicato, L. Julien, P.E. Knowles, F. Kottmann,

E. Le Bigot, Y.-W. Liu, J.A.M. Lopes, L. Ludhova, C.M.B. Monteiro, F. Mulhauser, T. Nebel, F. Nez, R. Pohl, P. Rabinowitz, J.M.F. dos Santos, L.A. Schaller, K. Schuhmann, C. Schwob, D. Taqqu, J.F.C.A. Veloso :

"Lamb Shift in Muonic Hydrogen I : Overview"

"LambShift in Muonic Hydrogen II : Results from 2003 and Improvements for 2007".

[21] International Workshop on Advances in Precision Tests and Experimental Gravitation in Space, Florence, Italie, septembre 2006 (oral).

E. de Mirandes, M. Cadoret, P. Cladé, S. Guellati-Khélifa, C. Schwob, F. Nez, L. Julien et F. Biraben : "New determination of the fine structure constant with cold rubidium atoms".

[22] Congrès Franco-Russe pour Jeunes Chercheurs (RFWYS 06), Les Houches, octobre 2006 (oral).

E. de Mirandes, M. Cadoret, P. Cladé, S. Guellati-Khélifa, C. Schwob, F. Nez, L. Julien et F. Biraben : "Bloch oscillations of ultracold atoms and determination of the fine structure constant".